

Université
de Toulouse

THÈSE

En vue de l'obtention du

DOCTORAT DE L'UNIVERSITÉ DE TOULOUSE

Délivré par : *l'Institut National Polytechnique de Toulouse (INP Toulouse)*

Présentée et soutenue le 14 Mai 2019 par :

Pamphile Tupui ROY

Uncertainty Quantification in High Dimensional Problems Quantification des incertitudes pour des problèmes de dimensions élevées

JURY

M. ANDREA SALTelli	Professeur d'Université, Universitetet i Bergen/Universitat Oberta de Catalunya	Rapporteur
M. DIDIER LUCOR	Chercheur HDR (CNRS), LIMSI	Rapporteur
M. NICOLAS GOURDAIN	Professeur d'Université, ISAE-Supaero	Examinateur
M. BERTRAND IOoss	Chercheur Séniор, EDF R&D	Examinateur
MME BÉNÉDICTE CUENOT	Chercheuse HDR, CERFACS	Directeur de thèse
M. JEAN-CHRISTOPHE JOUHAUD	Chercheur HDR, CERFACS	Co-directeur de thèse
MME SOPHIE RICCI	Chercheuse, CERFACS	Invité
MME NICOLE GOUTAL	Chercheuse Sénior, EDF R&D	Invité

École doctorale et spécialité :

MEGEP : Dynamique des fluides

Unité de Recherche :

Centre Européen de Recherche et de Formation Avancée en Calcul Scientifique

Directeur(s) de Thèse :

Mme Bénédicte CUENOT et M. Jean-Christophe JOUHAUD

Rapporteurs :

M. Andrea Saltelli et M. Didier Lucor

Acknowledgements

I have committed myself to this project but I was not alone. I would like to express my thanks to all CERFACS employees for their help and support.

Thank you to Bénédicte Cuenot and Jean-Christophe Jouhaud for their supervision.

Thank you to Sophie Ricci for her constant support and for helping me to sort things in my life.

Thank you to my friends and especially Robin and Romain who have been there all along.

A PhD in CFD requires some tools and a solid IT department. Thank you to everyone at CSG. I spent quite some time with some of you. Thank you to Isabelle, Gérard, Fred, Patrice.

Now comes the time for some special thanks. A massive thank you to Chantal Nasri and Marie Labadens. They are the heart of CERFACS.

Finally, I would like to thank my live-in companion and my family for their constant support.

Résumé

Les incertitudes font partie du monde qui nous entoure. Se limiter à une seule valeur nominale est bien souvent trop restrictif, et ce d'autant plus lorsqu'il est question de systèmes complexes. Comprendre la nature et l'impact de ces incertitudes est devenu un aspect important de tout travail d'ingénierie. D'un point de vue sociétal, les incertitudes jouent un rôle important dans les processus de décision. Les dernières recommandations de la Commission européenne en matière d'analyses des risques souligne l'importance du traitement des incertitudes.

Afin de comprendre les incertitudes, une nouvelle discipline mathématique appelée la quantification des incertitudes a été créée. Ce domaine regroupe un large éventail de méthodes d'analyse statistique qui visent à lier des perturbations sur les paramètres d'entrée d'un système (plan d'expérience) à une quantité d'intérêt.

L'objectif de ce travail de thèse est de proposer des améliorations sur divers aspects méthodologiques de la quantification des incertitudes dans le cadre de simulation numérique coûteuse. Cela passe par une utilisation des méthodes existantes avec une approche multi-stratégie mais aussi la création de nouvelles méthodes.

Dans ce contexte, de nouvelles méthodes d'échantillonnage et de rééchantillonnage ont été développées afin de mieux capturer la variabilité dans le cas d'un problème de grande dimension. Par ailleurs, de nouvelles méthodes de visualisation des incertitudes sont proposées dans le cas d'une grande dimension des paramètres d'entrée et d'une grande dimension de la quantité d'intérêt.

Les méthodes développées peuvent être utilisées dans divers domaines comme la modélisation hydraulique ou encore la modélisation aérodynamique. Leur apport est démontré sur des systèmes réalistes en faisant appel à des outils de mécanique des fluides numérique. Enfin, ces méthodes ne sont pas seulement utilisables dans le cadre de simulations numériques, mais elles peuvent être utilisées sur de réels dispositifs expérimentaux.

Mots clés : Quantification d'incertitudes, Plan d'expériences, Grande dimension, Visualisation de données, Mécanique des fluides numérique

Abstract

Uncertainties are predominant in the world that we know. Referring therefore to a nominal value is too restrictive, especially when it comes to complex systems. Understanding the nature and the impact of these uncertainties has become an important aspect of engineering work. On a societal point of view, uncertainties play a role in terms of decision-making. From the European Commission through the *Better Regulation Guideline*, impact assessments are now advised to take uncertainties into account.

In order to understand the uncertainties, the mathematical field of Uncertainty Quantification (UQ) has been formed. UQ encompasses a large palette of statistical tools and it seeks to link a set of input perturbations on a system (design of experiments) towards a quantity of interest.

The purpose of this work is to propose improvements on various methodological aspects of uncertainty quantification applied to costly numerical simulations. This is achieved by using existing methods with a multi-strategy approach but also by creating new methods.

In this context, novel sampling and resampling approaches have been developed to better capture the variability of the physical phenomenon when dealing with a high number of perturbed inputs. These allow to reduce the number of simulation required to describe the system. Moreover, novel methods are proposed to visualize uncertainties when dealing with either a high dimensional input parameter space or a high dimensional quantity of interest.

The developed methods can be used in various fields like hydraulic modelling and aerodynamic modelling. Their capabilities are demonstrated in realistic systems using well established computational fluid dynamics tools. Lastly, they are not limited to the use of numerical experiments and can be used as well for real experiments.

Keywords: Uncertainty Quantification, Design of Experiments, High dimensions, Data visualization, Computational Fluid Dynamics

Contents

I Introduction	1
1 Context	3
2 Literature Review	9
2.1 Design of Experiments	10
2.2 Uncertainty Quantification	14
2.2.1 Uncertainty Propagation	14
2.2.2 Sensitivity Analysis	17
2.3 Surrogate Models	24
2.3.1 Snapshot Method	26
2.3.2 Polynomial Chaos Surrogate Model	27
2.3.3 Gaussian Process Surrogate Model	29
2.3.4 Multifidelity	31
2.3.5 Model Validation	33
2.4 Uncertainty Visualization	36
2.4.1 Highest Density Region	38
3 Scientific Questions	41
II Methodological Contributions	43
4 Scientific Dissemination	45
Articles	45
Conferences	46
Reviews	46
European Projects	47
Training	47
5 Batman	49
5.1 Description	49
5.2 Implementation	51
5.3 Functionalities	52
5.3.1 General functionment	52
5.3.2 Using it	53
5.3.3 Content of <i>test_cases</i>	53
5.4 Dissemination	53
6 Constructing a Design of Experiments	55
6.1 Introduction	55
6.2 Presentation of the Method	56

6.2.1	Determination of the Exclusion Field	56
6.2.2	Sampling and Selection Procedures	57
6.3	Results	61
6.3.1	Uniformity of the Design	61
6.3.2	Integration Convergence	63
6.4	Advantages	65
6.5	Summary	69
7	Resampling the Design of Experiments	71
7.1	Introduction	71
7.2	Presentation of the Methods	72
7.3	Construction of the Hypercube	73
7.4	Evaluation of the Methods	74
7.4.1	Restriction of the DoE	75
7.4.2	Application on Analytical Functions	77
7.5	Summary	81
8	Uncertainty Visualization	83
8.1	Introduction	83
8.2	Uncertainty Visualization of Functional Output Data	84
8.2.1	Dynamic Visualization of Functional Outputs's Statistics	84
8.2.2	Sonification of Functional Outputs's Statistics	84
8.3	Uncertainty Visualization of Large Number of Input Variables	86
8.4	Summary	89
III	Applications	93
9	Comparison of PC and GP surrogates for UQ of spatially distributed open-channel steady flows	95
9.1	Introduction	96
9.2	Hydraulic Modelling	98
9.2.1	1-D Shallow Water Equations (SWE)	98
9.2.2	Garonne River Case Study	99
9.2.3	Sources of Uncertainties and Quantity of Interest .	101
9.3	Comparison of PC and pGP Surrogates	102
9.3.1	Reference Monte Carlo (MC) Results	102
9.3.2	Convergence Analysis for Surrogates	103
9.4	Summary	108
10	The Aerothermal Flow around the LS89 Blade Cascade	111
10.1	Introduction	111
10.2	Case Description	112
10.3	Numerical Setup	115
10.4	Uncertainty Quantification Results	117
10.5	Summary	119

11 UQ-Driven Robust Design Assessment of a Swirler Geometry	123
11.1 Introduction	124
11.2 Configuration and Numerical Setup	126
11.2.1 The Swirled Injector	126
11.2.2 Numerical Setup	126
11.2.3 Geometrical Uncertainties of the Swirler	129
11.3 Dimensionality Reduction and Statistical Analysis of Un- certain Parameters	130
11.4 Generation of Datasets	131
11.5 Results and Discussion	133
11.6 Summary	136
12 Optimization of Helically Roughened Heat Exchanger	139
12.1 Introduction	140
12.2 Case Description	141
12.2.1 Geometrical and Meshing Considerations	141
12.2.2 Numerical Set-Up	143
12.2.3 Optimization Problem	144
12.3 Results	146
12.3.1 Continuous Rib	146
12.3.2 Discontinuous Rib	147
12.3.3 Optimal Discontinuously Ribbed Heat Exchanger .	151
12.4 Summary	157
IV Conclusion	161
V Annexes	169
A Functions and Datasets	171
A.1 Analytical Functions	171
A.2 Datasets	172
B Optimization Method	173
C Computational Fluid Dynamics	175
C.1 Governing Equations of Compressible Flows	175
C.2 Turbulence Modelling	176
D Batman's API	179
Bibliography	185

I

Introduction

1	Context	3
2	Literature Review	9
2.1	Design of Experiments	10
2.2	Uncertainty Quantification	14
2.2.1	Uncertainty Propagation	14
2.2.2	Sensitivity Analysis	17
2.2.2.1	From Local to Global Sensitivity Analysis .	17
2.2.2.2	Variance-Based Sensitivity Analysis	17
2.2.2.3	Moment-based Sensitivity Analysis	20
2.3	Surrogate Models	24
2.3.1	Snapshot Method	26
2.3.2	Polynomial Chaos Surrogate Model	27
2.3.2.1	Polynomial Basis	28
2.3.2.2	Truncation Strategy	28
2.3.2.3	Spectral Projection Strategy	29
2.3.3	Gaussian Process Surrogate Model	29
2.3.3.1	Regression Procedure	29
2.3.4	Multifidelity	31
2.3.5	Model Validation	33
2.3.5.1	Mean Square Error and Alike	33
2.3.5.2	Coefficient of Determination: Q_2	34
2.3.5.3	Kolmogorov-Smirnov Statistical Test	34
2.3.5.4	Graphical Quality Assessment	34
2.3.5.5	Holdout as Opposed to K -fold or Cross Validation	35
2.4	Uncertainty Visualization	36
2.4.1	Highest Density Region	38
3	Scientific Questions	41

1 | Context

Ce chapitre présente le contexte dans lequel ce travail de thèse s'inscrit.

L'optimisation robuste et le processus de conception lui-même sont des objectifs majeurs des travaux d'ingénierie réalisés en simulation numérique, notamment dans l'industrie aéronautique [61]. Afin de réduire le nombre d'itérations entre la conception et les essais, les outils de simulation numérique des fluides (CFD) sont de plus en plus utilisés. Aujourd'hui, des simulations complexes sur des grilles à haute résolution sont possibles grâce aux développements continus des modèles numériques et des ressources de calculs (HPC). Or, les simulations déterministes ne fournissent qu'une connaissance limitée d'un système. Les incertitudes dans le modèle numérique et dans la formulation du problème se traduisent inévitablement par des incertitudes sur les résultats [197].

Les méthodes classiques en quantification des incertitudes (UQ), basées sur l'approche Monte-Carlo (MC), nécessitent un grand nombre de simulations [201], qui dépassent rapidement les limites des ressources disponibles. Le coût de l'étude UQ peut toutefois être considérablement réduit lorsque l'expérience est remplacée par un modèle de substitution [154]. La construction du modèle de substitution nécessite un ensemble d'expériences (DoE) dont la définition est primordiale afin d'imiter correctement l'expérience réelle.

*Le but de cette thèse est de proposer des pistes d'amélioration sur divers aspects méthodologiques en UQ appliqués à des environnements numériques coûteux. Les méthodes développées peuvent être utilisées dans divers domaines et sont démontrées par de multiples applications. De plus, ces méthodes ne se limitent pas à l'utilisation d'expériences numériques et peuvent également être utilisées pour des expériences *in vivo*.*

Ce manuscrit est divisé en quatre parties : Part I passe en revue la littérature sur les concepts et méthodes de UQ ; Part II présente mes contributions méthodologiques ; Part III propose quelques applications des nouvelles méthodes—dans un environnement numérique coûteux— ; Part IV fait le point sur ces travaux et donne des perspectives pour de futurs travaux de recherche.

ROUST optimization and the design process itself are major purposes of engineering works dealing with numerical simulations,

especially in aeronautical or automotive industry [61]. Despite the large amount of work that has been devoted to the design of efficient optimization techniques, the design process still requires important investments (financial and human) [77]. Design errors which appear after the industrialization phase and their possible implications may be critical. A classical example of such failure is the Space Shuttle *Challenger* disaster in 1986 [59]. During the Space Shuttle's ascent, a failure of O-ring seals on its right solid rocket booster caused its disintegration. It has been shown that an uncertainty on the behaviour of this O-ring had been a key factor to the accident. On the launch day, the temperature was particularly low and the effect of such low temperature on the O-ring was not known. Engineers had to extrapolate the response of the system to this event. Linked to a strong pressure at NASA for this launch, the decision to maintain the launch was made even-though engineers warned about the uncertainties of their findings. This case led to the creation of NASA's Safety, Reliability, Maintainability, and Quality Assurance (SRM&QA) program.

In order to decrease the number of iterations between conception and experiments, and to avoid irreversible errors during the preliminary design phase, Computational Fluid Dynamics (CFD) tools have been used more and more in the past decades. Nowadays, CFD codes have reached maturity and are able to represent accurately physical flow phenomena. Complex flow simulations on high-resolution grids are possible thanks to the continuous developments in numerical models and in High Performance Computing (HPC). Nevertheless, deterministic simulations only provide limited knowledge about a system. Uncertainties in the numerical model as well as in the problem formulation or inputs are undoubtedly present and translate into uncertainties in the outputs [197]. Thus, how to answer the question: what is the probability that the model output exceed a threshold? In Fig. 1.1, uncertainties coming from two uncertain parameters x_1, x_2 are propagated through the model \mathcal{M} leading to a probabilistic distribution of possible values of \mathbf{Y} the Quantity of Interest (QoI). In this examples, a threshold is represented by the *dashed-line*.

The output variability of a system can be confusing regarding the source of these uncertainties. Does it come from our model or from the physics? Uncertainties can be classified as:

Aleatoric errors: intrinsic to the system,

Epistemic errors: due to a lack of knowledge,

Numerical error: due to the construction of the numerical scheme.

Ideally, our model should only contain aleatoric uncertainties as it represents the physical variability of the system. However, the diversity of uncertainties due to the boundary conditions or initial conditions as well as to model parameters (input data, geometry, simplification of the model physics, etc.) limits the predictivity of the simulations:

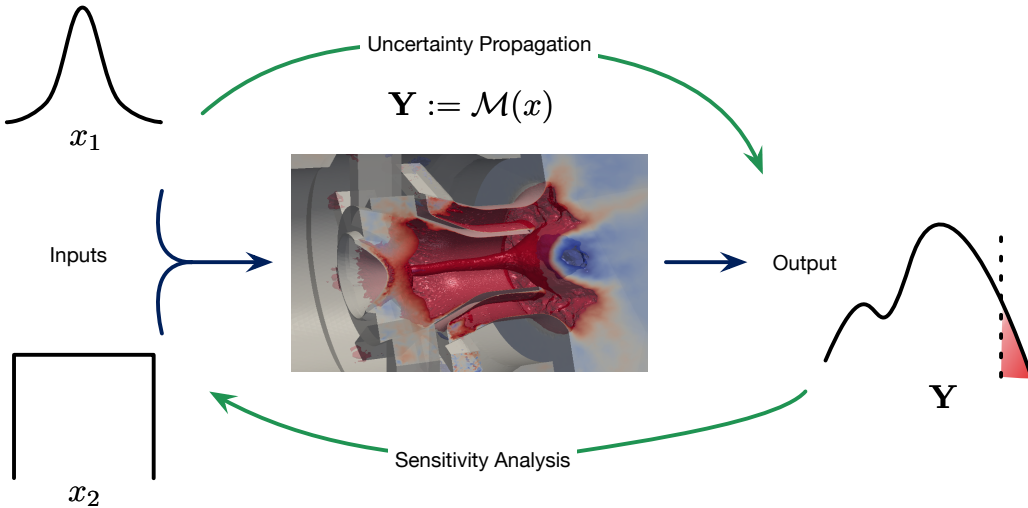


Figure 1.1 – Schematization of the Uncertainty Quantification procedure in case of two uncertain input parameters perturbing a numerical model \mathcal{M} .

the QoI can be easily affected and shadowed by the conjugation of all these types of uncertainties. This assessment explains why Uncertainty Quantification (UQ) is now becoming a mandatory step in application-oriented modelling for operational and industrial purposes [55, 155]. It provides insight into the level of uncertainty in the numerical simulation results but also gives access to a sensitivity analysis which aims to describe the respective influences of the input parameters on the QoI. The inclusion of UQ in a design optimization cycle hence allows manufacturers to design quicker and obtain better, cheaper and more robust products. Depending on the question we seek to answer, we have to determine the type of UQ study to perform:

- *Uncertainty Propagation*,
Propagate an initial perturbation within the system and observe its outputs.
- *Sensitivity Analysis*,
Rank the input parameters regarding their impact on the output.
- *Risk Assessment*.
Observe the probability to exceed a threshold or get the probability of a particular quantile.

Each question is answered using specific tools and special care has to be taken if one wants to conduct different analysis. For instance, some formulations to compute sensitivity indices have requirements which are not conform with both Uncertainty Propagation and Risk Assessment.

Classical UQ methods, based on the Monte-Carlo approach, require a large number of simulations [201], which quickly go beyond the limits of available resources (such as CPU, financial costs). This is especially

true when it comes to large-dimensional problems, both with respect to the domain discretization and to the number of uncertain input parameters. The cost of the UQ study can, however, be significantly reduced when the experiment is replaced by a proxy, or surrogate model, which is formulated in a parameter space and which is fast to evaluate for any set of uncertain variables [154]. The construction of the surrogate model requires a set of experiments, Design of Experiments (DoE), to learn from. To correctly emulate the real experiment, the definition of the DoE is paramount.



- The purpose of this thesis is to propose directions of improvement on various methodological aspects of UQ applied to costly numerical environments. The methods developed can be used in various fields and are demonstrated through multiple applications. Moreover, these methods are not limited to the use of numerical experiments and can be used equally for *in vivo* experiments.

Organization

This manuscript is divided into four parts and is tailored as follows:

Part I *After a general introduction about the context of this thesis, Chapter 2 reviews the literature on concepts and methods for UQ, Section 2.1 goes from a state-of-the-art on the different methods to design experiments; then Section 2.2 describes the different techniques commonly used in UQ, as well as the latest advances. Section 2.3 details the construction of a surrogate model which may be required to perform such statistical analysis. Section 2.4 presents how uncertainties are commonly visualized. After this literature review, some scientific questions arise and the complete scope of this thesis work is given in Chapter 3.*

Part II *presents my methodological contributions,*

In Chapter 5, a new UQ open-source tool is introduced. It serves as a demonstrator for all the methods developed. Following chapters are the responses to the scientific questions rose. Chapter 6 introduces a new iterative and versatile sampling method while Chapter 7 addresses question of the resampling of an existing DoE. Finally, Chapter 8 proposes novel visualization techniques to visualize uncertainty in high dimensions.

Part III *some applications of the new methods—in a costly numerical environment—are proposed,*

Chapter 9 is a comparison between two surrogate models. Chapter 10 demonstrates the new resampling techniques capabilities, to perform the first UQ analysis using Large Eddy Simulation on the

LS89 blade cascade. Chapters 11 and 12 present two applicative cases of Batman. In Chapter 11, the focus is put on the dimensionality of the input parameter space while in Chapter 12, the toolchain is used to perform and UQ analysis to understand the physical phenomena and to perform an optimization of the parameters.

Part IV *puts a point on this thesis work and draw some perspectives for future work.*

2 | Literature Review

Ce chapitre présente une revue de la littérature sur les concepts et les méthodes associées à la quantification des incertitudes (UQ) dans un environnement numérique coûteux : de la définition d'un plan d'expériences (DoE) pour construire un modèle de substitution, à l'utilisation de ce modèle de substitution pour calculer les statistiques et finalement visualiser les résultats.

Les avancées et les limites actuelles du DoE sont présentées Section 2.1. Les séquences OLHS et Sobol' sont toutes deux considérées comme des pratiques de référence bien qu'elles présentent certaines limites telles que les propriétés itératives et la randomisation, respectivement.

En utilisant cet échantillon, on peut effectuer une analyse UQ avec des méthodes détaillées en Section 2.2. L'analyse de sensibilité globale (GSA) est recommandée par rapport à une analyse locale de sensibilité. Concernant les méthodes à proprement dit, une SA basée sur la variance reste prédominante, mais les méthodes basées sur les moments semblent être un bon complément dans une étude. Dans un environnement numérique coûteux, il n'est pas possible d'effectuer directement une UQ et l'utilisation d'un modèle de substitution offre une solution. La Section 2.3 expose deux des méthodes les plus utilisées : Processus gaussien (GP) et Chaos polynomial (PC). Enfin, la Section 2.4 introduit le problème de la visualisation des incertitudes. Il s'agit d'un domaine relativement nouveau avec un corpus d'études limité. Il n'y a actuellement aucune recommandation claire sur la façon de visualiser les incertitudes. À partir de cette revue, le Chapter 3 détaille les trois questions auxquelles cette thèse vise à répondre :

- *Comment construire un DoE dans un espace de paramètres à haute dimension ?*
- *Comment rééchantillonner un DoE en considérant la QoI d'expériences déjà évaluées ?*
- *Comment visualiser les incertitudes dans des cas de grande dimension ?*

2.1 Design of Experiments

ONE of the main objectives when performing numerical—or real—experiments is to understand the variation of a QoI with respect to the variation of some input parameters [197]. Each experiment, or sample, corresponds to a particular set of input parameters x_k with $k \in [1, \dots, d]$, where d is the number of dimensions. As a result, the group of N_s samples, or DoE, is noted as $\mathbf{X}_d^{N_s}$. For simplicity either the dimensionality d or the number of samples N_s is omitted in the manuscript. Nevertheless, the subscript denotes d while the superscript denotes N_s . Then the forward model (or experiment) \mathcal{M} can be simulated for each sample

$$(\mathbf{X}_d^{N_s}, \mathcal{Y}) = (\mathbf{x}^{(i)}, \mathbf{Y}^{(i)})_{1 \leq i \leq N_s}, \quad (2.1)$$

where \mathcal{Y} is the QoI and $\mathbf{Y}^{(i)} := \mathcal{M}(\mathbf{x}^{(i)})$ corresponds to the deterministic integration of the forward model \mathcal{M} as a black box for the i th set of input parameters $\mathbf{x}^{(i)}$ —see Fig. 2.1.

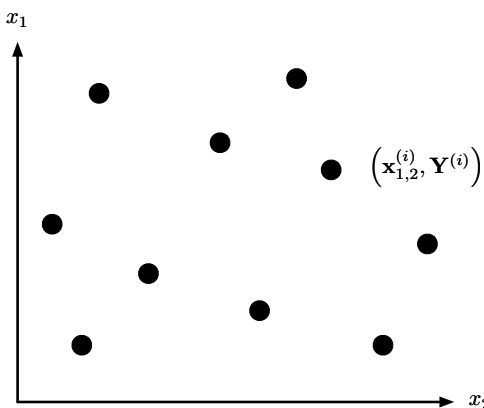


Figure 2.1 – Sketch of a 2-dimensional Design of Experiments. Every *black dot* represents an experiment $x_{1,2}^{(i)}$ used to compute the output $\mathbf{Y}^{(i)}$.

In its basis form, a DoE is described by a d -dimensional cube: a hypercube—see Fig. 2.2. A hypercube is parametrized by the minimal and maximal values of each parameter. If parameters depends on each other, or if there are constrains on the parameters, non-rectangular domains [137] have to be considered.

From exploratory phases to more advanced analyses, such as UQ and robust optimization, DoE aims at helping better understand the physical mechanisms governing the problem of interest [201]. Therefore, the objective of efficient DoE is to maximize the coverage of the input space, i.e. space filling, with the aspiration of capturing most of the underlying physics. Such analyses typically require a large number of experiments in order for the statistics of the QoIs to converge (especially for extreme quantiles). However, depending the complexity of the experiment, its

2.1. DESIGN OF EXPERIMENTS

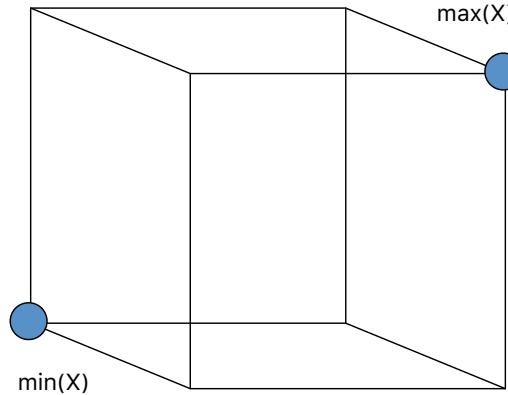


Figure 2.2 – Sketch of a 3-dimensional hypercube.

intrinsic cost or its return time, the total number of experiments may be limited. In this regard, many studies have focused on the optimization of the space-filling properties for a given number of experiments.

Beyond random design also called *Monte Carlo* experiments, One-At-a-Time (OAT) design is the most trivial form of engineered DoE. It consists in changing only one parameter at a time. While this method is simple to implement and allows for a quick interpretation on a physical aspect, this sampling procedure requires a huge number of simulations as requiring $(N_s)^d$ samples. This exponential growth is called the *curse-of-dimensionality*. Let's consider the unit-hypercube, all bounds range from 0 to 1. Now, having a distance of 0.1 between each point, the number of points required to fill the unit interval would be 10. In a 2-dimensional hypercube the same spacing would require 100 and in 3-dimensions 1000 points. As the number of dimensions goes, the number of experiments which is required to fill the space evenly rises exponentially as the volume of the space increases—see Fig. 2.3. To mitigate this problem, one could sparse the DoE. The problem comes to an assessment of the quality of this DoE.

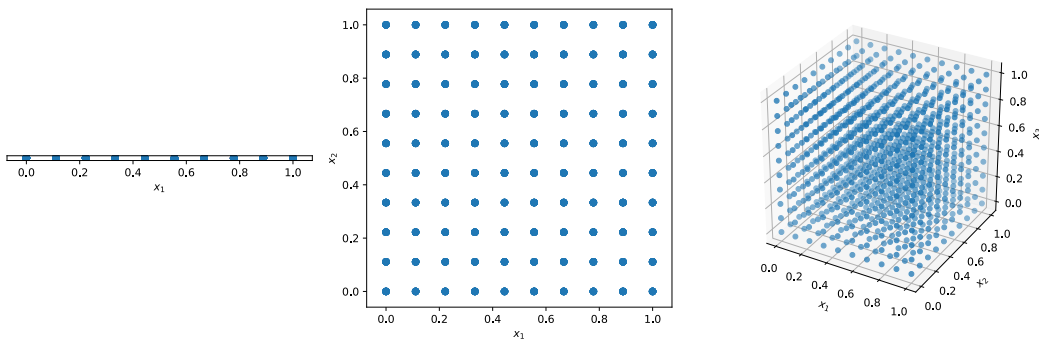


Figure 2.3 – Sketch of the *curse-of-dimensionality*. Visualization of the volume of the parameter space in 1, 2 and 3 dimensions. OAT design with points separated by a distance of 0.1.

Different metrics are commonly used to assess the space filling of a DoE. They can be categorized into (i) geometrical and (ii) uniformity

criteria. Among the most used geometrical criteria are the *maximin* and *minimax* [184]. They, respectively, maximize the minimal distance between all points or minimize the maximal distance between any location in space and all points of the sample. A similar criterion is found by using a *minimum spanning tree* [79] in which the best design corresponds to a maximization of the mean distance between all connections and the minimization of the variance in these distances. The uniformity criterion, instead, measures how the spread of the points deviates from a uniform distribution. The centred discrepancy C^2 is commonly used to measure the uniformity [71, 51]:

$$C^2(\mathbf{X}_d^{N_s}) = \left(\frac{13}{12} \right)^d - \frac{2}{N_s} \sum_{i=1}^{N_s} \prod_{k=1}^d \left(1 + \frac{1}{2} |x_k^{(i)} - 0.5| - \frac{1}{2} |x_k^{(i)} - 0.5|^2 \right) \\ + \frac{1}{N_s^2} \sum_{i,j=1}^{N_s} \prod_{k=1}^d \left(1 + \frac{1}{2} |x_k^{(i)} - 0.5| + \frac{1}{2} |x_k^{(j)} - 0.5| - \frac{1}{2} |x_k^{(i)} - x_k^{(j)}| \right). \quad (2.2)$$

There are three main methodologies for defining a DoE: (i) MC, (ii) *Latin Hypercube Sampling* (LHS) and (ii) Quasi-Monte Carlo (QMC) methods [41, 83]. Kucherenko *et al.* [127] have recently compared MC and LHS against the low discrepancy sequence of *Sobol'*, which is a well-established QMC method. They concluded that both LHS and QMC offer superior integration performance over MC. Integrating a complexe function requires a good space coverage and this performance is assimilable to a discrepancy measure. Figure 2.4 is an example of these three methods to construct samples of size $N_s = 256$ in dimension $d = 2$. In this low dimensional space, the superiority in terms of space coverage of both LHS and *Sobol'* over MC is clear. MC exhibits lots of clustered regions and it translates in a two orders difference in terms of centred discrepancy compared to the other methods.

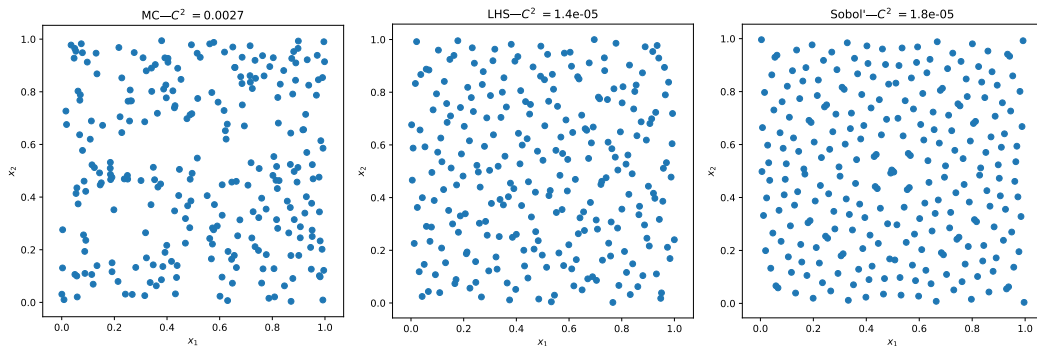


Figure 2.4 – Example of DoE constructed with MC, LHS and the low discrepancy sequence of *Sobol'* with $N_s = 256$.

On the one hand, LHS-based sampling methods are one-shot design strategies [158, 71]. The principle is simple: considering N_s samples, in each 1-dimensional subprojection of the parameter space there should be N_s samples. It means that samples are not sharing coordinates with

each other. Orthogonal arrays are a slight evolution of this principle. Each 1-dimensional subprojection is spitted into N_s to form an orthogonal grid of size N_s^d and only one sample is allowed per cell. Figure 2.5 shows two different orthogonal LHS with $N_s = 10$. Although both valid, they do not cover the parameter space equally. In Fig. 2.5(b) lots of points are aligned preventing some regions to be explored. Constructing such design is numerically easy and it is possible to optimize the space-filling properties by swapping elements for instance [71, 51]. A basin-hopping algorithm [230] is commonly used to resolve this global optimization problem. This is a stochastic algorithm used to find global optima which combine a random perturbation of the parameters, a local minimization and an accepting or rejecting of new coordinates depending on a decaying parameter.

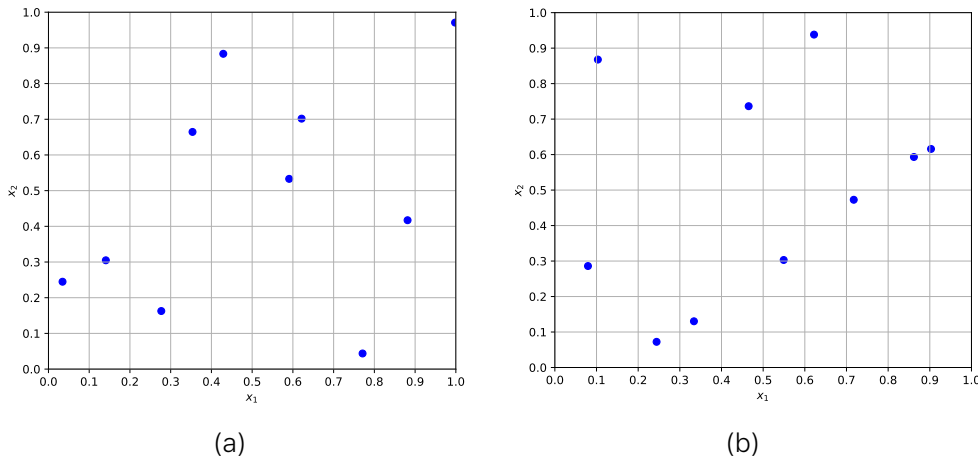


Figure 2.5 – Two orthogonal LHS examples with $N_s = 10$ demonstrating the qualitative difference in terms of space-filling.

The use of LHS requires the practitioner to set *a priori* the total number of samples contained in the DoE. Although there have been some attempts to construct progressive LHS, they still require an initial design to work properly [212].

On the other hand, low discrepancy sequences are iterative designs which can be continued without compromising the discrepancy. The practitioner is then able to increase the number of samples afterwards for quality reasons or if other experiments can be afforded.

Liu et al. [145] recently reviewed iterative DoE in a metamodeling context. In their study, it is shown that most iterative methods need an initial design as a starting point. A particular benefit of this approach is that it allows the use of physics information from the system to guide further exploration of the DoE. In this case, such iterative methods are called adaptive methods. Here as well, basin-hopping-based methods are commonly used to find the coordinates of the new sample. Except for some work in [50], the number of iterative methods not requiring an initial design is limited. This can be explained both by the quality of the

initial designs (using LHS of Sobol' sequence) and by the performance of the refinement algorithm. There are even fewer options if the iterative design cannot take advantage of the output of the experiments. Low discrepancy sequences are an example of such methods. In some context, stochastic methods may be required —to compute sensitivity indices for instance [200]. Scrambling the sequences [170] can avoid this pitfall but then the method is no longer iterative.

2.2 Uncertainty Quantification

2.2.1 Uncertainty Propagation

UNCERTAINTY PROPAGATION (UP) seeks to transmit uncertainties throughout the system. But are we talking about the uncertainties of the input parameters or the output QoI? In this section we focus on a *direct problem* which relate to the transmission of uncertainties from the input to the output. The other way around is called an *inverse problem* and is discussed in Section 2.2.2.

Uncertainties can be described using a probabilistic approach through the use of Probability Density Functions (PDF). This function computes the probability of occurrence of a phenomenon. Thus, propagating uncertainties comes to determining the PDF of the QoI.

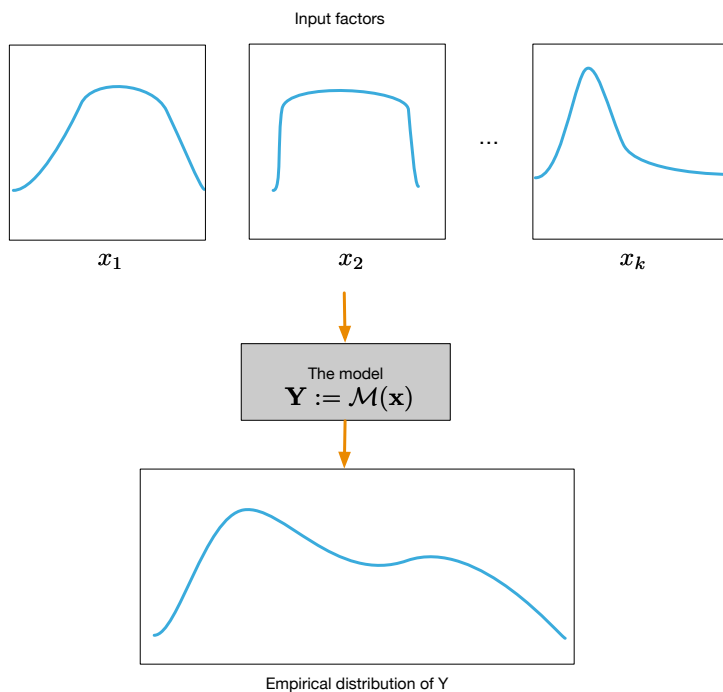


Figure 2.6 – Sketch of the UP procedure.

Figure 2.6 is a representation of the UP procedure. In practice, propagating uncertainties comes to sampling the PDFs of inputs and observing the impact on the QoI. It should be emphasized that the

outcome of the UP depends on the prescribed PDFs for the inputs. The nature of the PDF and the ranges of each parameter is paramount. Without any prior knowledge on input parameters, uniform distributions are traditionally used. As for the ranges, some fixed percentage of variation is commonly used. While this strategy could indeed correspond to the correct variability of some parameters, this may lead to wrong analysis. In [179], the example of radioactive waste transport on the Yucca Mountain is taken. In this UP analysis, the percolation rate of the water from the surface to the disposal was wrongly estimated between 0.02 and 1 millimetre per year while its true value was close to $\sim 3\,000$ mm. The underestimation of this parameter led to an underestimation of 4 orders of magnitude of the transport of some radioactive components.

As we are interested in computing statistics on the QoI, this requires a statistically significant sampling. A high number of samples is required to recover the empirical PDF of the QoI. One must note that in order to find the tail of the PDF—the least frequent event—it requires an even larger number of samples.

Discrete representations such as histograms can be used to represent the PDF. However, continuous functions can be obtained using a technique called Kernel Density Estimation (KDE) [231]. The probability to observe a QoI's value Y^* is given by the PDF estimator $\hat{f}(Y^*)$

$$\hat{f}(Y^*) = \frac{1}{N_s} \sum_{i=1}^{N_s} K_{h_i}(Y^* - Y^{(i)}), \quad (2.3)$$

where N_s is the number of samples. $K_{h_i}(\cdot) = K(\cdot/h_i)/h_i$ is the scaled kernel chosen for the modal probability density function with h_i the bandwidth for the i th component. In the present work K is the Gaussian kernel and h_i are optimized by cross-validation of the log-likelihood of the data. It reads

$$K(Y^*, Y^{(i)}) = \exp\left(-\frac{D(Y^*, Y^{(i)})^2}{2h^2}\right), \quad (2.4)$$

with D as a distance function. Having a Gaussian kernel does not restrict the estimated PDF to be Gaussian and this should not be mistaken. It should be noted that estimating the density in a high-dimensional parameter space is challenging [205, 208]. See Section 2.4 for a n -dimensional representation of the PDF.

Depending on the number of samples available and on the parameters of the method, this process can lead to a PDF which is far from the real one. The principle of KDE is fairly easy to understand—see Fig. 2.7. Each sample value Y is represented on the x -axis. Around each value, a rectangle of fixed width and fixed height is drawn. When there is an overlap, the rectangle values are summed up. The value of the width represents the bandwidth, and the general shape of the rectangle is called the kernel. As previously stated, Gaussian kernel is classically used and corresponds to a bell-curve shape. From this procedure, it can

be seen that the resulting PDF can be of any shape and is not limited to the nature of the kernel. In a sense, the kernel act as a filtering artefact.

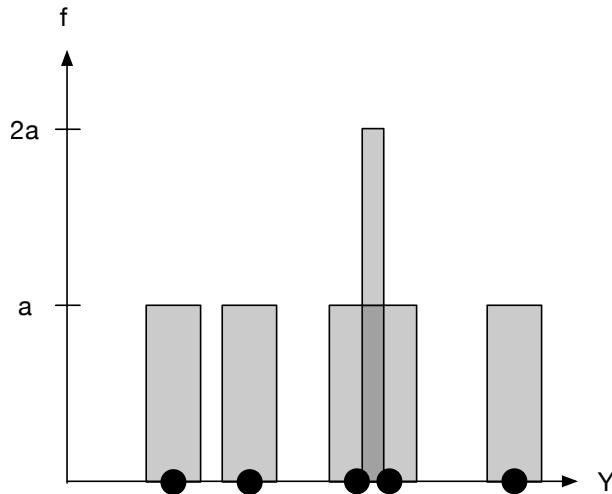
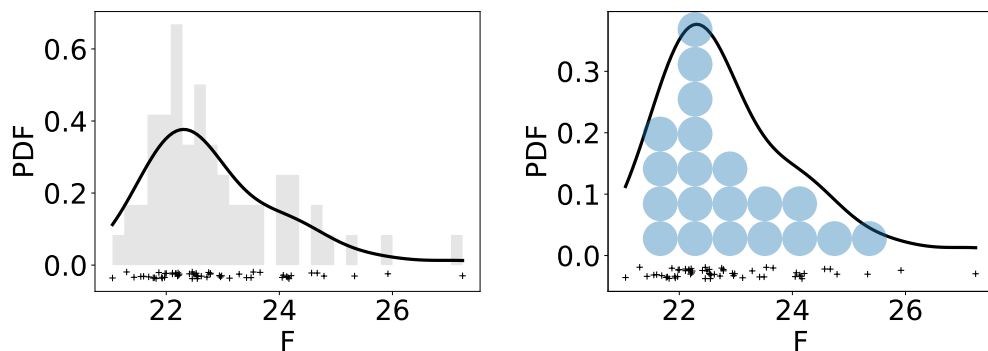


Figure 2.7 – Sketch of a Kernel Density Estimation procedure with a rectangular kernel.

Figure 2.8(a) presents a KDE of a 1-dimensional QoI along with a histogram representation of the data. The KDE acts as a smoothing procedure of the histogram as previously highlighted. Another possibility—Fig. 2.8(b)—is to use the quantile dotplot [117] which allows to directly count the quantiles. In this example, there are 20 circles, and below $F = 22.5$ there are 11 circles. Thus >50% of the samples are located below $F = 22.5$.



(a) Kernel Density Estimation and histogram (b) Kernel Density Estimation and quantile dotplot

Figure 2.8 – Visualization of a 1-dimensional PDF.

Once the PDF of the QoI is available, it can be used to: (i) observe the probability of exceeding a threshold; (ii) compute the probability to have a certain event; or just (iii) get general statistics (mean, variance, quantiles).

2.2.2 Sensitivity Analysis

SENSITIVITY ANALYSIS (SA) refers to the determination of the contribution of different parameters on quantities of interest [201, 108]. The most natural way to do SA would be to consider the derivatives. But this information is known to be too local or restrictive—although there are some works extending the capabilities of these methods [128]. In the literature, a distinction is made between local and global SA. In the following both local-based SA (derivative) and global-based SA (variance-based and moments-based) methods are presented.

2.2.2.1 From Local to Global Sensitivity Analysis

An intuitive way to characterize the importance of each parameter on a QoI is to compute the derivatives of the output with respect to an input. This method is called *elementary effects* and a successful implementation is found with Morris [164]. An elementary effect $d\mathbf{x}_k^*$ is defined as

$$d\mathbf{x}_k^* = \frac{|Y(\mathbf{x}_k^*) - Y(\mathbf{x}_k)|}{|\mathbf{x}_k^* - \mathbf{x}_k|}, \quad (2.5)$$

with \mathbf{x}_k a given sample and \mathbf{x}_k^* a sample which differs from \mathbf{x}_k by an increment δ . This effect can be computed with respect to N_s samples and d dimensions which induce to a total number of samples $N = N_s \times (d + 1)$. It is called a screening method and it corresponds to an OAT walk of the DoE. Figure 2.9 is an example with $N_s = 5, d = 3$. Then the mean of absolute elementary effects reads

$$\hat{\mu}_k = \frac{1}{N_s} \sum_{i=1}^{N_s} \frac{|Y(\mathbf{x}_k^*) - Y(\mathbf{x}_k^i)|}{|\mathbf{x}_k^* - \mathbf{x}_k^i|}. \quad (2.6)$$

A popular extension of this method is found with the derivative-based global sensitivity measures (DGSM) [128, 28]. Although these methods perform well in high dimensions and with a low sampling size, they are not exempt of flaws. As local methods, the construction of the indices is based on local OAT variations which are not able to take into account correctly correlations between the input parameters.

It should be noted that some solvers directly give access to the derivative information for each sample for a reduced extra cost. Although this capability requires some effort in terms of code, some automatic derivative software can alleviate this effort.

2.2.2.2 Variance-Based Sensitivity Analysis

Variance-based Sensitivity Analysis allows obtaining the contribution of the parameters on the QoI's variance [73]. Classical Sobol' [217] method, which is presented, gives not only a ranking but also quantifies

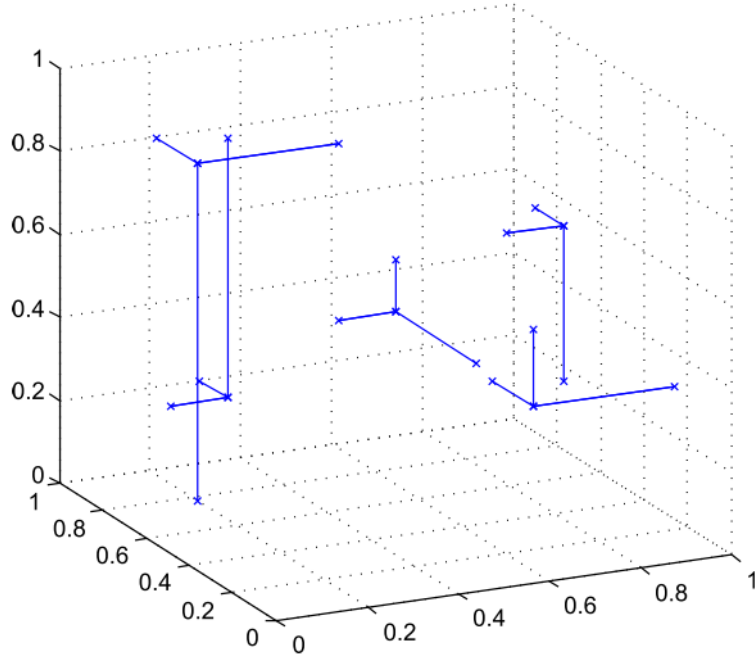


Figure 2.9 – Sketch of Morris's screening method. Source [28].

the importance factor using the variance. This method makes the hypothesis of the independence of the input variables. It uses a functional decomposition of the variance of the function to explore

$$\mathbb{V}(Y) = \sum_i^d \mathbb{V}_i(Y) + \sum_{i < j}^d \mathbb{V}_{ij}(Y) + \dots + \mathbb{V}_{1,2,\dots,d}(Y), \quad (2.7)$$

introducing conditional variances:

$$\begin{aligned} \mathbb{V}_i(Y) &= \mathbb{V}[\mathbb{E}(Y|x_i)] \\ \mathbb{V}_{ij}(Y) &= \mathbb{V}[\mathbb{E}(Y|x_i x_j)] - \mathbb{V}_i(Y) - \mathbb{V}_j(Y), \end{aligned}$$

Sobol' indices are expressed as

$$S_i = \frac{\mathbb{V}_i(Y)}{\mathbb{V}[Y]} \quad S_{ij} = \frac{\mathbb{V}_{ij}(Y)}{\mathbb{V}[Y]}. \quad (2.8)$$

S_i corresponds to the first-order term which apprises the contribution of the i -th parameter, while S_{ij} corresponds to the second-order term which informs about the correlations between the i -th and the j -th parameters. These equations can be generalized to compute higher order terms. However, the computational effort to converge them is most often not at hand and their analysis and interpretations are not simple.

Total indices represent the global contribution of the parameters on the variance of the QoI and express as:

$$S_{T_i} = S_i + \sum_j S_{ij} + \sum_{j,k} S_{ijk} + \dots = 1 - \frac{\mathbb{V}[\mathbb{E}(Y|x_{\sim i})]}{\mathbb{V}[Y]}. \quad (2.9)$$

Figure 2.10(a) is an example using *Ishigami* function [109]

$$Y(\mathbf{x}) = \sin x_1 + 7 \sin^2 x_2 + 0.1x_3^4 \sin x_1, \quad (2.10)$$

with $\mathbf{x} \in [-\pi, \pi]^3$. This function exhibits strong non-linearity and non-monotonicity. It is particularly interesting because the first order indice of $S_{x_3} = 0$ whereas its total order is $S_{T_{x_3}} = 0.244$. Note that on second order indices, $S_{x_1, x_3} = 0.244$. It means that almost 25% of the observed variance on the QoI is due to the correlations between x_3 and x_1 , although x_3 by itself has no impact on the QoI.

Looking at Fig. 2.10(b), it can be noted that the convergence of these indices requires a large sampling size. The required sampling size is case dependant as it depends on the number of input parameters and on the complexity of the function of interest.

Figure 2.11 gives a visual explanation of *Sobol'* indices. It shows scatter plots of the output with respect to each parameter. By conditioning the output value by given values of the parameter (*black lines*), the conditional output mean is computed. It corresponds to the term $\mathbb{E}(Y|x_i)$. Taking the variance of this term gives the numerator of the *Sobol'* indices. Looking at x_3 , the variance of the mean is zero leading to $S_{x_3} = 0$. But we can further observe that the variance of the output is not constant along the parameter values of x_3 . This heteroscedasticity is explained by higher order interactions. Moreover, an heteroscedasticity is also noticeable on x_1 leading to an interaction between x_3 and x_1 . On x_2 , the variance seems to be constant and thus null interaction with this parameter can be supposed. This case is fairly simple to analyse visually—although it is only a qualitative analysis. Nevertheless, when the number of input parameters increases such analysis becomes unrealistic as it would be difficult to conclude on high-order terms.

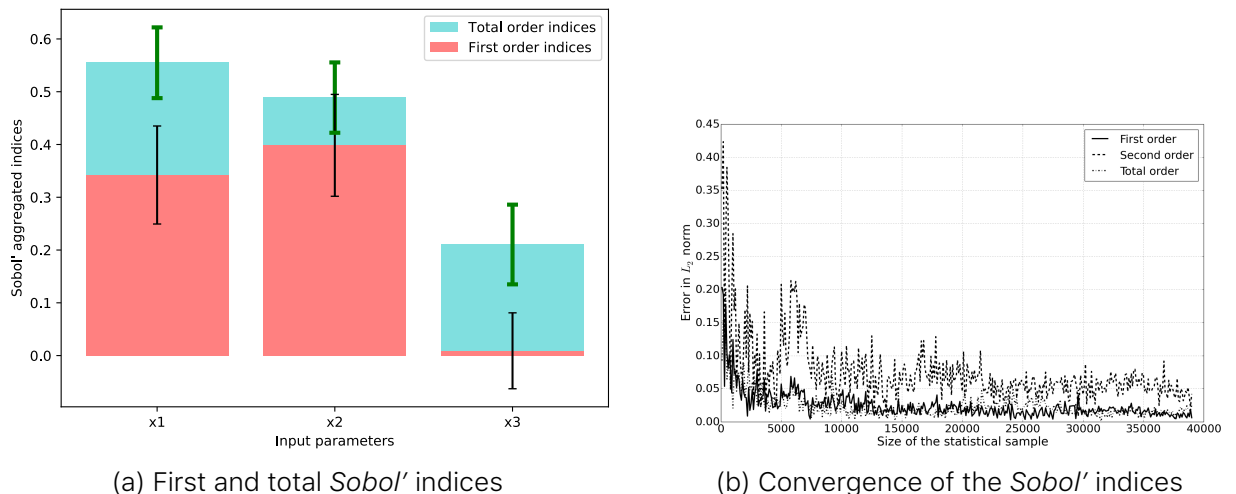


Figure 2.10 – First and total *Sobol'* indices with confidence intervals on the Ishigami function.

Classical empirical formulations of *Sobol'* indices require the use of 3 (resp. 4) matrices to compute first and total (resp. and second

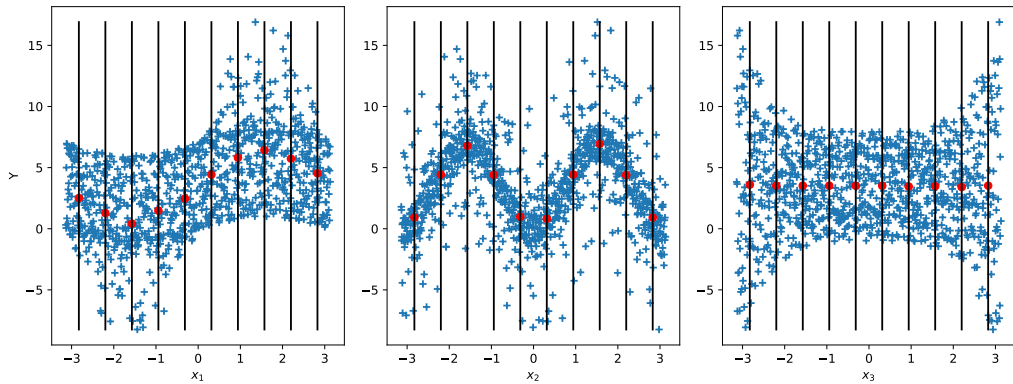


Figure 2.11 – Scatter plot per component of the *Ishigami* function. *Blue crosses* represent the outputs, *black lines* the conditioning over a given parameter, *red dots* the mean given a conditioning.

order indices) [200]. The computation requires two independent samplings A , B of size N and a matrix AB which is a combination of both matrices (resp. BA). AB_n corresponds to the matrix A with the column n from the matrix B . Hence the number of forward model evaluation is $N_s = N(d + 2)$. In [26], they showed that *Martinez*'s formulation is stable and provides asymptotic confidence intervals—approximated with Fisher's transformation—for first order and total order indices. *Martinez*'s estimators write

$$\hat{S}_i = \rho(Y(B), Y(AB_n)) \quad \hat{S}_{Ti} = 1 - \rho(Y(A), Y(AB_n)), \quad (2.11)$$

where ρ is the linear correlation coefficient.

For a functional output, as for the *LS89* blade case—see Chapter 10 and Fig. 2.12—, *Sobol'* indices can be computed all along the output vector and retrieve a map or create composite indices. As described by Marrel [153], aggregated indices can also be computed as the mean of the indices weighted by the variance at each point or temporal step

$$S_i = \frac{\sum_{l=1}^m \mathbb{V}[\mathbf{Y}^l] S_i^l}{\sum_{l=1}^m \mathbb{V}[\mathbf{Y}^l]} \quad (2.12)$$

A note regarding the independence of the input parameters. If the nature of the dependence in terms of probability distribution function is known—through copula-based approach for instance [40]—, the *Sobol'* formulation can be extended [130, 129, 107].

2.2.2.3 Moment-based Sensitivity Analysis

Variance-based SA are standard methods (although elementary effects or classical regression are still commonly used among practitioners [73]) but they do not come without flaws [35]:

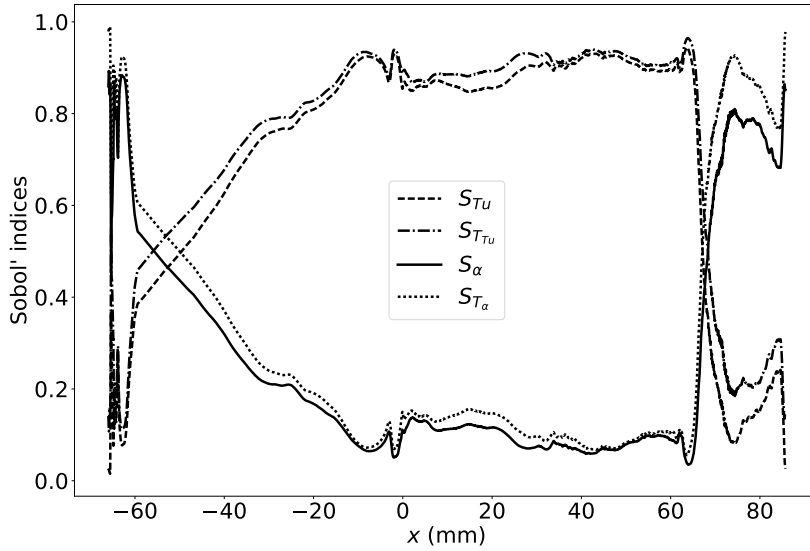


Figure 2.12 – Map of Sobol' indices of two input parameters T_u and α along the curvilinear abscissa x of the LS89 blade.

- Only the second order moment is taken into account,
It means that if the QoI's PDF is highly skewed, multimodal or with heteroscedastic data, this information will be lost. Hence, the variance is only a good measure if the distribution is close to normal.
- The parameters need to be independent,
This assumption can be mitigated by using some correlation matrices but the procedure is not really trivial.
- Null first order indices does not imply that the parameter is independent with the QoI,
Computation of high-order terms and total effect require a lot of samples to converge. It may be impractical to compute these quantities.

Moment-based methods are based on the whole PDF to mitigate these issues [34]. Based on the unconditional PDF, a conditional PDF per parameter is computed. The more the conditional PDF deviates from the unconditional PDF, the more the parameter has an impact on the quantity of interest. The same procedure can be done using the Empirical Cumulative Density Function (ECDF), respectively with the unconditional ECDF. Figure 2.13 visually shows this procedure. Bins of samples (red circles) are used to compute a conditional PDF of the output. This PDF is compared to the unconditional PDF.

Figure 2.14 shows the computation of both conditional and unconditional PDF (resp. ECDF). Based on these moment estimations, distance criteria can be computed such as: L_1 , Kolmogorov-Smirnov or the Kuiper distances. The method does not require any particular sampling nor does the parameters require to be independent. The limitations

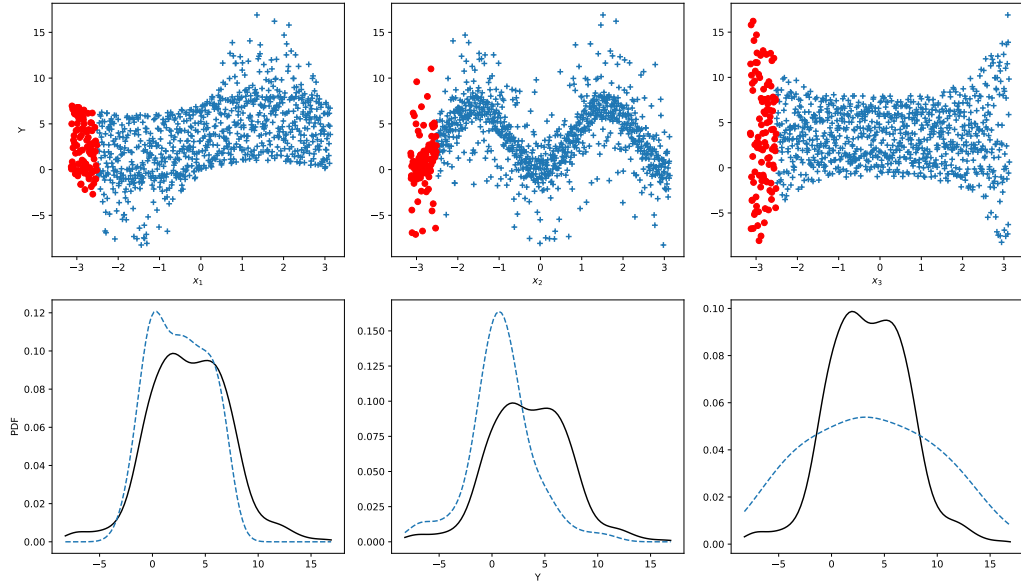


Figure 2.13 – Scatter plot per component of the *Ishigami* function. *Black line* represents the unconditional PDF and *red dots* the samples used to compute the conditioned PDF shown in *dashed line*.

come from the ability to correctly estimate the density and from the interpretation of some metrics as they might not be adimensionalized as *Sobol'* indices.

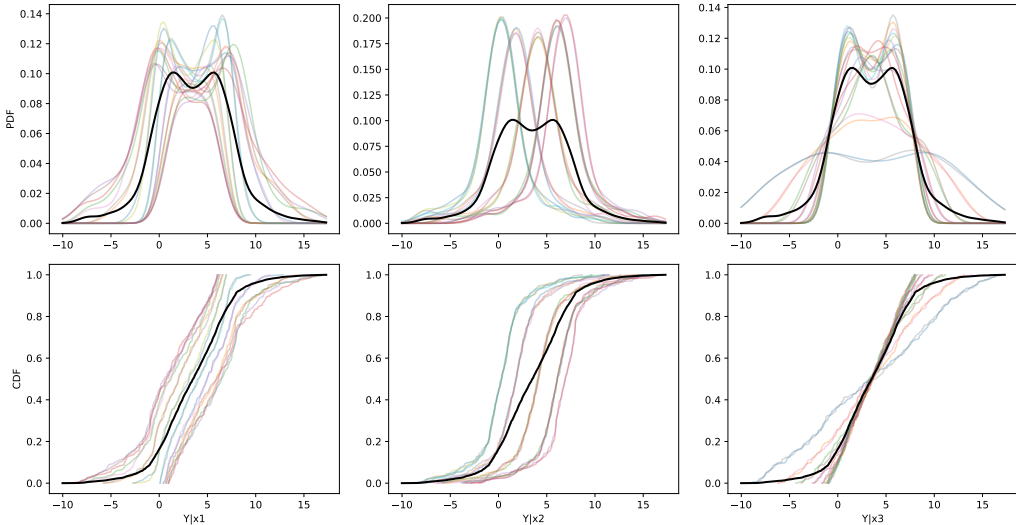


Figure 2.14 – Moment independent SA on the *Ishigami* function.

Another visual approach is found with the Cumulative Sums Of Normalized Reordered Output method (CUSUNORO) [180]. The output is normalized and ordered in function of a given parameter. Then, its cumulative sum vector is computed. In other words, this corresponds to the conditional ECDF after normalization. Here as well, the more the curve is far from the unconditional ECDF (a flat line after normalization),

2.2. UNCERTAINTY QUANTIFICATION

the more the output is sensitive to the parameter—see Fig. 2.15.

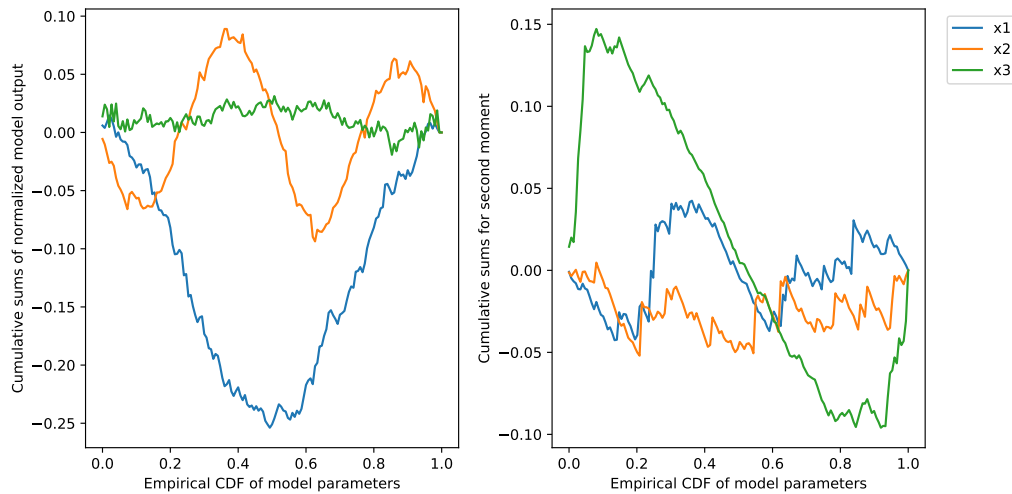


Figure 2.15 – CUSUNORO on the *Ishigami* function.

2.3 Surrogate Models

C^{LASSICAL} UQ methods, based on the Monte-Carlo approach, require a large number of experiments [106, 108, 131, 135, 201, 219], which quickly go beyond the limits of available resources (CPU cost, budget). In the following, numerical simulations are considered and especially CFD simulations. These limits are especially true when it comes to large-dimensional problems, both with respect to the domain discretization and to the number of uncertain input parameters. Depending on the fidelity sought, one high fidelity simulation can cost millions hours of computing time. The cost of the UQ study can, however, be significantly reduced when the CFD code is replaced by a surrogate model which is formulated in a parameter space and which is fast to evaluate for any set of uncertain variables [154].

Before going further, let us clarify the nature of the forward model. The ensemble \mathcal{Y} constitutes a set of observed QoI. Each element can either be a scalar or a vectorial—or functional—QoI. When considering scalar QoI, a global physical parameter such as the mean temperature for instance, a single surrogate model mapping $Y^{(i)} := \mathcal{M}(\mathbf{x}^{(i)})$ can be constructed. In case of a multidimensional output, one can consider independent surrogate for each element but the computational cost can rapidly become intractable. Moreover, the elements of the vectorial QoI can be correlated. A classical solution is found through the use of a Proper Orthogonal Decomposition (POD) [21]. By performing a POD on the QoI, each mode being orthogonal, they can be treated as independent and then a surrogate model can be built on a reduced space. In [37, 150], this method was used to reduce the computational cost and conserve the spatial/temporal correlation of the QoI.

Formulating the surrogate model relies on a limited number of forward model integrations referred to as the DoE. Several surrogate models are found in the literature, among whom generalized linear models, polynomial models, splines, Polynomial Chaos (PC) expansions, artificial neural networks or Gaussian Process (GP) models. In this work, two types of surrogate models are used to approximate the behaviour of forward models. PC expansion on the one hand, GP regression on the other hand.

PC approach has received much attention lately [60, 220, 239, 240, 44]. The PC surrogate model is formulated as a polynomial expansion, in which the basis is defined according to the distribution of the uncertain inputs \mathbf{x} and the coefficients relate to the statistics of the output \mathbf{Y} . The coefficients are computed so as to fit the training set $(\mathbf{X}, \mathcal{Y})$, either using regression or spectral projection methods. The merits of PC surrogates were demonstrated in various fields, e.g. structural mechanics [60, 30], CFD [99, 148, 196], hydrology [56], hydraulics [141, 67], wildfires [192]. A complementary approach between PC and EnKF was presented in Li and Xiu [140] and tested in the framework of wildfire behaviour forecasting in Rochoux et al. [192].

GP, that is strongly related to Kriging in geostatistics, is also of increasing interest [188, 134, 147, 153]. The GP formalism treats the forward model response as a realization of a Gaussian stochastic process indexed by \mathbf{x} and fully characterized with mean and covariance functions conditioned by the training set $(\mathbf{X}, \mathcal{Y})$. The GP surrogate is built first, by defining a covariance kernel function between output values and a trend function and then, by estimating the hyperparameters (e.g. variance, characteristic length scale) that provide a good fit to the training set. GP surrogates were introduced in the context of SA for estimating Sobol' indices [168, 152, 133]. In an industrial context—which is the case here—, some benefits of this method are: (i) it does not require any prior knowledge of the probability distribution of the uncertainties on the input parameters ; (ii) it does not need a specific sampling of the parameter space which could lead to *curse-of-dimensionality* or mis-evaluation of the space ; and (iii) it provides an estimation of the predictive error.

PC and GP surrogate models have recently been compared for UQ and SA studies [134, 171, 204]. Owen et al. [171] evaluated the performance of each type of surrogate in terms of output mean, variance and PDF estimation. Le Gratiet et al. [134] compared Sobol' indices with applications in structural mechanics; for a given size of the training set, PC and GP surrogate models were found to feature a similar predictive quality—with respect to the predictive coefficient Q_2 , also called Nash-Sutcliffe model efficiency coefficient, which is equivalent to the coefficient of determination R^2 for residuals's prediction [125] (see Section 2.3.5). Le Gratiet et al. [134] also emphasized that the ranking between PC and GP approaches remains problem-dependent.

Considering the general case of a functional QoI, the common idea of PC and GP approaches is to design for each element (with or without considering a POD) $a \in \{a_1, \dots, a_M\}$ a surrogate with a weighted finite sum of basis functions:

$$\hat{Y}_a(\mathbf{x}) = \sum_{i=0}^r \gamma_{a,i} \Psi_i(\mathbf{x}), \quad (2.13)$$

where the coefficients $\gamma_{a,i}$ and the basis functions Ψ_i are calibrated by the training set \mathbf{X}^{N_s} . The main difference between PC (Sect. 2.3.2) and GP (Sect. 2.3.3) approaches stands in the nature of these models: GP interpolates the training points and captures local variations, while PC is a regression method focusing on the global behaviour of the model. Basis functions and calibration methods also differ between these two approaches.

Section 2.3.1 presents the POD while Section 2.3.2 and Section 2.3.3 respectively define the PC and the GP surrogate methods. An overview of methods combining several level of fidelity is done in Section 2.3.4. Finally, in Section 2.3.5 we present quality metrics associated with surrogate models.

2.3.1 Snapshot Method

The key idea of the snapshot method [214] is to achieve a POD of the centred snapshot matrix $\mathcal{Y} \in \mathbb{M}_{M,N}(\mathbb{R})$, which gathers the discretized QoI for the N_s snapshots, from which the sample mean is subtracted. For simplicity purpose, the QoI anomaly element a is denoted y in the following. Thus, $\mathcal{Y} = \left(y_{a_i}^{(j)} \right)_{\substack{1 \leq i \leq M \\ 1 \leq j \leq N_s}}$. The snapshots correspond to the column vectors; the k th snapshot of size M is denoted by $\mathbf{y}^{(k)}$.

Based on many observations of a random vector, the POD gives the orthogonal directions of largest variances (or modes) in the probabilistic vector space in order to reduce the vector space dimension [22]. Note that for simplicity purpose, the adjective *centred* is dropped in the following when referring to the centred snapshot matrix \mathcal{Y} .

The POD of the snapshot covariance matrix $\mathbf{C} = N_s^{-1} \mathcal{Y}^T \mathcal{Y} \in \mathbb{M}_{N_s}(\mathbb{R})$ is equivalent to the Singular Value Decomposition (SVD) of the snapshot matrix \mathcal{Y} :

$$\mathcal{Y} = \mathbf{U} \Lambda \mathbf{V}^T = \sum_{k=1}^{r_p} \lambda_k \mathbf{u}_k \mathbf{v}_k^T, \quad (2.14)$$

where $\mathbf{U} \in \mathbb{M}_M(\mathbb{R})$ is an orthogonal matrix diagonalizing $\mathcal{Y} \mathcal{Y}^T$ (\mathbf{u}_k , the k th column of \mathbf{U} , is a left singular vector of \mathcal{Y}), where $\mathbf{V} \in \mathbb{M}_{N_s}(\mathbb{R})$ is an orthogonal matrix diagonalizing $\mathcal{Y}^T \mathbf{Y}$ (\mathbf{v}_k , the k th column of \mathbf{V} , is a right singular vector of \mathcal{Y}), and where $\Lambda \in \mathbb{M}_{M,N_s}(\mathbb{R})$ is a rectangular diagonal matrix including $r_p = \min(M, N_s)$ singular values on its diagonal. The singular values $\{\lambda_k\}_{1 \leq k \leq r_p}$ are the square roots of the eigenvalues of \mathbf{C} . Note that in the following, we do not reduce further the rank of the snapshot matrix \mathcal{Y} .

For a given element a , any snapshot $h_a(\mathbf{x}^{(k)})$ can then be retrieved as a linear combination of r_p modes $\{\Psi_i\}_{1 \leq i \leq r_p}$:

$$y_a(\mathbf{x}^{(k)}) = (\mathbf{U} \Lambda \mathbf{V}^T)_{ak} = U_{a:} (\Lambda \mathbf{V}^T)_{:k} = \sum_{i=1}^{r_p} \gamma_{a,i} \Psi_i(\mathbf{x}^{(k)}), \quad (2.15)$$

where for any $i \in \{1, \dots, M\}$, $\gamma_{a,i} := U_{a,i}$ and $\Psi_i(\mathbf{x}^{(k)}) := (\Lambda \mathbf{V}^T)_{i,k}$.

Figure 2.16 is a visual explanation of the POD on the El Niño dataset—see Appendix A.2. A POD is performed on the dataset composed of $N_s = 54$ curves. The first two modes account respectively for 73% and 15% of the variance of the data. Figure 2.16(a) presents a visualization of the same dataset in this 2-dimensional reduced space. Hence, each point of the reduced space is associated to a curve in the original space. Figure 2.16(c) shows the individual contribution of each modes for a given sample while Fig. 2.16(d) is the sum of these contributions (plus the sample mean). Due to the modal truncation, there is a loss of information.

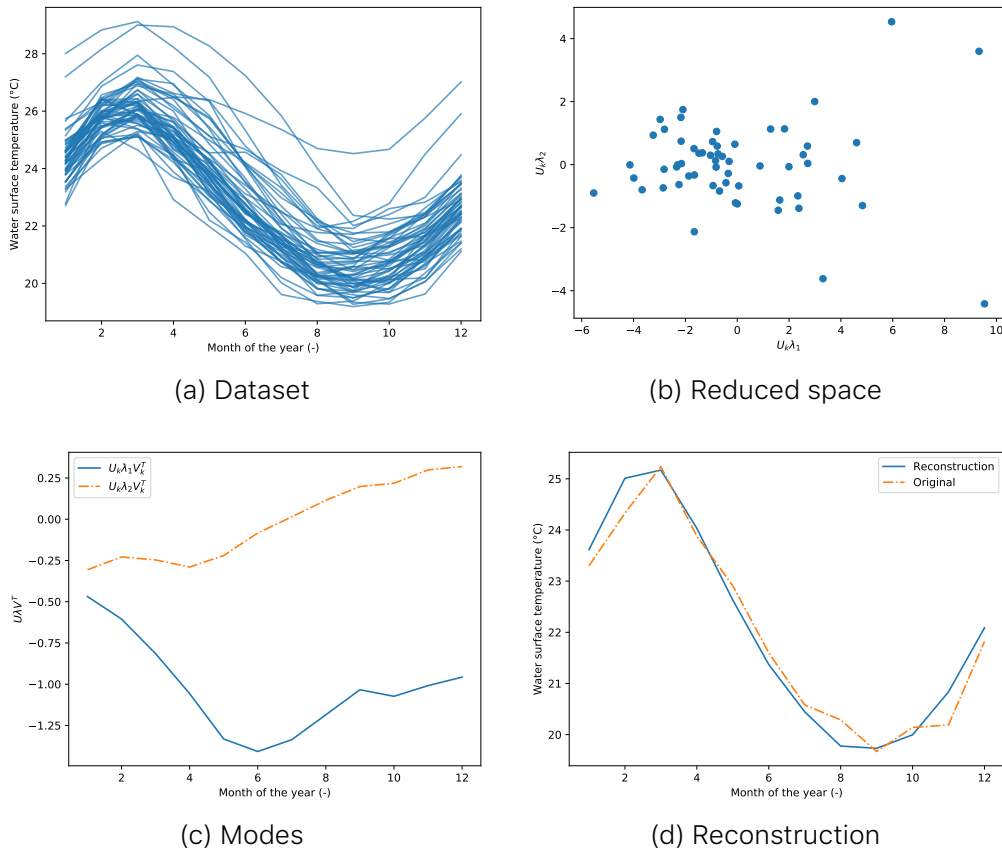


Figure 2.16 – POD reconstruction principle applied to the El Niño dataset. *Top figures* present a decomposition of the dataset into a reduced space using two components. *Bottom figures* present the reconstruction of a sample.

2.3.2 Polynomial Chaos Surrogate Model

The algorithm to build the PC surrogate proceeds as follows:

1. choose the polynomial basis $\{\Psi_i\}_{i \geq 0}$ according to the assumed PDF of the inputs \mathbf{x} ,
2. choose the total polynomial degree P according to the complexity of the physical processes,
3. truncate the expansion to r_{pc} terms to keep the predominant information given by the forward model using standard truncation strategy (r_{pc} depends on d and P and is defined further on),
4. apply spectral projection strategy (i.e. Gaussian quadrature rule) to compute the coefficients $\{\gamma_{a,i}\}_{\substack{i \in \mathbb{N}^d \\ |i| \leq P}}$ for each element a (can use a POD or not) using $N_s = (P + 1)^d$ snapshots,
5. formulate the surrogate model M_{pc} at each element a , which can be evaluated for any new pair of parameters \mathbf{x}^* .

Note that we use standard truncation and projection strategies presented in [135] and [239].

2.3.2.1 Polynomial Basis

Each component of the random vector \mathbf{x} defined in the input physical space is standardized and noted by ζ in the following way: $\zeta_i = \frac{x_i - \mu_i}{\sigma_i}$ where $\mu_i = N_s^{-1} \sum_{k=1}^{N_s} x_i^{(k)}$ and $\sigma_i = \sqrt{(N_s - 1)^{-1} \sum_{k=1}^{N_s} (x_i^{(k)} - \mu_i)^2}$.

y_a is projected onto a stochastic space spanned by the orthonormal polynomial functions $\{\Psi_i\}_{i \geq 0}$. These functions are orthonormal with respect to the joint density $\rho(\zeta)$, i.e.

$$\int_Z \Psi_i(\zeta) \Psi_j(\zeta) \rho(\zeta) d\zeta = \delta_{ij}, \quad (2.16)$$

with δ_{ij} the Kronecker delta function and $Z \subseteq \mathbb{R}^d$ the space in which ζ evolves.

In practice, the orthonormal basis is built using the tensor product of 1-D polynomial functions: $\Psi_i = \Psi_{i,1} \dots \Psi_{i,d}$ where i is the multi-index $(i_1, \dots, i_d) \in \{0, 1, \dots, P\}^d$. The choice for the basis functions depends on the probability measure of the random variables. According to Askey's scheme, the Hermite polynomials form the optimal basis for random variables following the standard Gaussian distribution, and the Legendre polynomials are the counterpart for the standard uniform distribution [240].

2.3.2.2 Truncation Strategy

In practice, the sum in Eq. (2.13) is truncated to a finite number of terms r_{pc} . Using a standard truncation strategy r_{pc} is constrained by the number of random variables d and by the total polynomial degree P as:

$$r_{pc} = \frac{(d + P)!}{d! P!}, \quad (2.17)$$

meaning that all polynomials involving the d random variables of total degree less or equal to P are retained in the PC expansion. The PC-approximated QoI at each element $y_{pc}(a)$ is formulated as:

$$\hat{y}_{pc,a}(\mathbf{x}) := \mathcal{M}_{pc,a}(\zeta) = \sum_{\substack{i \in \mathbb{N}^d \\ |i| \leq P}} \gamma_{a,i} \Psi_i(\zeta). \quad (2.18)$$

Note that for small d , advanced truncation strategies that consist in eliminating high-order interaction terms or using sparse structure [32, 160] are not necessary.

2.3.2.3 Spectral Projection Strategy

We focus here on non-intrusive approaches to numerically compute the coefficients $\{\gamma_{a,i}\}_{\substack{i \in \mathbb{N}^d \\ |i| \leq P}}$ in Eq. (2.18) using N_s snapshots from \mathbf{X}^{N_s} .

The spectral projection relies on the orthonormality property of the polynomial basis. The i th coefficient $\gamma_{a,i}$ is computed using Gaussian quadrature as:

$$\gamma_{a,i} = \langle y_a, \Psi_i \rangle \cong \sum_{k=1}^{N_s} y_a^{(k)} \Psi_i(\zeta^{(k)}) w^{(k)}, \quad (2.19)$$

where $\mathbf{y}^{(k)} = \mathcal{M}(\mathbf{x}^{(k)})$ is the snapshot corresponding to the k th quadrature root $\mathbf{x}^{(k)}$ of Ψ_i (in the physical space), and where w^k is the weight associated with $\mathbf{x}^{(k)}$. $(P+1)$ is the number of quadrature roots required in each uncertain direction to ensure an accurate calculation of the integral $\langle y_a, \Psi_i \rangle$. Hence, $N_s = (P + 1)^2$ at least for quadrature strategies.

More advanced techniques have been developed in order to reduce the number of samples required using sparse approach [32, 136, 160, 211]. Hence, only the most important terms of the expansion are kept in order to lower the sample budget.

2.3.3 Gaussian Process Surrogate Model

The algorithm to build a Gaussian Process surrogate proceeds as follows:

1. choose the size of the training set N_s ,
2. draw N_s samples (or snapshots) in the input random space \mathbf{x} ,
3. formulate the surrogate model \mathcal{M}_{gp} for the QoI at each element a (can use a POD or not), which can be evaluated for any \mathbf{x}^* .

2.3.3.1 Regression Procedure

A Gaussian Process (GP) is a collection of random variables which have a joint Gaussian distribution [188]. GP is equivalent to *Kriging* [126]. A *Gaussian Process* is described by its mean $\mu(\mathbf{x})$ and covariance $k(\mathbf{x}, \mathbf{x}')$ —where \mathbf{x}, \mathbf{x}' are different sets of inputs

$$\begin{aligned} Y_a(\mathbf{x}) &\sim \mathcal{GP}(\mu(\mathbf{x}), k(\mathbf{x}, \mathbf{x}')), \text{ with} \\ m(\mathbf{x}) &= \mathbb{E}[Y_a(\mathbf{x})], \\ k(\mathbf{x}, \mathbf{x}') &= \mathbb{E}[(Y_a(\mathbf{x}) - \mu(\mathbf{x}))(Y_a(\mathbf{x}') - \mu(\mathbf{x}'))]. \end{aligned} \quad (2.20)$$

Here the covariance function k (or kernel) is chosen as a squared exponential

$$K = k(\mathbf{x}, \mathbf{x}') = \sqrt{\pi} \sigma_x^2 \exp\left(-\frac{\|\mathbf{x} - \mathbf{x}'\|^2}{2\ell_i^2}\right), \quad (2.21)$$

where l is a length scale that describes the distance and strength of influence from one sample to another and σ_x is the variance of the output signal. Squared exponential kernel leads to satisfying results but other kernel functions could have been considered, such as a decreasing exponential one or a *Matérn* one – with their associated hyperparameters. The choice of the kernel is still an open problem and can be mitigated using the available information on the problem. The square exponential kernel leads to very smooth, thus stable results. Furthermore, it implies that the model is exact at sample points; it does not introduce any other strong assumptions, hence its wide usage among practitioners.

Then the GP model consists of a regression providing an interpolation \mathcal{M}_{gp} for a new set of input parameters \mathbf{x}^* :

$$\begin{aligned}\mathcal{M}_{\text{gp}_a}(\mathbf{x}^*) &= \bar{Y}_a(\mathbf{x}^*) = \sum_{i=1}^{N_s} \alpha_i k(\mathbf{x}^i, \mathbf{x}^*), \text{ with} \\ \alpha &= (K + \sigma_n^2 I)^{-1} \mathcal{Y}_a,\end{aligned}\quad (2.22)$$

where \bar{Y}_a is the mean realization, \mathbf{x}^i the i -th set of parameters, \mathcal{Y}_a the snapshot matrix considering element a and σ_n is the nugget effect that prevents ill-conditioning issues for the matrix K . Indeed, it is the mean realization of the conditioned process considering an artificial noisy observation which gives the prediction. The learning phase of the GP consists in selecting l , σ_n and σ_x so that Y_a passes through or close to the dataset points. These hyperparameters are optimized by maximizing the log likelihood applied to the data set \mathcal{Y}_a using a basin hopping technique [230]. A key advantage of this predictor is that it provides an inference about its prediction variance

$$\mathbb{V}[Y_a(\mathbf{x}^*)] = k(\mathbf{x}^*, \mathbf{x}^*) - \mathbf{k}(\mathbf{x}^*)^T (K + \sigma_n^2 I)^{-1} \mathbf{k}(\mathbf{x}^*). \quad (2.23)$$

The regression methodology is shown in Fig. 2.17. On Fig. 2.17(a), the GP is sampled on the input parameter space. In this case, a GP with zero mean and unit variance is used. It means that for each x^i , the QoI is estimated as a Gaussian process of zero mean and unit variance. Thus along the parameter x_k , the GP is defined as an infinite collection of GPs. The link between each GP is assured through the correlation matrix defined by the kernel. Once some observations are added—see Fig. 2.17(b)—, the GP is conditioned so that each realization of the GP passes through the observations. This intrinsic property of the GP can be relaxed by changing the diagonal of the correlation matrix. This can be used to take into account some noise in the data for instance. Moreover, the matrix can be adapted per observation if the variance of the noise is known to be different—heteroscedastic noise.

As said beforehand, the hyperparameters are chosen as to maximize the marginal log likelihood. It is the integral of the likelihood times the prior marginalized over the function values:

$$p(y|x) = \int p(y|\mathbf{f}, x) p(\mathbf{f}|x) d\mathbf{f}. \quad (2.24)$$

In other words, maximizing this quantity will tend to reduce the confidence interval between each point. It is to be noted that along each direction of the parameters space, having different set of hyperparameters is possible so that anisotropy can be taken into account.

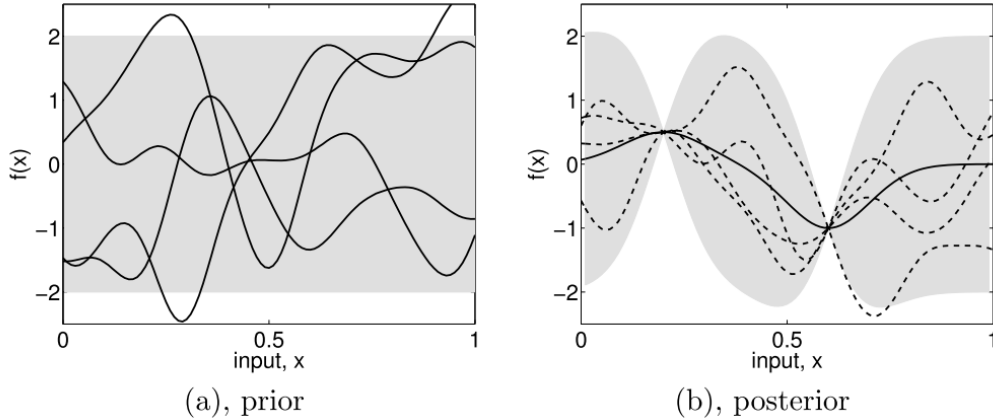


Figure 2.17 – Visualization of 4 Gaussian processes: **a** represents a sampling of the GP while in **b** these functions have been conditioned on two points. Shaded regions represent twice the standard deviation of the GPs. Source: [188].

2.3.4 Multifidelity

It is possible to combine several levels of fidelity in order to lower the computational cost of the surrogate building process. The fidelity can be either expressed as a mesh difference, a convergence difference, or even a different set of solvers. Starting from [118, 119], there has been numerous studies on this topic—see these reviews [132, 175, 72]. All in all, multifidelity approaches are commonly used [172, 232, 17].

In [49], an extensive review of the principal methods is presented. They concluded that the approach proposed by [75] was robust and performant. Their method uses a low fidelity model and corrects it using a model of the error:

$$\mathcal{M}(x) = \mathcal{M}_c(x) + \mathcal{M}_e(Y_e(x), Y_c(x)), \quad (2.25)$$

with \mathcal{M}_e the surrogate model representing the error between the two fidelity levels. For this method to perform optimally, nested design of experiments are required for the error model to be computed.

The process is explained in Fig. 2.18. In this example, we seek to represent the model \mathcal{M}_e . We have at our disposal a limited number of evaluations y_e of this model. Only using these samples produces a model which fails to predict the QoI for high values of the input parameter. On top of that, we have access to a model Y_c with lots of samples due to its lower cost. Hence, we are able to predict with fidelity this model.

Hence, the multifidelity approach allows to fix this low fidelity model with the few evaluations of the high fidelity model. This produces a surrogate model which exhibits the correct behaviour of the expensive model.

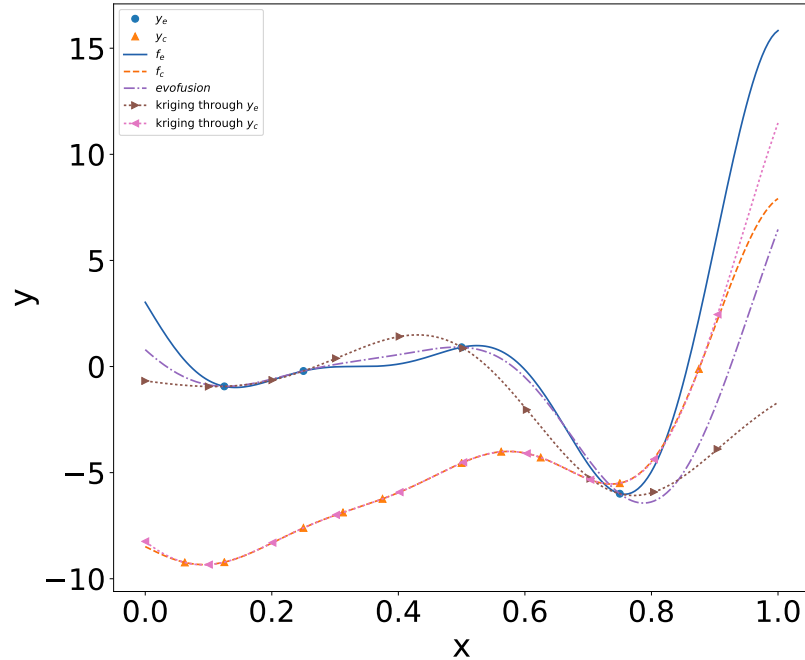


Figure 2.18 – Visualization of the multifidelity procedure on the analytical function of Forrester.

Considering two levels of fidelity Y_e and Y_c , respectively an expensive and a cheap function expressed as a computational cost. A cost ratio α between the two can be defined as:

$$\alpha = \frac{Y_e}{Y_c}. \quad (2.26)$$

Using this cost relationship and setting a computational budget C , it is possible to get a relation between the number of cheap and expensive realizations:

$$CY_e = N_e Y_e + N_c Y_c, \quad (2.27)$$

$$CY_e = N_e Y_e + N_c \frac{\alpha}{Y_e}, \quad (2.28)$$

$$C = N_e + N_c \alpha, \quad (2.29)$$

$$N_c = \frac{C - N_e}{\alpha}. \quad (2.30)$$

As the design being nested, the number of cheap experiments must be strictly superior to the number of expensive ones. Indeed, the opposite would result in no additional information to the system.

Multifidelity approaches have not been used in this thesis work as the focus was set on other aspects.

2.3.5 Model Validation

An important step after having constructed a surrogate model is to assess its validity. There are lots of ways to do this and the common method consists in comparing with a metric the prediction of the model at a given point with the direct model output. The classical approach is to use a validation set which is different than the training set. This holdout procedure requires to split the entire dataset into two disjointed datasets—see Fig. 2.19. There are no rules about the data sharing proportions. Things like the fitting time or the total number of samples lead to various splitting strategies. Depending on the number of simulations that can be afforded, the same dataset can be used to both construct the surrogate model and validate it. Independently of the strategy, various metrics can be used and common ones are given as follows. Note that only metrics used for regression are presented. The literature around classification metric is large and out of the scope of this work.

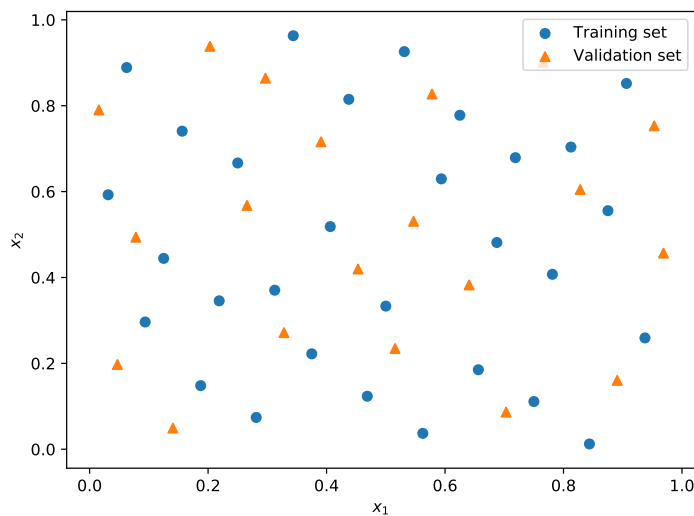


Figure 2.19 – 3-dimensional parameter space canonical visualization of training (triangles) and validation (circles) sets.

2.3.5.1 Mean Square Error and Alike

Various metrics are used to compare the results of a known sample over the result of a prediction from a model. The Mean Square Error (MSE) basically computes the sum of the square differences. Taking its root allows conserving the dimensionality of the QoI

$$\text{RMSE} = \sqrt{\frac{1}{N} \sum_{i=1}^N (Y_i - \hat{Y}_i)^2}. \quad (2.31)$$

However, this method is not robust to outliers as one or two values can lead to large errors. Mean absolute error and median absolute error

have a better behaviour toward this. In any case, the lower the error, the better the model.

2.3.5.2 Coefficient of Determination: Q_2

Another common indicator is the determination coefficient also called predictivity coefficient Q_2 [152]. It is composed of both the mean square error and the variance of the output. It is a normalization of the MSE by the spread of the data. The variance normalization makes this indicator strictly lower than 1. This is handy for comparing models with each other as the QoI's units does not counts.

$$Q_2 = 1 - \frac{\sum_{i=1}^N (Y_i - \hat{Y}_i)^2}{\sum_{i=1}^N (Y_i - \bar{Y}_i)^2}. \quad (2.32)$$

A perfect model is characterized by a $Q_2 = 1$. With a constant model, \hat{Y} is equal to the mean leading to $Q_2 = 0$. Finally, $Q_2 = 0$ can be negative, meaning that the model is arbitrary worse than a constant model.

2.3.5.3 Kolmogorov-Smirnov Statistical Test

The Kolmogorov-Smirnov test is a classical method used to evaluate the similarity between PDFs [46]. The difficulty of this method comes from the availability of the real PDF. Let T_F (resp. T_G) be a random variable with cumulative distribution function (CDF) F (resp. G). Let F_n (resp. G_m) be its empirical CDF built from n (resp. m) independent realizations of T_F (resp. T_G). Then, let us define the test statistics:

$$D = \sup_x |F_n(x) - G_m(x)|. \quad (2.33)$$

The null hypothesis for the Kolmogorov-Smirnov statistical test supposes that T_F and T_G are identically distributed, i.e. $F = G$. The Kolmogorov-Smirnov test leads us to reject this hypothesis with a type I error $\alpha \in]0, 1[$ when:

$$D > c(\alpha) \sqrt{\frac{n+m}{nm}}, \quad (2.34)$$

with $c(\alpha)$ a tabulated value found in the literature [215]. Considering $\alpha = 0.05$ and $n = m = N$, the null hypothesis is rejected if $D > 6,082 \cdot 10^{-3}$.

2.3.5.4 Graphical Quality Assessment

An easy way to visualize the quality of the model is to plot a joint plot. Its construction is simple. For a given sample, there is an observed value of QoI, let's say 5 (Fig. 2.20). Then for the same sample, we take

the predicted value of QoI, here also 5. These two values are used to construct a scatter plot. Thus, if the model is perfect, predicted values are equal to observed values leading to a line on this graph. On the right figure, the model is not as good as on the left, so an observed value of 5 is linked to a predicted value of 0.

A similar method consists in working on quantiles instead of absolute values of the output. Its interpretation is similar, a line would indicate a perfect fit.

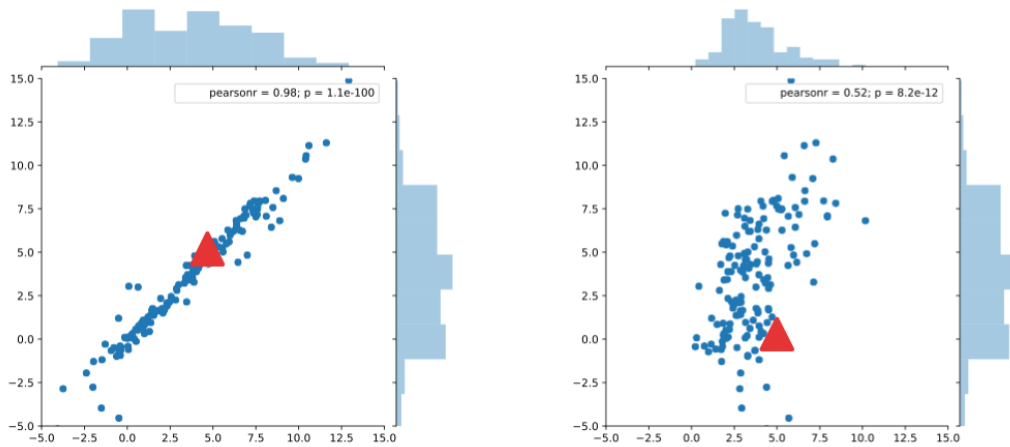


Figure 2.20 – Joint plot. QoI function of the predicted QoI given a parameter set. The triangle represents an observed value of 5.

2.3.5.5 Holdout as Opposed to *K-fold* or Cross Validation

Another method is to keep the same sample set for both training and validation. It is called cross-validation or *K-fold* [123]. In this case, K different models are constructed on subsets of the dataset and the metrics are computed on the points that are not used during the fitting of these different models. For *K-fold* to work optimally, it assumes that the model is fairly stable to these points removal. In Fig. 2.21, $K = 3$ which leads to 3 subsets of 6 points being created. These 6 points are used for training a model while the other 3 points are used for computing a metric. These operations are repeated 3 times and all metrics results are aggregated. A particular case is found with K being equal to the number of samples. This is called *Leave-One-Out* (LOO).



Figure 2.21 – Sketch of the *K-fold* methodology. $K = 3$ with $N = 9$ which leads to 3 subsets of 6 points.

2.4 Uncertainty Visualization

IN SPITE of a wide literature on UQ, the community has yet to propose efficient ways to visualize uncertainties. Indeed, to the author's knowledge, there is no chapter dedicated to visualization in UQ reference books [201, 221, 85]. This remains to be investigated, especially for Computational Fluid Dynamics (CFD) and geosciences applications [163] that involve complex fields of large dimensions. Classical ways of visualizing standard statistics can lead to misinterpretation [23]. The challenge for state-of-the-art visualization solutions stands in the dimension of the data. Assuming that the dimension of the data is limited (a set of scalars), for instance when dealing with input data, canonical subplots of subspaces are adapted. Parallel coordinate plots [104] or Kiviat plot (also referred to as the spider plot) [94] that are represented in Figure 2.22 offer an interesting alternative and share the same idea of dedicating one input variable (noted x_i) per axis; Kiviat (right panel) plot being the equivalent to parallel coordinates (left panel) plot in polar coordinates.

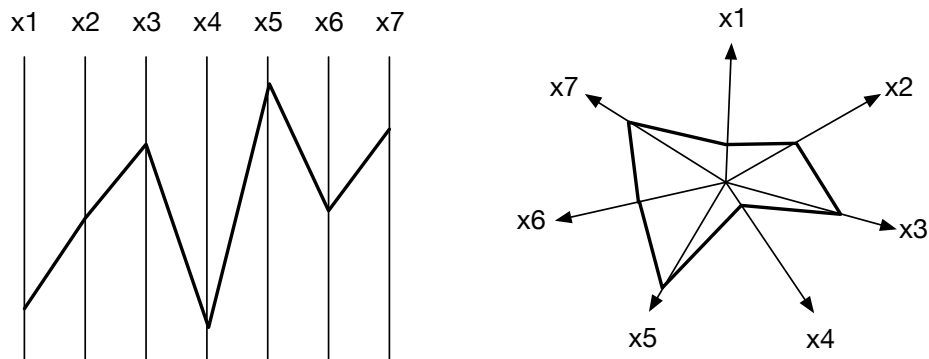


Figure 2.22 – Schematic representation of a parallel coordinate plot (left) and a Kiviat plot (right) for one sample.

When the dimension of the data increases, for instance when dealing with *functional* output fields discretized in both space and time on fine meshes, advanced strategies should be proposed. Different strategies are found in the literature to visualize statistics on the response variable [183, 38, 33]. Beyond deterministic simulations, moving on to ensemble-based approaches, the dimension of the data further increases.

A first approach is to look at each realization of the data set individually, in the output space with curves, maps or 3D-graphs. In the early work of Sir Francis Galton and its bean machine, the sampling process illustrated the demonstration of the central limit theorem stating that the binomial distribution approximates the normal distribution. The animated version of the sampling procedure is referred to as the Hypothetical Outcome Plots (HOPs) technique [65] and was generalized by [101] for a set of scalars as presented in Fig. 2.23.

HOPs consists in animating a succession of possible outcomes sampled from the data. It was proven to enable the exploration and the understanding of the dataset general characteristic, even for people lacking statistical background [29] with the possibility to visually grasp correlations in the outputs.

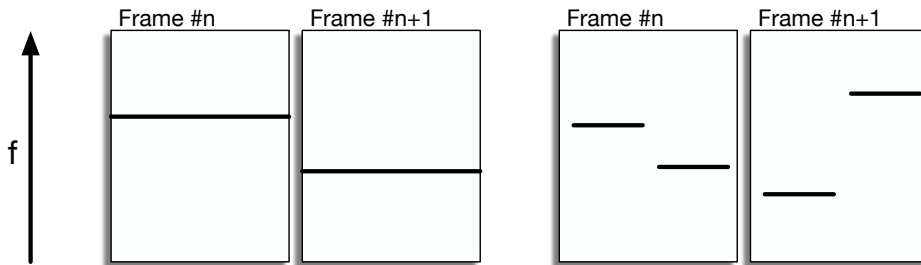


Figure 2.23 – Schematic representation of the HOPs method for single scalar output (*left*) or multiple scalar outputs (*right*).

Statistical moments and PDF plot are common tool for visualizing uncertainties in the context of ensemble simulation as illustrated in Fig. 2.24. They are useful for risk analysis as the probability of exceeding a threshold is directly observable. Figure 2.24(a) displays the PDF for a scalar response variable (noted f) where the mean, the mode and extreme probabilities can be observed. Figure 2.24(b) displays the principal mode of the PDF (solid black line) for a functional response variable discretized in the x -direction. The PDF standard deviation (added/removed to/from the mean) is plotted in dashed lines. These curves are computed for each x independently and they do not represent a possible solution of the numerical solver. The box plot in Figure 2.24(c) provides similar information while diminishing the false illusion of median/mean curves. It should be noted that users usually have a better understanding of frequency [87] than of PDFs and that there is a general misinterpretation of confidence intervals [29].

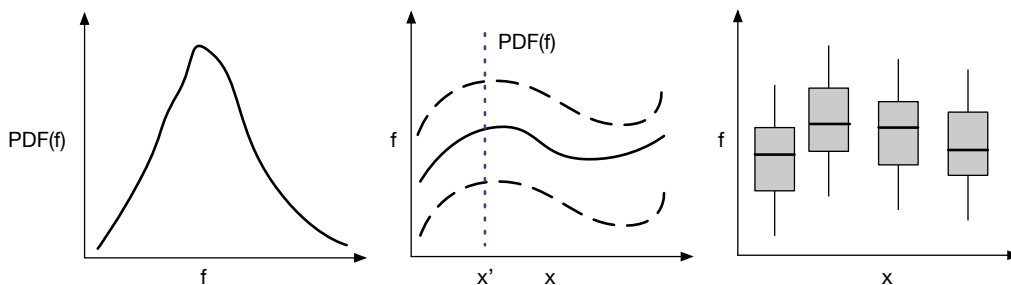


Figure 2.24 – Schematic representation of the PDF for a scalar output (*left*), for a functional output (*middle*) and with a boxplot solution (*right*). The PDF mode is represented with a solid line, the standard deviation added/removed to/from the mean is represented with dashed lines.

A complementary approach based on density criteria was proposed by [102, 222]; it is noted HDR for Highest Density Region and repre-

sented in Fig. 2.25. It allows depicting some statistics (for instance median or outliers) taking into account the functional response variable as a whole and working in a reduced space (POD) spanned by the most significant directions of the output space. Within this reduced space, metrics for functional outputs are computed such as the distance to the median (blue curve) so that abnormal or outlier outputs (red and green curves) can be detected and quantiles can be estimated (blue envelope). Each curve represents either a realization within the data set or an additional realization sampled in the reduced space; thus functional characteristics such as spatial or temporal correlation are preserved. From [182, 191], the HDR method is more robust to outlier detection than other methods such as functional boxplot [222, 237].

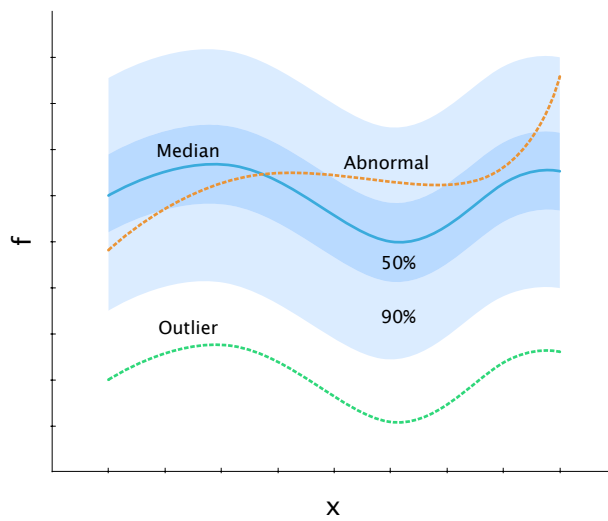


Figure 2.25 – Schematic representation of data set functional realizations characterized with HDR metrics. The median is represented by the solid blue line, the abnormal and outliers are represented by the red and green lines and the 50% and 90% quantiles are represented by blue shaded envelopes.

2.4.1 Highest Density Region

The dataset output is considered as a matrix where each line corresponds to a realization. This matrix is decomposed by POD. The modes are ordered by decreasing importance in terms of contribution to the variance and only a finite number of modes are kept. In this reduced space, the functional dataset of large dimensions is conveniently represented by a limited number of scalars mapped onto most significant directions that maximizes the variance of the response variable. Within this reduced space, the classification of different patterns or the computation of metrics is eased [190]. Hence, within this reduced space, the median realization corresponds to the HDR location. The distance to this point is computed in the modal space; the further a point is from

the HDR, the less probable is the realization ¹.

A multivariate KDE (see Section 2.2.1) technique is used to estimate the PDF $\hat{f}(\mathbf{x}_r)$ of this multivariate space. From this KDE, the HDR reads

$$R_\alpha = \mathbf{x}_r : \hat{f}(\mathbf{x}_r) \geq f_\alpha, \quad (2.35)$$

with f_α such that $\int_{R_\alpha} \hat{f}(\mathbf{x}_r) dx_r = 1 - \alpha$. With this definition, the HDR corresponds to the region of highest PDF with a cumulative probability of $1 - \alpha$. The 50% and 90% HDR are computed, corresponding respectively to $\alpha = 0.5$ and $\alpha = 0.1$. By construction a HDR develops around the maximum PDF $\max\{\hat{f}(\mathbf{x}_r)\}$ which identifies the most probable mode. Transposed using the inverse transform from the reduced space to the original space, this most probable mode corresponds to the "central curve"—also referred to as the median curve.

Except if the response variable of the system of interest is chaotic under the perturbation of its input parameters, the POD is expected to drastically reduce the dimensionality of the problem. Furthermore, as the system's response variable is also expected to oscillate around some modes, the points in the reduced space are likely to be relatively clustered around the modes. This mitigates the difficulty of the density estimation procedure.

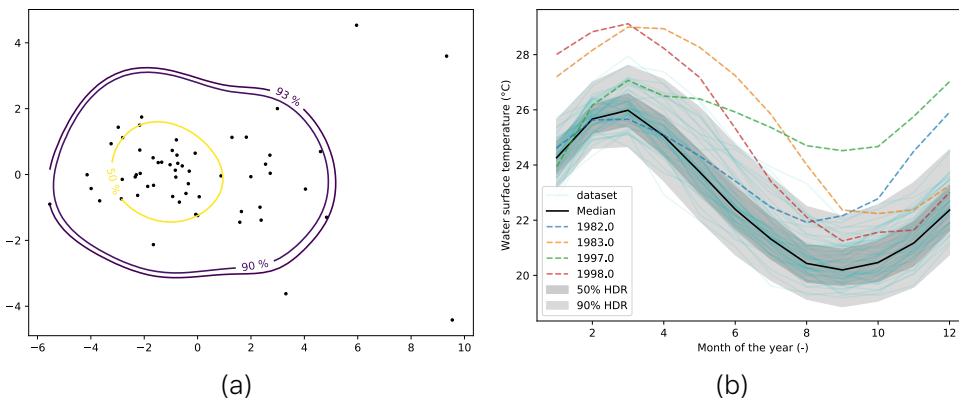


Figure 2.26 – HDR boxplot on the El Niño dataset. **a** scatter plot of the 2-dimensional reduced space with each dot as a realization. **b** dataset visualization with each curve as a realization from the database. Shaded areas are confidence intervals, *thick solid black line* is the mean realization and *highlighted-dashed curves* are outliers.

Fig. 2.26 illustrates the HDR boxplot for the El Niño dataset in the reduced space (*left*) when only two modes are retained ensuring that at least 80% of the response variable variance is conserved. Each realization is characterized with respect to the HDR metric. In the modal space, each dot represents a realization within the dataset and the contouring represents the 50% and 90% quantiles. In the response

¹The term *median*, which is used in the literature, is restrictive if there are multiple clusters of point in the reduced space.

variable physical space (*right*), *cyan curves* represent the realizations from the dataset, the outliers are *coloured-dashed curves*, the *thick black curve* is the median and the *grey shaded areas* represent 50% and 90% quantiles envelopes. It should be noted that additional realizations with chosen characteristics on the outputs could be drawn by sampling the input for specific HDR criteria.

3 | Scientific Questions

FROM this literature review, this thesis proposes to contribute to three axis:

- *How to construct a DoE in a high-dimensional parameter space?*
The number of simulations at hand is highly constrained by the computational power, the cost and the return time. A surrogate can only interpolate the physics which has already been seen, hence the need to explore uniformly the parameter space. When the number of parameters is high, controlling the sparsity in the DoE is challenging. I have developed a new sampling strategy that is versatile and performs well with such constraints.
- *How to resample a DoE by considering the QoI of already sampled experiments?*
Using the aforementioned novel method, it is possible to iteratively complete the DoE. This method does not incorporate any prior information on the shape of the response of the system. Here I propose a method which combines a Gaussian Process surrogate model with a LOOCV procedure in order to add a new sample in the DoE. This method has proven good behaviour in high-dimensional parameter space.
- *How to visualize uncertainties in high-dimensional cases?*
Analysing both input parameter space and QoI is challenging when the dimension is high. I present some new ways to help understand uncertainties in this context.

To support these methodological aspects, some industrial applications have been used.

CHAPTER 3. SCIENTIFIC QUESTIONS



Methodological Contributions

4 Scientific Dissemination	45
Articles	45
Conferences	46
Reviews	46
European Projects	47
Training	47
5 Batman	49
5.1 Description	49
5.2 Implementation	51
5.3 Functionalities	52
5.3.1 General functionment	52
5.3.2 Using it	53
5.3.3 Content of <i>test_cases</i>	53
5.4 Dissemination	53
6 Constructing a Design of Experiments	55
6.1 Introduction	55
6.2 Presentation of the Method	56
6.2.1 Determination of the Exclusion Field	56
6.2.2 Sampling and Selection Procedures	57
6.3 Results	61
6.3.1 Uniformity of the Design	61
6.3.2 Integration Convergence	63
6.4 Advantages	65
6.5 Summary	69
7 Resampling the Design of Experiments	71
7.1 Introduction	71
7.2 Presentation of the Methods	72
7.3 Construction of the Hypercube	73
7.4 Evaluation of the Methods	74
7.4.1 Restriction of the DoE	75
7.4.2 Application on Analytical Functions	77
7.5 Summary	81

8 Uncertainty Visualization	83
8.1 Introduction	83
8.2 Uncertainty Visualization of Functional Output Data . . .	84
8.2.1 Dynamic Visualization of Functional Outputs's Statistics	84
8.2.2 Sonification of Functional Outputs's Statistics . . .	84
8.3 Uncertainty Visualization of Large Number of Input Variables	86
8.4 Summary	89

4 | Scientific Dissemination

THE MAIN contribution of this thesis lies in the dissemination of my work through an open source python library called BATMAN. Thus, all the new methodologies developed are openly available to the community.

On a strict academic point of view, I have produced ¹:

- 7 articles (3 accepted, 4 in reviews),
- 7 communications in conferences,
- 3 reviews in international journals,
- 2 implications in European projects.

The following chapters provide an in-deep presentation of the new methodologies developed during this thesis.

Articles

- [1] Robin Campet, Pamphile T. Roy, Bénédicte Cuenot, Élénore Riber, and Jean-christophe Jouhaud. Design Optimization of Heat Exchanger using Gaussian Process. *In review for International Journal of Heat and Mass Transfert*, 2018.
- [2] Pamphile T. Roy, Lluis Jofre, Jean-christophe Jouhaud, and Bénédicte Cuenot. Versatile Adaptive Sampling Algorithm using Kernel Density Estimation. *In review for Technometrics*, 2019.
- [3] Pamphile T. Roy, Guillaume Daviller, Jean-christophe Jouhaud, and Bénédicte Cuenot. Uncertainty Quantification-Driven Robust Design Assessment of a Swirler Geometry. *In review for Computers & Fluids*, 2018.
- [4] Pamphile T. Roy, Sophie Ricci, Bénédicte Cuenot, and Jean-christophe Jouhaud. Sounding kiviat: representing uncertainties in high dimensions. *In review for Journal of Computational and Graphical Statistics*, 2018.
- [5] Pamphile T. Roy, Sophie Ricci, Romain Dupuis, Robin Campet, Jean-Christophe Jouhaud, and Cyril Fournier. BATMAN: Statistical analysis for expensive computer codes made easy. *The Journal of Open Source Software*, 3(21):493, 2018.

¹For an up-to-date list of my contributions, see my ResearchGate profile: https://www.researchgate.net/profile/Pamphile_Roy

- [6] Pamphile T. Roy, Luis Miguel Segui, Jean-Christophe Jouhaud, and Laurent Gicquel. Resampling strategies to improve surrogate model-based uncertainty quantification: Application to LES of LS89. *International Journal for Numerical Methods in Fluids*, 87(12):607–627, aug 2018.
- [7] Pamphile T. Roy, Nabil El Moçayd, Sophie Ricci, Jean-Christophe Jouhaud, Nicole Goutal, Matthias De Lozzo, and Mélanie C. Rochoux. Comparison of polynomial chaos and Gaussian process surrogates for uncertainty quantification and correlation estimation of spatially distributed open-channel steady flows. *Stochastic Environmental Research and Risk Assessment*, pages 1–29, oct 2017.

Conferences

- [8] Sophie Ricci, Vincent Lemiale, N. Andres-Thio, Matt Bolger, and Pamphile T Roy. Sensitivity Analysis on Flood Evacuation Model. In *SAMO*, 2019.
- [9] Corentin J Lapeyre, Nicolas Cazard, Pamphile T Roy, Sophie Ricci, and Fabrice Zaoui. Reconstruction of Hydraulic Data by Machine Learning. In *SimHydro*, 2019.
- [10] Matthias De Lozzo and *et al.* Applicative , methodological and software contributions to uncertainty quantification for environmental modeling. In *Symposium on Uncertainty Quantification in Computational Geosciences*, Orleans, 2018.
- [11] Pamphile T. Roy and *et al.* Uncertainty Quantification-driven Robust Optimization of a Swirler's Geometry. In *INCA*, page 7, 2017.
- [12] Pamphile T. Roy. Improving Surrogate Model-based Uncertainty Quantification in a Costly Numerical Environment. In *OpenTURNS Users Day 10*, 2017.
- [13] Matthias *et al.* De Lozzo. Méthodes de Monte-Carlo multi-niveaux pour la quantification d'incertitudes et l'assimilation de données - Application a modélisation fluviale. In *Journée des Statistiques 2017*, pages 1–6, 2017.
- [14] Paul Mycek and *et al.* Multilevel Monte Carlo estimation of covariances in the context of open-channel flow simulations. In *CEMRACS*, 2017.
- [15] Pamphile T. Roy. Improving Surrogate Model-based Uncertainty Quantification Application to LES. In G D R MASCOT-NUM, editor, *MASCOT-NUM 2017*, Paris, France, 2017. Institut Henri Poincaré et AgroParistTech.

Reviews

I have been reviewing manuscripts in the following journals ²:

- Computational Geosciences (IF 2.726),
- Stochastic Environmental Research and Risk Assessment (IF 2.668),
- Computer Methods in Applied Mechanics and Engineering (IF 4.441).

European Projects

EoCoE action: Estimates of hydraulic variables and uncertainty estimates for major rivers in France used for hydropower production, Grand Agreement Number: EINFRA-676629.

COST action: secondary proposer for: Model Auditing and Sensitivity Analysis (MASIA).

Training

I have participated in the creation of a Small Private Online Course (SPOC) called: *Fundamentals of Uncertainty Quantification*. All sessions are built upon evidence-based principles from cognitive psychology and learning research with the help of an expert researcher in active online learning.

<https://cerfacs.fr/description-s poc-uq/>

This online training course presents the fundamental concepts of UQ. The course content is divided in 3 consecutive weeks:

Week 1: introduction to uncertainty quantification,

Week 2: uncertainty propagation and sensitivity analysis,

Week 3: formulation, validation and application of surrogate models.

An interactive live conference closes the 3-week sessions, focussing on UQ analysis for an applicative test case in CFD.

At the end of this training, the trainee should be able to

- give a grounded opinion about various tools of UQ: sensitivity analysis, DoE, surrogate model,

²Reviews have been verified on publons: publons.com/a/1567681

- set up a UQ analysis on a simple problem: choose an appropriate set of tools for a case study,
- make the most of a UQ study (modelling the input uncertainties, sampling the uncertain input domain, quantifying the output uncertainty, analysing the output sensitivity with respect to the inputs).

This online course has been run twice, and I have been presenting the live sessions. We have received a lot of good feedbacks, we are improving and updating this product continuously.

5 | Batman

En raison de l'intérêt croissant pour la UQ au cours de la dernière décennie, un nombre important d'outils/bibliothèques dédiés à la UQ sont maintenant disponibles pour la communauté scientifique. Par exemple, OpenTURNS est une importante bibliothèque scientifique open-source (GNU LGPL) développée par EDF, Airbus, Phimeca et IMACS et utilisable comme module Python dédié au traitement des incertitudes et aux analyses de fiabilité dans une approche industrielle [27].

Bayesian Analysis Tool for Modelling and uncertainty quantification (batman) est un paquet Python open source dédié à l'analyse statistique basée sur une approche non intrusive [5] développée au CERFACS. La bibliothèque Batman fournit un cadre pratique, modulaire et efficace pour la conception de DoE, de modèle de substitution et pour la quantification de l'incertitude – voir Fig. 5.1. Batman s'appuie sur des paquets python open sources dédiés aux statistiques (OpenTURNS et Scikit-Learn [174]). Batman est sous licence CECILL-B ; il est activement développé et maintenu par les chercheurs du CERFACS via la plateforme GitLab.

Ce chapitre présente Batman, de sa genèse à son utilisation ainsi que quelques fonctionnalités clés.

5.1 Description

Due to the increasing interest in UQ over the last decade, a significant number of UQ-dedicated tools/libraries are now available for the scientific community. For example, OpenTURNS is a famous open-source (GNU LGPL) scientific library developed since 2005 by EDF, Airbus, Phimeca and IMACS and usable as a Python module dedicated to uncertainty treatment and reliability analysis in a structured industrial approach [27].

OpenTURNS offers a wide catalogue of features for UQ (e.g. PC expansion [64], Sobol' indices, DoE) and benefits from a well-organized developers' and users' community (forum, training, user guides). It can either be used as a Python module or as a component within a coupling platform. For further information on the OpenTURNS library, the reader is referred to the [online reference](#) and use case guides. OpenTURNS is a powerful and complete statistical library but as being used operationally, and being in a research mode thus inheriting

from existing developments at CERFACS, it was not envisageable to directly implement new methodologies. Moreover, as coded in C++, the development time is known to be one order slower than with Python. Thus it has been decided that this thesis would rely on an available in-house library.

Bayesian Analysis Tool for Modelling and uncertainty quantification (batman) is an open source Python package dedicated to statistical analysis based on non-intrusive ensemble experiment [5] developed at CERFACS. Batman library provides a convenient, modular and efficient framework for design of experiments, surrogate model and uncertainty quantification—see Fig. 5.1. Batman relies on open source python packages dedicated to statistics (OpenTURNS and Scikit-Learn [174]). Batman handles the workflow for statistical analysis. It makes the most of HPC resources by managing asynchronous parallel tasks. The internal parallelism of each task does not conflict with batman’s parallel environment. Batman analysis is launched from a *command line interface* and a setting file. Batman functionalities can also be accessed through an API. Batman is CECILL-B licensed; it is actively developed and maintained by researchers at CERFACS through the GitLab platform:

<https://gitlab.com/cerfacs/batman>

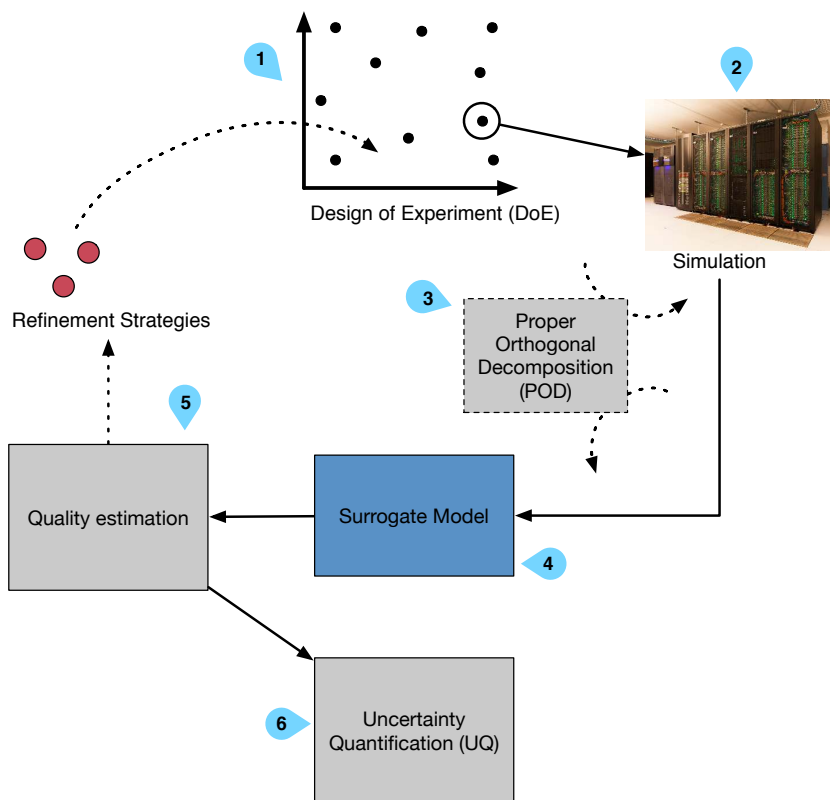


Figure 5.1 – General workflow of Batman.

This project, and the code related, was initiated in 2007 at CERFACS under the name JPOD (Jack Proper Orthogonal Decomposition) by T.

Braconnier and M. Ferrier, which were supervised by J-C. Jouhaud and J-F. Boussuge. During 5 years, the code has been successfully tested and validated on industrial configurations during the European SimSAC and ALEF (FP7) projects.

The project has been dormant until 2015 when Romain Dupuis (PhD student supervised by J-C. Jouhaud) started to be interested in surrogate models for aerothermal predictions. Around the same time, an UQ axis was started at CERFACS. After that, in 2016, Uncertainty Quantification capabilities were added by me leading to the new name: Batman. On November, 23th 2017 the UQ team of CERFACS have decided to release the code on GitLab as open-source under the CECILL-B free software license agreement.

The following people have been core contributors to batman's development and maintenance:

- Pamphile Roy,
- Romain Dupuis,
- Jean-Christophe Jouhaud,
- Sophie Ricci,
- Robin Campet,
- Cyril Fournier,
- Antoine Dechaume (JPOD),
- Thierry Braconnier (JPOD),
- Marc Ferrier (JPOD).

5.2 Implementation

The library is developed in Python 3.x and the code is compatibility with legacy Python (2.7.x). The code is structured by an object oriented approach by using classes. This allows to connect Batman with all Python's ecosystem.

The code is developed using a Test Driven Development (TDD) approach. Thus every function and class is tested by unit-tests, system tests and integration tests. Moreover, programming style standards are respected meaning that the code is completely documented and should be maintainable with low effort.

Git versioning system is used through the web interface of Gitlab. It allows to manage the project with issues and milestones. The git branching model follows the *gitflow* initiative. A *master* branch is used for releases while a *develop* branch incorporates the latest stable changes.

For each new code, *feature* branches are created. In order to synchronize to these branches, the code must have been reviewed by at least two trusted developers. Along with every synchronization of the branches on the server, Continuous Integration (CI) tools are used. All these processes ensure that both *master* and *develop* branches are bug free, tested and documented.

There is no fixed release cycle. When a new release is made on *master*, builds are created for easy installation with both *conda* and *pip*. The reader may refer to the online documentation:

<http://batman.readthedocs.io>

5.3 Functionalities

The Batman package includes three folders:

doc contains the documentation,

batman contains the module implementation,

test_cases contains some example.

5.3.1 General functionment

The package is composed of several python modules which are self contained within the directory *batman*. Following is a quick reference—see Appendix D for more details—:

ui command line interface,

space defines the (re)sampling space,

surrogate constructs the surrogate model,

uq uncertainty quantification,

visualization uncertainty visualization,

pod constructs the POD,

driver contains the main functions,

tasks defines the context to compute each snapshot from,

functions defines useful test functions,

misc defines the logging configuration and the settings schema.

5.3.2 Using it

After Batman has been installed, *batman* is available as a command line tool or it can be imported in python. Thus Batman is launched using:

```
batman settings.json
```

The definition of the case is to be filled in *settings.json*. An *output* directory is created and it contains the results of the computation splitted across the following folders:

- *snapshots*,
- *surrogate*,
- *predictions*,
- *uq*.

5.3.3 Content of *test_cases*

This folder contains ready to launch examples:

Basic_function is a simple 1-input parameter function,

Michalewicz is a 2-input parameters non-linear function,

Ishigami is a 3-input parameters,

G_Function is a 4-input parameters,

Channel_Flow is a 2-input parameters with a functionnal output,

Mascaret make use of MASCARET open source software (not included).

In every case folder, there is *README.rst* file that summarizes and explains the case.

5.4 Dissemination

Since batman was publicly made available in 2017, we have been using it with industrial partners:

- EDF,
- AIRBUS,
- SFRAN,
- Total.

Moreover, we are collaborating with academic and institutional partners:

- Stanford University,
- Basque center for applied mathematics (bcam),
- Cerema,
- SCHAPI,
- INSA Toulouse,
- ENSEEIHT,
- MONASH University,
- CSIRO,
- University of Hohenheim.

6 | Constructing a Design of Experiments

Dans ce qui suit, je propose une nouvelle méthode de construction d'un DoE stochastique et itératif — nommé KDOE — basé sur une estimation de densité de noyau (KDE). Il s'agit d'un processus en deux étapes : (i) les échantillons candidats sont générés en utilisant une chaîne de Markov basé sur un KDE, et (ii) l'un d'eux est sélectionné en fonction de certaines métriques. La performance de la méthode est évaluée au moyen du critère de remplissage de l'espace à savoir une discrépance C^2 .

KDOE semble être aussi performant que les méthodes classiques non itératives en faible dimension, alors qu'il présente des performances accrues pour les espaces de paramètres à haute dimension.

Ce travail propose une nouvelle méthodologie d'échantillonnage stochastique de l'espace des paramètres d'entrée permettant, de manière itérative, de prendre en compte toute contrainte, telle que des DoE non rectangulaires, des indices de sensibilité ou même des contraintes de qualité sur des sous-projections particulières comme dans [114].

C'est une méthode polyvalente qui offre une alternative aux méthodes classiques et, en même temps, est facile à mettre en œuvre et offre une personnalisation basée sur l'objectif du DoE.

6.1 Introduction

In the following, a new stochastic, iterative DoE — named KDOE — based on a modified Kernel Density Estimation (KDE) is presented. It is a two-step process: (i) candidate samples are generated using MCMC based on KDE, and (ii) one of them is selected based on some metric. The performance of the method is assessed by means of the C^2 -discrepancy space-filling criterion. KDOE appears to be as performant as classical one-shot methods in low dimensions, while it presents increased performance for high-dimensional parameter spaces. This work proposes a new methodology to stochastically sample the input parameter space iteratively allowing, at the same time, to take into account any constraint, such as non-rectangular DoE [137], sensitivity indices or even constraint on the quality on particular subprojections

as in [114]. It is a versatile method which offers an alternative to classical methods and, at the same time, is easy to implement and offers customization based on the objective of the DoE.

6.2 Presentation of the Method

In its basis form, the adaptive sampling strategy consists in adding a point far from the existing points in the parameter space. The notion of distance corresponds to a measure of discrepancy. However, instead of considering the whole hypercube, the technique proposed only focuses on empty regions defined using an Exclusion Field (EF). This exclusion field describes the probability of selecting a new point depending on its position.

By means of utilizing EF, it becomes possible to generate new samples that are located preferentially in these empty regions. Then, out of the n_{gen} generated samples from the EF, the one that leads to the best value of some criterion is selected. It is to be noted that there is no optimization process in the sense that it is just a selection process based on probable samples of the EF. The whole process ensures randomness in the generation of the parameter space.

Section 6.2.1 introduces the EF, and Section 6.2.2 describes the sampling procedure from the EF. In the following, the method is referred to as the Kernel-DoE (KDOE) method and is presented in Algorithm 1.

Algorithm 1 Sampling Strategy: Kernel-DoE

Require: $\mathbf{X}_d^{N_s}, N_{max}, N_s, n_{gen} \triangleright$ Start from a sample $\mathbf{X}_d^{N_s}$ composed of N_s samples in dimension d

- 1: **while** $N_s < N_{max}$ **do**
- 2: $f \leftarrow$ Construction of the Exclusions Field from $\mathbf{X}_d^{N_s}$
- 3: $\mathbf{Y}_d^{n_{gen}} \leftarrow$ pick n_{gen} samples using Metropolis-Hasting MCMC
- 4: $\mathbf{Y}_d^j \leftarrow$ point in N_{gen} which minimize the discrepancy
- 5: $\mathbf{X}_d^{N_s+1} \leftarrow \{\mathbf{X}_d^{N_s}, \mathbf{Y}_d^j\}$
- 6: **end while**

6.2.1 Determination of the Exclusion Field

Assumed that N_s samples have already been selected. The spatial probability density function used to draw a new sample is given by:

$$f(\mathbf{x}) = 1 - \sum_{i=1}^{N_s} K(\mathbf{x}, \mathbf{x}^{(i)}). \quad (6.1)$$

The N_s samples that have already been chosen are noted $\mathbf{x}^{(i)}$, with i between 1 and N_s . The dimension is noted d and K is a kernel expressed

by:

$$K(\mathbf{x}, \mathbf{x}^{(i)}) = \exp\left(-\frac{D(\mathbf{x}, \mathbf{x}^{(i)})^2}{2h^2}\right), \quad (6.2)$$

D is a distance function that will be expressed later. The general idea is to lower the probability of selecting a new point close to the samples already drawn. Hence a zone of exclusion is created around each of the already selected points, with a width parametrized by h , set here at $h = \sigma/N_s^{1/d}$ with $\sigma = 0.3$. This in particular allows to have a width of exclusion that decreases as the number of samples increases. In addition, the probability is set to 0 outside of the unit hypercube in order to prevent sampling outside of the region of interest. We also ensure that the probability is always greater or equal than 0. Note that this probability is not normalized. It will be shown in the next section that normalization is not required for the sampling procedure.

Various expressions of the distance function D allow to generate many different shapes. In the present case, alignment of samples on each axis should be avoided as done with Latin Hypercube Sampling designs. This is achieved by using a Minkowski distance [42] for D :

$$D(\mathbf{x}, \mathbf{x}^{(i)}) = \left(\sum_{j=1}^d |x_j - x_{ij}|^p \right)^{1/p}, \quad (6.3)$$

where p is the order of the distance. Setting $p < 1$ leads to a *star shape* for the PDF f , as shown in Fig. 6.1 starting from one already selected sample ($N_s = 1$), and using $p = 0.5$.

In Fig. 6.2, three samples were already selected in a 3-dimensional parameter space. The star shape is visible in all dimensions, its branches interact with each other as shown in Fig. 6.3 clearly illustrating the cumulative property of the PDFs. In this last case $\sigma = 0.8$ to highlight this property.

6.2.2 Sampling and Selection Procedures

The classical way to sample from a PDF is to use the inverse transform sampling method. However, finding the inverse cumulative distribution function of a complex PDF can be computationally intensive —the cost increases with dimensionality. The *Metropolis-Hastings* [96] MCMC algorithm was selected as an efficient way to sample from f . Contrary to methods such as HMC or NUTS [97], it does not require the calculation of the gradient of the log-probability density function, which is a costly operation. This algorithm provides a random walk of the parameter space that converges toward the targetted PDF.

Using an arbitrary distribution $g(\mathbf{x}|\mathbf{y})$, a new candidate \mathbf{x} is evaluated based on the previous point \mathbf{y} . This property makes it a *Markov Chain*

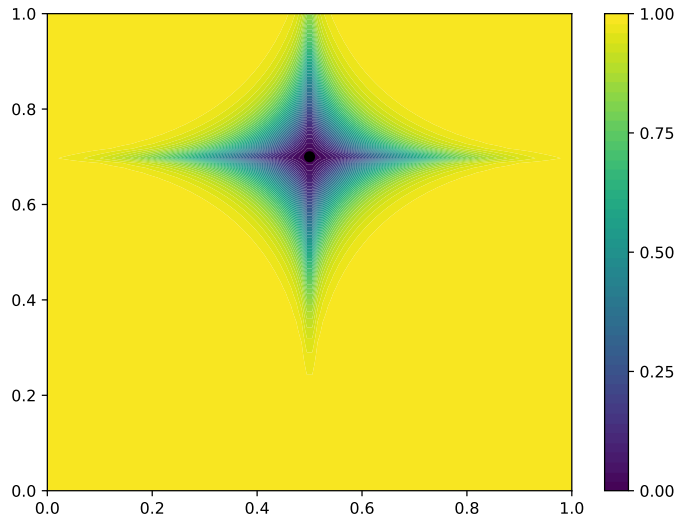


Figure 6.1 – Probability density function of presence in a 2-dimensional parameter space. Dot represents the sample already drawn at (0.5, 0.7).

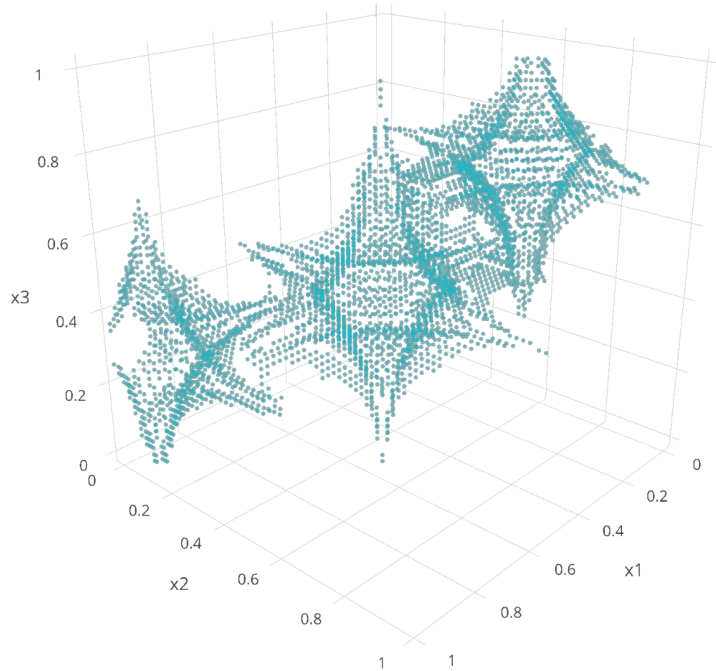


Figure 6.2 – Scatter plot representation of a 3-dimensional PDF with three points already set in the parameter space. Points represent an iso value of probability.

as the current value is only conditioned by the previous one. The distribution g is chosen as a Gaussian PDF so that samples close to the previous one are preferably sampled. This algorithm provides a random walk of the parameter space that converges toward the target PDF.

Figure 6.4 shows an example with two initial points already selected in the hypercube $[0, 1]^2$. Based on these two points (dots), f is built and

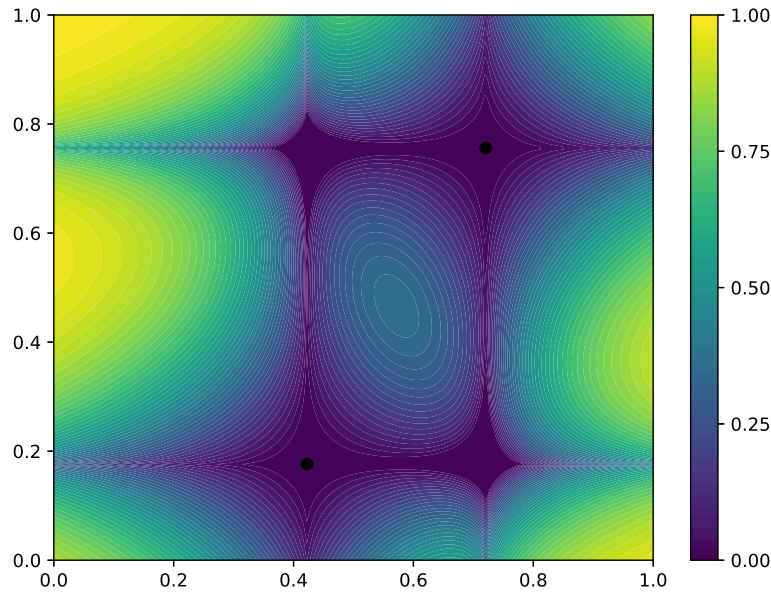


Figure 6.3 – Cumulative effects on the probability density function in a 2-dimensional parameter space. The *dots* represent 2 existing samples.

new samples are drawn (squares) using the MCMC method.

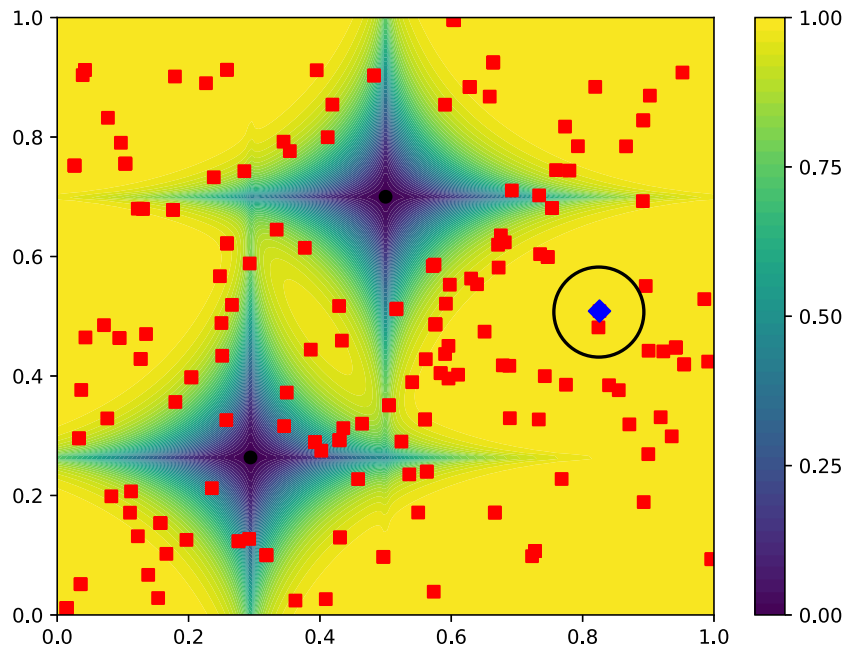


Figure 6.4 – Probability density in a 2-dimensional parameter space. *Dots* represent the samples already drawn, *squares* are the result of the Metropolis-Hasting sampling and *circled-diamond* is the sample selected based on the resulting centred discrepancy.

The next step consists in choosing a new sample from these candidates. Any metric can be chosen here depending on the final objective. In the following, the focus was made on the uniformity of the DoE. Hence,

the centred discrepancy C^2 is used [71]—see Eq. (2.3). Since the lowest values of C^2 -discrepancy result in more uniform samples, the sample minimizing it is chosen (*circled-diamond*). Thus, this iterative procedure acts like an optimizer on the C^2 -discrepancy where the candidates are not drawn totally randomly but with the knowledge of the current samples. Figure 6.5 shows an example with 10 points. The initial sample consisted of one point. The result is a low discrepancy sample constructed iteratively.

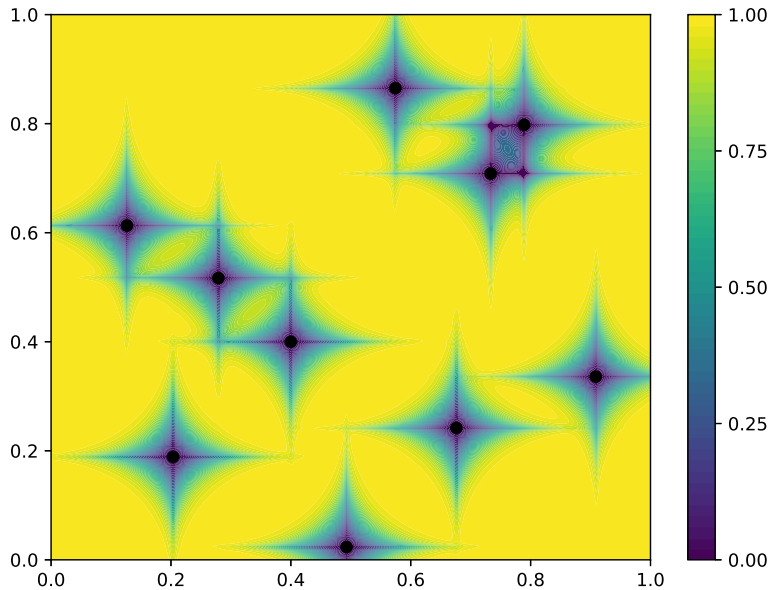


Figure 6.5 – Probability density in a 2-dimensional parameter space. The 10 dots represent the samples used to fit the KDE.

The method is not deterministic which is useful if one wants to generate a new independent set of experiments. To compute sensitivity indices of *Sobol'*, two independent samples are required [200]. As stated in [200], quasi-random sequences such as *Sobol'* are classically used but, as they are deterministic, it is not possible to generate an independent sample directly. One possibility is to get these two samples as one sample of shape $X_{2d}^{N_s}$. Splitting the matrix column wise-like ensures independence of the samples. However, as the dimensionality increases, the quality of the sequence deteriorates ($d > 10$). Hence, this technique is limited to a small number of dimensions. Our method does not share this limitation.

As stated, n_{gen} candidate samples are generated through MCMC. Figure 6.6 presents a convergence analysis of the quality of the final design X_2^{40} depending on the size of the MCMC sample at each iteration. Confidence intervals are calculated using 100 realizations of the same parametrization. The discrepancy converges to its final value after $n_{gen} > 100$. This allows to control the computational cost required to generate the DoE. Various configurations of $X_d^{N_s}$ have been tested and results are similar. In the following, n_{gen} was fixed to 100.

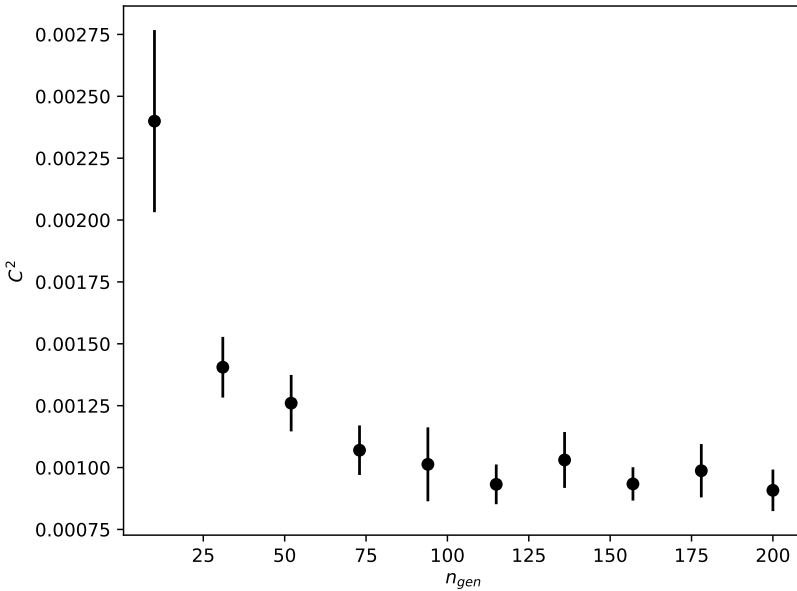


Figure 6.6 – Convergence of the C^2 -discrepancy function of n_{gen} the size of sample using Metropolis-Hasting for X_2^{40} .

6.3 Results

6.3.1 Uniformity of the Design

As stated previously, the uniformity of the DoE is paramount to ensure that the physics of interest are well captured. Figure 6.7 presents a convergence study of the KDOE method versus *Sobol'* sequences [218], classical LHS [158], and optimized LHS as proposed in [27]. Each point corresponds to a given sample size N_s for a given number of dimensions d . Due to the stochastic nature of the LHS algorithms and of the KDOE, confidence intervals are computed based on 100 realizations. To measure the improvement of a method with respect to the other, the C^2 -discrepancy is used [71, 20] and values are normalized by crude Monte Carlo (MC) results. This transformation shows that a uniform improvement factor is obtained in comparison to MC. Looking for instance at $d = 20$, LHS enables a 20% improvement in terms of C^2 -discrepancy over MC, *Sobol'* sequence gives 30% and both OLHS and KDOE roughly give 40%.

The obtained hierarchy between LHS, OLHS and *Sobol'* is quite stable. OLHS is the best method followed by *Sobol'* sequence and finally LHS. For KDOE, it performs closely to *Sobol'* sequence up to $d \lesssim 20$. For $d \gtrsim 20$, KDOE performs better than all the other methods tested.

Moving on to two standard deviation (2σ) — see Fig. 6.8 —, the results of KDOE always lies between LHS's and OLHS's.

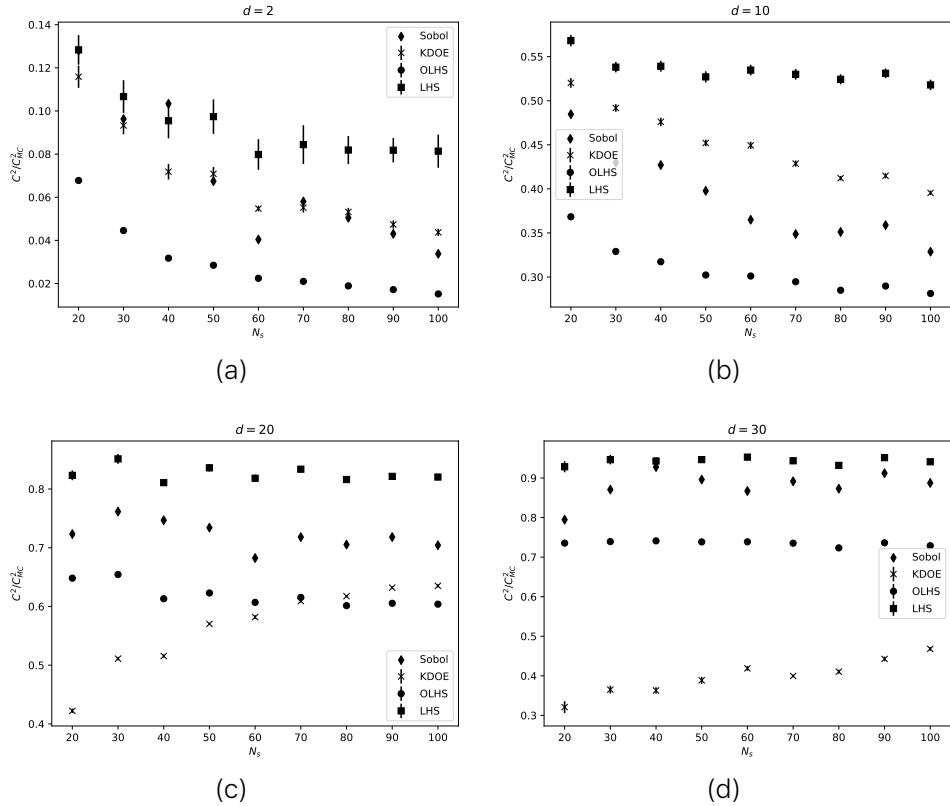


Figure 6.7 – Normalized C^2 -discrepancy function of the number of dimensions d of the parameter space and of the size N_s of the design for various DoE methods.

Figure 6.9 presents the convergence analysis of the C^2 -discrepancy as a function of the number of dimensions for $N_s = 100$. When the dimensionality increases, the gain with both LHS and Sobol' sequences is close to zero. On the contrary, OLHS seems to stabilize around a 30% improvement. Regarding KDOE, it performs equally with other methods up to $d \lesssim 20$, while for $d \gtrsim 20$ it becomes more performant. It can be seen that the method has not yet reached its minimum at $d = 40$.

In terms of C^2 -discrepancy, KDOE appears to perform better with respect to crude *Monte Carlo*, LHS, OLHS and Sobol' sequence. Figure 6.10 shows an example of a sample of size $N_s = 50$ in dimension $n_{dim} = 30$. The subprojection x_{20}/x_8 is represented. Figure 6.10(d) depicts the principal challenge with classical Sobol' sequences. In high dimensional parameter space, clear patterns may appear in some sub-projections. This behaviour was not observed with KDOE. In this case, the result of the KDOE may not appear optimized for 2-dimensional subprojections. This is due to the fact that the objective is to optimize the total discrepancy of the parameter space.

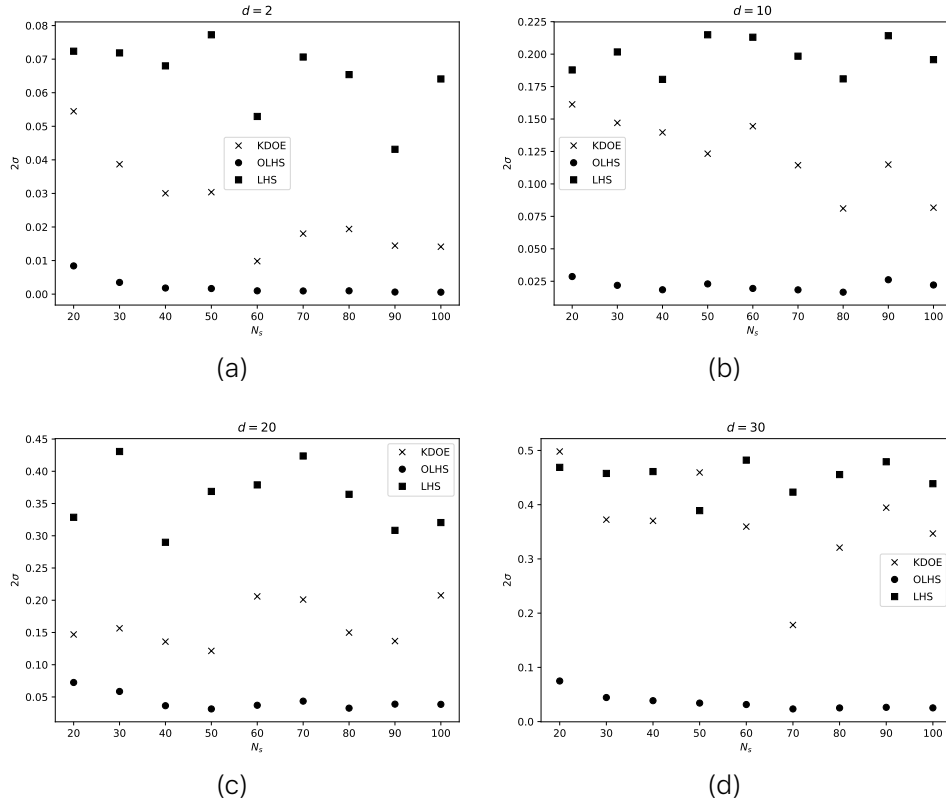


Figure 6.8 – Normalized deviation at 2σ on the C^2 -discrepancy function of the number of dimensions d of the parameter space and of the size N_s of the design for various DoE methods.

6.3.2 Integration Convergence

As stated previously in Section 2.1, integrating a multidimensional function require the use of a performant DoE. It can be assimilated to a discrepancy criterion.

Even if this method is not designed for integral evaluation, its performance is evaluated on small numbers of samples up to 512. The number of evaluations has been restricted as the purpose of the method is to generate a small design in high dimensions. Also, the use of an iterative method to generate such sample can be questioned due to the resulting computational cost. Moreover, although this method can be used to continue an existing design created using another technique, such possibility was not evaluated in the following. In [127], convergence plots are presented in order to assess the performance of Sobol' sequence versus LHS and Monte-Carlo sampling. The functions used are categorized into types A, B and C. These categories state how the variables are important with respect to the function output:

Type A: Functions with a low number of important variables,

Type B: Functions with almost equally important variables but with low interactions with each other,

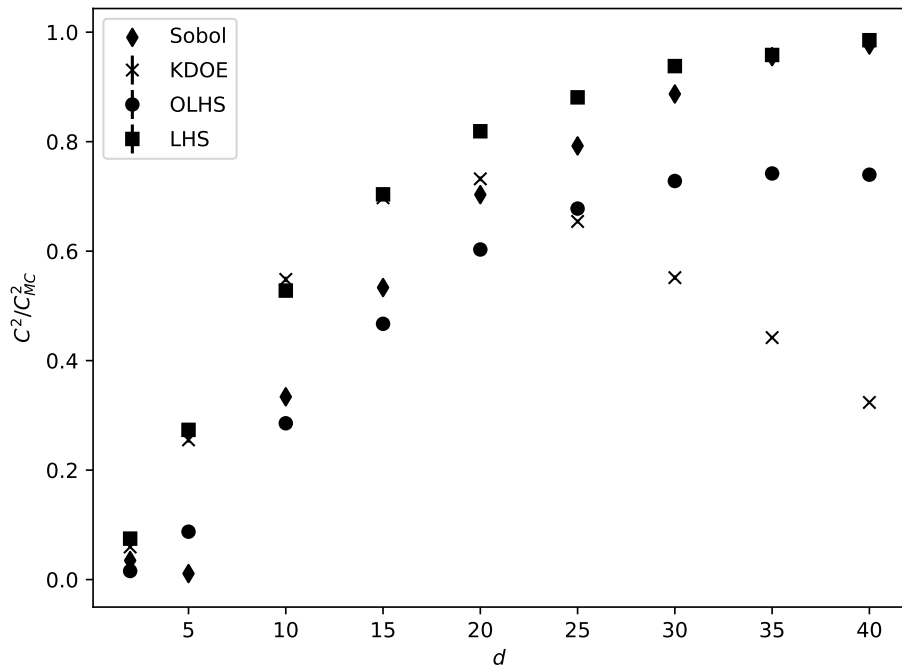


Figure 6.9 – Normalized C^2 -discrepancy function of the number of dimensions n_{dim} of the parameter space with a design of size $N_s = 100$ for various DoE methods.

Type C: Functions with almost equally important variables and with high interactions with each other.

Type C functions represent the most challenging case. In this work, one function per group is considered as detailed in Table 6.1. The theoretical integral for all these functions in the unit hypercube is 1. Quality of the integration is computed using the Root Mean Square Error (RMSE) defined as

$$\epsilon = \left(\frac{1}{K} \sum_{k=1}^K (I[f] - I_{N_s}^k[f])^2 \right)^{1/2}, \quad (6.4)$$

with $K = 50$ the number of independent trials and the estimate integral defined as

$$I_{N_s}^k[f] = \frac{1}{N_s} \sum_{i=1}^{N_s} f(\mathbf{X}_d^i), \quad (6.5)$$

with f the function to integrate.

Figure 6.11 presents the convergence study. KDOE is not the best method but seems to compare well to both LHS and Sobol' sequence. The convergence rates are correct for every function type.

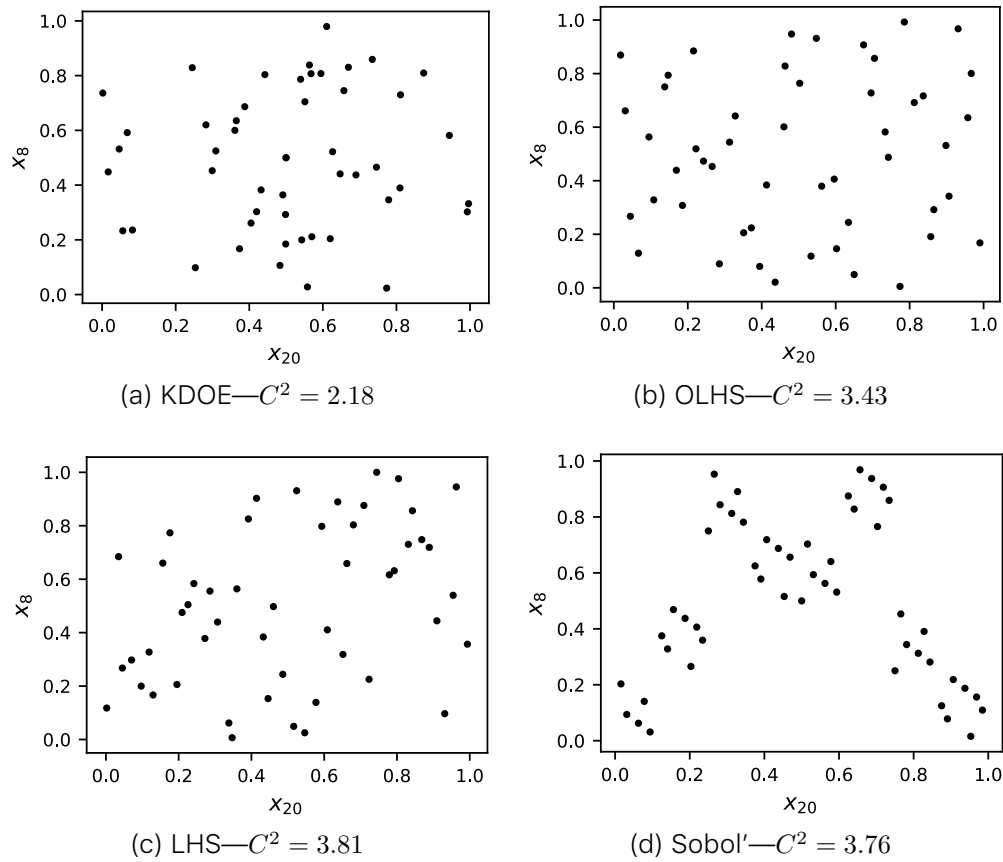


Figure 6.10 – Example of a 2-dimensional subprojection of the sample of size $N_s = 50$ in dimension $d = 30$ with various DoE methods.

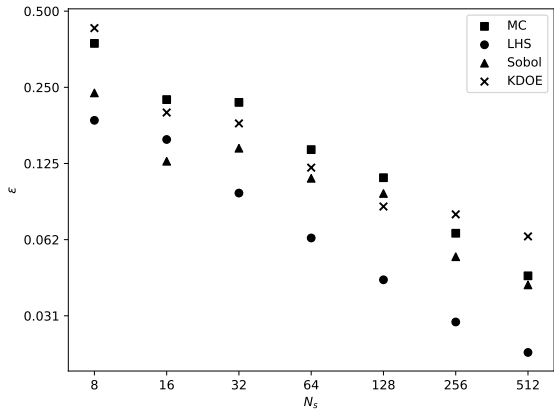
Table 6.1 – Type A, B and C functions used in the convergence analysis.

Type	Function $f(x)$	Dim d
A	$\prod_{i=1}^d \frac{ 4x_i - 2 + a_i}{1 + a_i}$	30
B	$\prod_{i=1}^d \frac{d - x_i}{d - 0.5}$	30
C	$2^d \prod_{i=1}^d x_i$	10

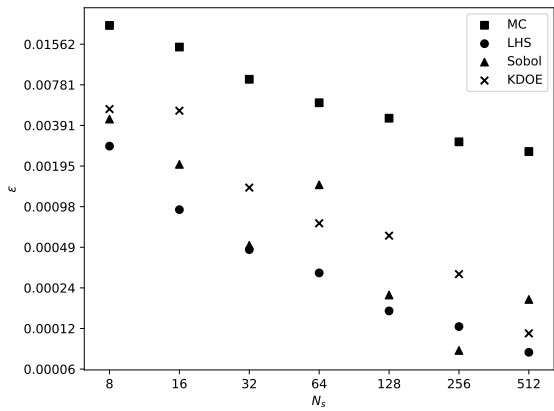
6.4 Advantages

Depending on the property sought, the combination of a Kernel and a metric allows for an infinite number of possible customizations of the method.

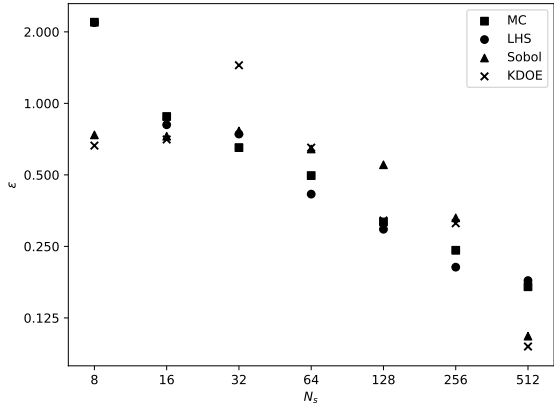
Using the Minkowsky distance as a metric, the LHS constraint is not strict which can be useful when dealing with discrete parameters.



(a) Type A



(b) Type B

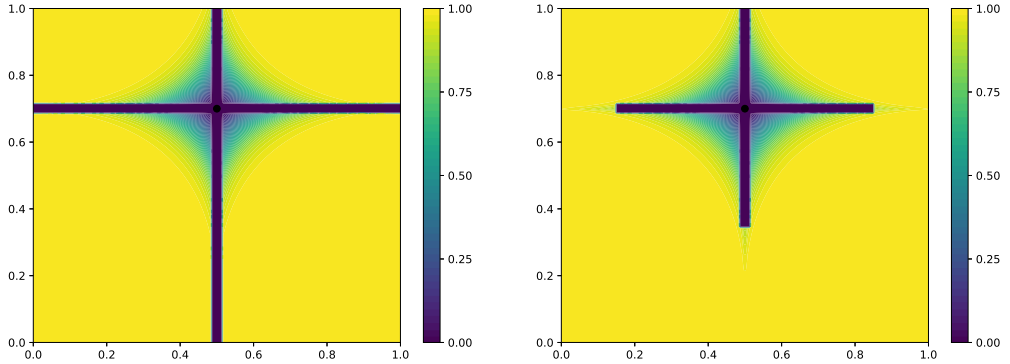


(c) Type C

 Figure 6.11 – RMSE function of the sample size N_s for type A, B and C functions.

Indeed, strict LHS would prevent from having more than one sample per discrete parameter. In Fig. 6.12(a), an additional constraint is added to strongly limit the probability to 0 when the L_∞ -norm is inferior to a threshold. This limitation can be restricted to a domain of influence using an additional L_2 -norm constrain (Fig. 6.12(b)). Hence, the presented

method acts as an iterative LHS strategy.



(a) Inverse Mindkowsky distance with LHS properties
 (b) Inverse Mindkowsky distance with LHS properties and constraint

Figure 6.12 – Probability density in a 2-dimensional parameter space. Dot represents the sample used to construct the KDE.

Using this method, it is also possible to consider non-rectangular domains [137]. This example presents a 2-dimensional domain with the constrain $0.5 < x_1 \times x_2 < 1$. In this case, the selection of the point criterion has to be changed as the C^2 -discrepancy assumes rectangular domains. Figure 6.13 shows a sampling of the aforementioned constrained design using a *maximin* criterion [71]. This criterion only considers the points of the sample resulting in an optimal sphere packing problem. The criterion seeks to maximize the minimal distance between the new point and the existing samples. This adaptation is to ensure that the new point is not penalized by existing samples that would be ill positioned in the parameter space.

The ability to change the selection criterion is even more useful. With a prior knowledge on the sensitivity of the parameters to the quantity of interest [201], it is possible to bias the design. Considering a 2-dimensional space —as the example in Fig. 6.14—, if the parameter x_2 is known to have a small impact, it might be more interesting to optimize the C^2 -discrepancy on the parameter x_1 . More complicated things can be performed if one wants to optimize a particular subprojection as in [114]. This is referred to as *Maximum Projection Design*.

Last but not least, this method can be used to generate designs by mixing continuous and discrete variables. The star shape of the kernel does not forbid from the presence of a new sample along a given axis, it lower its probability of being sampled up to a certain distance. In this case, a Gaussian kernel might be more appropriate in order to relax some constraint on the axes. Another option would be to modify the kernel to limit the point influence along the discrete axis.

The ability to change both with the kernel and the selection criteria is really powerful as it allows to manage most of the challenges in constrained optimization problems, use sensitivity information, and sample by means of following individual PDFs for each parameter.

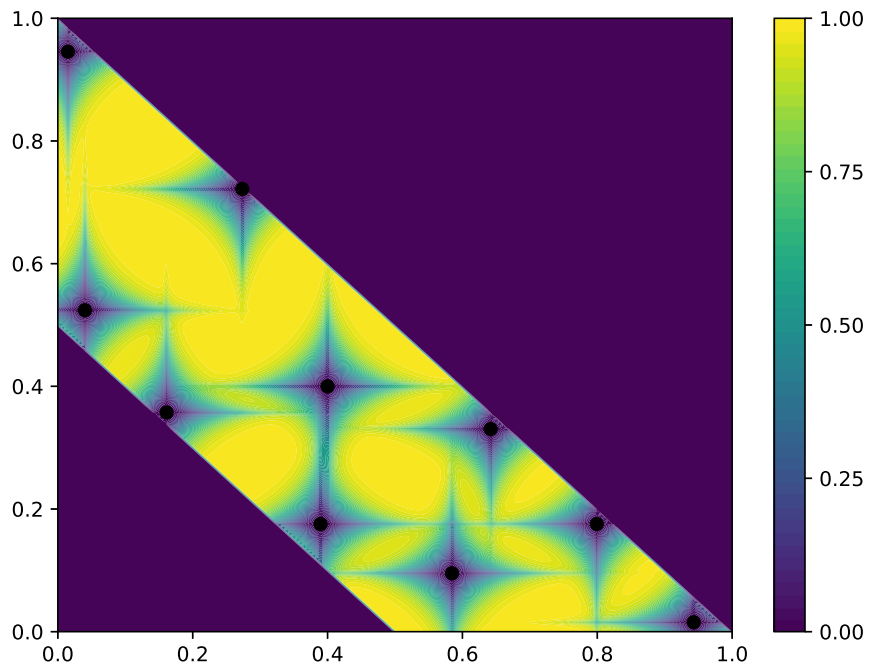


Figure 6.13 – Probability density in a non-rectangular 2-dimensional parameter space. The 10 dots represent the samples used to fit the KDE.

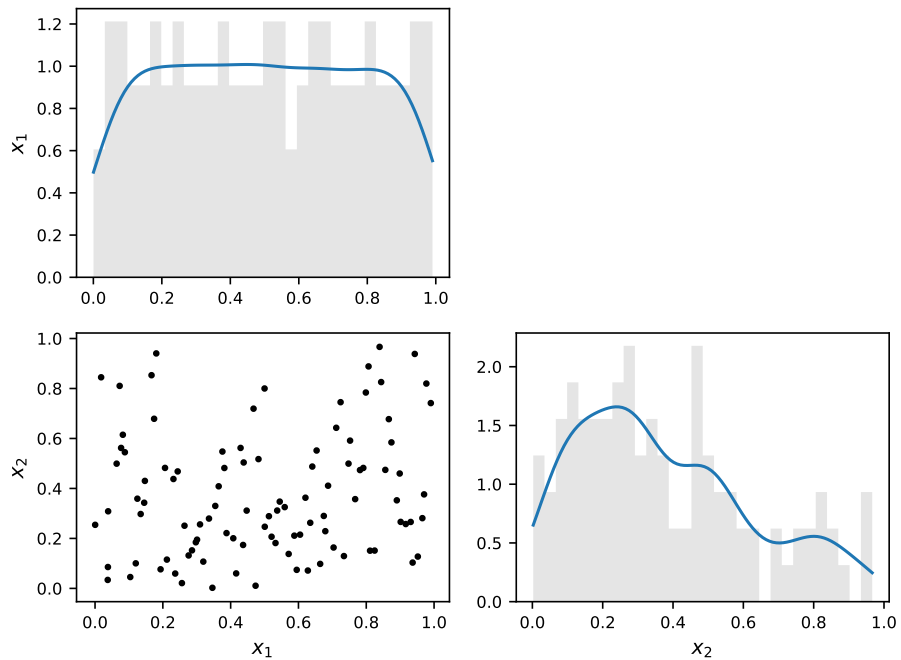


Figure 6.14 – 2-dimensional parameter space with x_0 the highest. Dots represent the sample. Sample distributions for each parameter are plotted along the diagonal.

6.5 Summary

This work proposes a new method to stochastically and iteratively sample a parameter space, referred to as KDOE method. This is a two-step process: *(i)* through a Kernel Density Estimation (KDE) some candidates are generated, then *(ii)* the best candidate is selected based on a criterion. This method does not take into account the physics of the problem of interest as adaptative strategies, but is purely iterative and case independent.

Compared to LHS and low discrepancy sequences, KDOE is totally iterative and stochastic. The space-filling properties of the new designs based on the C^2 -discrepancy are assessed and show good behaviour in high dimensions with small sample sizes. Moreover, it shows similar capabilities for numerical integration compared to classical methods. The KDOE method is versatile in the sense that it can be easily adapted to take into account constraints in the parameter space. Both discrete and continuous parameters can be used and sensitivity indices with respect to the parameters can be incorporated. This ability comes from the two-step process which can be independently tuned.

The quality of the design is of prime importance as it determines the quality of the analysis of the experiments. The proposed method provides an alternative to classical one-shot methods to generate initial designs and to continue existing ones. Its versatility and performance allow the analysis of expensive and high-dimensional cases to be within affordable budgets.

7 | Resampling the Design of Experiments

La précision d'une quantification d'incertitude étant directement corrélée à la qualité du modèle de substitution [106], le présent travail vise à améliorer sa construction en utilisant deux nouvelles stratégies pour rééchantillonner l'espace des paramètres.

Parmi les possibilités permettant de raffiner un DoE, on peut citer les méthodes tirant parti de la QoI [83]. Les méthodes présentées sont basées sur ce principe, tout en contrignant l'hypercube permettant le raffinement. Par conséquent, seule une fraction du volume original du DoE est utilisée dans le processus d'optimisation pour ajouter un nouvel échantillon. Cet hypercube réduit est construit en utilisant le résultat d'une procédure de LOO. Seule la zone entourant le point le plus critique est prise en compte. Cette technique s'appelle LOO- σ . Cette technique peut être encore plus limitée à l'aide d'informations sur la sensibilité. Ça mène à la technique LOO-Sobol'.

Les techniques présentées montrent une amélioration de la qualité prédictive du modèle avec des fonctions d'entrée analytiques de grande dimension.

7.1 Introduction

THE ACCURACY of an UQ being directly correlated to the quality of the surrogate model [106], the present work aims at improving its construction by using two new strategies for resampling the parameter space.

Among the possibilities to refine a DoE, are the methods taking advantage of the QoI [83]. The methods presented are based on this principle, while constraining the hypercube to consider for refinement. Hence only a fraction of the original volume of the DoE is used in the optimization process to add a new sample. This reduced hypercube is build using the result of a LOO procedure. Only the area surrounding the most critical point is considered. This technique is called LOO- σ . This technique can be further constrained using sensitivity information. It leads to the LOO-Sobol' technique.

The presented techniques show an improvement of the predictive quality of the model with high dimensional analytical input functions.

7.2 Presentation of the Methods

Aside from sequence designs that are intrinsically iterative, all designs can be increased step-by-step through several techniques. A natural way is to optimize the discrepancy or some other criteria such as the entropy or the distance between points [71]. These kinds of methods only take advantage of the position of the points in the parameter space as seen in Chapter 6.

A complementary strategy consists in exploring the space using as few points as possible and then refine the exploration around interesting zones. This is the fundamental difference with the already presented methods. Here the forward model has to be evaluate in order to resample the DoE.

In the work of [203, 37], a detection of optima, nul gradients and also information about the Gaussian processes variance. This method is denoted hereafter as the σ method. One caveat with crude σ method is that points are preferentially added at boundaries of the parameter space. This is further described in Section 7.4.1. This behaviour motivates the research of new refinement methods that would use this information without being constrained to boundaries. Aside from this baseline, two novel strategies—LOO- σ and LOO-Sobol'—have been developed and are presented in this work. The common strategy is detailed in Algorithm 2.

Algorithm 2 Refinement strategy

Require: N_{max} , $threshold$, \mathcal{M}_{gp} , N_s

- 1: **while** $LOO - quality < threshold$ and $N_s < N_{max}$ **do**
 - 2: $\mathbf{x}_L \leftarrow$ least stable point of the design
 - 3: $\mathcal{H}_{\mathcal{L}} \leftarrow$ hypercube around \mathbf{x}_L
 - 4: $\mathbf{x}_o \leftarrow \max \mathbb{V}[\mathcal{M}_{gp}]$, within $\mathcal{H}_{\mathcal{L}}$
 - 5: Compute a new snapshot at \mathbf{x}_o
 - 6: Update GP surrogate $\mathcal{M}_{gp}(\mathbf{x}_*)$
 - 7: **end while**
-

Starting from an initial parameter space, the quality of the current model gives the most sensitive point of the design. Around this point, a hypercube is constructed. Within this hypercube the model's variance is maximized which gives a new point. Each strategy is described hereafter:

- Variance (σ),

As stated in Section 2.3.3, one of the main advantages of Gaussian processes over other surrogates is to provide an insight into the variance of the solution. The first method consists in using this data and weight it with the eigenvalues of the POD:

$$\sum_{i=1}^k \lambda_i^2 \times \mathbb{V}[\mathcal{M}_{gp}(\mathbf{x}_*)]_i. \quad (7.1)$$

Global optimization of this indicator gives the new point to simulate [230].

- Leave-One-Out (LOO) and σ ,

A LOO is performed on the model and highlights the point where the model is the most sensitive to. The strategy here is to add a new point in the surrounding area. The creation of the hypercube is described in Section 7.3. Within this hypercube, a global optimization over σ is conducted giving the new point.

- LOO-Sobol',

Using the same steps as with the LOO- σ method, the hypercube around the point is here truncated using prior information about Sobol' total indices—see Section 2.2. For instance, in a 2-dimensional case if $S_{T_{x_1}} = 0.8$, $S_{T_{x_2}} = 0.2$, the hypercube will be shrunk by 80% along x_1 's axis and by 20% along x_2 's axis. The algorithm ensures indices to be bounded between 0.1 and 1. This prevents some dimensions from being squashed prematurely. The method requires that indices be close to convergence to avoid bias in the result. However, the bias can be intentional depending on the insight we have about the case.

- Hybrid.

This last method consists in a navigator composed by any combination of the previous methods.

The evaluation of the latter composite method is not presented in this work. Although the computation of the LOO metric is merely an attempt to characterize the model's global quality, this mainly serves to assess the surrogate model's stability. If the model's response surface is not affected by the removal of a particular point, it is interpreted as stability—or a non-sensitivity—of the model to this action. This technique aims at stabilizing the model.

7.3 Construction of the Hypercube

To resample locally the parameter space, a hypercube is constructed around point p which is the most sensitive in the construction of the surrogate model—LOO point, see Section 2.3.5. An optimization problem is defined to construct the largest hypercube bounded by the surrounding points \mathcal{P} as shown in Fig. 7.1. This allows to only consider the vicinity of the point.

The hypercube is defined by the cartesian product of the intervals of the d parameters i.e. $[a_i, b_i]^d$. The constrained optimization problem consists in finding the coordinates of the hypercube, hence the problem

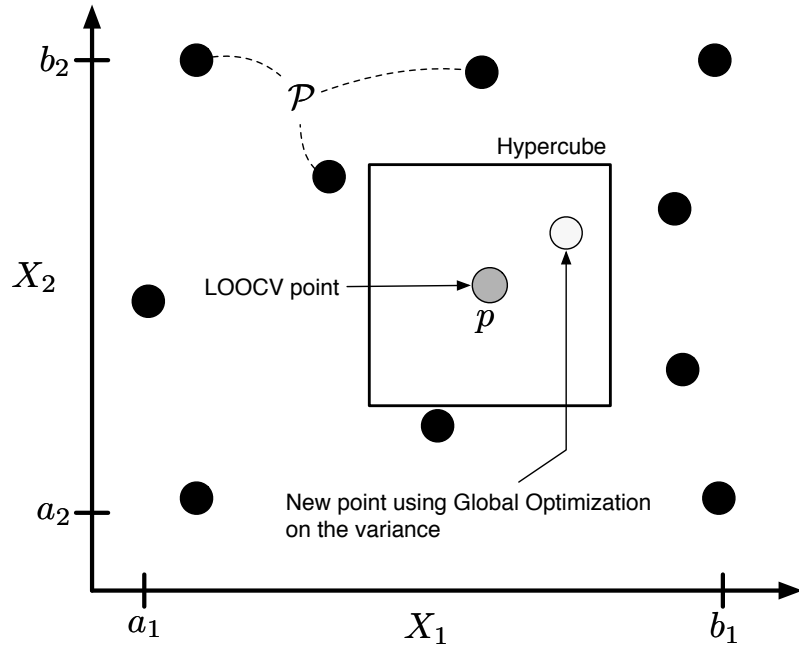


Figure 7.1 – Sketch of a hypercube of size $[a_i, b_i]^2$. The grey dot is the LOO point p , the black dots are the surrounding points \mathcal{P} and the white dot is the new point to evaluate.

reads

$$\left\{ \begin{array}{ll} \max & \|(\mathbf{b} - \mathbf{a})\|_2 \\ \mathcal{P} & \notin [a_i, b_i]^d \\ p & \in [a_i, b_i]^d \end{array} \right. . \quad (7.2)$$

A maximum cube-volume aspect ratio [216] is also defined in order to preserve the locality. This gives the new constrain

$$C : \sqrt[n]{\frac{\max(\mathbf{b} - \mathbf{a})}{\prod_{i=1}^d \max(b_i - a_i)}} < \epsilon, \quad (7.3)$$

with $\epsilon = 1.5$, set arbitrarily to prevent too elongated hypercubes. The global optimum is found using a two-step strategy: first, a discrete optimization using \mathcal{P} gives an initial solution; second a basin-hopping algorithm (see Section 2.1 for more details) finds the optimum coordinates of the hypercube.

7.4 Evaluation of the Methods

The benefits and mechanisms of the methods are first evaluated on complex analytical functions. The chosen functions are defined in Appendix A.1. Then, the treatment of the parameter space's boundary is presented in Section 7.4.1. Taking into account this issue, the analytical functions are tested in Section 7.4.2.

7.4.1 Restriction of the DoE

The first step when constructing a model is to define the DoE. This is done by defining the range of each input parameter, the boundaries that describe a hypercube. Then, using a low discrepancy sequence as described in Section 2.1, an initial pool of snapshots is computed within the hypercube. However, when constructing a model based on Gaussian Process regression, the error is important at the boundaries of the DoE due to the lack of information. The model is thus not able to extrapolate accurately at these locations. If using the variance technique as it is, the algorithm tends to add points around the corners and only after it considers other parts of the domain. When dealing with a low dimensional case—fewer than three parameters as with the *Michalewicz* function which uses two input parameters (see Appendix A.1), see Fig. 7.2—, a few iterations are “wasted” in the process.

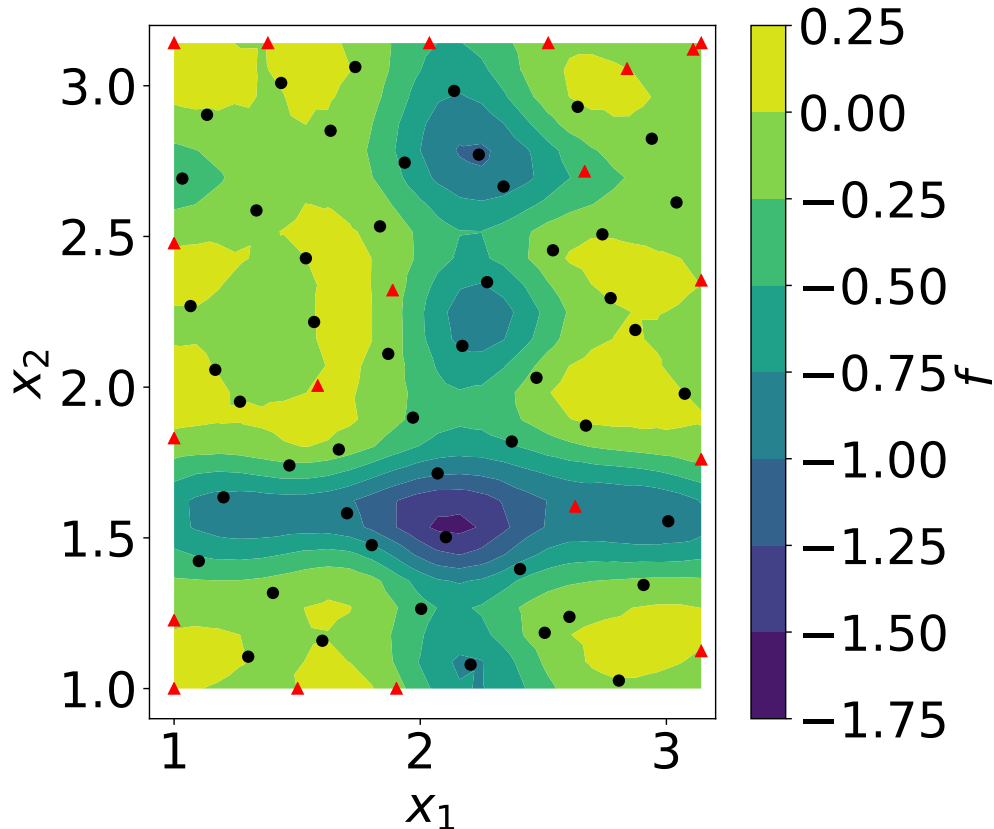


Figure 7.2 – *Michalewicz* function: dots represent the initial sample of 50 points and diamonds represent the 20 resampled points. The function was evaluated on the hypercube $[1, \pi]^2$

When increasing the number of parameters, there is a larger number of boundaries to cover. This has been confirmed on the *Ishigami* function (3 input parameters, Appendix A.1) for which the reported Q_2 values are even worse. As shown in Table 7.1, the optimization process is being over constrained in these regions and the global predictions

are degraded. To obtain this Table, the initial sample was increased using a constant number of resampling points (10 points) and the error was measured using a uniform distribution on the domain, confirming the importance of the boundary treatment.

Initial sample	Total size	Q_2
30	40	0.05
35	45	-0.02
40	50	-0.13
45	55	-0.19
50	60	-0.04
55	65	0.43
60	70	0.51
65	75	0.87
70	80	0.54
75	85	0.86

Table 7.1 – Error Q_2 on the *Ishigami* function of the size of the initial sample using a variance strategy with 10 points.

The possibility to widen the space by a delta space has been evaluated to address this question. The objective is to condition the predictor around the boundaries by adding information outside the domain of interest. A Halton sequence has been used to generate a sample of size $N_s = 80$ from the space

$$N_i \sim \mathcal{U}(20, 80) \quad \Delta_{space} \sim \mathcal{U}(0, 20\%), \quad (7.4)$$

with N_i the number of initial snapshots and Δ_{space} the widening factor, the outer delta space. For each case N_i , it is only the proportion of the initial sample over the number of resample point that varies (see Fig. 7.3). A fixed budget of $N_b = 80$ snapshots was considered. Then, the number of resampling points is equal to $N_{rs} = N_b - N_i$. The strategy used here was the σ model (see Section 2.1). After the resampling phase has been completed, the quality Q_2 of the model is computed. Applied to the *Ishigami* function, N_s simulations each performing N_b evaluations have been used to construct the response surface. These results were compared to a case without resampling: $N_i = N_s = 80$. The resulting predictivity quality being $Q_2 \simeq 0.8$.

As shown in Fig. 7.4, there is no benefit of adding points outside the domain. Aside from the uniform distributions usually employed on this function, a standard arcsine distribution was also tested to assess the quality around boundaries but no enhancement was observed. When the delta space is increased, there is a loss of quality due to the presence of points in non-interesting regions.

Complementary to this analysis using an outer delta space, an inner delta space factor has also been considered. The same methodology was used. Results are shown in Fig. 7.5. On the uniform case, the model

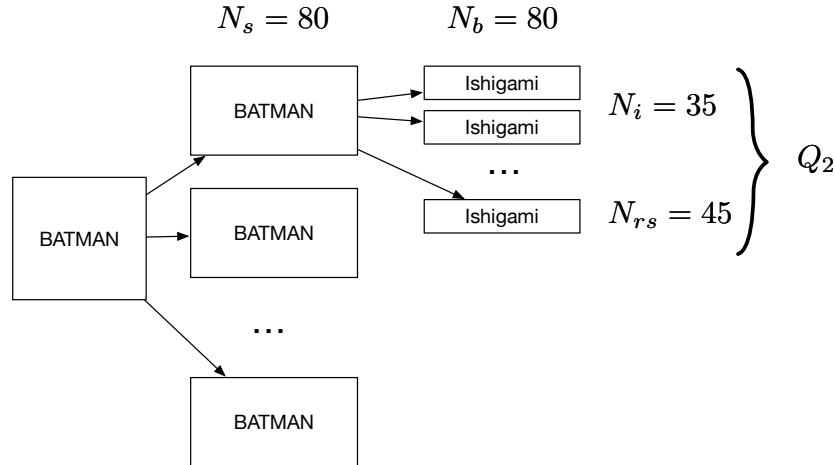


Figure 7.3 – Example showing a computation of Q_2 with $N_i = 35$, $N_{rs} = 45$.

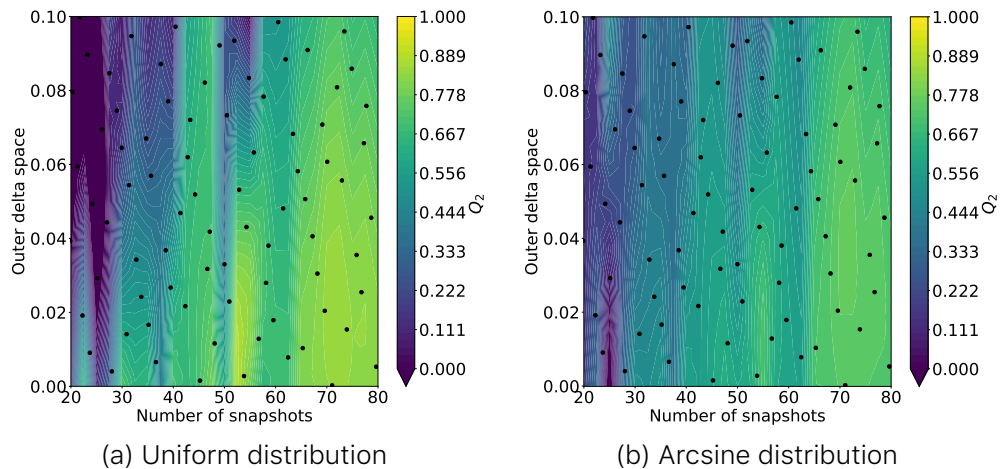


Figure 7.4 – Response surface of Q_2 function of the initial sample and the *outer delta space*. *Black dots* represent the simulations.

was not correctly computed due to high discontinuities caused by the 0% inner delta space cases. In [57], optimal design that tends to put more points near the boundaries was shown to be more effective. These results are coherent with their findings as an improvement of the quality is observed when using a low inner delta space. Indeed, a small value of the parameter limits the trend to add points close to the boundaries.

This work has shown that setting an inner delta space comprised between 5 and 10% is required to ensure the robustness of the model construction. Based on this observation, in the following the inner delta space is set to an arbitrary value of 8%.

7.4.2 Application on Analytical Functions

The operating mechanism and catches of the methods can be visualized on the Rosenbrock function—see Fig. 7.6. Starting from the σ

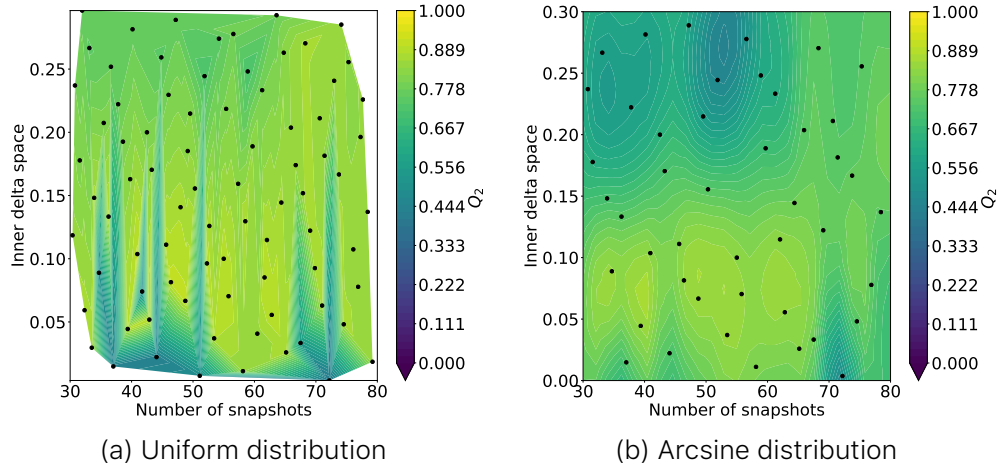


Figure 7.5 – Response surface of Q_2 function of the initial sample and the *inner delta space*. *Black dots* represent the simulations.

method: points are first added close to the top boundary despite the inner delta space parameter. However, the lack of surrounding points made this choice fairly legitimate. Other points seem to be located in interesting regions—where there is a gradient and no points. It can be seen as a low discrepancy sequence, which made its use relevant for studying the delta space impact in Section 7.4.1. On the other hand, the LOO- σ method does not seem to exhibit a boundary preference. But, on the bottom left-hand corner, there is an accumulation of points. Indeed, this method relies on the location of the most sensitive point. Considering the surroundings of a strong extremum—as it is the case here—the method tends to add points first in this zone preventing further exploration of the domain and, in this case, totally misses the second extremum. Lastly, the LOO-Sobol' method seems more balanced. Points have been added preferentially on the X_1 parameter axis, as it is slightly the most influent parameter ($S_{T_{X_1}} \simeq 0.7$).

A convergence study has also been performed. With a fixed total number of simulations, the size of the initial learning sample was changed to evaluate the impact of the ratio of the initial sampling over the total number of samples on the quality of the model. As in Section 7.4.1, a *Halton* sequence was used. The respective parameters are reported in Table 7.2. The Sobol' indices: for the *Ishigami* function are found in [151]; for the *g-function* function are found in [128]; while for the *Rosenbrock* function, a stochastic sample of 100 000 evaluations was used.

Results are shown in Fig. 7.7. The σ method appears to be one of the most, in some cases the most, effective method but it also exhibits more variability. Increasing dimensionality seems only to improve slightly this behaviour. There are multiple explanations to this phenomenon. The method relies on the use of an inference about the variance of the model. Starting from a given sample, if the fitting process does not converge,

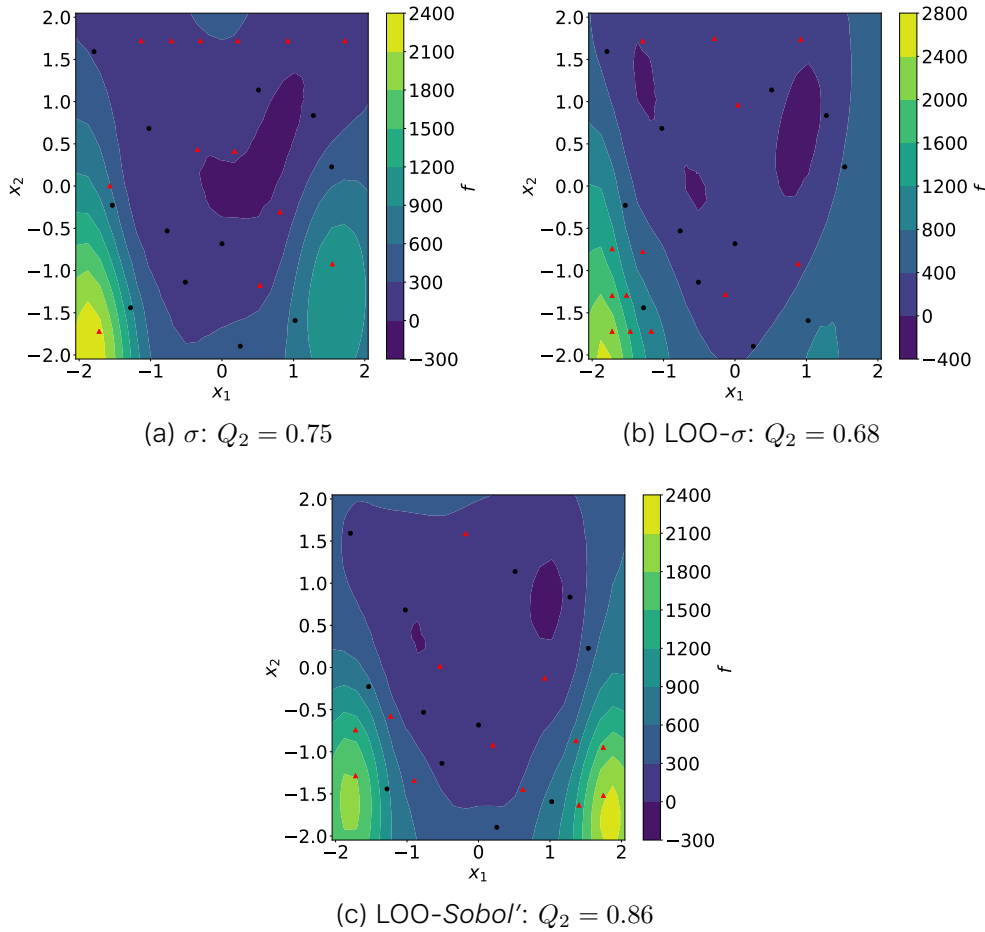


Figure 7.6 – Response surface of the *Rosenbrock* function. In each case, the initial learning sample is composed of 12 simulations and there are 13 resampling points—respectively represented in *black dots* and *red diamonds*.

the prediction of the variance will be far from correct leading to a wrong resampling. Of course, there is a chance for this new point location to be relevant. This can lead to an even worse model or an overfitting where the model is too closely linked to the outputs, so the model has memorized only the feature but not learned the underlining correlation between the data. Lastly, looking at Fig. 7.8, even if the points look well distributed over the parameter space, the GP model is absolutely wrong. The Gaussian Process reconstruction failed to recover the response surface of the function whereas a Radial Basis Function Networks model successfully did it.

The other two methods share the σ strategy, but the variability is conditioned by the LOO point. Indeed, the former only uses inference about the predictive variance whereas LOO's methods take into account the observed quality of the model.

LOO-Sobol' is even more stable especially when the contribution of the parameters to the QoI is not even. The quality evolves quasi-

Function	Sample Budget	Q_2	Total order Sobol' indices
Rosenbrock 2-D	25	0.82	[0.71, 0.50]
Ishigami 3-D	80	0.85	[0.557, 0.443, 0.244]
<i>g</i> -function 4-D	65	0.66	[0.60, 0.27, 0.15, 0.10]
<i>g</i> -function 11-D (i)	80	0.84	[0.69, 0.31, 0, ..., 0]
<i>g</i> -function 11-D (ii)	80	0.66	[0.47, 0.21, 0.21, 0.12, 0.12, 0.02, 0, ..., 0]

Table 7.2 – Reference Q_2 and Total order Sobol' indices. Theoretical values for both *Ishigami* and *g*-function and computed for *Rosenbrock*.

linearly with the initial sample size. This is due to the initial guess on the indices. The closer the indices are converged, the better the sizing of the hypercube used by the σ strategy. Indeed, some dimension of the hypercube could be neglected due to the indices. In the *Rosenbrock* case the method behaves like LOO- σ , the importance factors are close enough so that this collapse of dimension does not occur. On the other hand, with the *g*-function 4-D and *g*-function 11-D (i), the total order Sobol' indices of the last input parameters are so small that the algorithm tends not to take into account these dimensions. Finally, for the *g*-function 11-D (ii) case, more input parameters are active—meaning that their total order Sobol' indices are greater than 0.1—, so that the improvement is not as important as with the *g*-function 11-D (ii) case. Still, better results are found compared to the σ strategy. These results are comparable to the *Rosenbrock* case where LOO-Sobol' perform similarly to LOO- σ . Indeed, as the number of active parameters grows, improving the Q_2 would imply a better coverage of the parameter space. Thus, as the number of active dimension increases, it is expected that the optimal Q_2 , for a given number of samples, would converge to the Q_2 given by the use of a low discrepancy sampling. At worst the low discrepancy sampling's Q_2 will be a lower bound for these methods. In realistic engineering applications, the importance of the relative contributions of the input parameters being most of the time unknown, these methods seem promising.

For each function, as the initial sample gets close to the budget, the expected improvement is reduced. This is clear with the *Ishigami* function. When the initial sample is too small, the model is so poor that the points are not added efficiently. On the contrary, if we add an insufficient number of points, the impact is close to none but still there is an improvement. From the other cases, the effect of the ratio of the initial learning sample size over the total budget is not so clear. In 2-D the impact is null and after that, a ratio > 0.5 seems appropriate.

Thus, setting aside the possible non-fitting of the data, improving the quality of the surrogate model by resampling the parameter space appears to be guaranteed in high dimensional cases and using no more than half of the budget.

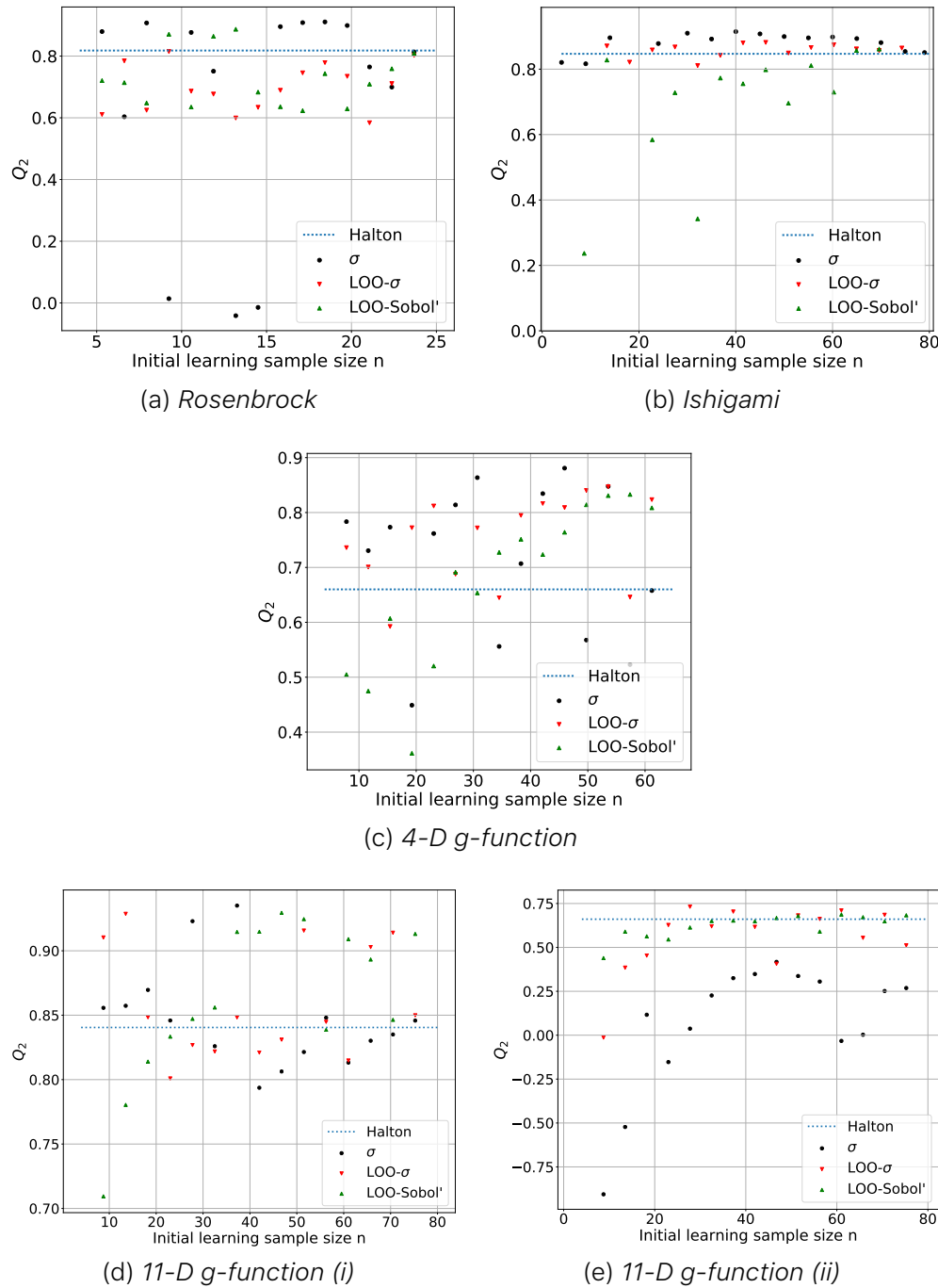


Figure 7.7 – Convergence of \tilde{Q}_2 of the different methods on each function by varying the initial learning sample size with a fixed budget.

7.5 Summary

Two new methods have been introduced in this work for resampling the parameter space in order to improve the predictivity coefficient of a surrogate model: namely LOO- σ and LOO-Sobol' methods. These methods do not only take advantage of the capability of Gaussian Process models to infer a prediction's variance, but they use information about

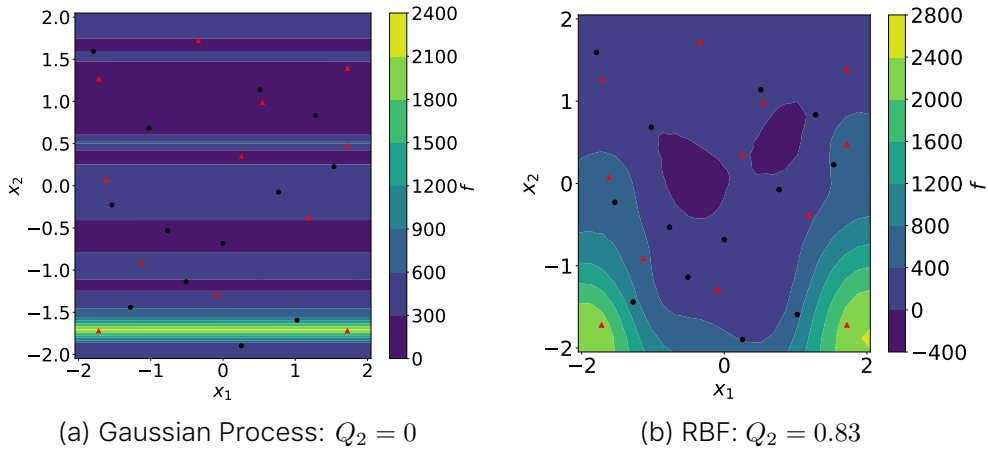


Figure 7.8 – Response surface of the Rosenbrock function. Comparison between two models. The initial sample is composed of 13 simulations and 12 resampling points—respectively represented in *black dots* and *red diamonds*.

the observed quality of the model. It was shown that an improvement of the quality of the model is guaranteed in high dimensional cases. Compared to a resampling method based on the predicted variance only, the proposed methods behaviour appears to be more stable and reliable. It was also found that the ratio of the initial learning sample space over the total budget of function evaluation should remain greater than 0,5. Which is to say that no more than half of the budget should be allocated to resampling the parameter space. In any case, the initial quality of the model should be reasonable when considering these techniques.

By taking into account the physics in this process, the proposed methods will help build better models at lower cost. This will also allow Uncertainty Quantification of high-dimensional or expensive cases to be within reach.

8 | Uncertainty Visualization

Ce chapitre présente de nouvelles stratégies de visualisation pour visualiser l'incertitude. Les méthodes sont conçues pour aider les praticiens de UQ en permettant la visualisation de l'espace des paramètres d'entrée et de la quantité d'intérêt (*QoI*) sur le même canevas.

Cette solution s'appuie sur les HOPs appliqués à une surface de réponse fonctionnelle, les métriques HDR, et une version tridimensionnelle du Kiviat. Pour le 3D-Kiviat, chaque couche représente un résultat hypothétique (une réalisation) coloré par une valeur scalaire liée à une grandeur d'intérêt. Cette grandeur est soit la *QoI* à un point et à un instant donnés, soit une distance calculée à l'aide des mesures du RDH. Cette solution peut être complétée par une sonification des données pour tracer les métriques HDR.

Le chapitre est rédigé comme suit : Section 8.2 présente une technique innovante pour visualiser les incertitudes de la sortie basées sur f-HOPS avec sonification à partir de la métrique HDR. Section 8.3 étend cette solution avancée à la visualisation des incertitudes d'entrée et de sortie en s'appuyant sur la représentation 3D-Kiviat augmentée de mesures HDR et de sonification. La Section 8.4 apporte des éléments de discussion et conclus sur ces travaux.

8.1 Introduction

THIS CHAPTER proposes a solution to visualize high input and output dimensions. This solution relies on HOPs applied to functional response surface, HDR metrics, and a 3-dimensional version of Kiviat plot. For the 3D-Kiviat, each layer stands for a hypothetical outcome (a realization) coloured by a scalar value related to the response variable. This value is either the response variable at a given point and time or some distance computed with the HDR metrics. This solution can be augmented with data sonification to traduce the HDR metrics.

The chapter is tailored as follows: Section 8.2 presents an innovative technique to visualize output uncertainties based on f-HOPS with sonification from HDR metrics. Section 8.3 extends this advanced solution to both input and output uncertainties visualization building on 3D-Kiviat representation augmented with HDR metrics and sonification. Conclusion and discussion are finally given in Section 8.4.

8.2 Uncertainty Visualization of Functional Output Data

8.2.1 Dynamic Visualization of Functional Outputs's Statistics

The HOPs dynamic visualization can be applied to functional outputs [115] as in Fig. 8.1 animating successive realizations of the data (for the El Niño dataset—see Appendix A.2), it is noted f-HOPs. When combined to HDR criteria, each realization is discriminated taking into account the functional characteristics of the output and outliers are easily detected. This solution is complementary to the classical PDF plot for functional outputs shown in Fig. 8.2 that displays the probability of monthly sea surface temperature. The median and standard deviation curves are shown but these statistics are computed point by point independently and the outliers cannot be represented. Yet, f-HOPs does not allow to exhibit multiple modes statistics that are shown by the PDF at a given location. For instance, Figure 8.3 shows both the functional PDF and a PDF at a precise location of the Hydrodynamics dataset—see Appendix A.2. It can be noted that there are multiple modes.

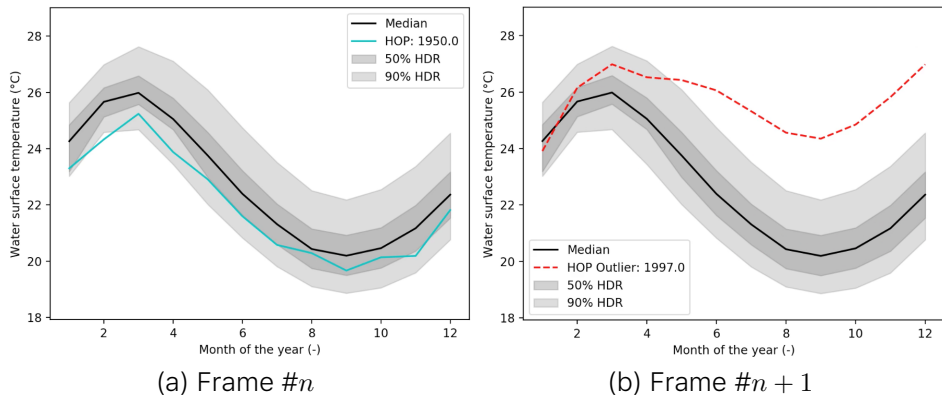


Figure 8.1 – Functional-HOPs. **a** close to median realization. **b** outlier realization.

8.2.2 Sonification of Functional Outputs's Statistics

When the number of realizations in the dataset is limited, a static or an animated visualization, using f-HOPs and HDR metrics, allow to depict the most significant characteristics of the ensemble members. When this number increases, the animation time increases and the analysis becomes harder. Sonification comes as an alternative for meaningful analysis of the dataset: it conveniently allows to draw the attention on specific realization discriminated by the HDR metric. It is proposed to compute the L_2 -norm between each realization and a reference realization within the reduced modal space. The reference realization

8.2. UNCERTAINTY VISUALIZATION OF FUNCTIONAL OUTPUT DATA

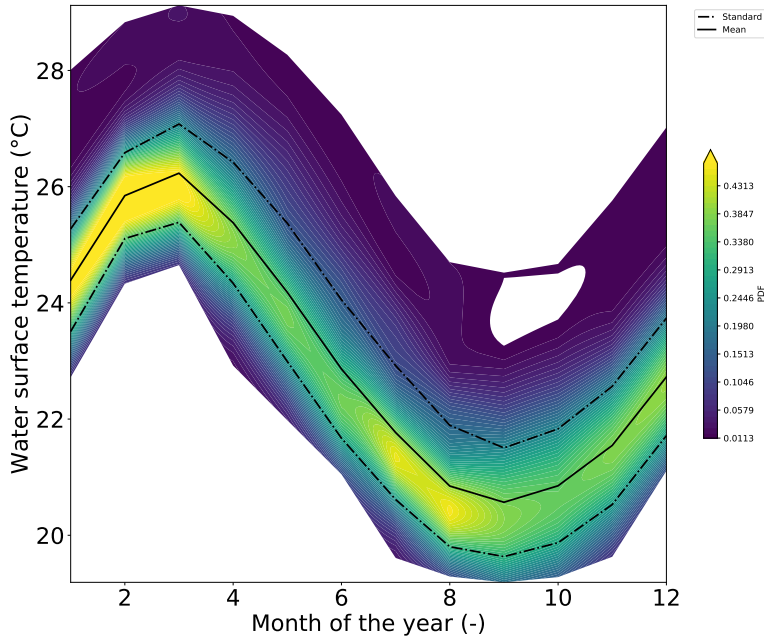


Figure 8.2 – Functional PDF of monthly sea surface temperature. Moments are computed with respect to the 58 realizations per month of the year.

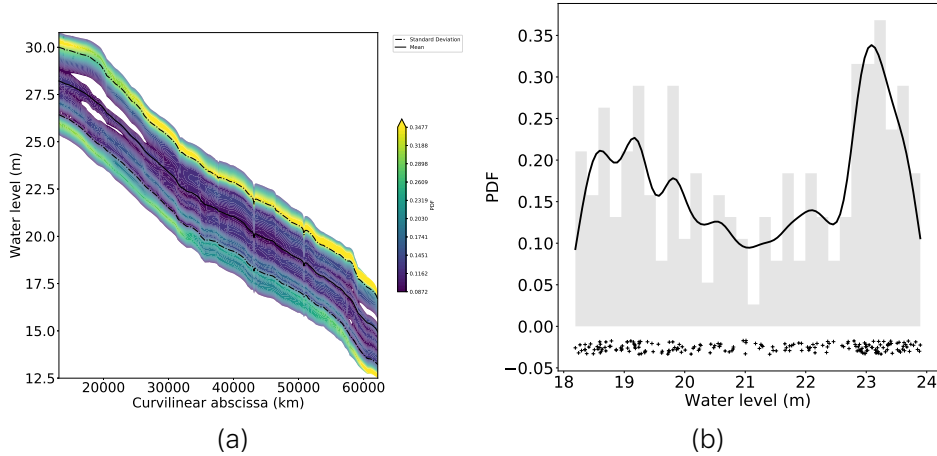


Figure 8.3 – Functional PDF of the water elevation, **a** along the 463 nodes along the river reach; **b** at Marmande station (36 km) revealing a bimodal PDF.

is here chosen as the median and is mapped into a base sound. The frequency associated with each realization increases, and the sound becomes higher as the distance between each realization and the reference increases. Evidently, the reference can differ from the median. [18] demonstrated that sonification allows for well-informed understanding of a large dataset and that practitioners usually develop a physics-dependent vocabulary that is adapted to specific need. In [100] sound is used to discriminate the types of gravitational waves. In this context,

sonification serves data exploration. It can also be an alert system: f-HOPs augmented with HDR metric sonification allows to get a fairly monotonous sound for realizations that are close to the median, while outliers are clearly spotted.

8.3 Uncertainty Visualization of Large Number of Input Variables

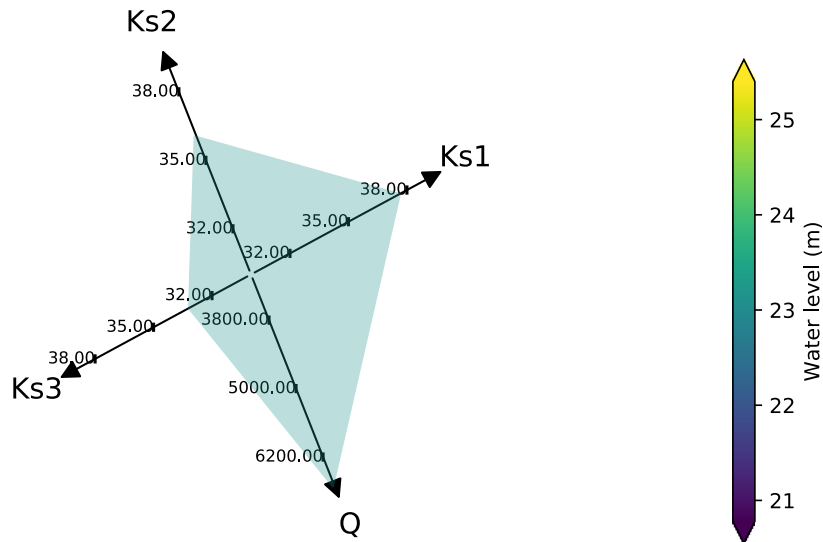


Figure 8.4 – Kiviat plot on the Hydrodynamics dataset: 2-dimensional Kiviat plane represents one sample of the data set. Colour maps the water level response variable value at Marmande (one location and one time).

In the previous section, the focus was made on visualizing the response variable, not taking into account the relation between inputs and outputs. As visualizing the input alone, especially in case of small input dimension, is classical, the dual representation of input and output data remains challenging especially for large dimension functional outputs. The response surface plot is adapted when the input space is 2D or 3D. When the input space dimensions further increases, other solutions should be preferred such as parallel coordinates plot [104, 105] or 3D-Kiviat proposed by [94]. In the literature, *Kiviat* plot were used to map uncertainties with density criteria [225] and confidence intervals are represented on a 2D plot.

3D-Kiviat plot is adapted to the visualization of both input and response variable spaces. Each plane of the Kiviat represents a realization within the dataset with as many directions as the input dimensions as shown in Fig. 8.4 for the hydrodynamics dataset—see Appendix A.2. The input variables here correspond to the friction coefficients (K_{s1} , K_{s2} , K_{s3}) and the constant inflow Q ; the output variable is the water

level at Marmande, it is colour-coded onto the Kiviat plane. For the 3D-Kiviat, planes are stacked into a 3D object with respect to the response variable (scalar or functional) related value that is colour-coded. It should be noted that each plane is filled with only one colour to preserve readability. The benefit of 3D-Kiviat stands in the choice of both the stacking and the colouring strategies as shown in Fig. 8.5 for the hydrodynamics dataset. Additionally, the 3D-Kiviat can be augmented with sound—as described in Section 8.2.2.

When representing functional output data, different stacking and colouring strategies allow to highlight different information in the dataset. Four choices of stacking and colouring are illustrated in Fig. 8.5; the stacking and colouring choices are indicated in the legend, they are achieved with respect to the response variable at a given location and time, with respect to the HDR metric or with respect to one of the input variables. In Fig. 8.5(a), stacking is done with respect to the response variable at a given location and time while the colouring is done with respect to the difference to the median realization computed with the HDR metric. This allows to get a sense of the spatial PDF represented in Fig. 8.3 augmented with the input parameter mapping. Another possibility in Fig. 8.5(b) consists in stacking with respect to the HDR metric and colouring with respect to the response variable value. In Fig. 8.5(c), stacking is done with respect to one of the input variable (in the present case Q) and the colouring is done with respect to the HDR metrics. Finally, Fig. 8.5(d) displays both stacking and colouring with respect to the response variable value.

By playing with the stacking order, the coloring scheme and selecting only a subset of parameters, one can introduce repetition to encode the same information. This can help to convey a particular information and even help people with disabilities.

From Fig. 8.5(a, c, d), the impact of Q on the water level is easily readable; water level increases with Q . High water level values are also obtained for low K_{s3} values while other parameters seem to have no significant impact on the response variable. K_{s1} and K_{s2} have barely any impact on the response variable. The manipulation of the animated 3D-Kiviat is even more adapted to data analysis. The coloured HDR in Fig. 8.5(a, c) indicates how each realization differs from the median realization. It appears that stacking for colouring with respect to response variable or HDR serves different purposes. Ordering by response variable allows to discriminate which input lead to specific response variable value while ordering by HDR illustrated the dispersion of the dataset with respect to a reference realization. Sounding is a supplementary way to emphasize the information, especially for large datasets.

3D-Kiviat comes as a complementary tool to classical sensitivity analysis criteria such as *Sobo'* indices [201]. When computed on a large dataset (100 000 members) for the hydrodynamics example and averaged over space, these indices show that most of the variance of

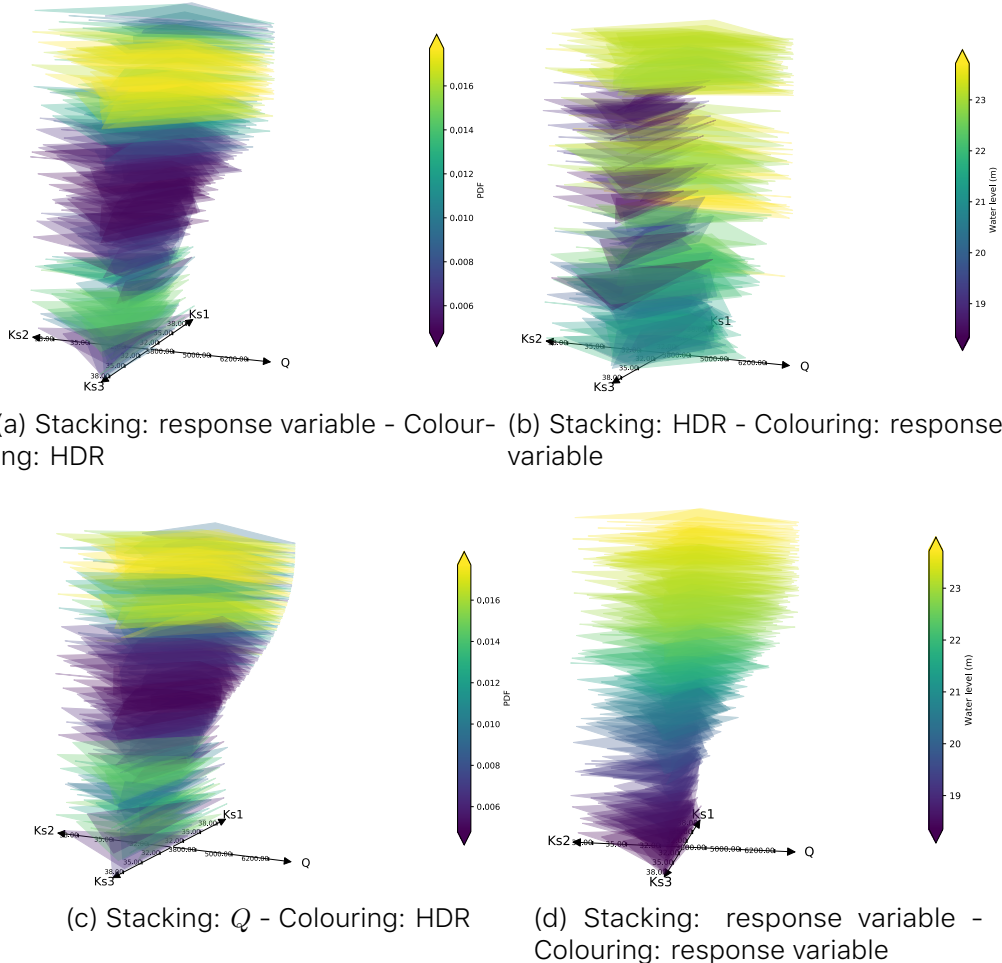


Figure 8.5 – Kiviat plot on the Hydrodynamics dataset: comparison of different stacking orders and colour map strategies. **a** samples stacked by response variable and coloured by HDR. **b** samples stacked by HDR and coloured by response variable. **c** samples stacked by Q and coloured by HDR. **d** samples stacked by response variable and coloured by response variable.

the water level is explained by Q with $S_Q = 0.98$. A small part of the variance is explained by $Ks3$ as $S_{Ks3} = 0.14$ and even smaller by $Ks1$ and $Ks2$ with $S_{Ks1} = 0.01$ and $S_{Ks2} = 0.07$.

While the Sobol' indices quantify the importance of each parameter on the response variable's variance, they do not indicate the nature of these contributions. Indeed, it is stated that Q has a significant impact but from Fig. 8.5(a, c, d), we can also add that the contribution is monotonous. Additionally, the weak impact of $Ks1$ and $Ks2$ is confirmed by the lack of a pattern in the 3D-Kiviat along these axes. Finally, while the $Ks3$ Sobol' index is weak, the 3D-Kiviat indicates that small $Ks3$ values lead to high-water level values.

It appears that 3D-Kiviat plot becomes difficult to manipulate when the dimension of the input parameter increases (> 10). To overcome this caveat, I have designed a method to generate a surface mesh of

the Kiviat plot as shown in Fig. 8.6. This allows the use of regular CAD viewers and thus facilitates the manipulation of the 3D object as well as the comprehension of the data structure. The construction is based on a vertex-vertex representation using quadrilateral elements.

The analysis from 3D-Kiviat is similar to that drawn from the parallel coordinates plot in Figure 8.7. The latter consists of $n + 1$ parallel axes, with $n = 4$ the number of input parameters for the hydrodynamics dataset. The last axis is dedicated to the output value, here water level at Marmande. Each grey line corresponds to one realization in the dataset; the red lines are discriminated for high-water level values resulting from high Q and small $Ks3$, independently of $Ks1$ and $Ks2$. It should be noted that parallel coordinate plot is not adapted to simultaneous representation of response variable and HDR metrics contrary to 3D-Kiviat. Finally, the linear relationship between water level and Q that was clear on the 3D-Kiviat is not readable on the parallel coordinate plot that is more adapted to clustering with the possibility of advanced strategies proposed by [45, 186].

The specific case of a 2D input space is treated with a *Tree plot* solution where Kiviat coloured planes are replaced by coloured segments that are stacked and coloured regarding to response variable related value. The vertical stacking and colouring are achieved with respect to the response variable value. The HDR metric is encoded as an azimuthal component: the angle is null if the realization corresponds to the median and the angle increases as the realization differs to the median. Figure 8.8 displays a tree plot for the hydrodynamics dataset where $Ks1$ and $Ks2$ are not accounted for (since they were previously shown to have barely any impact on the response variable) and the response variable is the water level at Marmande. Here again, stacking, colouring, angle and eventually sounding strategies can be adapted to convey information on a dataset and efficiently enhance meaningful information.

8.4 Summary

This work proposes a systematic way to look at uncertainties when dealing with high-dimensional environment. As uncertainty quantification related analysis are moving toward high dimensionality, I believe that this tool could help data analysis.

In this work, a new method to visualize input and output uncertainties was presented. The concept of Hypothetical Outcomes Plot is taken a step further and applied to functional data (f-HOPs) considering the HDR boxplot information that estimates a distance to a reference realization (here the median). HDR metrics allow to reduce the output space to a limited number of principal components and compute, in this reduced space, a distance between dataset realizations taking into account temporal or spatial discretization. This metric allows to discriminate the

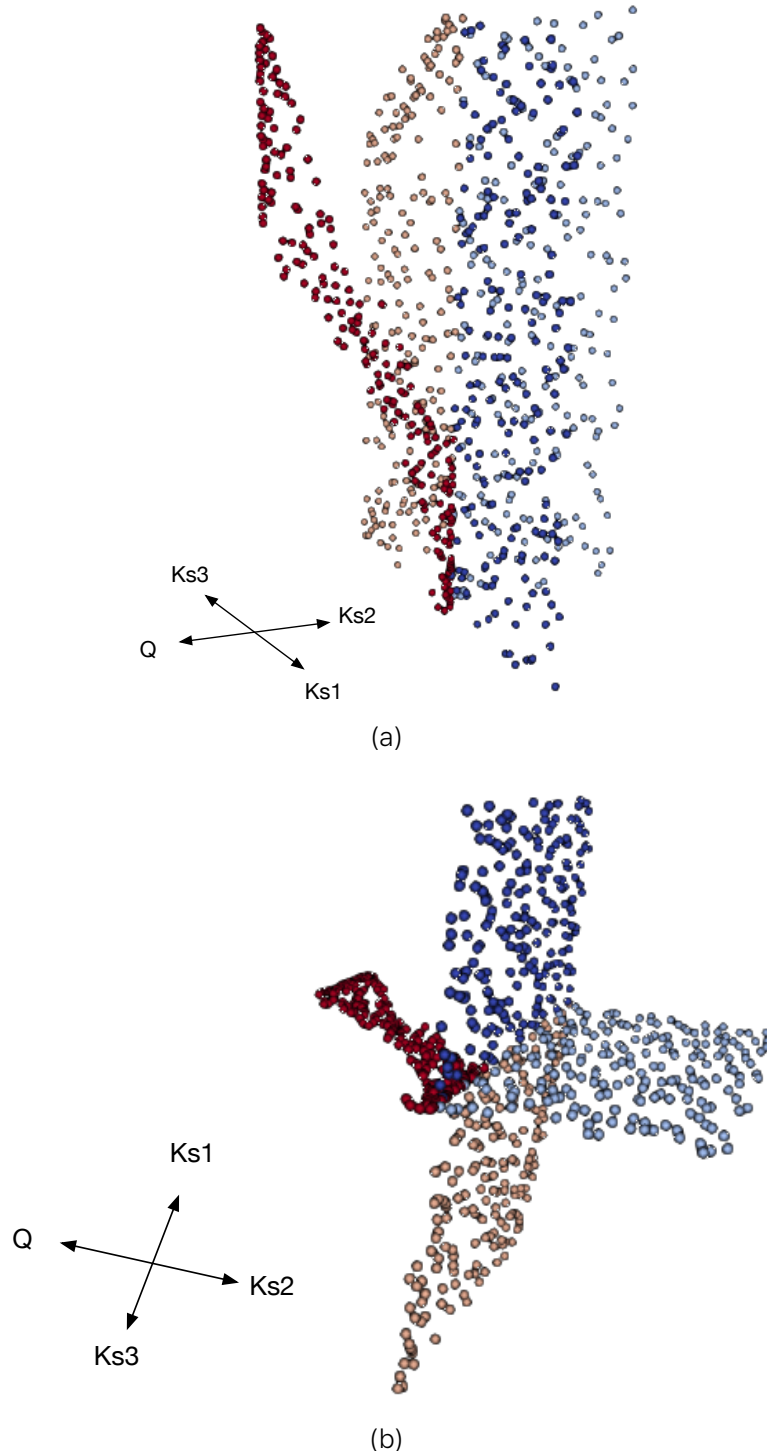


Figure 8.6 – 3-dimensional Kiviat in point representation stacking with respect to the response variable and colouring with respect to the input parameter.

realizations statistically regarding to the response variable value at a specific location and time. f-HOPs provides an animated version of members within a dataset; it can be augmented with data sonification which is efficient for outlier detection. Both input and output uncer-

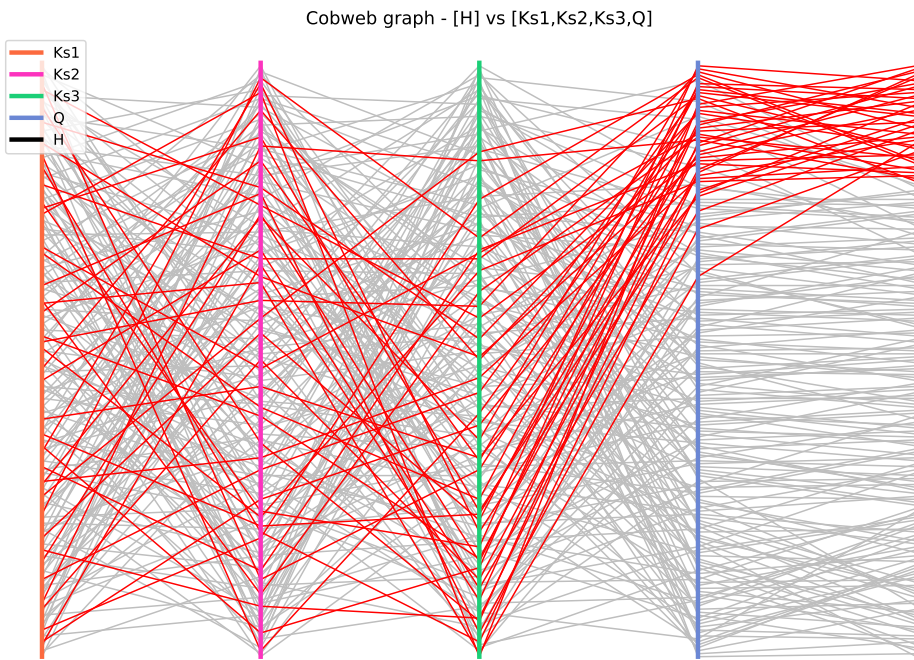


Figure 8.7 – Parallel coordinates plot for the hydrodynamics dataset with 80% of the lowest values of response variable filtered out (in grey) and high values in red.

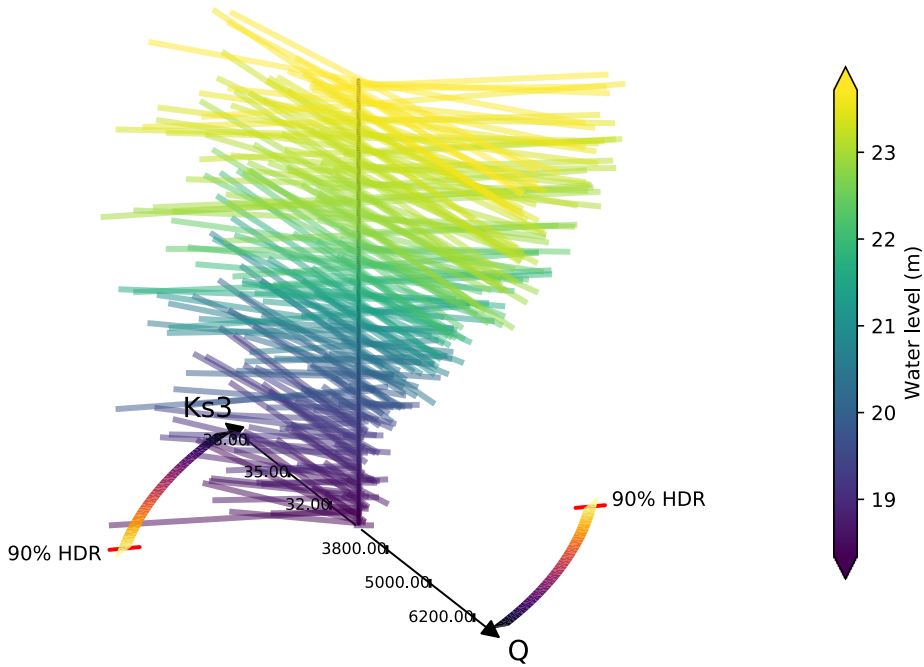


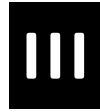
Figure 8.8 – Tree plot for the hydrodynamics dataset considering the most significant parameters $Ks3$ and Q . Here the response variable (water level at Marmande) is represented by stacked and coloured segments and HDR metric is represented by the azimuthal component.

tainties are finally visualized with a 3-dimensional version of the Kiviat where each realization is represented by a plane surface. Realizations are stacked along the vertical axis and colour-coded. The 3D-Kiviat can be augmented with data sonification. Stacking, colouring and sounding strategies are chosen with respect to the response variable value or the HDR metric to highlight some information within the dataset.

These visualization solutions were applied to two functional datasets: (*i*) El Niño and (*ii*) Hydrodynamics. The first one is a commonly used dataset that only provides temporal outputs, the second dataset presents an input-output relation with a large dimension output space and a 4-dimensional input space. For both datasets, f-HOPs and 3D-Kiviat have proven to be efficient at representing the nature of the dataset and highlighting important impact factors. Moreover, visualization of the 4-dimensional input space was eased by the Kiviat solution that was conveniently adapted to CAD objects for larger dimensions.

Perspective for this work stands in the adaptation of stacking, colouring and sounding to specific purposes. For instance, for extreme events detection, the HDR metrics can be computed with respect to the mean or the median, but it could also be computed with respect to high quantiles. The reference can also represent additional information to the dataset. For instance, in the context of data assimilation, it can stand for observation data that are usually distributed in space and time, in order to compute the innovation vector or to achieve observation quality control steps.

Our strategy finally can be applied to operational context with ensemble integration. Straightforward applications are for instance real-time weather and flood forecasting as well as structure failure risk assessment and outliers detection are at stake. In this context, our strategy would also be applied to larger dimension input and output spaces. The stacking strategy allows to create a 3D object that can easily be manipulated, even printed for deep analysis. Sounding is also an efficient way to draw the attention to an operator while the ensemble forecast is issued in case threshold exceed occurs. Finally, the complete solution with stacking, colouring and sounding offers social and human perspectives for statistical analysis of datasets by people with disabilities for which written information is not handy.



Applications

9 Comparison of PC and GP surrogates for UQ of spatially distributed open-channel steady flows	95
9.1 Introduction	96
9.2 Hydraulic Modelling	98
9.2.1 1-D Shallow Water Equations (SWE)	98
9.2.2 Garonne River Case Study	99
9.2.3 Sources of Uncertainties and Quantity of Interest .	101
9.3 Comparison of PC and pGP Surrogates	102
9.3.1 Reference Monte Carlo (MC) Results	102
9.3.2 Convergence Analysis for Surrogates	103
9.4 Summary	108
10 The Aerothermal Flow around the LS89 Blade Cascade	111
10.1 Introduction	111
10.2 Case Description	112
10.3 Numerical Setup	115
10.4 Uncertainty Quantification Results	117
10.5 Summary	119
11 UQ-Driven Robust Design Assessment of a Swirler Geometry	123
11.1 Introduction	124
11.2 Configuration and Numerical Setup	126
11.2.1 The Swirled Injector	126
11.2.2 Numerical Setup	126
11.2.2.1 Mesh Adaptation Strategy	127
11.2.2.2 Simulation Strategy for UQ	128
11.2.3 Geometrical Uncertainties of the Swirler	129
11.3 Dimensionality Reduction and Statistical Analysis of Un- certain Parameters	130
11.4 Generation of Datasets	131
11.5 Results and Discussion	133
11.6 Summary	136

12 Optimization of Helically Roughened Heat Exchanger	139
12.1 Introduction	140
12.2 Case Description	141
12.2.1 Geometrical and Meshing Considerations	141
12.2.2 Numerical Set-Up	143
12.2.3 Optimization Problem	144
12.3 Results	146
12.3.1 Continuous Rib	146
12.3.2 Discontinuous Rib	147
12.3.3 Optimal Discontinuously Ribbed Heat Exchanger .	151
12.3.3.1 Flow Dynamics	151
12.3.3.2 Heat Transfer	155
12.4 Summary	157

9 | Comparison of PC and GP surrogates for UQ of spatially distributed open-channel steady flows

L'objectif de ce chapitre est d'évaluer la performance des modèles de substitutions PC et GP imitant le comportement des écoulements en canal ouvert 1-D pour réaliser une UQ et SA. La quantité d'intérêt est le niveau d'eau 1-D discrétisé le long de 50 km de la Garonne (Sud-Ouest de la France). Dans un premier temps, on se concentre sur des écoulements stationnaires tout en restant fluvial. Les principales sources d'incertitude sont le débit en amont qui est constant en régime permanent et le coefficient de frottement qui est une fonction constante par morceaux. Sous ces hypothèses, ce travail présente des entrées scalaires et des sorties spatialement variables en raison de l'hétérogénéité bathymétrique de la Garonne. Une étude de convergence est d'abord effectuée pour déterminer la taille de l'ensemble d'apprentissages N qui est nécessaire pour construire un substitut valide en utilisant soit des PC ou des GP. Les substituts PC et GP sont ensuite comparés lorsqu'un budget de calcul est établi, i.e. pour le même nombre de simulations N utilisés pour construire chaque substitut. La comparaison est effectuée par rapport au regard des trois mesures suivantes : PDF; indices de Sobol' spatiaux et matrice de corrélation.

Les deux substituts ont démontré leur capacité à remplacer correctement le simulateur par un faible nombre de simulations numériques. Dans un contexte opérationnel, le remplacement d'un simulateur numérique par un modèle de substitution est intéressant même si le modèle original n'est pas coûteux à évaluer. Il permet de produire plus fréquemment et avec plus de précision des prédictions à l'aide de matériel moins coûteux.

La structure du chapitre est la suivante. Section 9.2 présente les équation qui sont résolus avec le code MASCARET et l'étude de cas de la Garonne. Section 9.3 présente les résultats de l'étude comparative entre PC et GP par rapport à une référence MC. Les conclusions et les perspectives sont présentées Section 9.4.

9.1 Introduction

THE PREDICTIVE skills of hydraulic models have greatly increased with advances in free surface flow numerical modelling and computational resources. Real-time flood forecasting relies on the use of sparse in situ observations as well as imperfect hydrology or hydraulic models usually solving the 1-D Shallow Water Equations (SWE). Assessing the predictive capabilities of these hyperbolic partial differential equations remains an important challenge as public safety and water resource management are at stake [235]. SWE solve for spatially varying water level and river discharge (referred to as the river state) using physical parameters (e.g. friction coefficients, bathymetry), initial conditions and boundary conditions described as a hydrograph or water-level time series. These input data are subject to epistemic uncertainties due to an imperfect knowledge of the river properties as well as to aleatory uncertainties related to environmental and meteorological intrinsic hazards. Both types of errors translate into uncertainties in the simulated river state, thus preventing the hydraulic model from being effective in forecast mode. In practice, these uncertainties can be reduced when complementary data become available.

Data assimilation (DA) offers a convenient framework to reduce model uncertainties by combining observations with the model simulation taking into account errors in both sources of information. Prior to DA, the main sources of uncertainties should be identified and included in the control vector; this is achieved with a sensitivity analysis (SA) study that allows classifying uncertainties in the inputs with respect to their impact on the model outputs, for instance in terms of variance using Sobol' indices [108]. Several studies in the framework of hydraulics demonstrated the merits of DA [25, 47, 54, 93, 162] to provide a more accurate river state. This is achieved by inferring an optimal set of parameters (e.g. river and floodplain friction coefficients, upstream and lateral river discharge, bathymetry) and/or by directly correcting the river state.

Ensemble-based methods such as the Ensemble Kalman Filter (EnKF) [63, 162, 69] and the Particle Filter (PF) [156, 173] are popular algorithms; they articulate as a two-step procedure derived from Bayesian inference: (1) a forecast step to sample the uncertain inputs and propagate the uncertainty through the model, thus providing an ensemble of river states; and (2) an analysis step to weight each member or particle of the ensemble based on its discrepancies to the available observations and to derive in the case of parameter estimation, a correction on the inputs that is then propagated to the river states by model integration. In the EnKF algorithm, the weights are provided by the stochastic estimation of covariance matrices between errors in model inputs and outputs. In contrast, in the PF algorithm, the weights correspond to likelihoods associated with the probability density function (PDF) of the control vector conditioned upon the observations; PF provides an alternative to EnKF

when the model is subject to strong non-linearity and non-Gaussian errors.

Both PF and EnKF algorithms usually rely on Monte Carlo (MC) random sampling techniques to carry out the forecast step, i.e. sample the uncertain input space and obtain the sample of output variables through the integration of the forward model. Provided these input and output samples, they rely on the stochastic estimation of error statistics such as PDF for PF, covariances between spatially distributed model outputs or covariances between model inputs and outputs for EnKF. MC techniques are generic, robust and easily portable on massively parallel supercomputers; yet they remain computationally expensive due to their slow convergence rate scaling as the inverse of the square root of the number of particles [139]. As shown in Barthélémy [25] and Bozzi et al. [36], a large number of forward model evaluations should be carried out to converge the stochastic evaluation of error statistics such as PDFs, Sobol' indices and covariance matrices. This is often not compatible with operational constraints or high-dimensional problems.

To overcome the issue of crude MC techniques, there is a need to develop efficient and robust uncertainty quantification (UQ) methods in the context of DA for hydraulics to limit (1) the number of significant sources of uncertainties and (2) the computational cost of quantifying uncertainties on the river state, e.g. moments (mean, covariance) and PDF, while preserving the accuracy of the mapping \mathcal{M} between the uncertain inputs \mathbf{x} and the vector of M river water heights \mathbf{h} :

$$\mathbf{x} \in \mathbb{R}^d \quad \rightarrow \quad \mathbf{h} = \mathcal{M}(\mathbf{x}) \in \mathbb{R}^M. \quad (9.1)$$

The key idea of non-intrusive UQ methods is to build a cost-effective surrogate to perform UQ and SA steps [106, 108, 131, 135, 201, 219] (see Section 2.3).

The objective is to evaluate the performance of PC and GP surrogates mimicking the behaviour of 1-D open-channel flows for UQ and SA steps that are important in the design of EnKF and PF algorithms. The quantity of interest is the 1-D water level discretized along 50 km of the Garonne River (South-West France). As a preliminary step, the focus is made on steady flows and the flow remains fluvial. The treatment of strong non-linearity and discontinuity induce by fluvial/supercritical transitions is beyond the scope of this study. The main sources of uncertainties are the upstream discharge that is constant in steady state conditions and the friction coefficient that is a piecewise constant function. Under these hypotheses, the present work features scalar inputs and spatially varying outputs due to the heterogeneous bathymetry of the Garonne River. A convergence study is first carried out to determine the size of the training set N that is required to build a valid surrogate using either PC expansion or GP model. GP and PC surrogates are then compared when a computational budget is set, i.e. for the same number of snapshots (also called simulations here) N used to construct each surrogate. The comparison is carried out with respect to the following

metrics on \mathbf{h} : PDF that is of interest for Bayesian inference and PF algorithms; spatially varying Sobol' indices (associated with the correlation between each uncertain input and the spatially distributed output) and correlation matrix (associated with the spatial correlation of the output) that are of interest for variational and EnKF algorithms.

The structure of the chapter is as follows. Section 9.2 introduces the 1-D SWE solved using MASCARET and the Garonne River case study. Section 9.3 presents the results of the comparative study between PC and GP with respect to a MC reference. Conclusions and perspectives for the study are given in Section 9.4.

9.2 Hydraulic Modelling

The SWE represent the dynamics of open-channel flows, typically in rivers with small bathymetry variations [98]. They form a hyperbolic system of partial differential equations that characterize subcritical and supercritical flows subject to hydraulic jumps. Here, we only deal with subcritical flows, in the plain.

9.2.1 1-D Shallow Water Equations (SWE)

We consider a 1-D hydraulic model commonly used in hydraulic engineering and flood forecasting. The main channel is described by a hydraulic axis corresponding to the main flow direction, implying that the river channel is represented by a series of cross-sections (or profiles) identified by a curvilinear abscissa a ranging from a_{in} upstream of the river to a_{out} downstream. 1-D SWE are derived from mass conservation and momentum conservation. The equations are written in terms of discharge (or flow rate) Q ($\text{m}^3 \text{s}^{-1}$) and hydraulic section A (m^2) that relates to water level (or water height) h (m) such that $A \equiv A(h)$. The non-conservative form of the 1-D SWE for non-stationary flow reads [224]

$$\begin{cases} \partial_t A(h) + \partial_a Q = 0 \\ \partial_t Q + \partial_a \left(\frac{Q(h)^2}{A(h)} \right) + g A(h) \partial_a h - g A(h) (S_0 - S_f) = 0 \end{cases} \quad (9.2)$$

with g the gravity, S_0 the channel slope and S_f the friction slope. In the present study, the SWE are combined with the Manning-Strickler formula to parameterize the friction slope S_f such as:

$$S_f = \frac{Q^2}{K_s^2 A(h)^2 R(h)^{4/3}}, \quad (9.3)$$

where $R(h) = A(h)/P(h)$ (m) is the hydraulic radius written as a function of the wet perimeter $P(h)$, and where K_s ($\text{m}^{1/3} \text{s}^{-1}$) is the Strickler friction coefficient. The pair (h, Q) forms the hydraulic state varying in time and

space. For steady flows in case of smooth solutions, Eq. (9.2) simplifies to:

$$\begin{cases} \partial_a Q = 0 \\ \partial_a h = \frac{(S_0 - S_f)}{1 - Fr^2} \end{cases} \quad (9.4)$$

where Fr is the dimensionless Froude number

$$Fr^2 = \frac{Q^2}{gA^3} \frac{\partial A}{\partial h}. \quad (9.5)$$

The solutions for Eq. (9.4) are called *backwater curves* when the downstream boundary condition is prescribed in a deterministic way for subcritical flow. To solve Eq. (9.4), the following input data is required: bathymetry, upstream or downstream boundary conditions, lateral inflows and roughness coefficients. It should be noted that the evolution in time of the bathymetry or the roughness coefficients are not taken into account in this study. The imperfect description of this data translates into errors in the simulated hydraulic state h . To understand the structure of these errors, it is of prime importance to determine which input variables contribute, and to what extent, to the variability in the hydraulic state at different curvilinear abscissas a along the river channel, for instance via a SA study.

We use the MASCARET software to simulate the 1-D SWE in Eq. (9.2) and predict (h, Q) along the discretized curvilinear abscissa of the hydraulic network $a \in [a_{\text{in}}, a_{\text{out}}]$. The SWE are solved here with the steady kernel of MASCARET based on a finite difference scheme [91, 90], meaning that (h, Q) only varies in space. MASCARET is part of the TELEMAC-MASCARET open-source modelling package developed at EDF (*Électricité de France R&D*) in collaboration with CEREMA (*Centre d'Étude et d'expertise sur les Risques, l'Environnement, la Mobilité et l'Aménagement*); it is commonly used for dam-break wave simulation, reservoirs flushing and flooding.

9.2.2 Garonne River Case Study

The present study is carried out on a real hydraulic network over the Garonne River in South-West France. The Garonne river flows along 647 km from the Pyrenees to the Atlantic Ocean draining an area of 55,000 km² (corresponding to the fourth-largest river in France). The present study focuses on a 50 km reach from Tonneins ($a_{\text{in}} = 13$ km) to La Réole ($a_{\text{out}} = 62$ km) with one observing station at Marmande ($a = 36$ km) as presented in Fig. 9.1a. The mean slope over the reach is $S_0 = 3.3 \text{ m km}^{-1}$; the mean width of the river is $W = 250 \text{ m}$; the bank-full discharge is approximately $\bar{Q} = 2550 \text{ m}^3 \text{s}^{-1}$. Despite the existence of active floodplains, this reach can be accurately modelled by a 1-D hydraulic model using Eq. (9.2) [31].

Figure 9.1b presents the non-uniform bathymetry profile along the 50 km reach, interpolated from 83 on-site bathymetry cross-sections. Friction for the river channel and its floodplain is prescribed over three zones separated by dashed lines. The Strickler coefficients K_{s_1} , K_{s_2} and K_{s_3} are used to characterize friction through Eq. (9.3) and are uniform per zone. The observing station at Marmande is located at the beginning of the third zone associated with K_{s_3} .

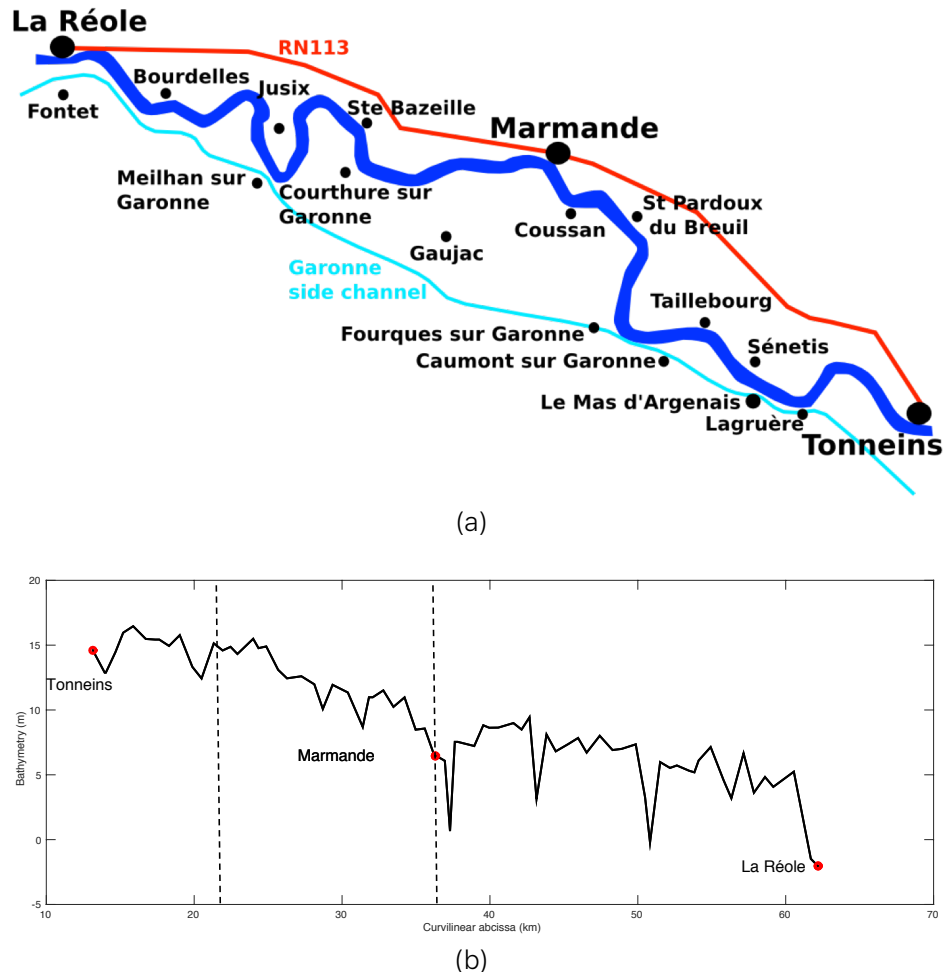


Figure 9.1 – Garonne River case study (South-West France). (a) Reach between Tonneins (upstream, $a_{in} = 13$ km) and La Réole (downstream, $a_{out} = 62$ km) with Marmande located at $a = 36$ km. (b) Bathymetry profile along the curvilinear abscissa a (km) between Tonneins and La Réole. The Strickler friction coefficient K_s spatially varies as a constant piecewise function; the changes in the value of K_s are indicated by vertical dashed lines.

The upstream steady boundary condition is prescribed by $Q(a_{in}) = Q_{in}$; the discharge Q is constant along the reach ($Q = Q_{in}$). The downstream boundary condition is prescribed with a local rating curve RC established at La Réole that sets $h(a_{out}) = RC(Q_{out}) = h_{out}$. The hydraulic model has been calibrated using channel and floodplain roughness coefficients as free parameters [31].

9.2.3 Sources of Uncertainties and Quantity of Interest

UQ and DA for flood forecasting are essential to ensure the predictive capability of the surrogate model at the observing stations such as Marmande. Previous work [68] has shown that in steady state conditions and given some assumptions on the statistics of the input uncertain variables, the sensitivity of the hydraulic state at Marmande to K_{s_3} is predominant; the sensitivity at Marmande to K_{s_1} and K_{s_2} is null because of the steady state assumption and given the present hydraulic model. Hence, the main sources of uncertainties taken into account here are the upstream mass flow rate Q and the Strickler coefficient K_{s_3} . We denote by $\mathbf{x} = (Q, K_{s_3})$ the random vector of size $d = 2$. From expert knowledge, Q and K_{s_3} are considered as independent random variables—even though this hypothesis is limiting as K_s may decrease when Q increases. Q ($\text{m}^3 \text{s}^{-1}$) follows the normal distribution $\mathcal{N}(4031, 400)$: the mean is set to the average flow in the Garonne River; the standard deviation (STD) is chosen in order to remain in subcritical flow. K_{s_3} ($\text{m}^{1/3} \text{s}^{-1}$) follows the uniform distribution $\mathcal{U}(15, 60)$: the range of the uniform distribution is chosen following calibration results. This range for the variables Q and K_{s_3} allows testing how the surrogates are affected by non-linearities.

MASCARET provides as output the water height over 463 cross-sections for the Garonne case. In this work, we focus on the water height at $M = 14$ stations evenly distributed along the 50 km reach, among which Marmande at $a = 36$ km. Even though the surrogate models are formulated with respect to the predominant uncertain variables for water level at Marmande and downstream, the surrogates are computed over the entire network. On this hydraulic network, in-situ observations are only available at Marmande and the improvement of the water level at Marmande and downstream of Marmande relies on the improvement of Q and K_{s_3} only. Yet, the correlation function between the water-level error at Marmande and the other locations is needed in the DA algorithm. We denote by \mathbf{h} the vector of M observed water levels for one realization of MASCARET.

A database noted $\mathcal{D}_{N_{\text{ref}}}$ and containing $N_{\text{ref}} = 100,000$ MASCARET simulations was compiled as a reference for the study. Each simulation corresponds to a different pair of inputs (Q, K_{s_3}) resulting from a MC random sampling following $Q \sim \mathcal{N}(4031, 400)$ and $K_{s_3} \sim \mathcal{U}(15, 60)$. In the present study, $\mathcal{D}_{N_{\text{ref}}}$ is partly used to build the PC and GP surrogates via the training set $\mathcal{D}_N = (\mathcal{X}, \mathcal{Y}) \subset \mathcal{D}_{N_{\text{ref}}}$ of size N ; it is fully used to validate them a posteriori over a large ensemble (Section 2.3.5). As outlined in Section 2.2.2, the analysis is highly dependant of the nature of the prescribed PDFs.

9.3 Comparison of PC and pGP Surrogates

9.3.1 Reference Monte Carlo (MC) Results

We first present the results obtained using the MC reference sampling ($N_{\text{ref}} = 100,000$ in $\mathcal{D}_{N_{\text{ref}}}$) in terms of water level mean, STD, PDF, correlation matrix as well as Sobol' indices associated with Q and K_{s_3} . These results are used as reference to evaluate the accuracy of the PC and pGP surrogate models—as defined in Section 2.3 and with pGP referring to the use of a POD with a GP surrogate model.

Figure 9.2a displays the water level PDF computed from $\mathcal{D}_{N_{\text{ref}}}$ data set integrated with a MC approach for the $M = 14$ stations along the curvilinear abscissa $a \in [a_{\text{in}}, a_{\text{out}}]$. The mean water level is represented with a thick black line; the interval between two STD is represented with dotted lines; and the minimum and maximum water level values are represented with dashed lines. In steady state, water level of the upstream part is mostly sensitive to Q . The dispersion of the ensemble is thus mostly driven by the dispersion of Q . At the very downstream part of the river ($a = 60$ km), the dynamics is driven by the downstream boundary condition where the water level and discharge are related by the local rating curve RC . The water level is a function only of discharge and the roughness coefficient has no influence; thus the spread of the ensemble tends to decrease near the downstream boundary condition. After Marmande, the flow is driven both by K_{s_3} and Q , the dispersion of the ensemble is larger than upstream of Marmande. At Marmande ($a = 36$ km), the flow is complex due to strong variation of the local bathymetry (Fig. 9.1b), the ensemble spread is larger and the PDF plotted in Fig. 9.2b features two main modes due to the change in backwater curves solutions for subcritical flow.

The Sobol' indices for the water level S_Q and $S_{K_{s_3}}$ computed from $\mathcal{D}_{N_{\text{ref}}}$ with respect to Q and K_{s_3} are presented in Fig. 9.3a along the curvilinear abscissa a . These indices confirm the previously mentioned spatial sensitivity. The water level variance is mostly explained by the upstream discharge variability for $a = [0; 30]$ km—the variability of K_{s_3} has a small impact in the upstream part of the river in steady state conditions. It is then mostly explained by the Strickler coefficient variance for $a = [30; 60]$ km. Near the downstream boundary condition, the water level is related to the discharge by the local rating curve RC , the very last part of the network is thus under the influence of the discharge. First and total order indices are almost equal, meaning that the correlation between the variability in the input parameters is weak. One should keep in mind that these observations are the results of the PDFs and hydraulic regime assumptions that were made.

Figure 9.3b displays the water-level correlation matrix along the 50 km reach that is estimated from $\mathcal{D}_{N_{\text{ref}}}$. The n th column of the matrix describes the water-level error correlations between one given location on the channel a_n and the rest of the channel a_m with $a_m \in [a_{\text{in}}, a_{\text{out}}]$. By

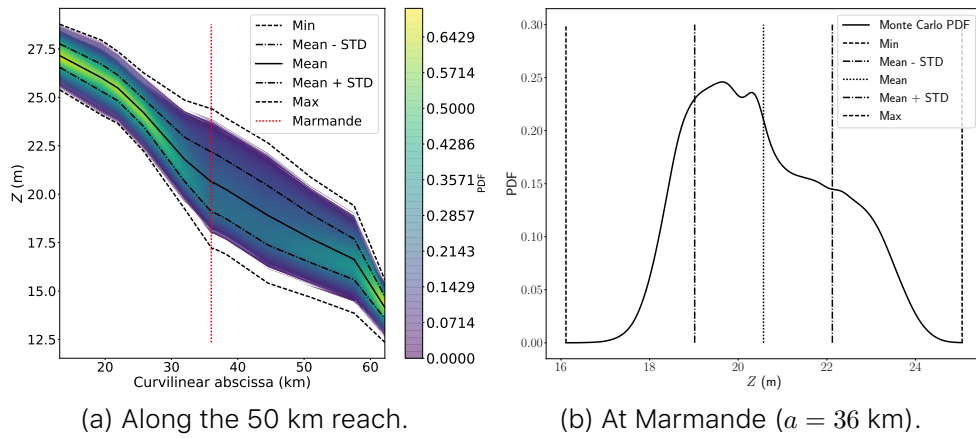


Figure 9.2 – Reference PDF of the water elevation obtained with the $N_{\text{ref}} = 100,000$ snapshots in $\mathcal{D}_{N_{\text{ref}}}$ derived from MC random sampling: (a) at the $M = 14$ stations along the 50 km river reach; (b) at Marmande. The solid line indicates the mean water level with respect to the curvilinear abscissa; the dotted lines indicate the spread corresponding to 2 STD; the dashed lines indicate the maximum and minimum water level values; and the vertical dotted line indicates Marmande’s location.

definition, the correlation is equal to 1 on the diagonal, it decreases when the distance between a_n and a_m increases. We first analyse the correlation function for a point located upstream of the river ($a_i = 15$ km) where $S_Q = 0.9$ and $S_{K_{s_3}} = 0.1$. Water level errors are strongly correlated in the upstream part of the river, which is under the influence of the upstream discharge boundary condition, where S_Q is large. Errors between $a = 15$ km and the rest of the river tend to de-correlate when the influence of K_{s_3} increases (i.e. where $S_{K_{s_3}}$ is larger). We then analyse the correlation function for Marmande ($a = 36$ km) where $S_Q = 0.15$ and $S_{K_{s_3}} = 0.85$. The correlation between water-level errors at Marmande and the rest of the river is large in the vicinity of Marmande, where the influence of K_{s_3} prevails. It then decreases for upstream and downstream locations that are under the influence of the upstream discharge and the downstream rating curve RC (where S_Q is large), respectively.

9.3.2 Convergence Analysis for Surrogates

We now use the metrics defined in Section 2.3.5 to evaluate the accuracy of both PC and pGP surrogates with respect to the MC solution. The surrogate models are built using a training set $(\mathcal{X}, \mathcal{Y})$ of size N that is much smaller than that of the reference sample N_{ref} ; they are then validated with respect to the reference MC results. The PC surrogate is built using a Gaussian quadrature rule with $N = (P + 1)^2$ particles in the training set (P is the total polynomial degree to be determined). The pGP approach is built using an approximate low-discrepancy Halton’s sequence of the same budget as for the PC approach. This is approxi-

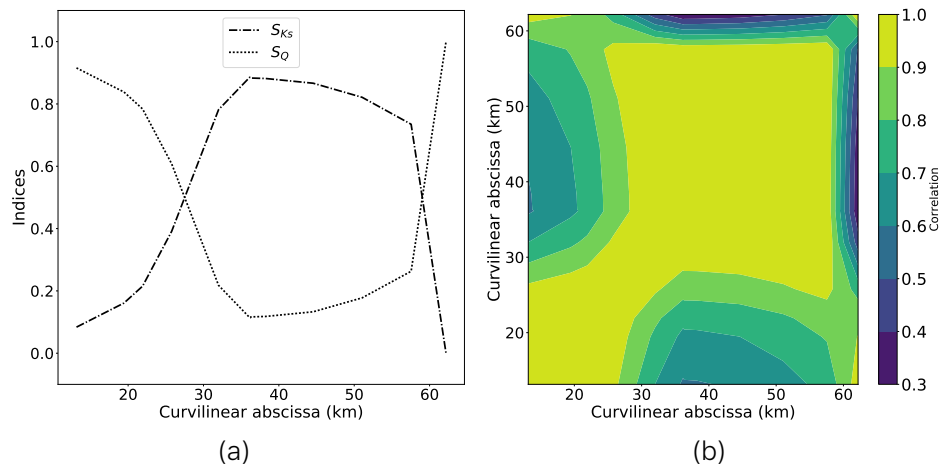


Figure 9.3 – Measures of importance using MC random sampling. (a) Reference Sobol' first order indices along the 50 km reach. Dashed-dotted line corresponds to the Sobol' index associated with the Strickler coefficient K_{s_3} . Dotted line corresponds to that associated with the upstream discharge Q . (b) Reference spatial correlation matrix \mathbf{C}_{mc} associated with the spatially distributed water level \mathbf{h} .

mate in the sense that we consider the closest values to the standard Halton's sequence that are part of the data set $\mathcal{D}_{N_{ref}}$. The sensitivity to the value of P and thus to the size of the training set N is investigated.

Both surrogates are computed with a fixed budget N of 49, 121 and 256 MASCARET evaluations. For PC, this value of N corresponds respectively to $P = 6$, $P = 10$ and $P = 15$. The pGP and PC response surfaces at Marmande are presented in Fig. 9.4 for $N = 49$ and $N = 121$. The design of experiment is represented by black dots. The colour map is evaluated by sampling each surrogate over the full data set $\mathcal{D}_{N_{ref}}$ made of $N_{ref} = 100,000$ particles. It is found that the water level increases with increasing discharge Q and decreasing Strickler coefficient K_{s_3} , consistently with MASCARET behaviour. Due to the quadrature rule, increasing the number of snapshots (from $P = 6$ in Fig. 9.4c to $P = 10$ in Fig. 9.4d) allows building a higher order PC surrogate valid on a wider input range for Q that is described by a Gaussian PDF. For $P = 10$, some of the quadrature roots are outside of the MC sample and require additional MASCARET evaluations to build the PC surrogate \mathcal{M}_{pc} . Looking at the pGP design of experiments, the input space interval for Q has been arbitrarily fixed to optimally represent the PDF. Since we consider a Gaussian distribution, its range has been bounded to $[3000; 5000 \text{ m}^3 \text{ s}^{-1}]$. Following Chebyshev's theorem, this leads to a 90 % confidence interval.

The distribution of the particles in the design of experiments used by PC and pGP differ. On the one hand, the design of experiments for the PC surrogate is constrained by the PDF of the uncertain inputs. We use here a quadrature-based PC since it was found to be more cost-effective

than regression-based PC for a small dimensional problem ($d = 2$) on the Garonne case [68]. On the other hand, using the approximate Halton's sequence is known to be accurate for pGP surrogate [51]. This is indeed useful to cover the uncertain space without any bias and to have low discrepancy, meaning that most of the quantity of interest variance is captured and that a good Q_2 criterion is achieved. The choice of the design of experiments will be driven in future work according to the study objectives. For instance, DA usually relies on the assumption of Gaussian PDF for the input parameters, so the design of experiments can use this prior information. For risk analysis, threshold values are paramount and a design of experiment accounting for parameter space extrema is required.

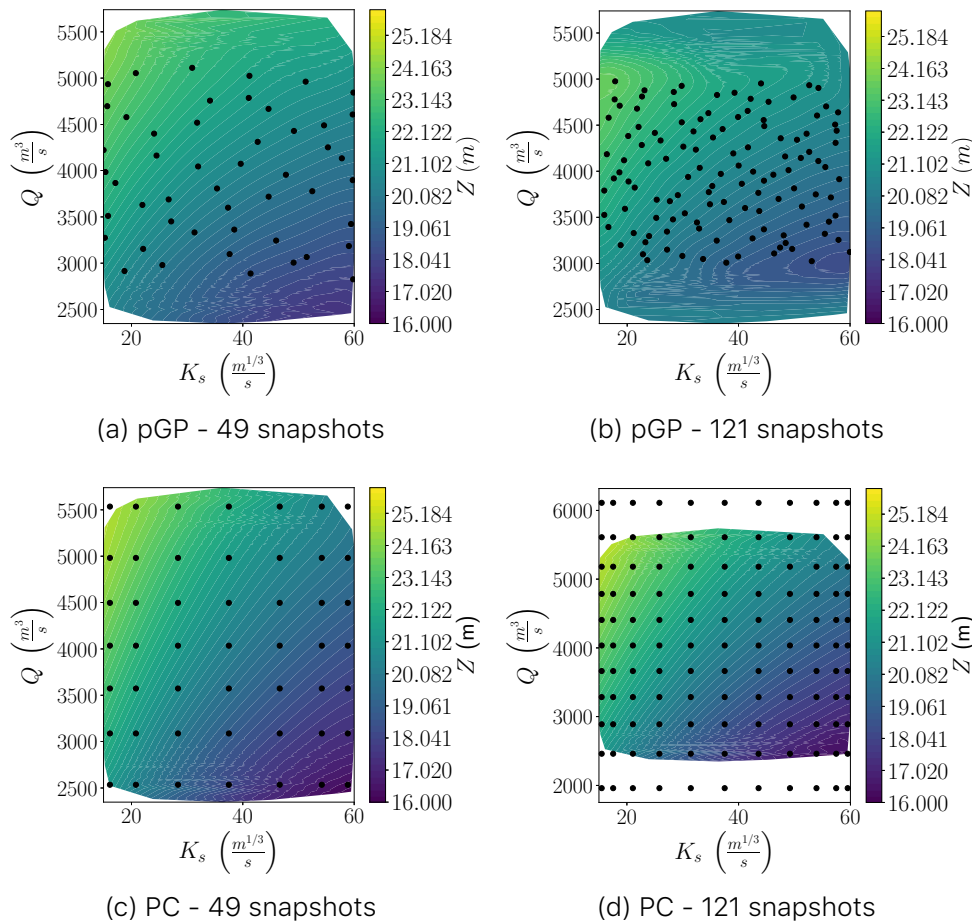


Figure 9.4 – Water level response surface at Marmande computed at $\mathcal{D}_{N_{\text{ref}}}$. Top: pGP using (a) $N = 49$ snapshots and (b) $N = 121$ snapshots. Bottom : PC using (c) $N = 49$ snapshots and (d) $N = 121$ snapshots. Black dots represent the design of experiments used to construct the surrogate models. The colour map corresponds to the evaluation of the surrogate over the full data set $\mathcal{D}_{N_{\text{ref}}}$.

⁰Scaling of (d) was set in order to show the entire design of experiments. This allows to grasp the fact that the parameter space is evaluated in regions that are not

The Q_2 error between the surrogate water level and the forward model water level for $D_{N_{\text{ref}}}$ averaged over the river is given in Table 9.1 for different sizes of training set N varying between 49 and 256. The error remains below 10^{-3} , even for $N = 49$ snapshots; it is only slightly improved when the number of snapshots N increases to 256 and beyond.

Table 9.1 – Q_2 error for pGP and PC surrogates computed with respect to the MC reference. The error corresponds to the average over the M stations with increasing number of snapshots N from 49 to 256.

N	pGP	PC
49	0.99965	0.99983
121	0.99514	0.99993
256	0.99143	0.99962

The water level PDF estimated with the PC and the pGP surrogate models based on 49, 121, 256 snapshots are compared in Fig. 9.5 at the curvilinear abscissa $a = 15$ km (near upstream boundary condition) and $a = 36$ km (Marmande). In the upstream part of the river, the PDF is unimodal and is well represented with a small number of snapshots for both surrogates. On the contrary, at Marmande, the dynamics of the flow is more complex and the PDF is bimodal. Both PC and pGP surrogates are able to retrieve the overall shape of the PDF at $a = 15$ km and $a = 36$ km. The shape is more accurate when the number of snapshots N increases. This is quantified using a Kolmogorov-Smirnov statistical test, which measures the fit between the water level CDF computed from each surrogate model and that computed from the reference MC. Table 9.2 indicates that the null hypothesis (Eq. (2.34)) is rejected for both surrogates computed with 49 snapshots (when $D > 6,082 \cdot 10^{-3}$) and accepted when at least 121 snapshots are used. For $N = 49$, Fig. 9.5b-d show that the location of the first mode is shifted compared to MC reference. Increasing N to 121 enables the PC approach to correctly locate this mode, while it enables the pGP approach to represent the second mode with an accurate amplitude, leading to an accepted null hypothesis. Each approach presents a particular limitation: the first mode is not well positioned by the pGP approach; the second mode is not captured by the PC approach. As for the tail of the PDF, it is correctly represented by the PC surrogate, while the pGP surrogate slightly oscillates around the shape of the reference MC PDF.

The RMSE for the Sobol' indices for both pGP and PC with a fixed computational budget of $N = 121$ simulations is of the order of 10^{-2} when computed over the 50 km reach. Figure 9.6 displays the squared error for the Sobol' indices along the curvilinear abscissa; the spatial

evaluated by the MC sampling.

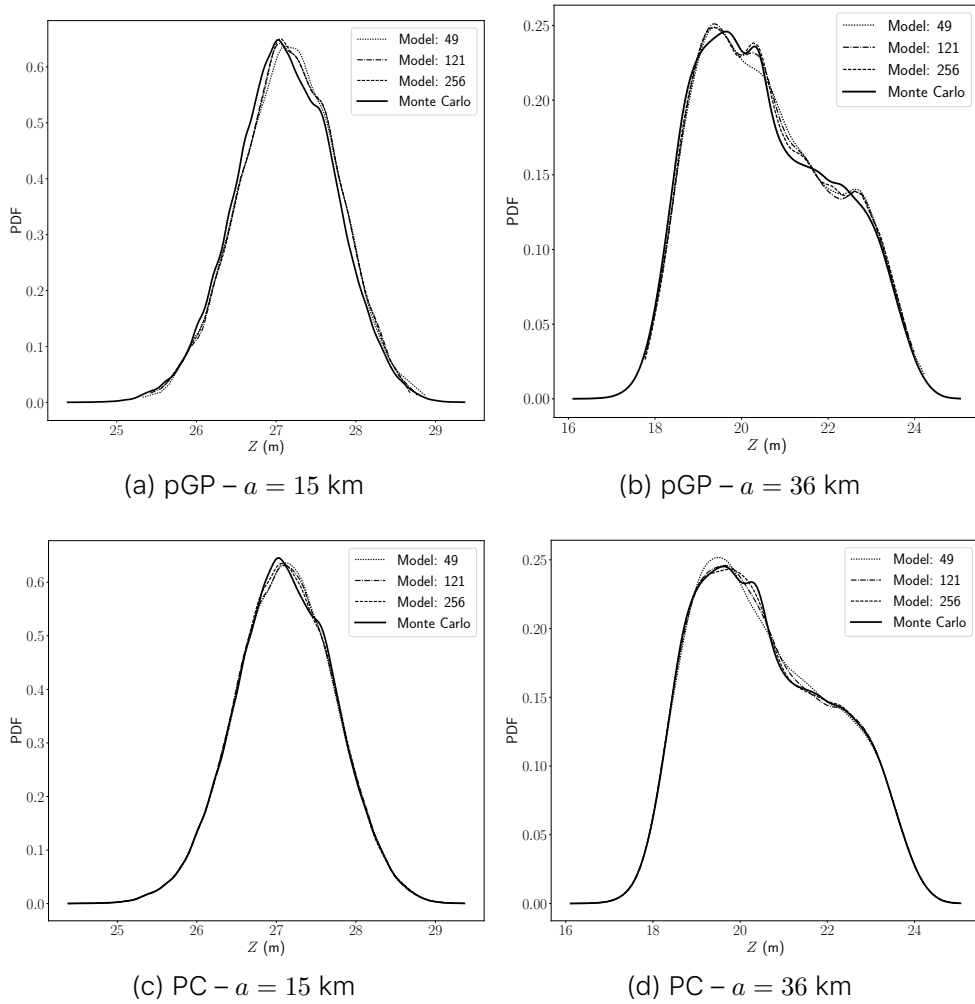


Figure 9.5 – Comparison of water level PDF obtained with pGP (top panel) and PC (bottom panel) (a)–(c) At $a = 15 \text{ km}$ (near upstream boundary condition). (b)–(d) At $a = 36 \text{ km}$ (Marmande). The comparison is carried out for different sizes of training set N (49, 121, 256); the MC result is provided as reference in solid black line.

pattern is similar for both surrogates and the squared error for each index is larger where the Sobol' indices are larger. The RMSE for the correlation matrix for both pGP and PC with $N = 121$ simulations are equal to $\text{RMSE}_{\text{pc}} = 3,67 \cdot 10^{-4}$ and $\text{RMSE}_{\text{gp}} = 4,59 \cdot 10^{-3}$. The spatial distribution of the squared error is plotted in Fig. 9.7. These results confirm the good behaviour of both PC and pGP surrogates with respect to MASCARET. For both Sobol' indices and correlation matrices, the PC surrogate slightly outperforms pGP.

Table 9.2 – Two-sample Kolmogorov-Smirnov statistical test for pGP and PC surrogates with respect to the MC reference at Marmande with increasing numbers of snapshots N (49, 121, 256). The null hypothesis is rejected if $D > 6,082 \cdot 10^{-3}$.

Surrogate	Snapshots	Statistics D	p -value
pGP	49	$7,95 \cdot 10^{-3}$	0.004
	121	$3,97 \cdot 10^{-3}$	0.409
	256	$3,02 \cdot 10^{-3}$	0.751
PC	49	$7,15 \cdot 10^{-3}$	0.012
	121	$4,95 \cdot 10^{-3}$	0.172
	256	$4,93 \cdot 10^{-3}$	0.175

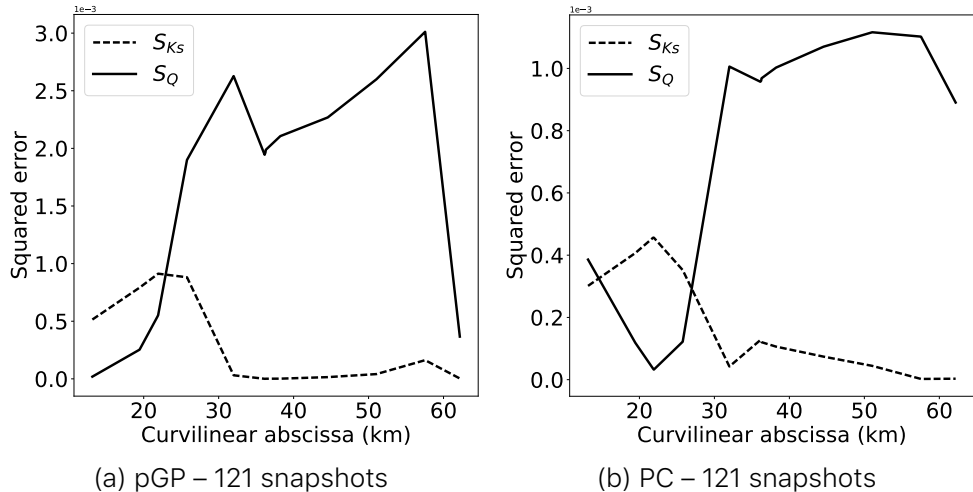


Figure 9.6 – Squared error of the spatial Sobol' indices along the 50 km reach for (a) pGP and (b) PC surrogate models built using $N = 121$ snapshots in the training set. Dashed lines correspond to the Sobol' index associated with K_{s_3} ; solid lines correspond to that associated with the upstream discharge Q .

9.4 Summary

The purpose of this work was to compare two popular strategies for building surrogate models, Polynomial Chaos (PC) and POD-based Gaussian Process (pGP). Both methods were applied to a hydraulic case corresponding to a spatially distributed open-channel steady flow along the Garonne River depending on the upstream discharge Q and on the Strickler friction coefficient K_{s_3} , with the long-term objective to determine which surrogate strategy could be useful in the framework of ensemble-based data assimilation. It is important to show how surrogate models could be used to estimate some statistical quantities in a cost-effective way. This is useful for sensitivity analysis studies to eval-

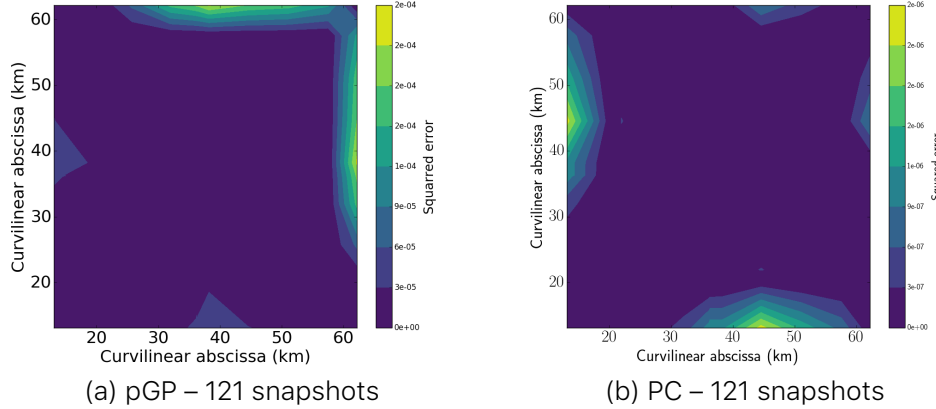


Figure 9.7 – Squared error of the correlation matrix for (a) pGP and (b) PC surrogate models built using $N = 121$ snapshots.

uate the impact of physical parameters and external forcing on the river state. This is also useful for data assimilation to estimate the correlation matrix and PDF related to the spatially distributed river state for the Ensemble Kalman Filter (EnKF) and the Particle Filter (PF), respectively.

We carried out a convergence study based on the following metrics: water level statistical moments, correlation matrix, PDF as well as *Sobol'* indices representing the contribution of the upstream discharge and the Strickler friction coefficient on the water-level variance. The accuracy of the PC and pGP surrogates were measured by their ability to retrieve the reference metrics obtained with a converged Monte Carlo (MC) random sample (including 100,000 MASCARET simulations). An in-depth comparison of these metrics was made using the same computational budget: 121 MASCARET snapshots. The sensitivity to the number of snapshots was carried out to ensure that 121 simulations were enough to make this comparison valuable.

Results showed that both surrogate models can be used in place of the MASCARET forward model for uncertainty propagation without loss of accuracy. None of the two surrogate models clearly outperforms the other. In both cases, the PC and pGP surrogate models are able to correctly retrieve all physical information. The PC strategy seems to be more precise to compute the spatially distributed correlations as well as the *Sobol'* indices, with the advantage that these indices do not need any further MASCARET evaluation as they are analytically computed from the PC expansion. Still, the multimodal water level PDF at Marmande (which is an important observation station along the Garonne River in operational context) was better captured by the pGP strategy that requires an additional sampling of the surrogate. Indeed, even increasing the number of snapshots to 256 and beyond was not enough to retrieve the second mode of the PDF using the PC surrogate model, while this was already captured with 121 snapshots by the pGP surrogate model. Still, it should be mentioned that the PC model better positions

the first mode than the pGP model when using the MC approach as reference. Last but not least, the PC strategy requires some insight about the uncertain inputs of the system. We may not have access to this information in practice, leading potentially to a poor robustness of the PC surrogate. The quantity of interest may also feature non-linearity and exhibit extrema, which could be difficult to account for using quadrature points that could miss some physics. Alternative (for instance sparse) projection strategies could be investigated in the future to overcome these limitations.

Conclusions for the present test case highlight the validity of both quadrature-based PC and POD-based GP surrogate strategies for SWE in permanent flow for a small dimensional problem (the size of the uncertain space is $d = 2$). The ranking between PC and pGP approaches will need to be further investigated when moving to open-channel unsteady flow modelling used for instance in the context of operational flood forecasting. The first challenge lies in the extension of the PC and pGP surrogates to larger uncertain dimension d , especially to address parameters that vary in space or over time or both, such as the bathymetry spatial field and the time series of the upstream discharge. This may require the evaluation of more advanced strategies to reduce the size of the basis, the uncertain dimension (for instance through the Karhunen-Loëve transformation) and the number of snapshots N in the training set. For instance, the quadrature method used to build the PC surrogate is known to suffer from the *curse-of-dimensionality*. This will have to be revisited for a larger size d of the uncertain space. The second challenge lies in the validity of the surrogate model over successive data assimilation cycles, implying that the flow is now unsteady. First, it is expected that the SA shows that the roughness coefficients from upstream and downstream locations have an influence on the flow at a given location in subcritical flow. Secondly, it may be necessary to adjust the coefficients of the surrogates to track the changes in the river state behaviour over time. The cycled data assimilation analysis will then allow to correct physical parameters over time, such as the roughness coefficient that may vary seasonally or between flood events. The uncertainty quantification and data assimilation strategies could also be extended to the bathymetry and thus allow for a time-varying correction of the river geometry that is usually fixed in a hydraulic model. Such solution would mimic the evolution of the river bed and flood plain at a much lower computational cost than when using a hydro-sediment coupled model.

Those are crucial steps for the complementary use of surrogate models within data assimilation algorithms.

10 | The Aerothermal Flow around the LS89 Blade Cascade

10.1 Introduction

Le nombre de simulations CFD nécessaires à la formulation du modèle de substitution est défini par la complexité de la physique et le nombre de paramètres d'entrée à prendre en compte. La présente étude vise à améliorer sa construction en utilisant les deux nouvelles stratégies de rééchantillonnage de l'espace de paramètres présentées Chapter 7.

Une application industrielle est visée : l'analyse aérothermique autour de la pale LS89. Une étude de quantification de l'incertitude a déjà été réalisée à l'aide de simulations RANS (Reynolds Averaged Navier-Stokes) [89, 70] mais la première analyse UQ utilisant la Simulation aux Grandes Échelles (SGE) de cette configuration est ici présentée. Les SGE sont des simulations instationnaires 3D haute fidélité (voir Appendix C pour plus de détails). Cette approche entraîne un coût CPU élevé qui nécessite l'utilisation de ressources HPC (High Performance Computing). Le code AVBP a été utilisé.

La difficulté de prédire correctement les caractéristiques d'écoulements, même pour une telle simulation haute fidélité, est révélatrice de l'incertitude des conditions aux limites. L'intensité de la turbulence et l'angle d'attaque sont connus pour affecter le flux aérothermique. Cette quantité est d'un grand intérêt pour les partenaires industriels afin de déterminer le cycle de vie des composants de la turbine. L'étude a permis de trouver une sensibilité spatiale du fluide aux paramètres d'entrée.

Le chapitre est rédigé comme suit : Section 10.2 présente le montage expérimental tandis que Section 10.3 présente la configuration de la simulation numérique. Enfin, Section 10.4 présente les résultats de l'analyse UQ.

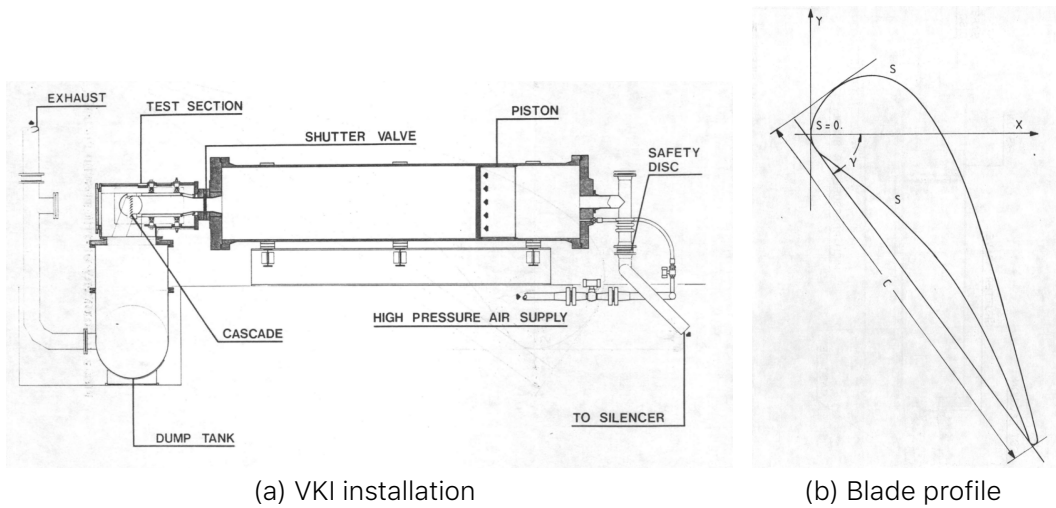
THE NUMBER of CFD simulations that is required for the formulation of the surrogate model is defined by the complexity of the physics and the number of input parameters to take into account. The present study aims at improving its construction by using the two new strategies for resampling the parameter space presented in Chapter 7. An industrial application is targeted: the aerothermal analysis around the LS89 vane [24]. An Uncertainty Quantification study has already been performed using Reynolds Averaged Navier-Stokes (RANS) [89, 70] but

its first UQ analysis using Large Eddy Simulation (LES) is presented. LES are high-fidelity full 3D unsteady simulations (see Appendix C for more details). This approach comes at a high CPU cost which requires the use of High Performance Computing (HPC) resources.

The chapter is tailored as follows; Section 10.2 presents the experimental setup while Section 10.3 presents its numerical simulation configuration. Finally, Section 10.4 presents the results of the UQ.

10.2 Case Description

The LS89 case is a blade cascade designed and tested experimentally at the Von Karman Institute for Fluid Dynamics (VKI) [24]. The linear cascade consists of five high-pressure turbine vanes although only the centre vane is studied—see Fig. 10.1. The vane is a 2D extruded profile unlike most industrial vanes that are much more complex geometrically. It, however, remains of great interest because the operating points are representative of values found in real engines today. This test case represents one of the largest turbomachinery databases available for the validation of CFD models in complex geometries.



c (mm)	67,647
g/c	0,850
γ (degr.)	55,0
o/c	0,2207
r_{LE}/c	0,061
r_{TE}/c	0,0105

(c) Geometrical Characteristics

Figure 10.1 – LS89 blade cascade experimental setup from the VKI. Source [24]

A large variety of operating points have been successfully simulated until now. Low levels of turbulence injection ($< 1\%$) do not represent an issue for most solvers [89, 70] using either Reynolds-Averaged Navier Stokes (RANS) or Large Eddy Simulation (LES). Higher levels of turbulence have also been studied successfully [236] but difficulties arise for higher Reynolds numbers and larger outlet Mach numbers. Simulations are not able to correctly predict experimentally obtained profiles, notably the heat transfer field which is of great importance for the blade life-cycle.

The operating point addressed in this document, selected from Arts [24], is the MUR235, a very rich case in terms of physics that presents the above-mentioned challenges (high Reynolds and outlet Mach numbers)—see Table 10.1 and Table 10.2. Figure 10.2 highlights the main physical interactions in such a flow. One of the most notable features is the presence of a shock wave on the suction side of the blade. This shock wave interacts with a transitional boundary layer due to the highly curved flow, a potential source of instabilities in the boundary layer which in turn determines the wake downstream. This wake issues acoustic waves that impact the neighbour blade affecting the stability of the boundary layer. Also, there is a high level of free-stream turbulence that undergoes stretching around the leading edge of the blade which modifies the position of the boundary layer transition on the suction side [209].

Total temperature (K)	413,30
Total inlet pressure (bar)	1,828
Static inlet pressure (bar)	1,800
Static outlet pressure (bar)	1,049
Wall temperature (K)	301,15
Free stream turbulence (%)	6,0
Incidence angle (degr.)	0,0

Table 10.1 – Measured parameters for the MUR235 case.

In the original experiments [24], an increase in heat transfer is observed on the suction side of the blade when a high turbulence intensity level at the inlet ($\sim 6\%$) as well as a large Reynolds number at the outlet ($> 1 \cdot 10^6$) are present. The simulations recover the shock wave that triggers an abrupt transition of the boundary layer, but turbulent spots may be found upstream of this position that can contribute to the overall heat transfer. These spots can be explained due to perturbations in the free-stream turbulence T_u that are capable of trespassing the sheltering effect of the shear layer and thereby increase the heat transfer. Turbulence values upstream of the blade are thus of upmost importance.

The original experiments give only the turbulence intensity level at an upstream distance from the vane, which is insufficient to characterize the turbulent flow at this location. Recent studies on the same test bench have measured the integral length scale for the same intensity

	Inlet	Outlet
Total temperature (K)	413,3	
Total pressure (bar)	1,828	
Mach number	0,150	0,927
Reynolds number	$2,6471 \cdot 10^5$	$1,1521 \cdot 10^6$
Temperature (K)	411,45	352,69
Pressure (bar)	1,800	1,049
Density (kg/m ³)	1,524	1,036
Velocity(m/s)	61,00	349,02
Dynamic viscosity (kg/ms)	$2,33750 \cdot 10^{-5}$	$2,1240 \cdot 10^{-5}$
Kinematic viscosity(m ² /s)	$1,5589 \cdot 10^{-5}$	$2,0494 \cdot 10^{-5}$

Table 10.2 – Free stream conditions for the MUR235 case.

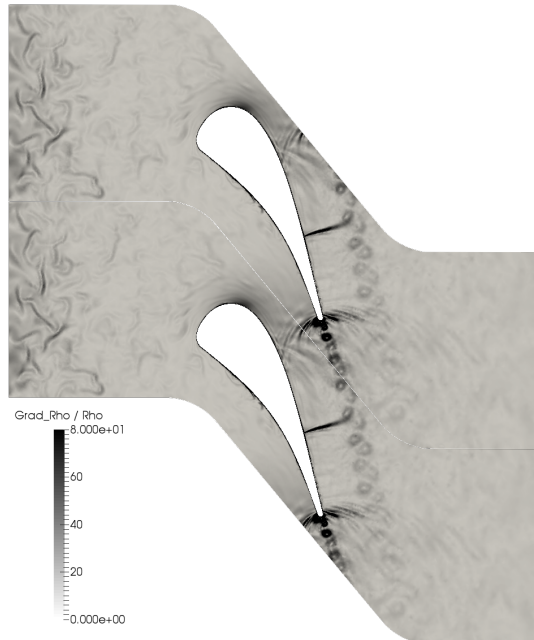


Figure 10.2 – $\frac{\nabla\rho}{\rho}$ (m^{-1}) with $Tu = 30\%$.

level [74]. In spite of this newly available information, simulations are not capable of recovering an important part of the heat flux on the suction side even when taking the correct length scale [178]. Uncertainties concerning the measured values in the experiments, that serve as boundary conditions in the simulation, appear as a path to be explored.

Apart from the turbulence intensity and the length scale, the angle of attack α of the incoming flow can also be seen as an uncertain parameter. There is no information related to this parameter in the experimental campaigns. In Fig. 10.3, the effect of α was numerically investigated with respect to Tu by studying the heat transfer coefficient response—hereafter defined as the QoI. Due to the computational effort required to modify and simulate a case correctly with a modified integral

length scale versus a modification of α , this parameter was not taken into account. Increasing Tu or α causes an increase of the QoI and Tu seems to have a larger impact than α . A deeper analysis would require more computations to obtain: (i) a correct response of the influence of these parameters on the QoI ; (ii) the contribution of each parameter ; and (iii) the probability density function of the QoI by propagating the uncertainties. Thus, the parameter space for this study was defined as

$$Tu \in [0, 30\%] \quad \alpha \in [-5, 5^\circ]. \quad (10.1)$$

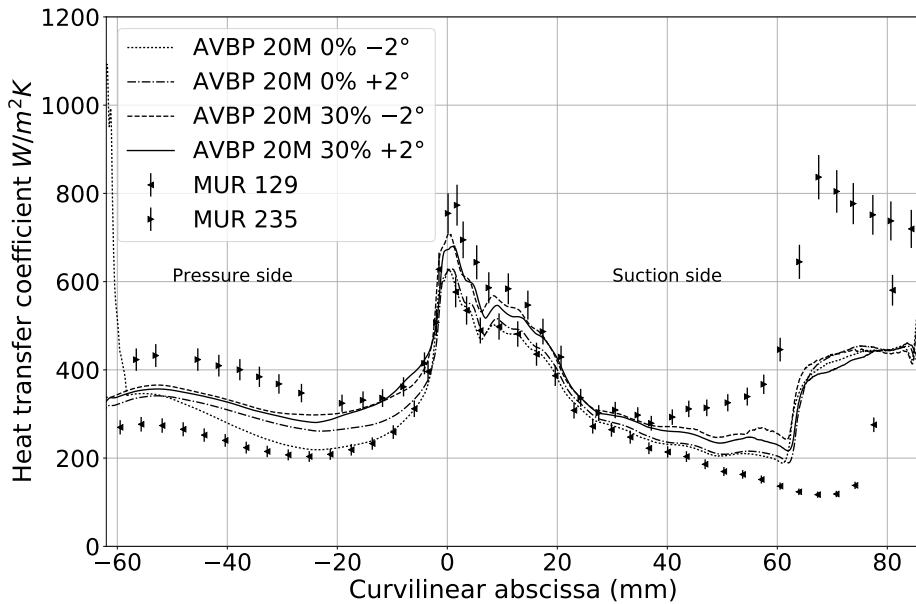


Figure 10.3 – Heat transfer coefficient variation compared to experimental data of MUR129 ($Tu = 1\%$, $\alpha = 0^\circ$) and MUR235 ($Tu = 6\%$, $\alpha = 0^\circ$).

10.3 Numerical Setup

The simulations have been performed using AVBP [86], a validated CFD LES solver co-developed by CERFACS and IFP-EN. This parallel code solves the three-dimensional compressible Navier-Stokes equations for both steady and unsteady reacting flows. The code is capable of handling hybrid unstructured meshes and allows addressing complex geometries. High-order numerical schemes based on the *Taylor-Galerkin* (TTG) family are used [185].

The simulations were performed on a 20 million cells mesh. Five layers of prisms in the near-wall region are present allowing a higher aspect ratio—see Fig. 10.4. The mean y^+ has a value of $\simeq 6.62$ which limits the physical time step to $1.94 \cdot 10^{-8}$ s. In this context, a wall-resolved computation using the WALE [167] model is used to take into account the proper turbulence scaling in the near-wall region. To gather enough

statistics, a simulation time of ~ 4.1 ms was performed. This led to a CPU cost, for a single computation, of ~ 7500 hours lasting ~ 5 hours on a cluster of 1440 cores.

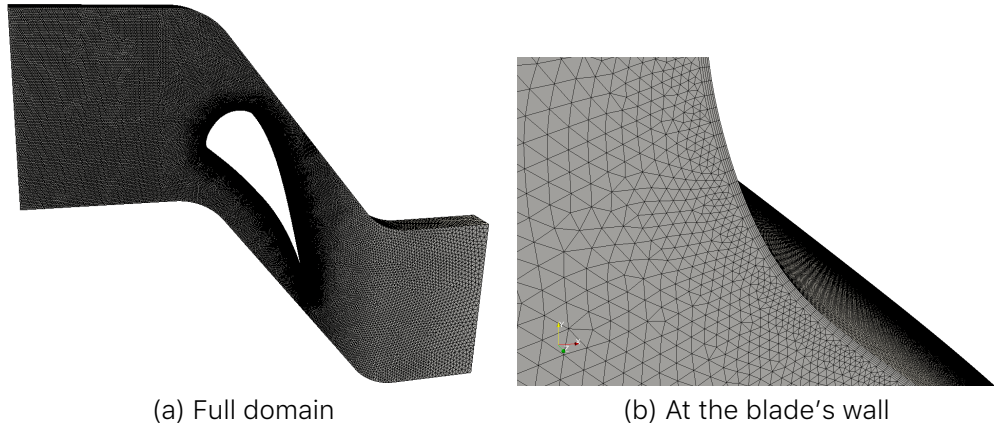


Figure 10.4 – Visualization of the 20 million cells mesh of the domain.

The resolution of the mesh and the LES quality must be guaranteed to be sufficient to capture the complex physics encountered. Indeed, the interaction between the free-stream turbulence and the boundary layer requires to carefully mesh the near-wall region. It is reasonable then to compare the profiles of heat transfer obtained using the mesh for this UQ study, from here on denoted as $M0$, to two finer meshes $M1$ and $M2$, see Fig. 10.5. The corresponding spatial distributions of y^+ are shown in Fig. 10.6 for the three meshes.

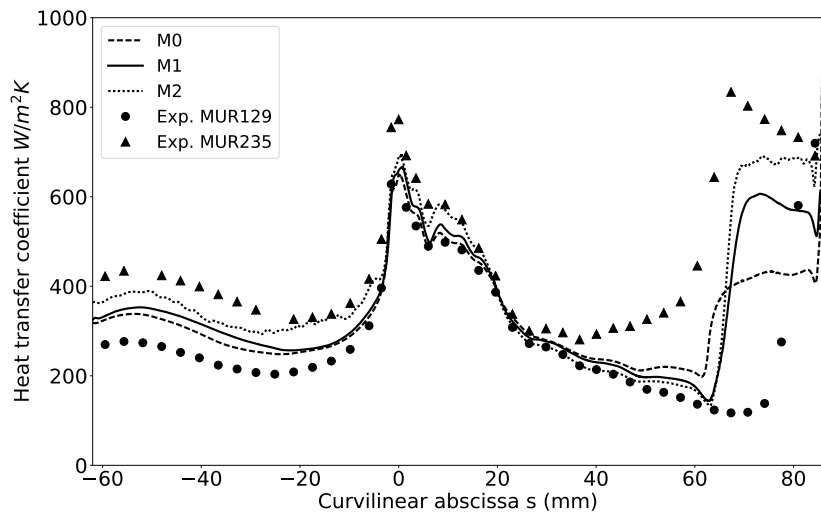


Figure 10.5 – Heat transfer coefficient between various meshes using MUR235 setup ($Tu = 6\%$, $\alpha = 0^\circ$).

The heat transfer coefficient is seen to be different on the pressure side for the finest mesh (M2). However, on the suction side the coarsest mesh (M0) leads to approximately the same results as the finest mesh (M2). This suggests that the value of y^+ does not have a first order

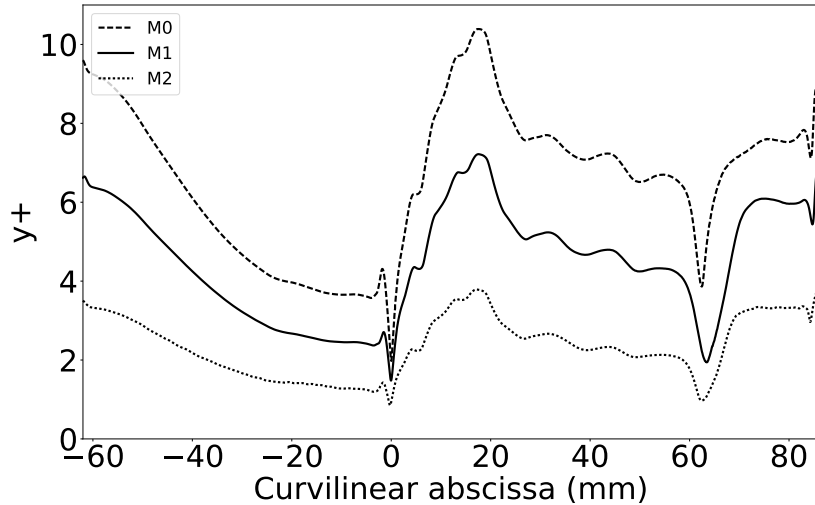


Figure 10.6 – Refinement over blade surface measured using non-dimensional y^+ parameter for MUR235 operating point ($Tu = 6\%$, $\alpha = 0^\circ$).

effect on the heat transfer coefficient for the meshes considered. The sensitivity to other effects such as turbulence intensity and angle of attack may thus be sought. Additionally, it can be noted that the shock wave on the suction side is located at approximately the same position for all meshes. This implies that the upstream boundary layer is similar in all cases although the heat transfer coefficient across the shock wave is affected by the mesh refinement.

10.4 Uncertainty Quantification Results

This section presents the comparison between the different resampling methods (see Chapter 7) on this complex case. In the following, an existing sample comprised of 16 simulations is used to generate a *Sobol'* low-discrepancy sequence. As seen in Section 2.1, the quality of *Sobol'* sequence is similar to *Halton*'s in low dimensional cases. Then a surrogate model based on GP and POD as described in Sections 2.3.1 and 2.3.3 is constructed. Using this initial set of simulations, the sequence has been continued adding 4 points to give a total of 20 simulations. Then using the same initial sample, the previous set is compared to the use of the σ method and the LOO-*Sobol'* method. The LOO- σ method gives similar results compared to LOO-*Sobol'* method. It is not tested on this case. Quality results evaluated by LOO as described in Section 2.3.5 are shown in Table 10.3.

As demonstrated in Appendix A.1, there is no guarantee that the quality of the model improves when using a refinement strategy other than continuing the low discrepancy sequence, given a low-dimensional case. The σ method was only able to improve a little the quality of the initial design. This improvement was inferior to the simple continuation

Method	Number of Simulations	\hat{Q}_2
Sobol'	16	0.638
Sobol'	20	0.821
σ	20	0.688
LOO-Sobol'	20	0.856

Table 10.3 – Estimated Q_2 function of the resampling method compared to an initial sample of 16 simulations.

of the sequence. However, we observed an improved quality using the LOO-Sobol' method. The importance factors' difference between the two input parameters make it feasible to further improve the quality of the model—see Fig. 10.7.

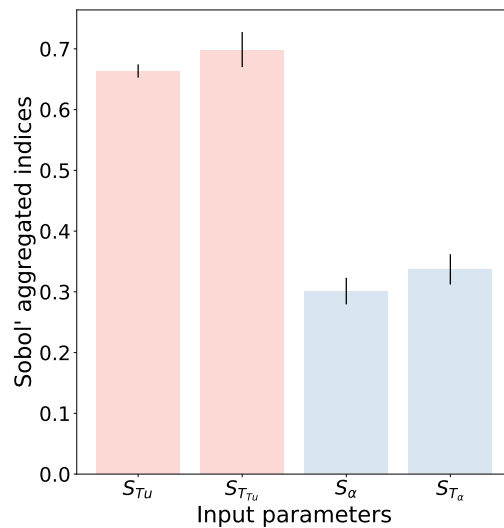


Figure 10.7 – Aggregated Sobol' indices of the input parameters with their asymptotic confidence intervals.

The response surfaces of the models are plotted in Fig. 10.8. The heat transfer coefficient has been integrated over the chord line to obtain this visualization. The first thing to notice is the correct distribution of sample points within the parameter space ensuring that most of the effects are captured. The predictions obtained using the models are then found to be in agreement with the observations made previously. The heat transfer coefficient increases with the turbulence intensity and is fairly stable regarding the angle of the incoming flow. The models are said to be additive with respect to the turbulence intensity. Contrary to the Sobol' sequence, the LOO-Sobol' method detected that the model was sensitive to low values of turbulence intensity. It is this physical information that helped improve the predictivity quality. In the following, the model constructed using the LOO-Sobol' method is used.

Without making any assumption on the uncertainties, the Probability Density Functions (PDF) of the input parameters are both defined using

uniform distributions over the parameter space

$$Tu \sim \mathcal{U}(0, 30\%) \quad \alpha \sim \mathcal{U}(-5, 5^\circ). \quad (10.2)$$

Using these PDFs, uncertainties are propagated by 5 000 predictions of the heat transfer coefficient along the blade. Then the QoI's PDF is reconstructed using a kernel smoothing procedure [231, 95]. Figure 10.9 reveals the expected concerning the propagation of such uncertainties to the heat transfer coefficient. As the two input distributions are uniform and the model is additive, the mean is centred between the extrema. From the experiments—see Fig. 10.3—the envelope of the heat transfer coefficient is correctly captured except after the shock region. Indeed, from past experiences, capturing this region requires a value of $y^+ \sim 1 - 2$ [210].

Finally, the Sobol' indices have been estimated using 200 000 predictions. As the response surface suggested, the heat transfer coefficient is mainly affected by the variation of the turbulence intensity. The spatial evolution of the indices in Fig. 10.10 shows a spatial dependency. On the pressure side, the inflow angle has a higher influence as its contribution rises to become the most important parameter at the trailing edge. On the suction side, the turbulence intensity contribution is stable until the shock region. Reaching the trailing edge, the angle contribution increases. Finally, aggregated indices are reported in Fig. 10.7. These indices confirm that the turbulence intensity is the most important parameter compared to the inflow angle when studying the heat transfer coefficient and for the range of angle variations retained. The turbulence intensity contributes to 70% of the total variance of the QoI whereas the inflow angle contributes to 30%. This behaviour was expected as downstream the shock, the incoming level of turbulence has little impact. The computation of the second order indices are not presented here because their values are negligible in comparison to the first order indices. This is in agreement with the small differences observed between the first and total order indices. There are no joint effects between the two parameters.

10.5 Summary

A first Uncertainty Quantification LES study of the LS89 is presented. The parameter space was comprised of the turbulence intensity and the inflow angle. In order to increase the quality of the surrogate model, the LOO-Sobol' method was used to refine the parameter space. We showed that it performed better than continuing the sampling sequence. Apart from an analysis of the variance, the model was used to propagate uncertainties. This study reveals that although the turbulence intensity is the main factor impacting the heat transfer coefficient, there is spatial evolution of its contribution along the blade.

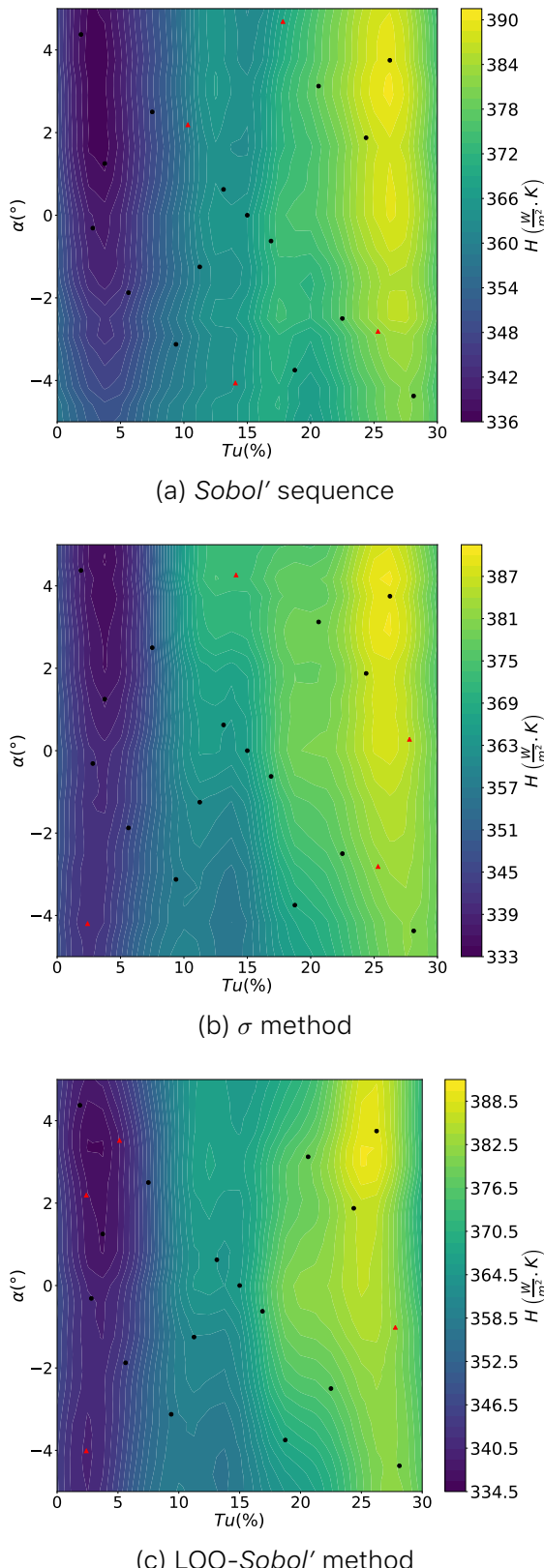


Figure 10.8 – Heat Transfer coefficient response surface. DoE is initially composed of 16 simulations sampled with *Sobol'* sequence. *Black dots* represent the initial LES simulations and *red diamonds* represent the resampled points.

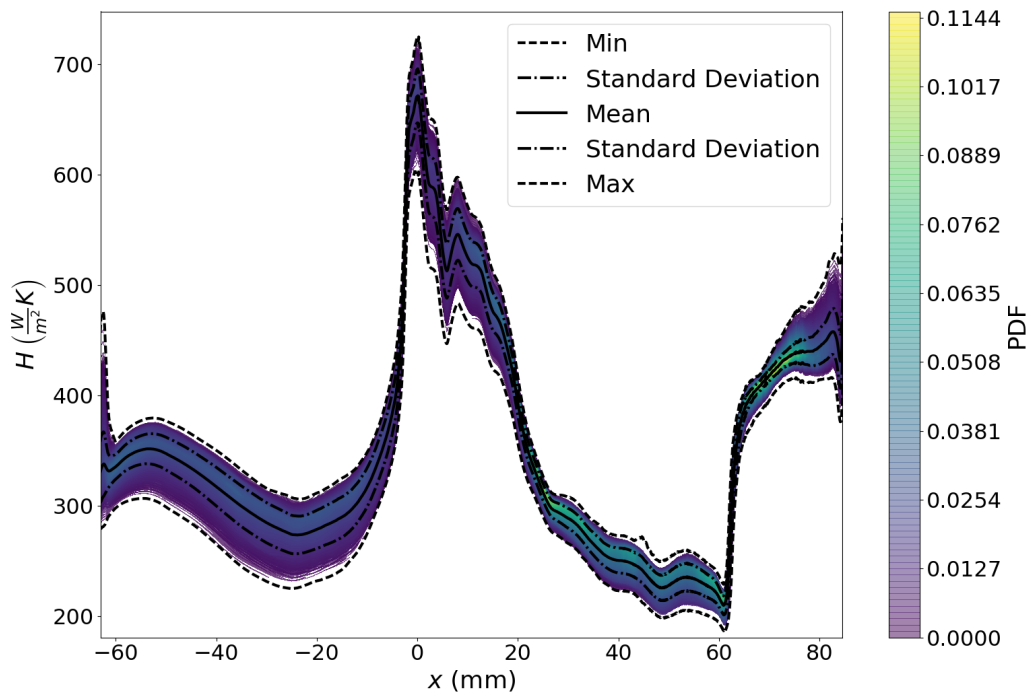


Figure 10.9 – Probability Density Function and moments of the heat transfer coefficient along the chord line of the blade.

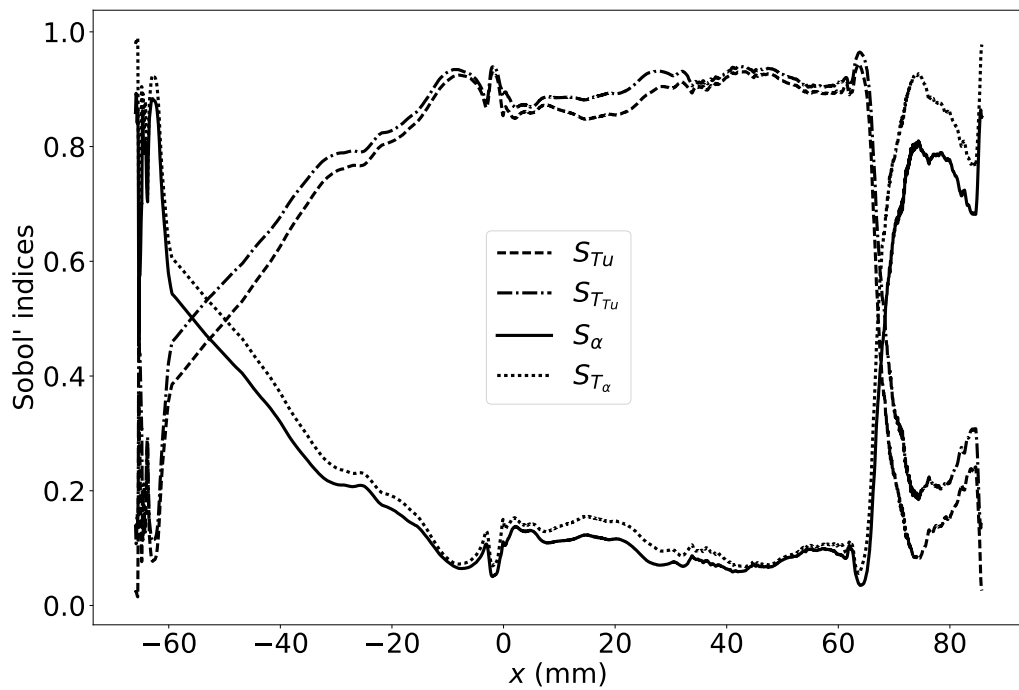


Figure 10.10 – First order and total order Sobol' indices along the chord line.

11 | UQ-Driven Robust Design Assessment of a Swirler Geometry

Pour accompagner le développement de futurs moteurs, les simulations numériques sont devenues des outils de conception fiables et essentiels [197, 77]. Récemment, l'utilisation de SGE couplée à une stratégie d'adaptation du maillage a démontré sa capacité à identifier la physique adéquate des écoulements tourbillonnaires [53].

La conception d'un tourbillonneur se déroule en trois étapes : (i) une phase exploratoire est d'abord réalisée à l'aide de calculs RANS ; (ii) les géométries résultantes sont installées dans la chambre de combustion et simulées en utilisant des SGE de combustion turbulente ; (iii) des prototypes sont fabriqués et des essais sont effectués.

Pour cette dernière étape, la fabrication d'additifs métalliques (AM) [81, 202] est maintenant utilisée. La technologie AM a gagné beaucoup d'attention, car elle n'impose aucune contrainte du point de vue de la conception sans sacrifier les propriétés mécaniques [138]. Cependant, l'AM induit certaines incertitudes quant à la composition structurelle des systèmes métalliques produits, ce qui en fait un sujet de recherche actif.

La présente étude vise à mesurer l'effet de l'AM sur l'écoulement du fluide. Ceci est réalisé par une UQ [108] basée sur des SGE en considérant une géométrie variable. Un POD est d'abord effectué pour construire un espace de paramètres réduit permettant de prendre en compte toutes les variables de conception. Ensuite, ces incertitudes sont propagées au travers de 30 SGE, fournissant des statistiques de synthèse. Cette étude a montré que les tolérances de fabrication pouvaient être réduites à mesure que l'impact de l'AM sur la QoI était comprise. D'un point de vue industriel, une telle analyse peut aider à réduire les coûts si la précision peut être réduite.

Le chapitre est organisé comme suit : Section 11.2 présente la configuration étudiée ainsi que la configuration numérique LES. Section 11.3 détaille la méthodologie utilisée pour réduire l'espace des paramètres. Les résultats de l'étude de l'UQ sont ensuite présentés et analysés respectivement dans les sections 11.4 et 11.5.

11.1 Introduction

AT THE HEART of a turbomachine is the combustion chamber, fed with fuel by injectors. Here, the combustion process releases the calorific capacity of the fuel mixture. This process is usually started using a spark which provides an energy deposit in the system. After the flame has been ignited, it needs a mechanism for it to stabilize within the chamber. Depending on the velocity of the laminar flame speed and on the power required, different devices are to be considered to stabilize a flame. Indeed, the output power being directly linked to the inlet velocity of the reactants, if a high power is required, the inlet velocity will be high. Thus, to stabilize the flame ones needs to equilibrate the consumption of the reactants accordingly to the flame speed. The flame stabilization is a major concern which can cause an extinction of the chamber or an oscillation of the flame.

When considering small velocities, a backward facing step is sufficient—see Fig. 11.1. This geometry creates a recirculation zone that traps the fuel mixture downward. However, as the inlet velocity increases, the flame speed does not. The chemistry not being infinitely fast, comes a point where the flame cannot sustain. Swirled injectors have been designed to overcome this issue [142]—see Fig. 11.2. By impinging a movement of rotation on the flow, a recirculation zone is created directly at the outlet of the injector. This ensures sufficient residence time for the fuel to be consumed. The design of swirled injectors is of prime importance when seeking to reduce fuel consumption and pollutant emissions. Indeed, this is usually achieved via lean combustion which may lead to combustion instabilities and reduced extinction margins. When considering environmental aspects, operability, efficiency, maintenance or even durability, the problem becomes a complex multiobjective optimization problem which remains a great challenge.

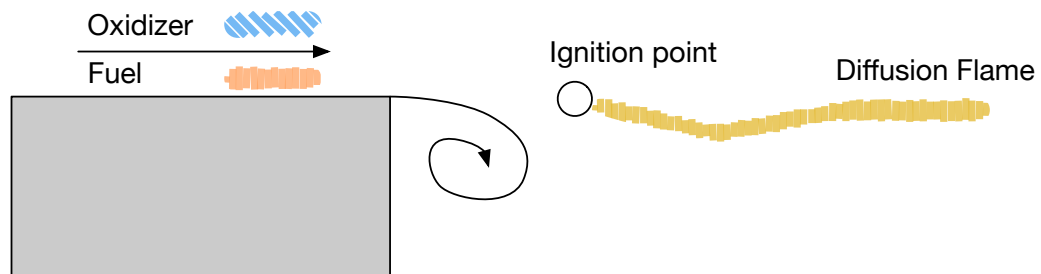


Figure 11.1 – Sketch of a backward facing step.

To help in the development of future engines, numerical simulations—and here CFD simulations—have undoubtedly become reliable and essential design tools [197, 77]. Recently, the use of LES coupled with a mesh adaptation strategy has demonstrated its capacity to identify the relevant physics of swirling flows [53]. From expert knowledge, the design of a swirlor proceeds in three steps: (i) an exploratory phase

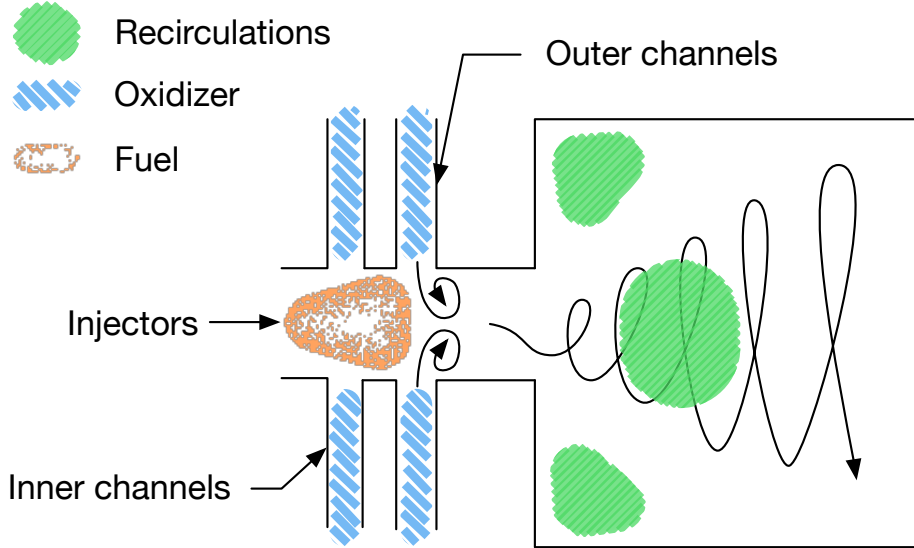


Figure 11.2 – Sketch of a swirler consisting of two contra-rotative sets of oxidizer channels.

is first performed using RANS computations; (ii) the resulting possible geometries installed in the combustion chamber are simulated using LES of turbulent combustion; (iii) prototypes are manufactured and tests are performed. The first step allows exploring a large range of possibilities in terms of geometrical modifications (angles, number of channels, etc.) to meet requirements such as the swirl number, effective surface and permeability. The second step is performed to assess the combustion stability and the combustor performances in various operating conditions. Finally, experiments are conducted to finalize the design.

For this last step, metal Additive Manufacturing (AM) [81, 202] is now in use. The AM technology has gained a lot of attention as it does not impose any constraint from the design point of view without sacrificing mechanical properties [138]. However, AM induces some uncertainties regarding the structural composition of the produced metallic systems, making this an active topic of research. In particular, geometrical uncertainties may result from the deposition method, the scanning method or even the powder size. Moreover, due to the complexity of some designs, it might not be possible to polish surfaces using standard mills. This may leave some defects which size depends on the quality of the whole process.

The present study aims to measure the effect of AM on the fluid motion. This is achieved through UQ [108] based on LES with varying geometry. A POD is first performed to build a reduced parameter space allowing taking into account all design variables. Then, uncertainties on the design variables are propagated in a series of 30 LES, providing summary statistics.

The chapter is organized as follows: Section 11.2 presents the studied

configuration as well as the LES numerical setup. Section 11.3 details the methodology used to reduce the parameter space. Results of the UQ study are then presented and analysed in Section 11.4 and Section 11.5, respectively.

11.2 Configuration and Numerical Setup

11.2.1 The Swirled Injector

Figure 11.3 presents a sketch of the swirler studied in this work (also described in [53]) together with the computational domain. The swirler consists of two counter-rotating stages of 8 tangential vanes resulting in a rotational flow. A recirculation zone appears just downstream the swirler, which is paramount to combustion stability. In this study, no fuel is injected.

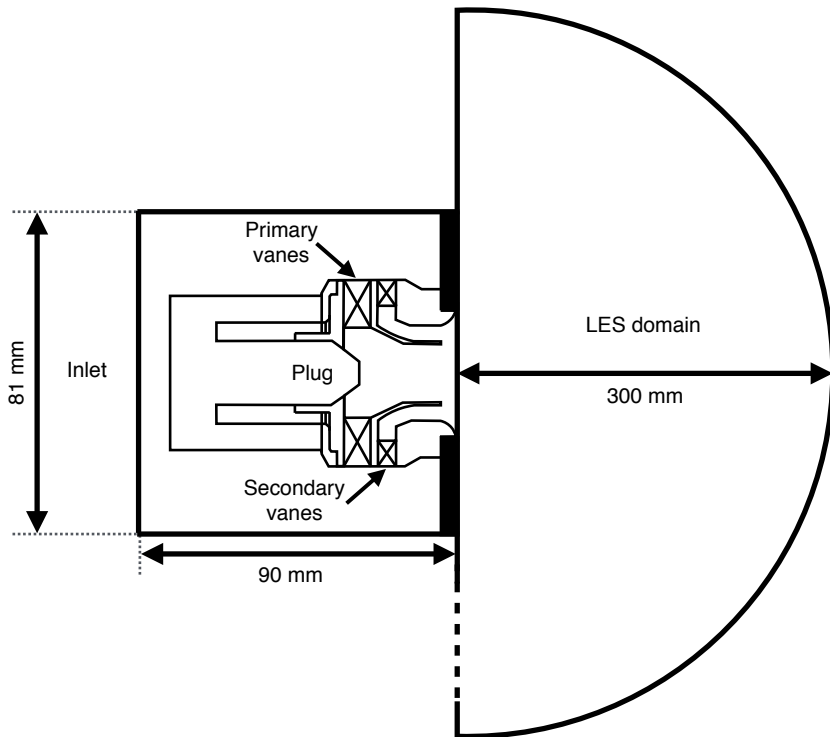


Figure 11.3 – Schematic view of the configuration and the LES computational domain.

11.2.2 Numerical Setup

All simulations were performed using the compressible Navier-Stokes solver AVBP [206]. The finite-element scheme TTGC [48] was used on a tetrahedral mesh and LES equations were closed using the σ -model [166]. At the inlet and outlet boundaries Navier-Stokes Characteristic Boundary Conditions (NSCBC) were applied [181], imposing

the mass flow rates and the pressure, respectively. All wall boundary conditions were specified as wall no-slip conditions without wall law models.

11.2.2.1 Mesh Adaptation Strategy

Due to the relative complexity of the geometry and the resulting mesh size, an Adaptive Mesh Refinement (AMR) strategy was used to reduce the CPU cost while preserving the quality of the solution, evaluated with the global pressure loss ΔP . The AMR strategy used in this study is based on the methodology proposed in [53]: from the result obtained on an initial arbitrary mesh, a metric based on the time-averaged viscous dissipation field $\overline{\Phi}$ is computed as:

$$\overline{\Phi} = (\mu + \mu_t) \left(\frac{\partial u_i}{\partial x_j} + \frac{\partial u_j}{\partial x_i} \right)^2, \quad (11.1)$$

where μ is the molecular viscosity and μ_t the turbulent viscosity.

Then the mesh of the computational domain is adapted using the MMG3D library [52] (noted AD1). This procedure is repeated with a second adaptation (noted AD2), so that the experimental pressure loss ΔP is recovered (see Fig. 11.4). The computational details of one adaptation run are summarized in Table 11.1. In the end, with two mesh adaptation steps, one run required 25 000 CPU hours to simulate 40 ms of physical time.

Table 11.1 – Summary of mesh adaptation for one simulation. Physical simulation time is constant at 40 ms.

	Coarse	AD1	AD2
number of cells ($\times 10^6$)	1.6	4.1	12.8
time step ($\times 10^{-7}$ s)	0.59	0.47	0.20
CPU hours	5h30	2h20	9h30
number of cores	560	2800	2800
ΔP relative error	57,8 %	6,5 %	4,8 %

As shown in [53], this method converges and finally recovers the physics with a limited error on the pressure loss ($\sim 5\%$). This is obtained thanks to the choice of the viscous dissipation—which controls the irreversible losses—as the refinement metric. From Fig. 11.5 showing the evolution of the mesh, it appears that the mesh has mostly been refined around the plug tip and at the swirler exit. These zones indeed correspond to the zones where the dissipation is highest as seen in Fig. 11.6. This result also indicates that any geometrical deviation in these zones may result in a modified pressure loss.

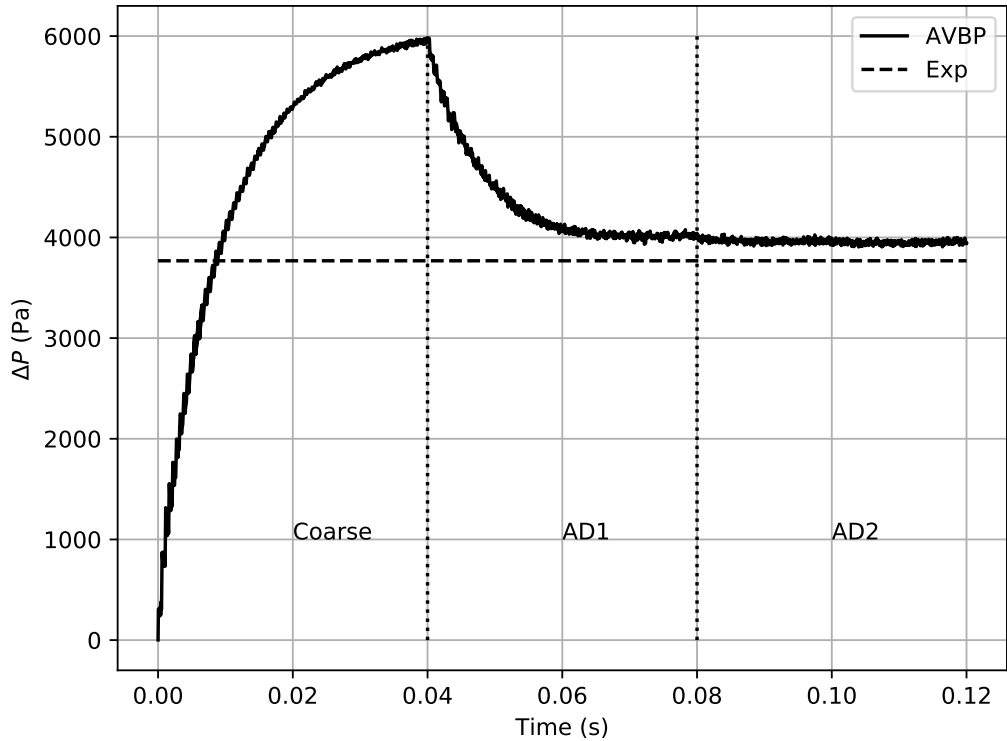


Figure 11.4 – Evolution of the pressure loss computed with LES on the three different meshes successively with increasing resolution: *Coarse*, *AD1* and *AD2*. The dash line represents the experimental value of ΔP .

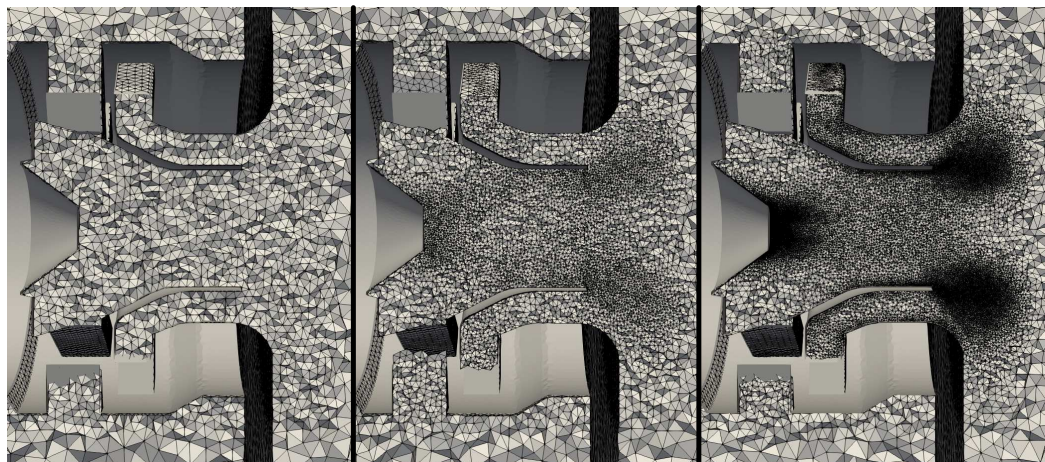


Figure 11.5 – From left to right: coarse mesh, first adaptation *AD1* and second adaptation *AD2*.

11.2.2.2 Simulation Strategy for UQ

In order to quantify the uncertainty on the flow physics, a sample of 30 LES was considered. The procedure used to generate this sample is detailed in Section 11.3. For each simulation, a new geometry has been constructed with up to 2% of variation in all channel dimensions—using the method presented in Section 11.3. Then, the mesh was automatically

adapted using the aforementioned methodology. This procedure ensures that the meshes are optimum for each configuration, with respect to the pressure loss. For the uncertainty analysis, results were averaged over 40 ms. The total computational cost for this UQ using LES is about 1 000 000 CPU hours. Thanks to high performance computing resources, the return time was only 2 days, which is satisfactory in the context of an industrial design process. Batman (Chapter 5) was used to handle all simulations and perform the UQ.

11.2.3 Geometrical Uncertainties of the Swirler

Discrepancies in the size of the channels generated by AM have been measured. Figures 11.6 and 11.7 illustrate how a change of $\sim 2\%$ in all channel dimensions—due to manufacturing dispersion—impacts the flow and the pressure loss ΔP . The two cases correspond to the maximum (case a) and minimum (case b) impact on the pressure loss. These results were obtained from LES and the numerical setup described in Section 11.2.2. Figure 11.6 shows the difference in total dissipation field $\bar{\Phi}$, which explains the difference in pressure drop. Compared to the pressure drop in the reference geometry, the two cases show a difference of 7.83% and 9.95% respectively for Fig. 11.6(a) and Fig. 11.6(b). A closer look allows identifying the main region of difference at the tip of the plug, directly related to the flow difference in the first stage of the swirler, as seen in Figs. 11.7 and 11.8. Indeed, a small recirculation zone (at the tip of the plug) appears in the left case (a), which almost disappears in the right case (b).

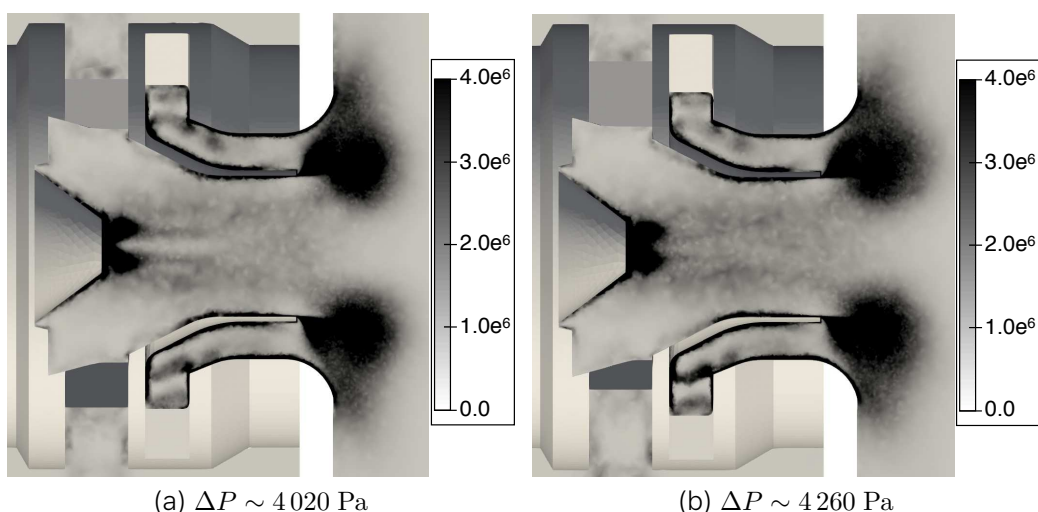


Figure 11.6 – Fields of mean kinetic energy dissipation (W/m^3) for two geometries with $\sim 2\%$ channel size difference with the reference case.

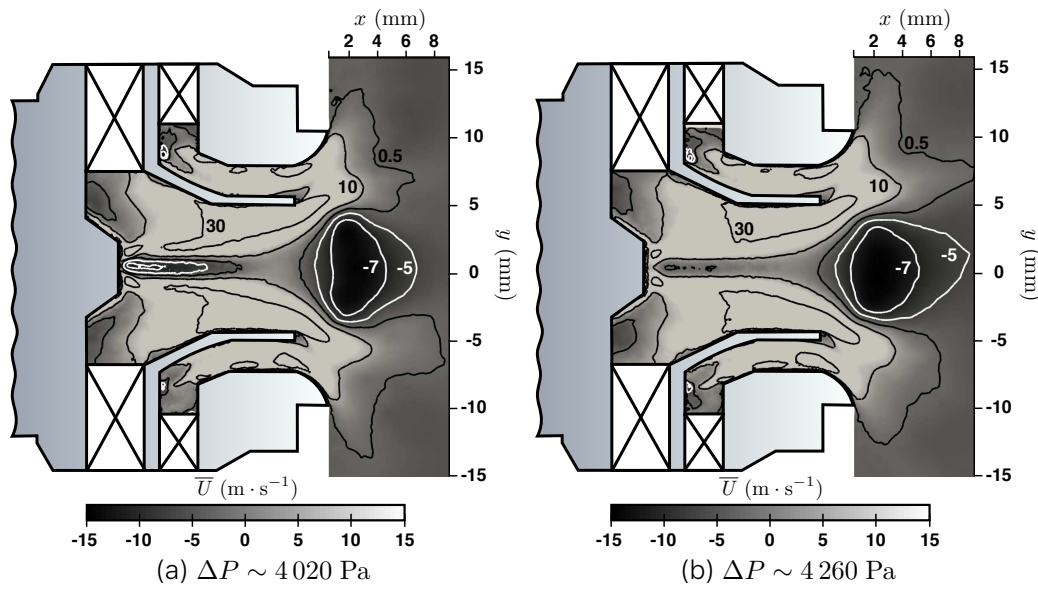


Figure 11.7 – Field of mean axial velocity for two geometries with $\sim 2\%$ channel size difference with the reference case. *Black* isocontours denote positive velocity, while *white* isocontours denote negative velocity.

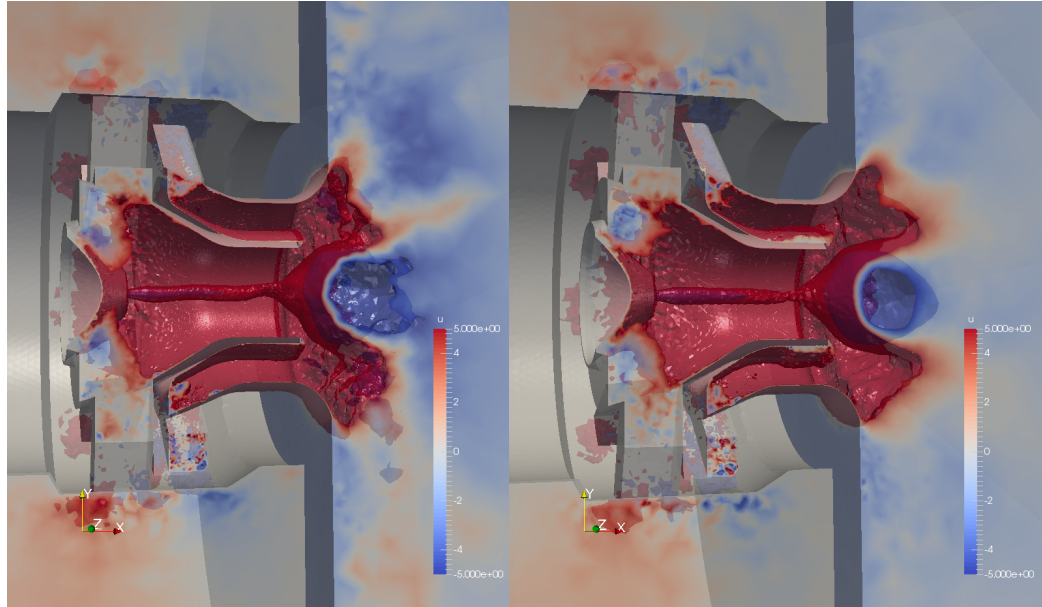


Figure 11.8 – Q-criterion coloured by mean axial velocity for two geometries with $\sim 2\%$ channel size difference with the reference case. *Left* $\Delta P \sim 4020 \text{ Pa}$, *right* $\Delta P \sim 4260 \text{ Pa}$.

11.3 Dimensionality Reduction and Statistical Analysis of Uncertain Parameters

Performing a UQ study requires a large number of numerical simulations in order to converge statistical moments. If the number of parameters is

also large, an even larger number of samples is required. In the present case (Section 11.2), the uncertain parameters are the dimensions of all 16 channels. For each channel, this parameter induces a modification of the cross section area. However the channel dimensions, resulting from AM, are not independent and the number of independent parameters can be reduced. Indeed, AM is a layer-by-layer process which precision relies on the ability of the machine to build up and polish these layers. All channels of one stage being built simultaneously, a systematic bias is introduced.

A set of 5 various real swirler geometries issued from AM was obtained from an engine manufacturer. Thanks to the layering process, two groups of channels are considered to separate the two stages: (i) the inner set (first stage) of channels is noted $s = \text{in}$, and (ii) the outer set (second stage) of channels is noted $s = \text{ou}$. Data of each of these two groups is aggregated in the form of a function: $d_s(i)$ with d the channel dimension, i the channel number and the subscript s standing for the inner or the outer set.

The dataset is then represented as a matrix, each line containing the curve $d_s(i)$ corresponding to each channel geometry. In order to reveal the correlations in the data and reduce the number of parameters for the UQ study, this matrix is decomposed using a POD, which allows representing data with a finite number of modes. This compression process turns the functional representation into a scalar representation in a reduced space. The retained variance from the initial data increases with the number of modes of the POD. In this work, more than 90% of the original dataset variance is retained with only three POD components per stage, as shown in Fig. 11.9. The 16 independent uncertain parameters are then reduced to 6 independent parameters (three for each stage), while still accounting for 90% of the total variance of the original dataset.

Within the reduced space of POD components noted \mathbf{x}_r , the Highest Density Region (HDR) boxplot method is used to summarize the data statistics and infer new swirler geometries—see Section 2.4.1. In the original space the median curve corresponds to the most probable set of values that defines a swirler geometry manufactured with AM, while the 50% and 90% HDR express the data dispersion. The PDF estimator and the HDR allow inferring new realizations that are statistically relevant to the original dataset and can be used for the UQ analysis. This is done in the next section.

11.4 Generation of Datasets

In the 3 POD-components space defined from the experimental database, a set of 30 points was sampled from a low discrepancy sequence of Sobol' (scrambled) [41, 127] which ensures a good coverage of low-dimensional parameter spaces. The 30 points are plotted in Figure 11.10 in 2D cuts of the 3D parameter space of each swirler stage.

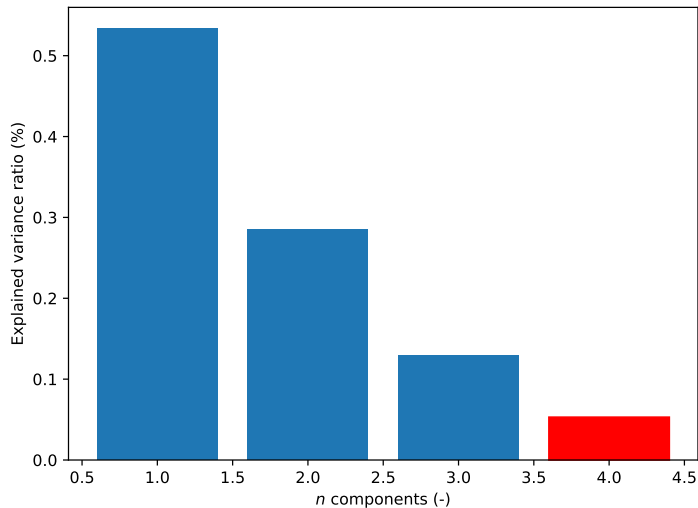


Figure 11.9 – Contribution to the explained variance of the first four modes for the outer channels (similar results for inner channels are not shown). Summing the first three modes only (in blue) and ignoring the fourth mode (in red) corresponds to more than 90 % of the variance of the original dataset.

The PDF estimators obtained for each POD component are shown in the plots placed along the diagonal of the figure.

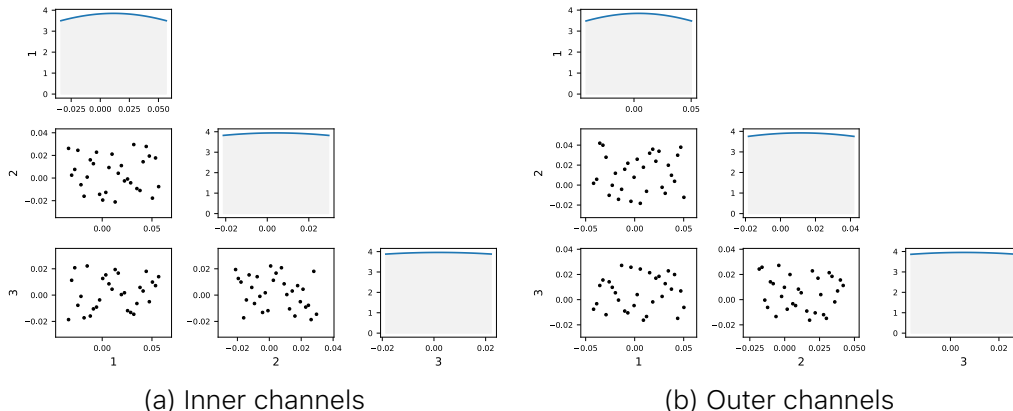


Figure 11.10 – Bivariate principal component score plots of the 30 generated samples in the reduced POD parameter spaces of the inner and outer stages. Each point corresponds to a curve sample. Probability distributions for each component are shown in the diagonal plots: *lines* represent the kernel PDF estimator and *Shaded areas* are histograms (from which are based the scaling of the y-axis).

Figure 11.11 shows the 30 curves in the initial parameter space (channel dimensions) corresponding to the inverse transform of the 30 generated datasets. It can be noted that 30 curves are well distributed around the median line, inside the 90% HDR, confirming that the sampling is

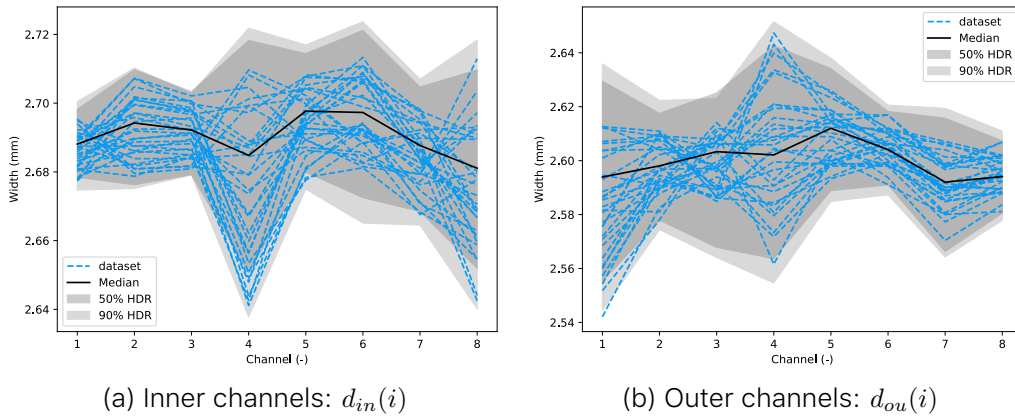


Figure 11.11 – Statistics of channel dimensions: median curve (***bold solid*** line) and 50% and 90% HDR (***shaded*** areas). Blue ***dashed*** lines represent the 30 generated samples.

statistically relevant to the original dataset. Thus this method is able to reproduce statistically relevant scenarios of swirl geometry.

The number of samples was chosen to minimize the computational time (see Section 11.2). From [76], it should be at least $10n_{dim}$, with n_{dim} the number of parameters, leading in our case to 60 samples. However, as we are interested in small variations in the parameter space the variation of the quantity of interest (pressure loss) is not expected to require as many samples and it can be said with confidence that 30 simulations are enough to describe it.

A larger initial database could reveal even more correlations between the parameters, allowing to further reduce the number of parameters. With the 5 datasets used here, a large dispersion of the different realizations is observed in Fig. 11.11 and there is no room for more reduction. Still, it is clear that the 16 initial parameters of the 5 datasets are not independent, which is essential for the current study as keeping all 16 parameters independently would have required a huge number of simulations.

11.5 Results and Discussion

Figure 11.12 shows the evolution of the pressure loss by varying the channel dimensions. As the design of experiments consists of 6 parameters, the response is presented in a 2-dimensional plot where the first modes of both inner and outer channels are used. Indeed the first modes contribute the most to the variance of the data. In Fig. 11.12 no cluster of points appears at any particular level of pressure drop and the pressure loss distribution is relatively uniform among the samples. Summary statistics are presented in Table 11.2 and the probability distribution of the ensemble is shown in Fig. 11.13. All these results indicate that the response of the system to these geometrical modifications is

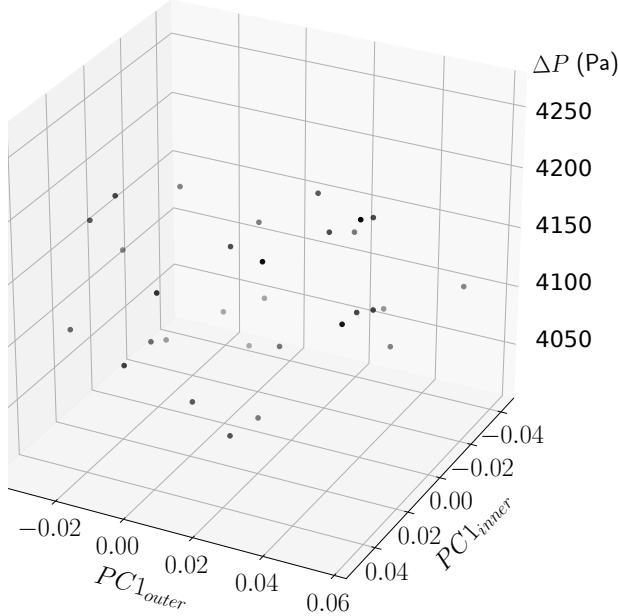


Figure 11.12 – Pressure loss function of the first components of the reduced space.

rather uniform: the geometrical uncertainties are transmitted through the system without amplification.

Table 11.2 – Summary statistics of the pressure drop of the 30 LES.

	Mean	Median	Std	Min	Max
Pressure drop (Pa)	4128	4133	65	4020	4260

As a consequence of this uniformity with no clear structure, it is difficult to build a reduced model. Several surrogate model strategies available in BATMAN—see Section 11.2—such as Gaussian process, polynomial chaos and Radial Basis Functions were tested, but none of these methods were able to fit the data and infer a satisfactory result. The reported quality—assessed by Leave-one-out cross validation [123]—was negative, which implies that the tested surrogate models are worse than a simple constant guess.

To further analyse the results, Fig. 11.14 shows the variation of the pressure loss with the total channel section area for each simulation. Again no clear pattern is making out. The swirl numbers—definition from Merkle [159]—for cases with maximum, minimum and middle value of pressure drop are summarized in Table 11.3. It is interesting to see that despite pressure drop variation, the swirl number which drives the characteristics of the flow stays within negligible variation close to the theoretical value of $S = 0.76$ in all three cases. These observations are confirmed by the comparison of the mean axial velocity profiles

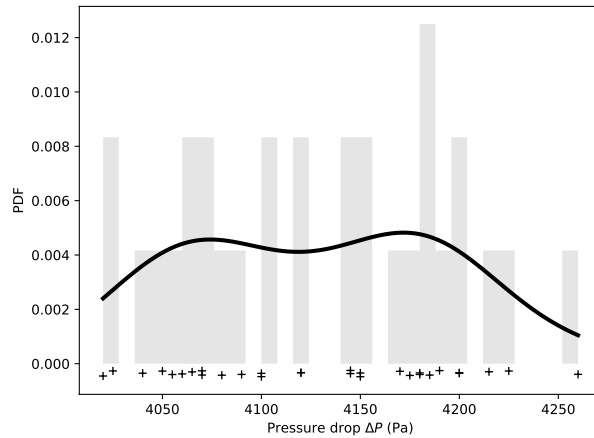


Figure 11.13 – PDF of the pressure loss over the dataset (black line) reconstructed using KDE. Crosses represent the samples, and the shaded area is a histogram view.

downstream the nozzle exit compared with PIV measurement for the same three cases (Fig. 11.15). Details and discussion about PIV are given in Daviller *et al.* [53]. Very close curves are obtained for the three LES at the shown positions. This means that, in accordance with the unchanged swirl number, no significant change occurs in the flow field downstream the nozzle. This is confirmed by the PSD of mean axial velocity at the plug tip in Fig. 11.16. Each simulation exhibit a $k^{-5/3}$ slope over a range of frequency $5 \cdot 10^3 \leq f(\text{Hz}) \leq 5 \cdot 10^4$, characteristic of the inertial range of turbulent flows.

All in all, it ensures that the flame will be stable even though there is a change in pressure loss.

Table 11.3 – Swirl numbers for three different geometries.

	$\Delta P_{middle} = 4\,145 \text{ Pa}$	$\Delta P_{min} = 4\,020 \text{ Pa}$	$\Delta P_{max} = 4\,260 \text{ Pa}$
Swirl number	0.7609	0.7582	0.7639

Although the construction of a surrogate model is not feasible in this case, the present uncertainty analysis highlights the intrinsic and chaotic variability of a self-compensation mechanism in the generated statistical data. This can be explained by: (i) the nature of the geometrical modifications, where some channels are widened while others are tightened, limiting the overall impact on the pressure loss; and (ii) the amplitude of these modifications which is very small compared to the width of the channels. Indeed, manufacturing defects were limited to a maximum 2% of the cross section area of a channel, consistently with real observation of AM. Note that in such situation, the ability of the solver to respond with the correctly adapted physics is paramount. To check this, the relative numerical error on the pressure drop was estimated and found less than 1% which is sufficient to capture with ac-

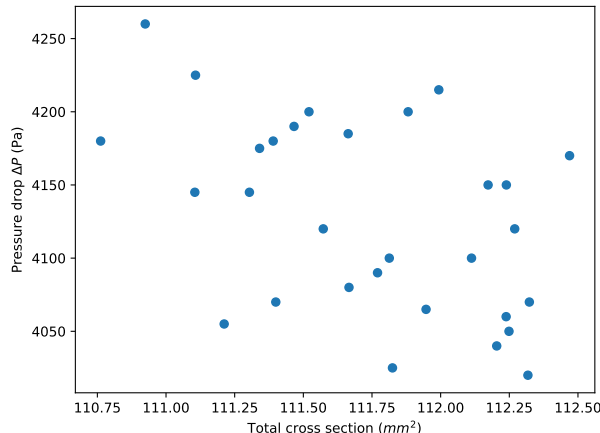


Figure 11.14 – Pressure drop as a function of the total cross section channel area. Each point represents a sample.

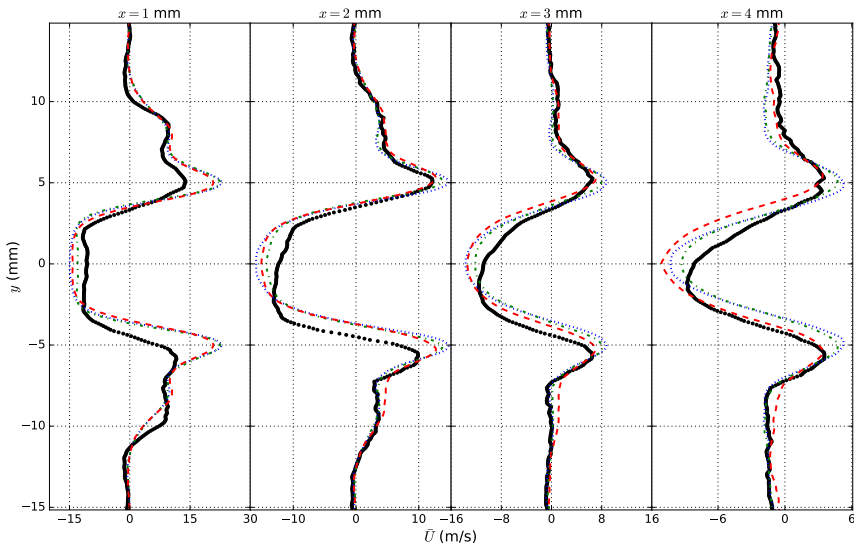


Figure 11.15 – Mean axial velocity profiles at four axial locations (from left to right $x = 1, 2, 3, 4 \text{ mm}$) obtained with LES and in the experimental setup (black circles). Dotted lines $\Delta P_{middle} = 4145 \text{ Pa}$, dashed-dotted lines $\Delta P_{min} = 4020 \text{ Pa}$, dashed lines $\Delta P_{max} = 4260 \text{ Pa}$.

curacy the pressure drop induced variation by geometrical modification of the order of $\simeq 5\%$. Thus, the solver accuracy is sufficient and the results are considered reliable.

11.6 Summary

The purpose of this work was to perform an Uncertainty Quantification (UQ) study of a swirl geometry. More precisely, this study focused on geometry deviations due to Additive Manufacturing (AM) and their

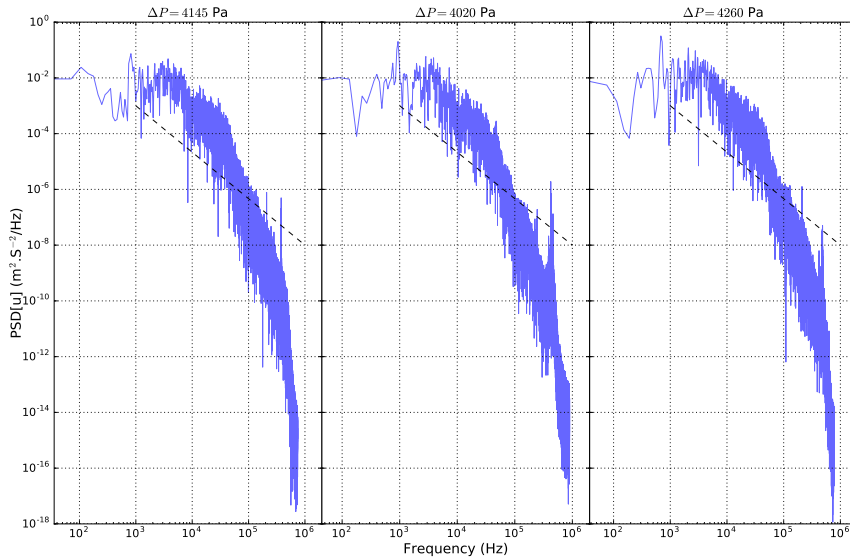


Figure 11.16 – Power spectral density of axial velocity fluctuations for three different geometries at the plug tip.

effects on the pressure loss. As the number of parameters required to characterize the configuration was high, a Principal Component Analysis (POD) was used, allowing to cut down the number of parameters from 16 to 6 independent variables. Statistic analysis based on Highest Density Region (HDR) highlighted the non-independence of the geometrical parameters and thus the impact of AM. Thanks to a mesh adaptation strategy, a set of 30 different statistically representative cases was accurately simulated with Large Eddy Simulations (LES). The uncertainty analysis then led to an overall view of the variation of the pressure drop induced by geometry changes. Results show that slight discrepancies in the swirler channel dimensions lead to slight differences in the pressure loss, without amplification or damping. This conclusion also holds for the flow, as shown by the comparison of the swirl numbers and velocity profiles. This is a critical information for engine manufacturers, as it means that AM will not affect the flow exiting the swirler and the stability of the flame developing downstream.

The analysis of the intrinsic variability of the system did not exhibit any noticeable pattern. As a consequence, no surrogate model could be built. This is explained by the nature of the modifications and most importantly by their amplitude. Augmenting the range of variability in the system, exploring for example other designs, would increase the impact on the pressure loss.

The UQ method used in this work, combining data reduction and high-fidelity LES, paves the way for systematic uncertainty studies in the design phase of industrial systems to take into account manufacturing defects. This may lead to the determination of optimized manufacturing tolerances, and finally to significant cost saving.

12 | Optimization of Helically Roughened Heat Exchanger

L'augmentation artificielle de la rugosité des surfaces internes des échangeurs de chaleur est une méthode passive et efficace pour améliorer l'efficacité du transfert de chaleur, ce qui a conduit à de nombreuses conceptions. Le choix d'une forme de rugosité spécifique dépend du régime d'écoulement, des propriétés du fluide et peut dépendre de l'application du dispositif. Mais ce procédé induit toujours une augmentation de la perte de charge qui nuit à l'efficacité globale de l'échangeur de chaleur et doit être limitée.

En raison de la grande variété de formes de rugosité possibles, toutes les géométries ne peuvent pas être testées expérimentalement ou numériquement et les formes de rugosité optimales pour les échangeurs de chaleur restent inconnues à ce jour. L'objectif de ce travail est de trouver une forme de rugosité optimale pour les applications d'échangeurs de chaleur industriels. Des séries de SGE sont utilisées pour construire un modèle de substitution (GP) fiable représentatif de l'efficacité de l'échangeur de chaleur pour différentes formes de rugosité. Ce modèle de substitution a permis de prédire une conception optimale, ce qui permet de comprendre le comportement complexe de l'écoulement aboutissant à un important transfert thermique et à une perte de pression limitée. L'une des principales conclusions de cette analyse est que l'effet d'interaction entre le pas des nervures et le rapport de séparation entre celles-ci est important.

Le chapitre est conçu comme suit : Section 12.2 présente la méthodologie numérique utilisée pour la simulation de l'écoulement turbulent chauffé. En particulier, la géométrie de la surface interne du tube, la méthode de maillage, les équations gouvernantes et la fonction objective à optimiser sont présentées. Après cette présentation méthodologique, Section 12.3 présente les résultats de la procédure d'optimisation conduisant à une première géométrie de tube à nervures discontinues optimale, et étudie plus en détail la dynamique d'écoulement et le comportement thermique à l'intérieur. Enfin, Section 12.4 résumant la contribution ainsi que les orientations possibles de ce travail.

12.1 Introduction

ARTIFICIALLY increasing the roughness of heat exchanger inner surfaces is a passive and efficient method to improve the heat transfer efficiency, which has led to numerous internal designs. The choice of a specific roughness design depends on the flow regime, the fluid properties and might depend on the device application. This method however always induces an increase in pressure loss which is detrimental to the heat exchanger global efficiency and needs to be limited.

In this context, numerous experimental studies have investigated various turbulence promoter geometries, such as transverse ribs [234, 19] or helical ribs [84, 226, 43, 157]. More complex three-dimensional geometries were also investigated such as dimpled tubes [227]. Garcia et al. [82] compared the behaviour of corrugated tubes, dimpled tubes and wire coils, concluding to a larger impact of the internal geometry on the pressure drop than on the heat transfer. They also highlighted that better efficiencies are reached with helically corrugated tubes and dimpled coils for Reynolds number greater than 2000, which are geometries comparable to helically continuous and discontinuous ribbed tubes respectively. This result motivates further investigation on the optimal discontinuous helical rib shape in the current work. Based on those studies, empirical correlations for the prediction of friction and heat transfer efficiency in roughened heat exchangers can be found in the literature. In particular, correlations for simple, 2D roughness geometries such as transverse ribs or helical ribs predict quite accurately the heat exchanger efficiencies in a specific range of operating conditions and fluid properties thanks to numerous experimental investigations. However, because of the very wide possible roughness shapes, operating conditions and fluid properties, empirical correlations are not reliable enough to give the best suited heat exchanger geometry given a specific industrial application, or might be non-existent when considering complex 3D roughness shapes such as helically discontinuous ribs.

Numerical simulations of roughened heated tubes is a less expensive alternative for the investigation of heat exchanger efficiencies. Reynolds-Averaged Navier-Stokes (RANS) simulations are heavily used for this purpose, and various simulations of ribbed tubes can be found in the literature [144, 213, 146, 169, 103, 143, 121, 120, 194, 195, 116, 66, 16, 149]. Recently, Large Eddy Simulations (LES) have been introduced for the simulation of ribbed heat exchangers [113, 229, 228, 241, 39]. Being more predictive than RANS, LES appears as a more reliable tool for the investigation of pressure loss and heat transfer in a heat exchanger.

Because of the wide variety of possible roughness shapes, all geometries cannot be experimentally or numerically tested and optimal roughness shapes for heat exchangers remain unknown to this day. The objective of this work is to find an optimal roughness shape for industrial

heat exchangers applications. Series of LES are used in addition to Gaussian Process regression [188] to construct a reliable surrogate model representative of the heat exchanger efficiency for various roughness shapes. This surrogate model lead to the prediction of an optimal design, which enables to understand the complex flow behaviour resulting in important heat transfer and limited pressure loss.

The chapter is tailored as follows; Section 12.2 starts with a presentation of the numerical methodology used for the simulation of turbulent heated flow inside various internally ribbed heat exchanger. In particular, the tube inner surface geometry, the meshing method, the governing equations and the objective function to optimize are presented. After this methodological presentation, Section 12.3 presents the results of the optimization procedure leading to a first optimal discontinuously ribbed tube geometry, and investigates more in detail the flow dynamics and the thermal behaviour inside it. Finally, Section 12.4 put a closure to this work by summarizing its contribution along with potential directions for future works or applications.

12.2 Case Description

12.2.1 Geometrical and Meshing Considerations

Simulated reactors are tubular geometries, with a single-started helical rib added on the inner surface which constitutes the artificial roughness responsible for the heat transfer enhancement. Figure 12.1 represents an example of simulated ribbed reactor geometry. For comparison purpose, all reactors have an identical diameter $D = 38.1$ mm. The rib has a rounded shape, illustrated on Fig. 12.2, with a floor width w equal to 3.2864 times the rib height e , so $w = 3.2864 \times e$. The rib cross-section is then fully characterized only by its height e . In addition to e , an important geometrical parameter for the rib shape is the rib pitch p . Both e and p are uncertain geometrical parameters for the optimization process. Note that in this study the pitch-to-height ratio p/e always remains larger than 8. All ribbed reactor geometries then belong to the K-type roughness ($p/e > 4$) following the classification introduced in [110, 165]. K-type roughness is known to greatly affect the bulk flow and enhance heat transfer. As stated by Perry [176], K-type roughness opposes to D-type roughness ($p/e < 4$) for which the ribs are so closely spaced that the eddy shedding from the roughness element has little impact on the bulk flow, which decreases heat transfer. As highlighted by the experimental work of Ravigururajan et al. [189], the shape of the rib cross-section only has little influence on the heat transfer enhancement compared to its height and pitch, justifying a constant rounded shape in the current work. Discontinuities are included in the rib as a geometrical parameter to optimize. Size and positions of the rib discontinuities are fully characterized by the number of discontinuities per rib pitch N_D and

the length of the discontinuity relative to the length of the remaining rib, called the emptiness ratio E_r . N_D and E_r are also uncertain geometrical parameters to optimize, making the total number of input geometrical parameters to optimize equal to 4.



Figure 12.1 – Geometry of an helically ribbed tube reactor. 3 pitches are represented.

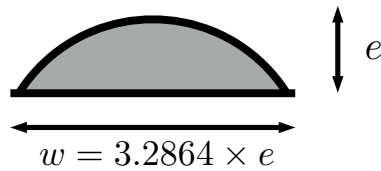


Figure 12.2 – Illustration of the rounded rib cross-section.

The computational domains consist in one pitch long periodic tubes, as periodic tubes have been used for long to study steady turbulent flows and proved to give accurate results [193, 122, 111], including for helically ribbed tubes [39]. Previous works on helically ribbed tubes using periodic conditions [241, 39] showed that the result does not depend on the number of periodic patterns that are computed, as turbulent structures are always found smaller than the rib pitch, even for smaller pitch-to-diameter ratios p/D than studied in the current work. Following the numerical methodology validated by Campet et al. [39] for steady turbulent flows in similar geometries, the meshes are fully unstructured and constituted of tetrahedral cells. Because of the complex flow behaviour, in particular in the near-wall region, due to the presence of the rib, no wall law is applied. Consequently it has been chosen to systematically refine the grid in the near-wall region and in the rib vicinity, as shown on Fig. 12.3. The influence of the distance to the wall for the first grid point on turbulent flow for this kind of geometry was first investigated by Zhu [241], demonstrating that a dimensionless wall resolution $y^+ = yu_\tau/\nu \approx 10$ gives good results and saves a lot of computational time when compared to finer grid resolutions ($y^+ \approx 1$). As all simulations are performed at similar Reynolds number, a wall distance of the first grid point away from the wall $y = 0.323$ mm is imposed between two ribs in all simulations, holding a wall resolution $y^+ \approx 10$, despite the numerous simulated geometries. Because of the expected flow acceleration of the fluid in the rib vicinity, the cell size is twice smaller on the rib surface to ensure the same resolution criterion. The cell size is progressively increased toward the centreline

of each computational domain. Finally, the smallest cell volume is fixed to $2.0 \times 10^{-13} \text{ m}^3$ in all computational domains in order to control the computational time step. Depending on the simulated geometry, one mesh is constituted of 2 to 6 million nodes. Each simulation is first run for approximately 50 convective times $\tau_{conv} = \frac{p}{U_b}$ before the flow statistics are gathered in order to reach steady state and then the averaging of the flow is performed on approximately 100 more convective times τ_c . The corresponding mean CPU time of one simulation is about 45,000 hours.

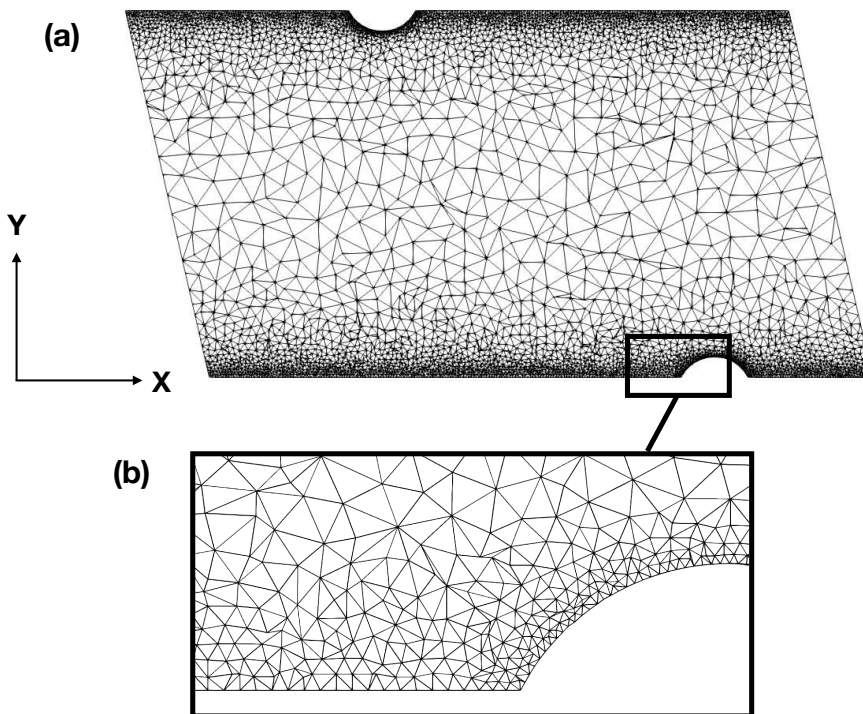


Figure 12.3 – Example of a mesh cut in the Z-normal plane for (a) a full computational domain and (b) a detail of the near-wall region.

12.2.2 Numerical Set-Up

As in Chapter 10, the simulations have been performed using the AVBP solver. For comparison purpose, all geometries are computed for the same flow regime $Re = U_b D / \nu = 76800$, with U_b the bulk velocity, D the pipe diameter and ν the viscosity of the fluid. Bulk velocity U_b and bulk temperature T_b are set constant and similar in all geometries, ensuring similar viscosity and Reynolds number. A no-slip condition is imposed at the walls. Moreover, a spatially and temporally constant wall heat flux is imposed at the walls, providing heat to the fluid. In order to compare all geometries at similar operating conditions, all simulated heat exchangers receive the same amount of heat per metre, the imposed wall heat flux being scaled by the wall surface. The total

Flow parameter	Re [-]	U_b [m/s]	T_b [K]	ν [m 2 /s]	Φ_w [W/m]
Value	76,800	110	1150	5.46×10^{-5}	9,576

Table 12.1 – Operating conditions common to all simulations.

Geometrical Parameter	Minimal value	Maximal value
e [mm]	0.5	4.5
p [mm]	40	160
N_D [-]	0	5
E_r [-]	0.20	0.80

Table 12.2 – Geometrical parameters to optimize and their minimal and maximal considered values.

heat provided to the fluid Φ_w is set equal to 9,576 W/m in all geometries, which correspond to a wall heat flux of 80,000 W/m 2 in a smooth tube of diameter D. The operating conditions and the fluid properties have been chosen to be representative of the thermal cracking process. They are summarized in Table 12.1.

In these periodic configurations, an artificial source term S_{qdm} is added to the momentum equation, together with its work counterpart $u \times S_{qdm}$ in the energy equation, to compensate the pressure loss and ensure a constant flow motion inside the domain. S_{qdm} is uniformly imposed in the entire domain to avoid artificial perturbations and its value is dynamically adapted to the flow conditions in order to reach the targeted mass flow rate. Similarly, as a heat flux is imposed at the wall, an energy source term S_e is added to the energy equation, which balances the heat provided to the wall to keep the bulk temperature constant.

12.2.3 Optimization Problem

The objective of this study being the geometrical optimization of the helical rib for heat exchanger applications, several geometrical parameters related to the rib are uncertain and constitute the optimization input parameters. All geometrical parameters to optimize are summarized in Table 12.2, with their corresponding minimum and maximum values investigated in this work. Maximal values for p and N_D were selected in order to keep the computational cost of the study to a reasonable value, the required simulation time increasing greatly with the increase of those parameters. The allowed range for E_r is wide, as $E_r = 1$ corresponds to the already extensively studied smooth tube geometry and $E_r = 0$ reduces to the case of a continuous rib, already investigated with $N_D = 0$.

The objective when designing a heat exchanger is to increase the heat transfer efficiency at the wall, while keeping to a minimum the

pressure loss. The heat transfer efficiency of a system under forced convection being characterized by the heat transfer coefficient h , the optimization procedure should lead to a maximization of h or of the dimensionless Nusselt number $Nu = hD/\lambda$. Similarly, pressure losses in a circular pipe flows are made dimensionless introducing the friction factor f , with the following relation:

$$f = \frac{\Delta P D}{2 \rho L U_b^2} \quad (12.1)$$

with ΔP the global pressure loss in the domain, L the length of the considered geometry and ρ the fluid density. Based on those considerations, the cost function to optimize is expected to depend on Nu and f .

Webb and Eckert [233] developed equations for the estimation of heat exchanger performances, based on the comparison between the heat conductance K , which is the thermal power provided to the fluid, and the pumping power P_P required to ensure the motion of the flow. In their work, they focus on the use of rough surfaces in order to maximize the heat exchange capacity for similar pressure drop and exchange surface, or to minimize the pressure drop given the heat exchange capacity and the exchange surface. The heat conductance of the tube is given by $K = hA$, with h the heat transfer coefficient and A the exchange surface. Equivalently, this relation leads to:

$$\frac{K}{K_s} = \frac{St}{St_s} \times \frac{A}{A_s} \times \frac{G}{G_s} \quad (12.2)$$

with St the Stanton number, G the mass flow per unit area and the subscript s indicating values for a smooth tube geometry. Similarly, the pumping power P_P can be expressed as a function of the mass flow G :

$$P_P = \frac{G}{\rho} \times S \times \Delta P \quad (12.3)$$

Considering the global friction factor defined in Eq. (12.1), the pumping power becomes:

$$\frac{P_P}{P_{Ps}} = \frac{f}{f_s} \times \frac{A}{A_s} \times \left(\frac{G}{G_s} \right)^3 \quad (12.4)$$

Finally, by eliminating G/G_s between Eq. (12.2) and Eq. (12.4), Webb and Eckert obtained the following expression containing the heat conductance, the pumping power and the exchange area as functions of the Stanton number and the friction factor:

$$\frac{K/K_s}{(P_P/P_{Ps})^{1/3}(A/A_s)^{2/3}} = \frac{St/St_s}{(f/f_s)^{1/3}} \quad (12.5)$$

In the current work, a maximization of the heat conductance K/K_s is targeted for a given pumping power, i.e. $P_P/P_{Ps} = 1$. It is important to note that in order to reach similar pumping power, the comparison

between the smooth and the roughened tube should be done at different operating conditions. This is archived here considering similar exchange surface, i.e. $A/A_s = 1$, but different mass flow rates. The cost function to optimize therefore reduces to:

$$F_{cost} = K/K_s = \frac{St/St_s}{(f/f_s)^{1/3}} \quad (12.6)$$

The optimization is carried out using the *Efficient Global Optimization* (EGO) method which is described in Appendix B.

12.3 Results

12.3.1 Continuous Rib

When considering a continuous rib, i.e. $N_D = 0$, the emptiness ratio parameter E_r becomes irrelevant and the problem reduces to an optimization of 2 input parameters: e and p . The response surface constructed with the Gaussian Process method is shown on Fig. 12.4. A total of 8 simulations were performed for heat exchangers with a continuous rib, indicated by symbols \bullet on Fig. 12.4. Note that few simulations are performed for a continuous rib, geometries with a discontinuous rib being more promising for the cost function optimization.

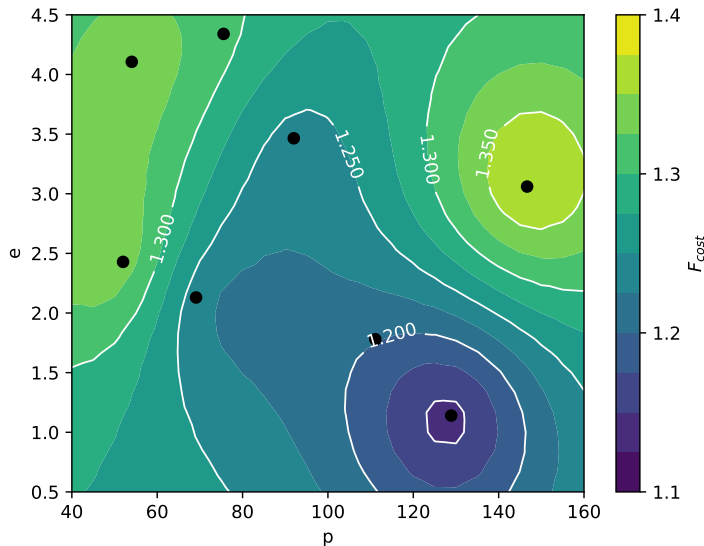


Figure 12.4 – Response surface for a continuous rib.

Two optimal regions for the maximization of the objective function appear on the response surface. A first optimal is found for high e and low p , while a second optimal is found for high e and high p . Based on this observation, it appears that low e always lead to a poor efficiency of the heat exchanger and high e ($e > 2.0$ mm) should be favoured. Note, however, that the objective function is always evaluated greater than

1.0, assessing better thermal efficiencies than a simple smooth heat exchanger. In the low-pitch optimal region, it appears that the influence of the rib height on the cost function is of little importance, the cost function remaining quite constant in this zone. Indeed, the combination of small pitch and high height leads to very important pressure loss, which balances the advantage of higher heat transfer efficiency. The high-pitch optimal region seems even more promising than the previous optimal region, the simulation performed in this zone leading to the sample point with maximum cost function. The optimal predicted value of the objective function is found to be $F_{\text{cost}} = 1.374$ for $e = 3.16$ mm and $p = 150$ mm. Few observations are made in this zone due to the limited computational cost allocated to the optimization process and more promising reactor design with discontinuous ribs.

Figure 12.5 shows the first and total order Sobol' indices for the two input parameters p and e . Both input parameters have an important impact on the response surface, e impacting slightly more as $S_p = 0.322$ and $S_e = 0.444$. The two parameters are, however, correlated since the Sobol' total order indices are found significantly higher than the Sobol' first order indices ($S_{Tp} = 0.538$ and $S_{Te} = 0.632$). Those remarks are in good agreement with the conclusions drawn from the response surface.

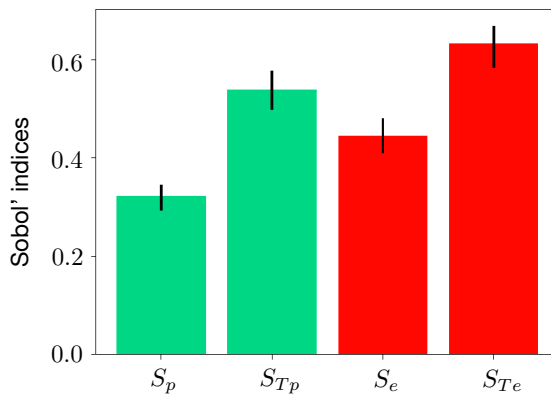


Figure 12.5 – First order and total order Sobol' indices for continuous rib optimization.

12.3.2 Discontinuous Rib

As previously stated, discontinuities are also introduced in the rib leading to a total of 4 geometrical parameters to optimize. Figure 12.6 shows examples of response surfaces predicted for ribs including one discontinuity per rib pitch and for different values of E_r . The total number of simulations performed with discontinuous ribs is equal to 34, the initial design of experiment consisting of 20 simulations and 14 simulations being added thanks to the EGO method.

Results show similarities between the continuous rib response surface given in Figure 12.4 and response surfaces obtained with one small

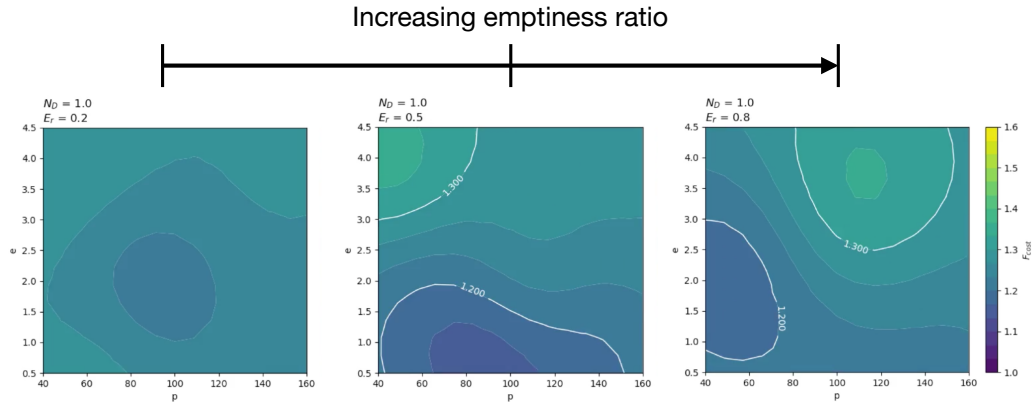


Figure 12.6 – Examples of response surfaces for a rib with 1 discontinuity per pitch ($N_D = 1$). $E_r = 0.2$ (left), $E_r = 0.5$ (middle), $E_r = 0.8$ (right).

discontinuity ($N_D = 1$ and $E_r < 0.5$). In both cases maximum values of the cost function are found for large e , while the minimum values for F_{cost} are encountered for small e and large p . It should be noted, however, that for discontinuous ribs with $E_r < 0.5$, the region of main interest is found to be the high e and small p region, large p reducing the thermal efficiency of the heat exchanger. On the other hand, a very different response surface is observed when dealing with a larger discontinuity, and $0.5 < E_r < 0.6$ constitutes a transition zone between two behaviours. With the discontinuity becoming larger than the rib itself, the optimal p value suddenly shifts from 50 mm to about 115 mm. This has however few influence on the optimal rib height, and optimal value of e remains around 4.0 mm. When associated with large E_r , p only has a significant influence on the cost function in the $e > 2.0$ mm region.

More discontinuities are included in the rib when increasing the value of N_D . Response surfaces are plotted for N_D varying from 1 to 5, and some examples are displayed on Figure 12.7. For all investigated number of discontinuities, the response of the system to the input parameters is very similar and the same observations as for geometries with $N_D = 1$ apply. In particular, the sudden transition in optimal roughness shape for $0.5 < E_r < 0.6$ is always observed. The main influence of the number of discontinuities is a slight increase of F_{cost} in the large E_r region when increasing N_D , which tends to favour a high number of discontinuities. This is explained by the lower pressure drop found with a larger number of discontinuities while increasing heat transfer enhancements. For $N_D > 1$, the global optimal design that maximizes the cost function clearly appears in the large e , large E_r region and for moderate values of p . Based on those results, the best predicted geometry is shown on Figure 12.8, and has the following geometrical parameters: $e = 3.14$ mm, $p = 105$ mm, $E_r = 0.75$ and $N_D = 5$. The corresponding value for the cost function is $F_{cost} = 1.583$. The dynamic and thermal behaviour of the flow in the optimal predicted geometry is described in more details in the next section.

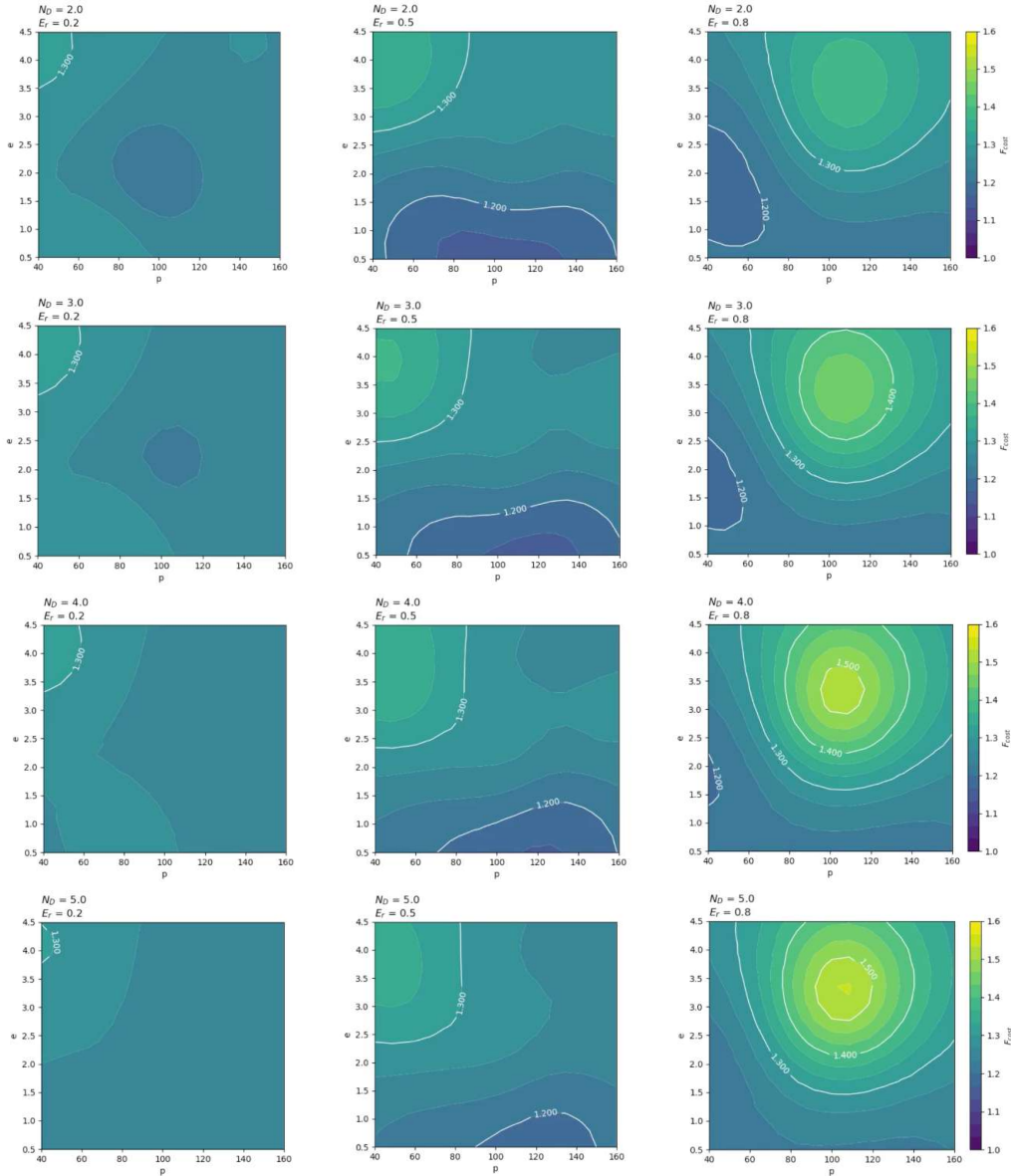

 Figure 12.7 – Examples of response surfaces for various N_D and E_r .

Figure 12.9 represents the first and total order Sobol' indices for each input parameter. For the optimization of a discontinuous ribbed heat exchanger, the parameters do not have a similar impact on the cost function. The rib height e one of the most influential parameter, the first order Sobol' indices reaching a value of $S_e = 0.290$. The total order Sobol' indices for e is even higher ($S_{Te} = 0.539$), traducing an influence that depends on the other parameters, and in particular on E_r . This is in good agreement with the observed response surfaces, high e being always more favourable, especially when associated with high values of E_r . Input parameters p and E_r have small first order Sobol' indices ($S_p = 0.006$ and $S_{Er} = 0.070$), but their total order indices are much higher ($S_{Tp} = 0.395$ and $S_{TEr} = 0.620$), meaning non-negligible but complex influence of those parameters on the cost function. Indeed,

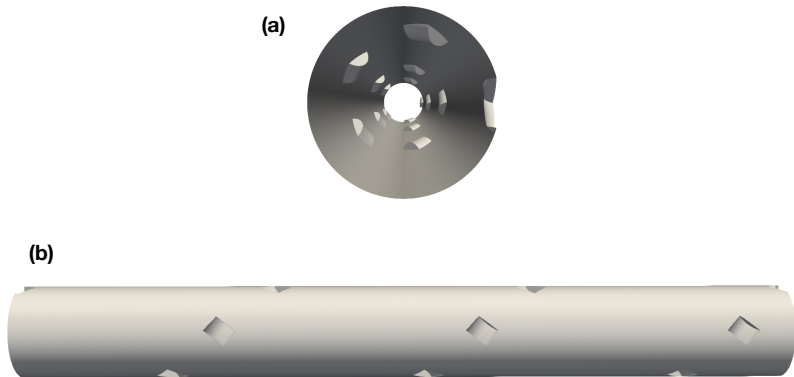


Figure 12.8 – Optimal predicted ribbed tube geometry for heat exchanger applications. Three pitches are represented. (a) Cut in the X-normal plane showing the inner surface and (b) view of the wall surface from the outside of the tube.

the influence of p appears to be coupled with both e and E_r , as small e and large E_r always lead to a small impact of p on the cost function, due to geometries having fewer impact on the bulk flow and with no swirling motion. On the contrary, large values of e lead to a roughness greatly impacting the flow, and p is highly coupled to e then. Finally, N_D is the least influential parameter on the cost function. In particular, $S_{N_D} = 0.023$ which is quite small. The total Sobol' index is, however, not completely negligible ($S_{TN_D} = 0.138$), assessing a small impact of N_D on the cost function.

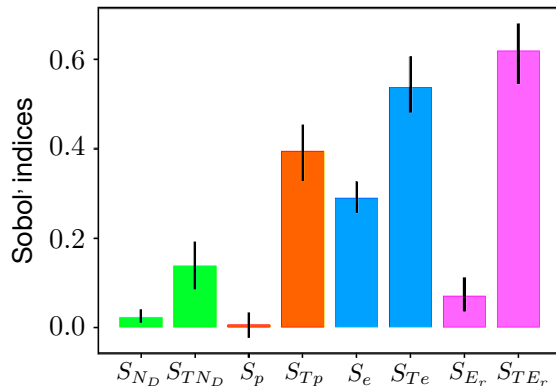


Figure 12.9 – First order and total order Sobol' indices for discontinuous rib optimization.

12.3.3 Optimal Discontinuously Ribbed Heat Exchanger

12.3.3.1 Flow Dynamics

Due to the presence of the discontinuous rib, the average flow parameters are considered as functions of both the radial and axial coordinates. The radial coordinate is normalized by the pipe radius R , ranging from $r/R = r^+ = 0$ at the pipe centre to $r^+ = 1$ at the pipe wall. The axial distance X is normalized by the rib height, $X/e = X^+ = 0$ being the position just downstream the rib crossing the left periodic plane. Moreover, because of the rib discontinuities and the existing planes of symmetry, profiles are shown in two different longitudinal planes: the plane cutting the rib by its centre, called plane ①, and the plane being equidistant of two ribs called plane ②, as represented on Figure 12.10.

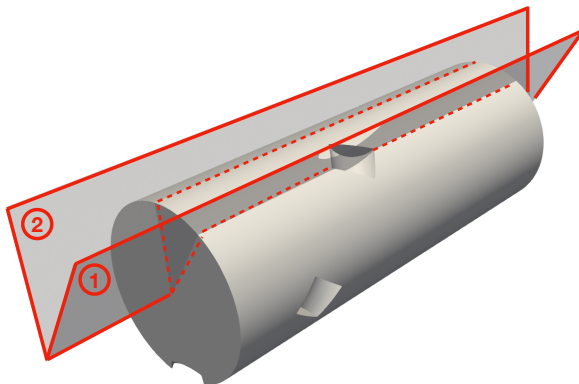


Figure 12.10 – Representation of the two symmetry planes of interest. Plane ① is the longitudinal plane cutting the centre of the rib, and plane ② is the longitudinal plane equidistant of the two ribs.

The mean axial velocity profiles normalized by the bulk velocity in plane ① are represented in Figure 12.11 (top) for positions $X^+ = -1$ (rib top), 2.5, 7.5, 12.5, 17.5, 22.5 and 27.5. Mean axial velocity is strongly decelerated in the rib wake. The flow, however, fully establishes few rib heights further and all axial velocity profiles are found almost similar from $X^+ = 7.5$ to $X^+ = 27.5$. Because of the rib shape, the recirculation zone is very small and does not appear in Figure 12.11, the first represented profile downstream the rib being at position $X^+ = 2.5$. The recirculation zone actually exhibits a very characteristic 'S' shape due to the rectangular rib shape, including two vertical planes slantwise to the flow direction inducing a flow detachment, as represented on Figure 12.14. Mean axial velocity in plane ② are also displayed on Figure 12.11 (bottom). In the path between two ribs, the axial velocity profiles are similar at every position, showing no impact of the rib roughness in those zones of the heat exchanger.

Mean radial velocity is investigated in Figure 12.12 in both planes ① and ②. Radial velocity remains very small in plane ②, assessing the low impact of the roughness in this plane. However, a strong negative radial

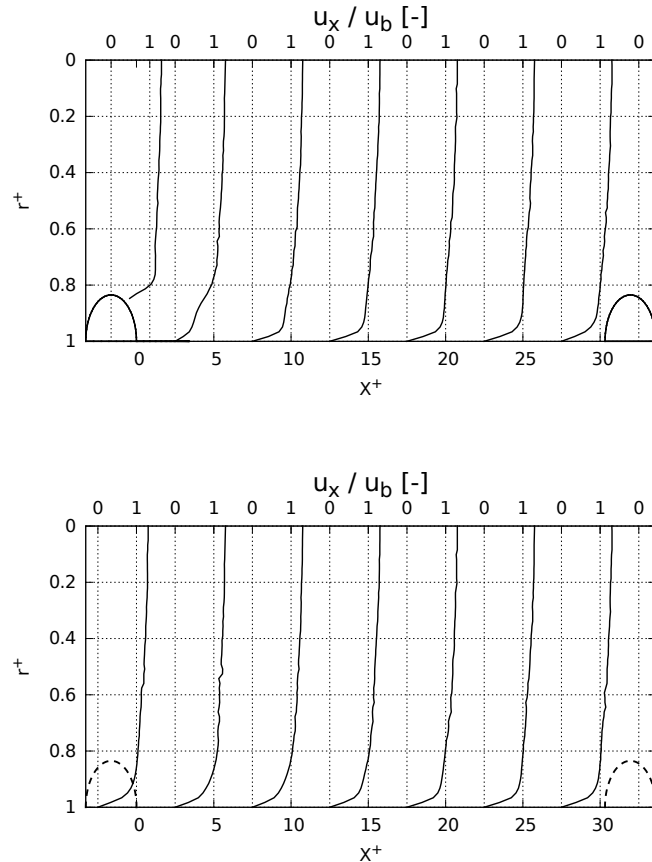


Figure 12.11 – Mean axial normalized velocity profiles at various axial locations, both in plane ① (top) and in plane ② (bottom). Dashed line indicates a rib behind the considered plane.

velocity is found in the rib wake, reaching up to $0.10 \times U_b$, the mean flow going toward the wall downstream the recirculation zone. The radial velocity is slightly positive upstream the rib, as the flow goes toward the pipe centre to bypass the obstacle.

Mean azimuthal velocity profiles are displayed on Figure 12.13. Similarly to the radial flow motion, the main azimuthal motion is located in the rib wake. Note that at this location, mean azimuthal velocity is negative, meaning a mean flow motion swirling in the opposite direction than the rib helix. This is due to the shape of the rib, and in particular to the flow impacting rib walls oriented perpendicularly to the helix direction in the near-wall region. Upstream the rib, a positive mean azimuthal velocity is found in the near-wall region, also due to the rib shape orienting the flow. In the rest of the domain, azimuthal motion remains very low, the large discontinuities between the ribs preventing the development of the swirling motion. Indeed, the disappearing of the swirling motion occurs for $E_r > 0.6$, the rib length becoming shorter than the rib width leading to a different orientation of the flow. This also explains the sudden change in the shape of the cost function when dealing with larger E_r , the swirling motion being detrimental to the heat transfer efficiency. Figure 12.15 shows streamlines of the mean flow in the rib vicinity. The

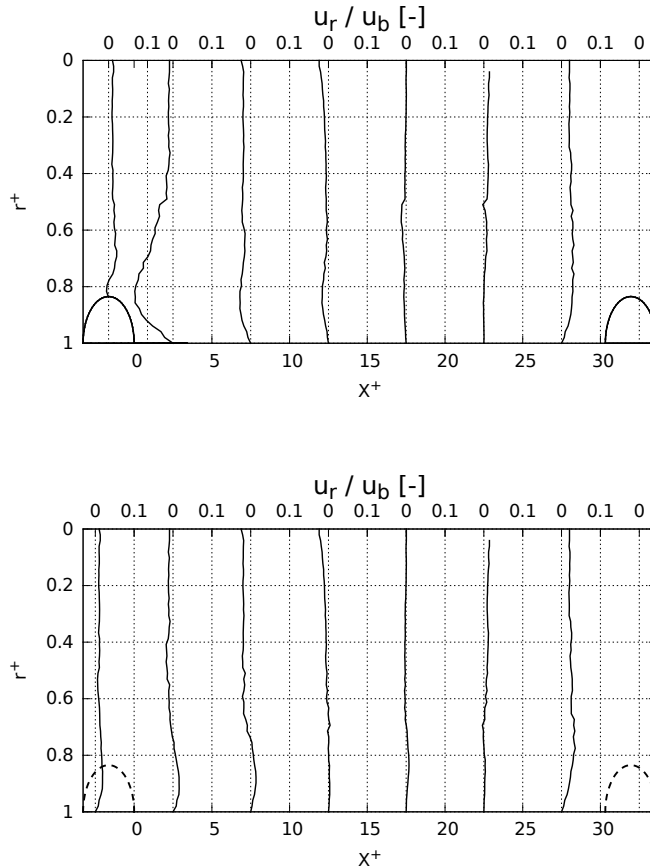


Figure 12.12 – Mean radial normalized velocity profiles at various axial locations, both in plane ① (top) and in plane ② (bottom). Dashed line indicates a rib behind the considered plane.

flow impacting the rib appears to bypass the roughness by both sides, explaining the azimuthal velocity profiles.

Finally, integrating the steady momentum equation with periodic conditions gives:

$$0 = \underbrace{- \oint_{\Omega} P \vec{n}_x d\vec{S}}_{\text{pressure drag}} + \underbrace{\oint_{\Omega} \vec{\tau}_x d\vec{S}}_{\text{friction drag}} + \underbrace{\int_V S_{qdm_x} dV}_{\text{pressure loss}} \quad (12.7)$$

where Ω and V are respectively the surface and volume of the computational domain, and n_x and τ_x are respectively the axial component of the (inward) wall-normal vector and the axial component of the stress vector defined in Eq. (12.8) using the summation convention:

$$\vec{\tau} = \bar{\vec{\tau}} \cdot \vec{n} = \begin{pmatrix} \tau_{xj} & n_j \\ \tau_{yj} & n_j \\ \tau_{zj} & n_j \end{pmatrix} = \begin{pmatrix} \vec{\tau}_x \\ \vec{\tau}_y \\ \vec{\tau}_z \end{pmatrix} \quad (12.8)$$

While in a smooth tube, only the friction drag contributes to the pressure loss, in a ribbed tube the pressure loss is due to both the pressure drag and the friction drag. The relative contributions of the

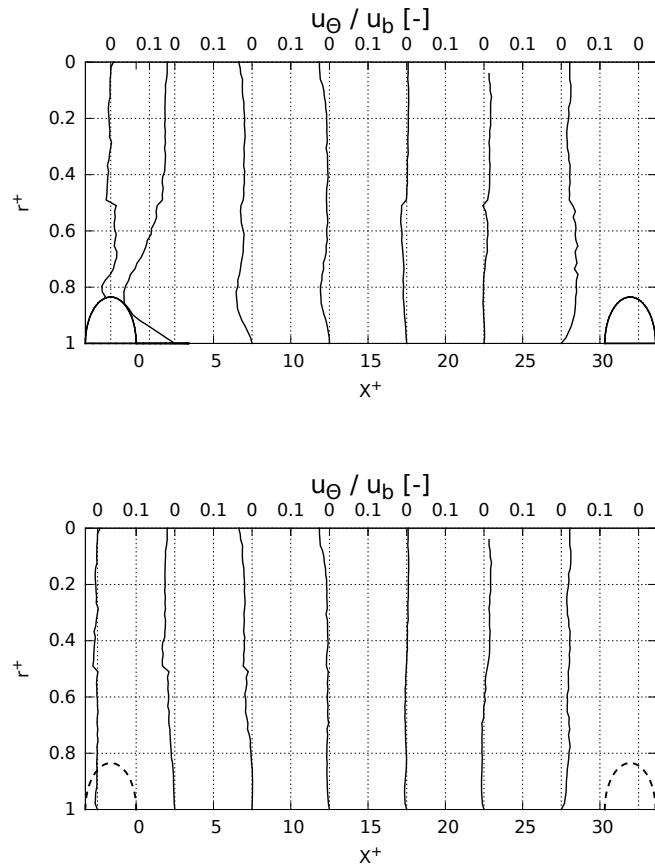


Figure 12.13 – Mean azimuthal normalized velocity profiles at various axial locations, both in plane ① (top) and in plane ② (bottom). Dashed line indicates a rib behind the considered plane.

pressure drag and the friction drag in the optimal geometry are given in Table 12.3, based on the integration of the drags over the surface. It appears that pressure drag is more important than the friction drag, due to the flow directly impacting the rib. Pressure drag is responsible for 63% of the total pressure losses in the optimal geometry. The friction drag is less important than in a smooth tube, because of the recirculation zone reducing the axial velocity in the near-wall region. Table 12.4 compares the total pressure losses in the ribbed tube compared to the pressure losses in a smooth tube of the same diameter according to the Petukhov correlation [177] (Eq. (12.9)). Pressure losses are found more than 2 times larger in the ribbed tube.

$$f_s = \frac{1}{(1.58 \ln(Re) - 3.28)^2} \quad (12.9)$$

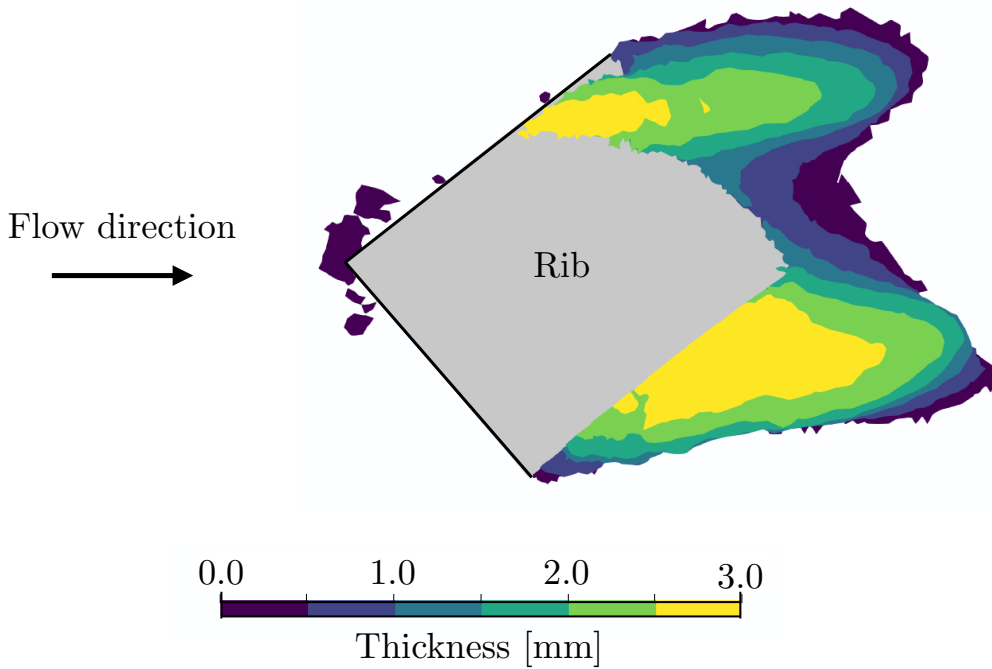


Figure 12.14 – Representation of the mean recirculation zone downstream the rib viewed from above the rib. The iso-surface of null axial velocity is used as the limits of the recirculation, and is coloured by the thickness of the recirculation zone.

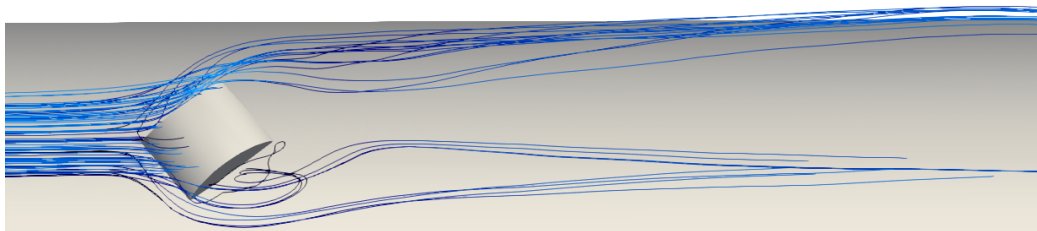


Figure 12.15 – Flow streamlines impacting the rib, coloured by velocity magnitude.

12.3.3.2 Heat Transfer

Wall temperature on the coil inner surface is represented on Figure 12.16. Wall temperature strongly decreases in the recirculation zone and downstream of the rib, because of the important radial mixing at this location. This induces large cold zones in the wake of the ribs. Skin temperature is also low on the rib surface, thanks to the flow acceleration on the rib top inducing important heat transfer. In opposition, because of the lack of swirling motion in the near-wall region, the skin temperature is more important in plane ②. Quantitative results are given on Figure 12.17,

Case	Friction drag ($\times 10^{-3}$)	Pressure drag ($\times 10^{-3}$)	Total drag ($\times 10^{-3}$)
Optimal geometry	3.57 (78.3 %)	6.06 (133 %)	9.63 (211 %)
Smooth tube (Eq. (12.9))	4.56 (100 %)	0 (0 %)	4.56 (100 %)

Table 12.3 – Integrated drag contributions normalized by $(0.5 \rho_b U_b^2)$ for the optimal geometry and a smooth tube with the same diameter. Percentages represent the contribution relative to the total drag in a smooth tube according to Eq. (12.9).

Case	ΔP [Pa/m]
Optimal geometry	6210
Smooth tube (Eq. (12.9))	2308

Table 12.4 – Global pressure loss for in the optimal heat exchanger geometry and in a smooth tube according to Eq. (12.9).

showing skin temperature in both plane ① and plane ②. In plane ②, skin temperature remains approximately constant to 1230 K, as all velocity profiles are similar at every axial location, and no swirl motion is responsible for azimuthal mixing of the temperature. In plane ①, skin temperature is slightly lower on the rib surface, reaching approximately 1210 K, thanks to the flow acceleration of the rib top. Downstream of the rib, skin temperature decreases to 1203 K, as the radial motion brings cooler flow from the central region of the pipe in the near-wall region. Moreover, the flow recirculation and the azimuthal motion in the rib wake increase the flow turbulence in this region, increasing the heat transfer. Skin temperature progressively increases downstream until reaching the maximum skin temperature of 1232 K at location $X^+ = 25$.

The global Nusselt number is found equal to 389 in the optimal heat exchanger geometry. In a smooth tube, the Nusselt number is evaluated from the Dittus-Boelter correlation [58] (Eq. (12.10)), and is found equal to 189 for similar operating conditions. This represents an increase of + 105 % due to the shape of the artificial roughness and to better mixing, assessing better heat transfer efficiency and important reduction of the wall temperature. Spatial distribution of the Nusselt number is displayed on Figure 12.18. In plane ②, the Nusselt number is approximately constant, which is a consequence of the constant skin temperature. Despite the absence of swirling motion in this plane, the heat transfer efficiency remains much higher than in a smooth tube, probably because of the flow acceleration in the near-wall region caused by the narrowing of the tube section at the passage of the rib and the small radial mixing. In plane ① however, the Nusselt number appears much higher on the rib surface and in the recirculation zone,

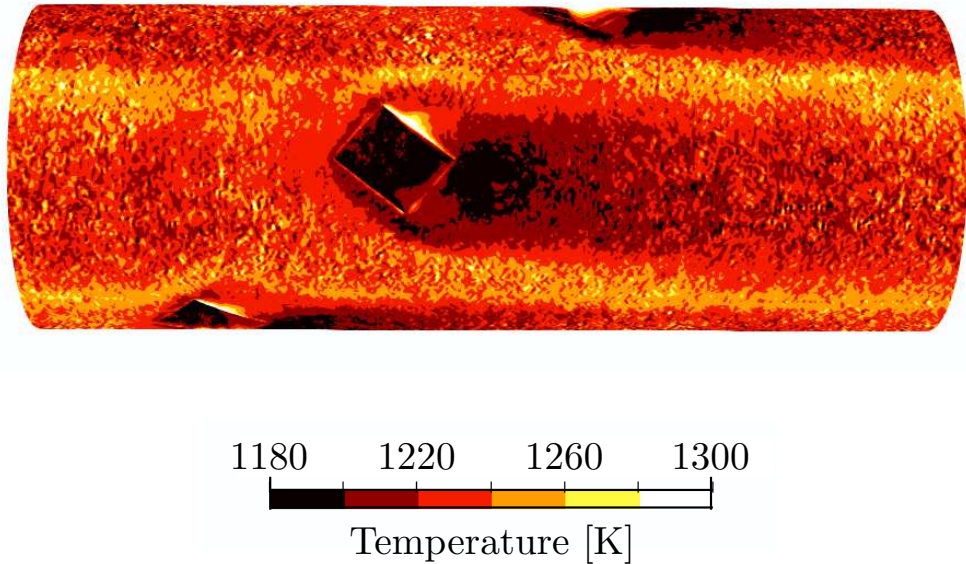


Figure 12.16 – Mean skin temperature in the optimal geometry.

reaching up to 563. This is due to the flow acceleration on the rib top and to the complex recirculation zone enhancing turbulence in the rib wake and increasing the heat transfer at those locations. In the light of those results, suppressing the swirl motion in the near-wall region of the heat exchanger thanks to large discontinuities seems to increase heat transfer efficiency thanks to an acceleration of the flow in each rib vicinity while conserving important radial mixing.

$$Nu_s = 0.023 \times Re^{0.8} \times Pr^{0.4} \quad (12.10)$$

12.4 Summary

In this work, a methodology for the simulation and optimization of turbulent flows in heat exchangers has been proposed. It relies on a series of wall resolved LES, using periodic domains. Four geometrical parameters are considered for the optimization, leading to a wide variety of continuous and discontinuous single-started internal roughness geometries. The objective function aims at maximizing the heat transfer efficiency while limiting the pressure loss, as proposed by Webb and Eckert [233]. To avoid running a high number of LES, a surrogate model is built using Gaussian processes. The optimization leads to a heat exchanger geometry which increases the wall heat transfer efficiency by a factor 2.1 compared to a smooth tube, while increasing the pressure loss only by a factor 2.7 for the considered operating conditions, thanks to a roughness with low azimuthal blockage ratio. The introduction of large discontinuities in the rib is responsible for this important increase of heat transfer, because it suppresses the swirling motion, accelerating

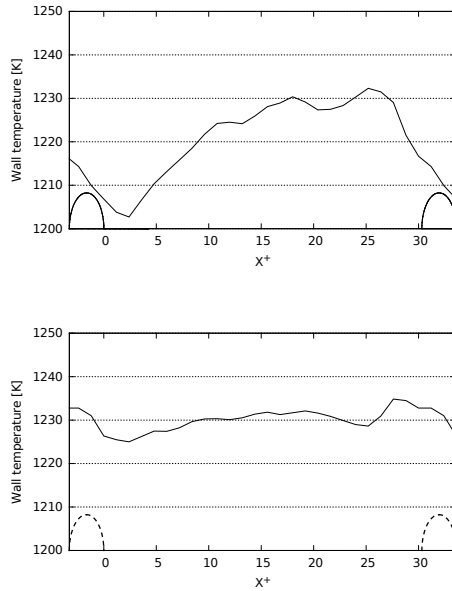


Figure 12.17 – Profiles of mean skin temperature, in plane ① (top) and in plane ② (bottom). Dashed line indicates a rib behind the considered plane.

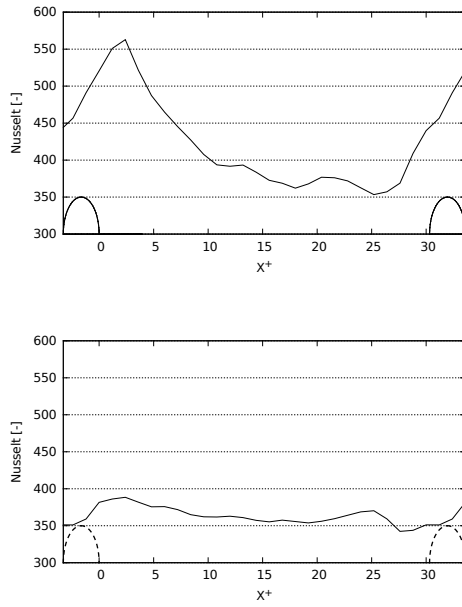


Figure 12.18 – Profiles of mean local Nusselt number, in plane ① (top) and in plane ② (bottom). Dashed line indicates a rib behind the considered plane.

the flow in the rib vicinity and preserving important radial mixing. The investigation of the optimum roughness for heat exchangers might be extended to more geometrical parameters, such as the radius of curvature of the smooth edges for dimpled tubes. The swirling motion being detrimental to the heat transfer efficiency, transverse roughness elements might also be considered instead of helical ones, along with more complex forms.

To summarize, the proposed methodology is found well adapted for geometrical optimization based on few parameters and was successfully applied, leading to innovative geometrical designs for heat exchangers. These heat exchangers may be used for industrial application requiring important heat transfer and limited pressure loss in comparable operating conditions. The optimization methodology may be used in the future with other objective functions for specific industrial applications, such as thermal cracking.

IV

Conclusion

Conclusion

THIS THESIS work proposes some methodological improvements related to Uncertainty Quantification (UQ). Apart from the novelty of these methods, they proved to be useful in various costly numerical experiments.

The first part of the document reviews the literature on various aspects of UQ. The reader is walked through all the steps required to perform a UQ study in a costly numerical environment: from the definition of a Design of Experiments (DoE) to construct a surrogate model, to the use of this surrogate to compute statistics and ultimately visualize the results.

The current advances and limitations of DoE are presented in Section 2.1. OLHS and Sobol' sequences are both considered as best practice although they exhibit some limitations such as the iterative properties and the randomization, respectively.

Using this sample, one can perform a UQ analysis with methods detailed in Section 2.2. Global Sensitivity Analysis (GSA) is recommended over local SA. Looking at the method themselves, variance-based SA is still predominant but moment-based methods appear as good complement in a study. In a costly numerical environment, it is not tractable to directly perform a UQ and the usage of a surrogate model comes as a solution.

Section 2.3 exposes two of the most used methods: Gaussian Process (GP) and Polynomial Chaos (PC). Finally, Section 2.4 introduces the problem of visualizing the uncertainties. This is a fairly new field with only a limited corpus of study. There is currently no clear recommendations about how to visualize uncertainties.

From this review, Chapter 3 details the three questions which this thesis aims to answer:

- *How to construct a DoE in a high-dimensional parameter space?*
- *How to resample a DoE by considering the QoI of already sampled experiments?*
- *How to visualize uncertainties in high-dimensional cases?*

The following part seeks to answer these questions. It begins with Chapter 4 outlining all the methodological contributions of this thesis.

A new UQ tool is presented in Chapter 5: Batman. Batman is an open-source Python library dedicated to UQ which has been developed during this thesis. It is based on state-of-the-art statistical libraries, such as OpenTURNS, and it allows to easily perform an uncertainty

analysis. All further methodological developments of this work have been consolidated through this tool.

Chapter 6 presents a new iterative and versatile sampling method named KDOE. It relies on a Kernel Density Estimation (KDE) that serves as an exclusion field which allows constraining the samples not to be too close to each other. This procedure is used to iteratively fill the parameter space uniformly. It is shown that this method provides good space filling properties, especially for high-dimensional cases.

Chapter 7 answers the resampling problematic when QoI have been computed. Two novel methods based on both the Leave-One-Out (LOO) error and the variance of the surrogate model constructed by GP are presented: LOO- σ and LOO-Sobol'. It is shown that an improvement of the quality (over classical methods) of the surrogate model is guaranteed in high-dimensional cases.

Lastly, Chapter 8 introduces novel visualization strategies to visualize uncertainty. The methods are designed to help UQ practitioners by allowing the visualization of both input parameters space and Quantity of Interest (QoI) on the same canvas by means of a 3-dimensional version of the Kiviat plot (also called spider plot). In case of functional output data, the use of sound is proposed to convey this information. The functional data is analysed using the Highest Density Region (HDR) technique, and distance from the most probable output is mapped through sound.

These methods are applied on various complex configurations in the last part. First of all, Chapter 9 compares GP and PC in a hydraulic context with the 1-dimensional code: MASCARET. Both surrogate showed their ability to correctly substitute the simulator with a low number of numerical simulations. In an operational context, replacing a numerical simulator with a surrogate model is of interest even if the original model is not expensive to evaluate. It allows to produce more frequently, and more accurately, predictions using less expensive hardware.

Chapter 10 illustrates the benefits of the novel resampling methods on a configuration known in the literature to be difficult to reproduce: the aerothermal flow around the LS89 blade cascade. It is reminded that this is the first uncertainty quantification study performed using Large Eddy Simulation (LES). The code AVBP was used. The difficulty to correctly predict the flow features even for such a high-fidelity simulation, points towards the uncertainty of the boundary conditions. The turbulence intensity and the angle of attack are known to affect the aerothermal flow. This quantity is of great interest for industrial partners to determine the life-cycle of the turbine components. The study allowed to find a spatial sensitivity of the flow to the input parameters.

Following, Chapter 11 presents the use of HDR in order to reduce the dimensionality of the input parameter space for a complex case: a swirler geometry. Using LES and Adaptative Mesh Refinements (AMR) the physic is captured with precision allowing assessing manufac-

ing dispersion coming from Additive Manufacturing (AM). This study allowed to find that the manufacturing tolerances could be reduced as the impact of additive manufacturing on the QoI was controlled. On an industrial point of view, such analysis can help reduce cost if the precision can be lowered.

In Chapter 12, the whole toolchain is used to perform a global optimization of the geometry of a heat exchanger—consisting in a ribbed tube. The Efficient Global Optimization (EGO) method was used to lower the computational cost of the study. The obtained surrogate model was then used to perform a UQ analysis. One of the main conclusions from this analysis is that the interaction effect between the pitch of the ribs and the emptiness ratio between the ribs was important.

The perspectives of this work are numerous. They are presented under three subsections: (i) surrogate models, (ii) uncertainty tools and (iii) visualization.

- *Surrogate models,*

As outlined in the literature review, lots of work has already been devoted to the definition of surrogate models and (re)sampling strategies. New approaches are still being proposed as in [187] where a deep learning approach is used to construct deep GP models or in [204] where PC and GP are used in the same framework.

Considering the dimensionality of the DoE and QoI, a common practice is to use a Proper Orthogonal Decomposition (POD) in order to reduce the dimensionality. While this method produces good results—as presented in this work—, other reduction techniques such as Linear Discriminant Analysis (LDA) or Autoencoder could be investigated [88]. It becomes even more challenging to take into account a temporal high dimensional phenomenon. A parallel with Long Short Term Memory (LSTM) methods from deep learning can be made.

Another challenge is to take into account bifurcations in the physics. A bifurcation is a qualitative change of the behaviour of a system resulting from a small smooth change (contrary to an impulsion or Dirac) made to the parameter values. The identification of classes in the input space that lead to bifurcations in the output space can be achieved by expert knowledge or with machine learning algorithms as proposed in [62]. Properly separating the input parameter space depending on the physics is a difficult task as the dimensionality increases and the use of automatic tools comes at hand. Still, there are lots of possibilities and finding the right criterion for a given problem still requires some expertise.

Efforts are also concentrated on other aspects such as the cost of construction of the models and how to frame the problem. The optimization of weights is a key step in deep learning algorithms. During the past years, there has been an incentive toward Bayesian

optimization to solve this problem. But deep learning makes use of large dataset which is a concern with Gaussian Process. Some effort are being done to improve the scalability [238] (going from $\mathcal{O}(n^3)$ to $\mathcal{O}(n)$). An interest in Bayesian model is foreseen, not only on an applicative point-of-view but also on more theoretical aspects.

- *Uncertainty tools,*

Concerning the statistical tools to assess uncertainties, from the literature review it was shown that variance based methods have become a standard. Some improvements are still possible—as shown by [198] where the proposed algorithm requires less samples to converge while being iterative. *Sobol'* indices are still demanding in terms of computational ressources and iterative strategies seek to control the cost of such analysis [223]. However, these methods still require a group of $d+2$ (with d the number of input parameters) coherent simulations at each iteration to proceed. In case of a large number of parameters and a complex simulation procedure, some sample might fail to return a result. In such case, the procedure is not robust and lots of samples are lost—for 1 sample missing, $d+1$ samples are lost. Hence the need of robust strategies.

Moving on to other sensitivity indices, more work is expected concerning moment-based indices. There are a lot of metrics that can be used to discriminate the conditional and unconditional probability density functions but no clear recommendation and comparison is available.

There is a wide range of mature solutions available and the challenge, as outlined in [199], is toward educating people to use them. Going further, the whole community would benefit from common and updated guidelines on how to handle uncertainties. This is one of the goal of the COST action proposal: *Model Auditing and Sensitivity Analysis*. This project seek to federate the community and create tools and teaching materials which would be updated as per the latest research.

- *Visualization.*

As for the visualization of uncertainty, and more generally the way to convey it in a useful way, it is still an open question. The uncertainty community is lacking interest on the matter as opposed to the *data visualization* community. Interesting work around uncertainty are being published but a link between the two community is still required. Linking uncertainty visualization with deep learning is even more challenging due to the curse-of-dimensionality.

Complex visualization schemes are being proposed but there is still reluctance about these new representations. To paraphrase Sheelagh Carpendale, alphabet itself is an incredibly complex visual

system which requires years to learn. Once mastered, it reveals to be a powerful communication tools. Uncertainty visualization is today limited as to be quickly understandable which constrain these innovations to be adopted. Another limit is found with the incentive not to use 3-dimensional visualizations or the need to find equivalent representations in 2-dimensions for printing purpose for instance. In that regard, the literature around 3-dimension and interactive uncertainty is slim not to say inexistant.

This work has proven the feasibility of UQ in a LES context and more generally in a high computational environment. Distributing Batman openly, and thus all the novelty of this thesis work, has allowed a multitude of international collaborations with both institutional and industrial partners. It alleviate the usage of UQ in complex configuration and also permit a collaboration around a common tool. On a methodological aspect, this work proposes new directions to explore. In every aspect, an influence of the data science community is foreseen. From a bus arrival prediction to impact and risk assessment at the European Commission level, the treatment of uncertainties has become an important societal and engineering preoccupation. This thesis paves the way, not to a less uncertain world, but to a population more aware and empowered with uncertainty.



Annexes

A Functions and Datasets	171
A.1 Analytical Functions	171
A.2 Datasets	172
B Optimization Method	173
C Computational Fluid Dynamics	175
C.1 Governing Equations of Compressible Flows	175
C.2 Turbulence Modelling	176
D Batman's API	179

A | Functions and Datasets

A.1 Analytical Functions

Analytical functions—see Table A.1—with increasing numbers of input dimensions are presented, namely: (i) *Rosenbrock* ; (ii) *Michalewicz* ; (iii) *Branin* ; (iv) *Ishigami* ; and (v) *g-function* [161, 109, 201, 92, 78]. They are all widely used because they are nonlinear and nonmonotonic. Moreover, two versions of the *g-function* 11-D are also used. *g-function* (i) 11-D demonstrates the behaviour of the methods with a small number of input parameters contributing to the QoI, whereas *g-function* (ii) 11-D exhibits more influent input parameters.

Function	Hypercube	Definition
<i>Rosenbrock</i> 2-D	$[-2.048, 2.048]^2$	$f(X_1, X_2) = \sum_{i=1}^{d-1} [100(x_{i+1} - x_i^2)^2 + (x_i - 1)^2]$
<i>Michalewicz</i> 2-D	$[0, \pi]^2$	$f(X_1, X_2) = -\sum_{i=1}^d \sin(x_i) \sin^{2m} \left(\frac{ix_i^2}{\pi} \right)$
<i>Branin</i> 2-D	$[-5, 10] \times [0, 15]$	$f(X_1, X_2) = \left(x_2 - \frac{5.1}{4\pi^2} x_1^2 + \frac{5}{\pi} x_1 - 6 \right)^2 + 10 \left[\left(1 - \frac{1}{8\pi} \right) \cos(x_1) + 1 \right] + 5x_1$
<i>Ishigami</i> 3-D	$[-\pi, \pi]^3$	$f(X_1, X_2, X_3) = \sin X_1 + 7 \sin^2 X_2 + 0.1 X_3^4 \sin X_1$
<i>g-function</i> 4-D	$[0, 1]^4$	$f(X_1, X_2, X_3, X_4) = \prod_{i=1}^4 \frac{ 4X_i - 2 + a_i}{1 + a_i}, \quad a_i = i$
<i>g-function</i> (i) 11-D	$[0, 1]^{11}$	$f(X_1, \dots, X_{11}) = \prod_{i=1}^{11} \frac{ 4X_i - 2 + a_i}{1 + a_i},$ $\mathbf{a} = [1, 2, 5, 10, 20, 50, 100, 500, 10^3, 10^3, 10^3]$
<i>g-function</i> (ii) 11-D	$[0, 1]^{11}$	$f(X_1, \dots, X_{11}) = \prod_{i=1}^{11} \frac{ 4X_i - 2 + a_i}{1 + a_i},$ $\mathbf{a} = [1, 2, 2, 3, 3, 10, 50, 50, 50, 100, 100]$

Table A.1 – Analytical functions considered sorted by increasing number of input parameters.

A.2 Datasets

Table A.2 presents two datasets. The first dataset (El Niño) has no input-output relation and only features a temporal output. The second dataset Hydrodynamics features an input-output relation with spatially varying output. The datasets are as follows:

- The *El Niño* dataset is a well-known functional dataset [102]. It consists in a time series of monthly averaged Sea Surface Temperature (SST) in degrees Celsius spatially averaged over the Pacific Ocean region ($0\text{--}10^\circ\text{S}$ and $90\text{--}80^\circ\text{W}$) from January 1950 to December 2007. The response variable is a vector of size 12 and the data set gathers 58 realizations. Data originate from NOAA ERSSTv5's database available at <http://www.cpc.ncep.noaa.gov/data/indices>.
- The *Hydrodynamics* dataset gathers water levels (in m) computed with the 1-dimensional Shallow Water Equation MASCARET solver (opentelemac.org) for a 50 km reach of the Garonne river in South-West of France [7]. Uncertain inputs relate to 4 scalars: the friction coefficients of the river bed K_{s1}, K_{s2}, K_{s3} defined over three homogeneous spatial areas, and the upstream boundary condition described by a constant scalar value for the inflow Q in stationary flow. The response variable is a vector of size 463 (number of computation nodes for the 1D mesh) and an ensemble of 200 realizations is considered here.

Dataset	Scalar input	Functional output	Sample size
El Niño	-	12	58
Hydrodynamics	4	463	200

Table A.2 – Description of the El Niño and Hydrodynamics datasets.

B | Optimization Method

Among the numerous methods that can be used to do an optimization [41] are the one taking advantages of a surrogate model [77]. When dealing with complex cases, the numerical cost is such that only a limited number of simulations can be performed. However, ensuring the convergence of an optimization requires a minimal number of such evaluations for both deterministic and stochastic methods. In this context, building a proxy of the simulation setup allows overcoming the computational cost. As this proxy is being used for optimizing the problem, its quality is paramount. At some point refining the space of parameters—leading to a quality improvement of the model—can improve the optimization.

Batman Chapter 5 was used to handle all the workflow from the design of experiments, to the creation of the surrogate and the optimization. Its workflow is presented in Algorithm 3.

Algorithm 3 Workflow using BATMAN

Require: N_{max} , N_s

- 1: Formulate the surrogate \mathcal{M} on N_s' output
 - 2: **while** $N_s < N_{max}$ **do**
 - 3: $\mathbf{x}_* \leftarrow$ optimization
 - 4: Compute a new sample at \mathbf{x}_*
 - 5: Update the surrogate \mathcal{M}
 - 6: **end while**
-

Efficient Global Optimization (EGO) [112] is a Bayesian optimization taking into account the variance of the model. The objective of the optimization is to improve the current solution Y_{min} . The improvement is computed as:

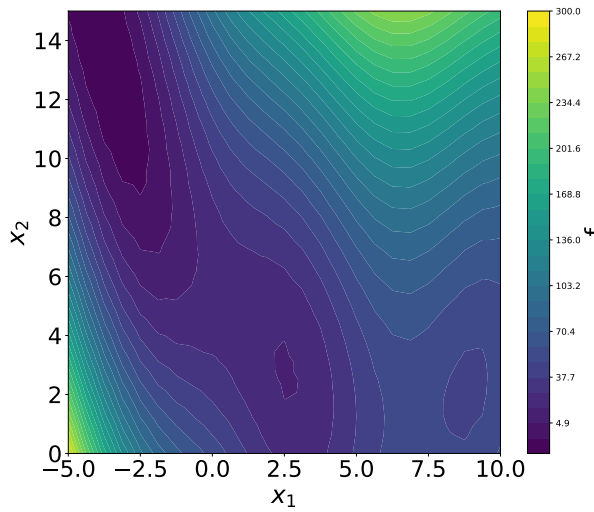
$$I(\mathbf{x}) \begin{cases} Y_{min} - \hat{Y}(\mathbf{x}) & \text{if } \hat{Y}(\mathbf{x}) < Y_{min} \\ 0 & \text{otherwise} \end{cases}. \quad (\text{B.1})$$

Using the surrogate, the prediction is expressed as a random process with $Y \sim \mathbb{N}(\hat{Y}, s^2)$. Thus, the objective is to get the maximal mean improvement. The expected improvement (EI) is computed as a tradeoff between the minimal value Y_{min} and an expected value given by the standard error s for a given prediction \hat{Y} . It reads:

$$\mathbb{E}[I(\mathbf{x})] = (Y_{min} - \hat{Y})\Phi\left(\frac{Y_{min} - \hat{y}(\mathbf{x})}{s}\right) + s\phi\left(\frac{Y_{min} - \hat{Y}(\mathbf{x})}{s}\right), \quad (\text{B.2})$$

with $\phi(\cdot)$, $\Phi(\cdot)$, respectively, the Probability Density Function (PDF) and Cumulative Distribution Function (CDF) of the normal distribution. Selecting the point with the highest expected improvement is achieved

either: (i) by maximizing the difference between the minimal value and the predicted response; or (ii) by increasing the standard deviation—see Fig. B.1. Hence, the first component is said to *exploit* the model while the other seeks to *explore* it. These two phases are here automatically selected. In [207], they proposed with the *Generalized Expected Improvement* a way to define a constant g to adjust the degree of *exploration vs exploitation*: $\mathbb{E}[I^g]$. The highest g is, the more exploratory the strategy is. Indeed, the initial EI strategy tends to add too much effort at improving the current solution and only then consider other regions of the parameters space. But this raises another concern about the value of this constant.



(a) Response surface of the Branin function

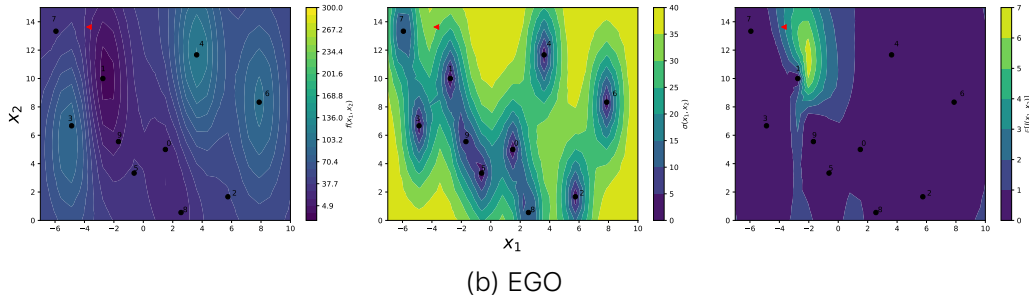


Figure B.1 – Visualization of EGO on the Branin function—see Appendix A.1. *Bottom-left* is the response surface of the current surrogate model constructed using samples represented by *black dots*. *Bottom-center* is the variance of the GP surrogate. *Bottom-right* is the expected improvement. The *red triangle* represents the global optimum of the function.

Thus, in this work we used the classical expected improvement formulation in order to avoid the definition of an additional constant. Due to the computational cost of the simulations, this parameter was not characterized.

C | Computational Fluid Dynamics

C.1 Governing Equations of Compressible Flows

To solve compressible flows, the governing equations are the total mass, the momentum and the energy conservation laws. They respectively write:

$$\frac{\partial \rho}{\partial t} + \frac{\partial(\rho u_i)}{\partial x_i} = 0, \quad (\text{C.1})$$

$$\frac{\partial(\rho u_i)}{\partial t} + \frac{\partial(\rho u_i u_j)}{\partial x_j} = -\frac{p}{\partial x_i} + \frac{\partial \tau_{ij}}{\partial x_j} + \rho f_j, \quad (\text{C.2})$$

$$\frac{\partial(\rho e_t)}{\partial t} + \frac{\partial(\rho u_i e_t)}{\partial x_i} = -\frac{\partial q_i}{\partial x_i} - \frac{\partial(p u_i)}{\partial x_i} + \frac{\partial(\tau_{i,j} u_i)}{\partial x_j} + \dot{Q} + \rho f_i u_i. \quad (\text{C.3})$$

These equations are the Navier-Stokes equations and they are here presented in Cartesian coordinates using the conventional Einstein notation.

In Eq. (C.1), x_i and u_i are the i th spatial coordinate, and ρ is the fluid density. In the momentum conservation equation (Eq. (C.2)), p is the static pressure, f_j is the volume force in the direction j and τ_{ij} is the viscous stress tensor:

$$\tau_{ij} = -\frac{2}{3}\mu \frac{\partial u_k}{\partial x_k} \delta_{ij} + \mu \left(\frac{\partial u_i}{\partial x_j} + \frac{\partial u_j}{\partial x_i} \right), \quad (\text{C.4})$$

where μ is the dynamic viscosity of the fluid ($\mu = \rho\nu$, with ν the kinematic viscosity), and δ_{ij} is the Kronecker symbol ($\delta_{ij} = 1$ if $i = j$, 0 otherwise).

Finally, Eq. (C.3) is the energy conservation equation, written with the total energy e_t . \dot{Q} is the heat source term and the energy flux q_i is defined as:

$$q_i = -\lambda \frac{\partial T}{\partial x_i}, \quad (\text{C.5})$$

where T is the fluid temperature and λ is the thermal conductivity of the fluid.

In this work, the Navier-Stokes equations are closed using the perfect gas state equation:

$$p = \rho R T, \quad (\text{C.6})$$

with the perfect gas constant $R = 8,314 \text{ J mol}^{-1} \text{ K}^{-1}$.

C.2 Turbulence Modelling

Turbulence is a natural regime of viscous flows characterized by an apparent random and chaotic behaviour of the flow structures. Despite turbulence being a complex phenomenon, its mechanism was identified by Kolmogorov [124] who theorized the idea of the energetic cascade of turbulence. Figure C.1 presents an illustration of the energetic cascade. The energy of turbulence $E(\kappa)$ is expressed as a function of the wavenumber κ . The turbulent kinetic energy is produced by the largest turbulent structures which are associated to the small values of κ . The characteristic size l_0 is called the integral scale and is related to the mean flow geometry. The turbulent energy is transmitted to smaller turbulent scales by stretching the largest eddies, leading to the formation of smaller coherent structures. The smallest eddies of the flow are defined by a characteristic size κ_η , called the Kolmogorov scale. At this point, the eddies dissipate the turbulent energy by viscous effect.

Different approaches may be used to solve the turbulent flow equations. The Direct Numerical Simulation (DNS) approach solves these equation on all fluid scales, which leads to a very good accuracy but also a high computational cost. Large Eddy Simulation (LES) and Reynolds-Averaged Navier-Stokes (RANS) are two approaches that model the turbulence. LES only models the smallest scales while RANS models all scales. It means that the result of a RANS computation correspond to an averaging over time. Turbulence is hence filtered with this approach and only DNS and LES are able to account for such physical phenomena.

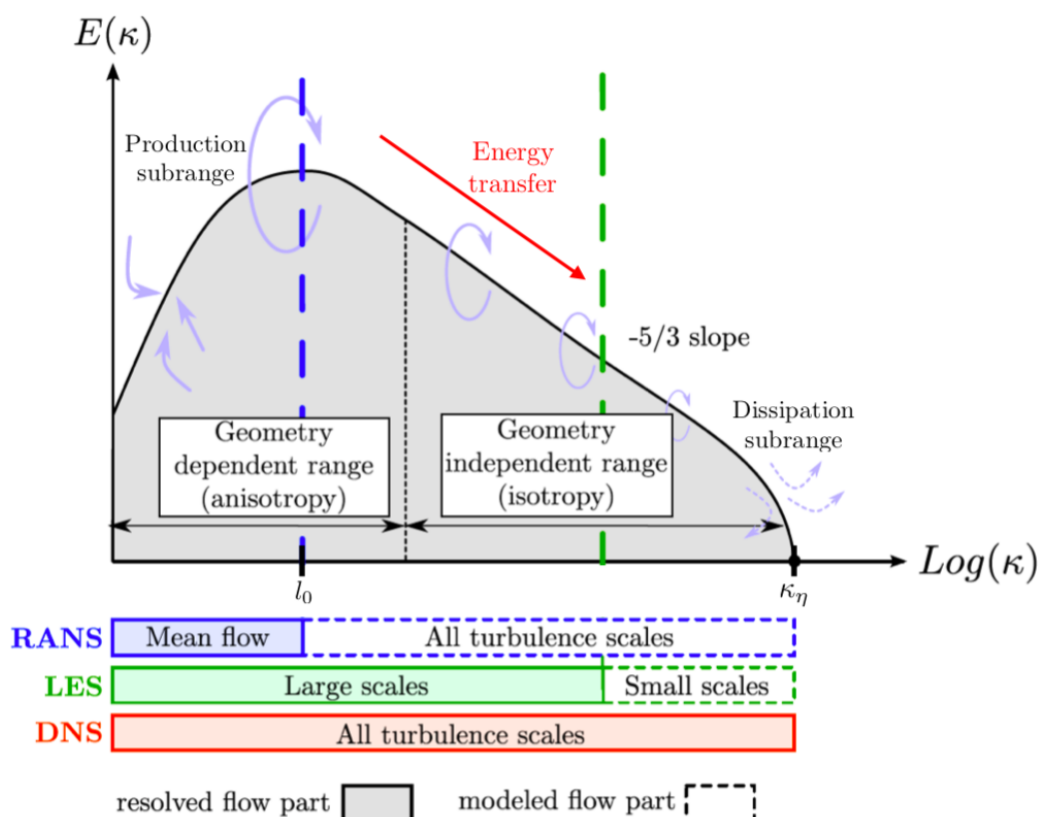


Figure C.1 – Energy spectrum associated to the different fluid scales.
Source [80].

D | Batman's API

Following is an extract of Batman's API. For an up to date version, refer to the only documentation:

<https://batman.readthedocs.io/en/develop/api.html>

API Reference

This is the class and function reference of batman. Please refer to previous sections for further details, as the class and function raw specifications may not be enough to give full guidelines on their uses.

batman.space: Parameter space

<code>space.Sample</code> ([space, data, plabels, ...])	Container class for samples.
<code>space.Space</code> (corners[, sample, nrefine, ...])	Manages the space of parameters.
<code>space.gp_sampler.GpSampler</code> (reference[, ...])	GpSampler class.
<code>space.Doe</code> (n_samples, bounds, kind[, dists, ...])	DOE class.
<code>space.Refiner</code> (data, corners[, delta_space, ...])	Resampling the space of parameters.

batman.surrogate: Surrogate Modelling

<code>surrogate.SurrogateModel</code> (kind, corners, ...)	Surrogate model.
<code>surrogate.Kriging</code> (sample, data[, kernel, ...])	Kriging based on Gaussian Process.
<code>surrogate.PC</code> (strategy, degree, distributions)	Polynomial Chaos class.
<code>surrogate.RBFnet</code> (trainIn, trainOut[, ...])	RBF class.
<code>surrogate.SklearnRegressor</code> (sample, data, ...)	Interface to Scikit-learn regressors.
<code>surrogate.Evofusion</code> (sample, data)	Multifidelity algorithm using Evofusion.
<code>surrogate.Mixture</code> (samples, data, corners[, ...])	Mixture class.

batman.uq: Uncertainty Quantification

<code>uq.UQ</code> (surrogate[, dists, nsample, method, ...])	Uncertainty Quantification class.
<code>uq.cosi</code> (sample, data)	Cosine transformation sensitivity.

batman.visualization: Uncertainty Visualization

<code>visualization.Kiviat3D</code> (sample, data[, idx, ...])	3D version of the Kiviat plot.
<code>visualization.Tree</code> (sample, data[, bounds, ...])	Tree.
<code>visualization.HdrBoxplot</code> (data[, variance, ...])	High Density Region boxplot.
<code>visualization.doe</code> (sample[, plabels, ...])	Plot the space of parameters 2d-by-2d.
<code>visualization.response_surface</code> (bounds[, ...])	Response surface visualization in 2d (image), 3d (movie) or 4d (movies).
<code>visualization.sensitivity_indices</code> (indices[, ...])	Plot Sensitivity indices.
<code>visualization.cusunoro</code> (sample, data[, ...])	Cumulative sums of normalised reordered output.
<code>visualization.moment_independent</code> (sample, data)	Moment independent measures.
<code>visualization.corr_cov</code> (data, sample, xdata)	Correlation and covariance matrices.
<code>visualization.pdf</code> (data[, xdata, xlabel, ...])	Plot PDF in 1D or 2D.
<code>visualization.kernel_smoothing</code> (data[, optimize])	Create gaussian kernel.
<code>visualization.reshape</code> (fig)	Create a dummy figure and use its manager to display <code>fig</code> .
<code>visualization.mesh_2D</code> (fname[, var, flabels, ...])	Visualization of specific variable on a user provided 2D mesh.

batman.pod: Proper Orthogonal Decomposition

<code>pod.Pod</code> (corners[, tolerance, dim_max])	POD class.
------------------------------------------------------	------------

batman.functions: Functions

<code>functions.data</code>	Data module
<code>functions.DbGeneric</code> ([space, data, fnames])	Generic database class.
<code>functions.analytical.SixHumpCamel</code> ()	SixHumpCamel class [Molga2005].

APPENDIX D. BATMAN'S API

<code>functions.analytical.Branin()</code>	Branin class [Forrester2008].
<code>functions.analytical.Michalewicz ([d, m])</code>	Michalewicz class [Molga2005].
<code>functions.analytical.Ishigami ([a, b])</code>	Ishigami class [Ishigami1990].
<code>functions.analytical.Rastrigin ([d])</code>	Rastrigin class [Molga2005].
<code>functions.analytical.G_Function ([d, a])</code>	G_Function class [Saltelli2000].
<code>functions.analytical.Forrester ([fidelity])</code>	Forrester class [Forrester2007].
<code>functions.analytical.ChemicalSpill ([s, tstep])</code>	Environmental Model class [Bliznyuk2008].
<code>functions.analytical.Channel_Flow ([dx, ...])</code>	Channel Flow class.
<code>functions.analytical.Manning ([width, slope, ...])</code>	Manning equation for rectangular channel class.
<code>functions.db_Mascaret ([fname, multizone])</code>	Mascaret class.
<code>functions.utils.multi_eval (fun)</code>	Detect space or unique point.
<code>functions.utils.output_to_sequence (fun)</code>	Convert float output to list.

batman.tasks : Tasks

<code>tasks.ProviderFunction (plabels, flabels, ...)</code>	Provides Snapshots built through an external python function.
<code>tasks.ProviderFile (plabels, flabels, file_pairs)</code>	Provides Snapshots loaded from a list of files.
<code>tasks.ProviderJob (plabels, flabels, command, ...)</code>	Provides Snapshots built through a 3rd-party program.

batman.misc : Misc

<code>misc.NestedPool ([processes, initializer, ...])</code>	NestedPool class.
<code>misc.ProgressBar (total)</code>	Print progress bar in console.
<code>misc.optimization (bounds[, discrete])</code>	Perform a discret or a continuous/discrete optimization.
<code>misc.import_config (path_config, path_schema)</code>	Import a configuration file.
<code>misc.check_yes_no (prompt, default)</code>	Ask user for delete confirmation.
<code>misc.ask_path (prompt, default, root)</code>	Ask user for a folder path.

<code>misc.abs_path</code> (value)	Get absolute path.
<code>misc.clean_path</code> (path)	Return an absolute and normalized path.

batman.input_output: Input Output

<code>input_output.available_formats</code> ()	Return the list of available format names.
<code>input_output.formater</code> (format_name)	Return a Formater.

Bibliography

- [16] Agra, O., H. Demir, S. Atayilmaz, F. Kantas, and A. Dalkilic (2011, December). Numerical investigation of heat transfer and pressure drop in enhanced tubes. *International Communications in Heat and Mass Transfer* 38(10), 1384–1391.
- [17] ahlfeld, b. r., s. laizet, f. montomoli, g. geraci, and g. iaccarino (2016). multi-fidelity uncertainty quantification using rans and dns. In *center for turbulence research annual research briefs*.
- [18] Alexander, R. L., S. O'Modhrain, D. A. Roberts, J. A. Gilbert, and T. H. Zurbuchen (2014, jul). The bird's ear view of space physics: Audification as a tool for the spectral analysis of time series data. *Journal of Geophysical Research: Space Physics* 119(7), 5259–5271.
- [19] Aliaga, D. A., J. P. Lamb, and D. E. Klein (1994, February). Convection heat transfer distributions over plates with square ribs from infrared thermography measurements. *International Journal of Heat and Mass Transfer* 37(3), 363–374.
- [20] Androulakis, E., K. Drosou, C. Koukouvino, and Y. D. Zhou (2016). Measures of uniformity in experimental designs: A selective overview. *Communications in Statistics - Theory and Methods* 45(13), 3782–3806.
- [21] Anindya Chatterjee (2000a). An introduction to the proper orthogonal decomposition. *Current Science* 78(7).
- [22] Anindya Chatterjee (2000b). An introduction to the proper orthogonal decomposition. *Current Science* 78(7).
- [23] Anscombe, F. J. (1973). graphs in statistical analysis. *the american statistician* 27(1), 17–21.
- [24] Arts, T., M. Lambert de Rouvroit, and A. W. Rutherford (1990). Aero-Thermal Investigation of a Highly Loaded Transonic Linear Turbine Guide Vane Cascade. Technical Report 174, von Karman Institute for Fluid Dynamics.
- [25] Barthélémy, S. (2015). *Assimilation de donnée ensembliste et couplage de modèles hydrauliques 1D-2D pour la prévision des crues en temps réel: application au réseau hydraulique Adour Maritime*. Ph. D. thesis, Institut National Polytechnique de Toulouse.
- [26] Baudin, M., K. Boumhaout, T. Delage, B. Iooss, and J.-M. Martinez (2016). Numerical stability of Sobol' indices estimation formula. In *8th International Conference on Sensitivity Analysis of Model Output*, Réunion Island.
- [27] Baudin, M., A. Dutfoy, B. Iooss, and A.-L. Popelin (2015, jun). Open-TURNS: An industrial software for uncertainty quantification in simulation.

-
- [28] Becker, W. E., S. Tarantola, and G. Deman (2018). Sensitivity analysis approaches to high-dimensional screening problems at low sample size. *Journal of Statistical Computation and Simulation* 88(11), 2089–2110.
 - [29] Belia, S., F. Fidler, J. Williams, and G. Cumming (2005). Researchers misunderstand confidence intervals and standard error bars. *Psychological Methods* 10(4), 389–396.
 - [30] Berveiller, M. (2005). *Eléments finis stochastiques : approches intrusive et non intrusive pour des analyses de fiabilité*. Ph. D. thesis, Université Blaise Pascal, Clermont-Ferrand.
 - [31] Besnard, A. and N. Goutal (2011). Comparaison de modèles 1D à casiers et 2D pour la modélisation hydraulique d'une plaine d'inondation–Cas de la Garonne entre Tonneins et La Réole. *La Houille Blanche* 3, 42–47.
 - [32] Blatman, G. (2009). *Adaptive sparse Polynomial Chaos expansions for uncertainty propagation and sensitivity analysis*. Ph. D. thesis, Université Blaise Pascal, Clermont-Ferrand.
 - [33] Bonneau, G. P., H. C. Hege, C. R. Johnson, M. M. Oliveira, K. Potter, P. Rheingans, and T. Schultz (2014). Overview and state-of-the-art of uncertainty visualization. *Mathematics and Visualization* 37, 3–27.
 - [34] Borgonovo, E. (2007). A new uncertainty importance measure. *Reliability Engineering and System Safety* 92(6), 771–784.
 - [35] Borgonovo, E. and E. Plischke (2016). Sensitivity Analysis: a Review of Recent Advances. *European Journal of Operational Research* 248(3), 869–887.
 - [36] Bozzi, S., G. Passoni, P. Bernardara, N. Goutal, and A. Arnaud (2014). Roughness and Discharge Uncertainty in 1D Water Level Calculations. *Environmental Modeling & Assessment* 4.
 - [37] Braconnier, T., M. Ferrier, J.-C. Jouhaud, M. Montagnac, and P. Sagaut (2011). Towards an adaptive POD/SVD surrogate model for aeronautic design. *Computers & Fluids* 40(1), 195–209.
 - [38] Brodlie, K., R. Allendes Osorio, and A. Lopes (2012). A review of Uncertainty in Data Visualization. *Expanding the Frontiers of Visual Analytics and Visualization*, 81–109.
 - [39] Campet, R., M. Zhu, E. Riber, and B. Cuenot (2018). Large eddy simulation of a single-started ribbed tube with heat transfer. *International Journal of Heat and Mass Transfer*.
 - [40] Caniou, Y. (2012). *Analyse de sensibilité globale pour les modèles imbriqués et multiéchelles*. Ph. D. thesis.

- [41] Cavazzuti, M. (2013). Design of Experiments. In *Optimization Methods: From Theory to Design*, pp. 13–42. Springer Berlin Heidelberg.
- [42] Cha, S.-h. (2007). Comprehensive Survey on Distance / Similarity Measures between Probability Density Functions. *International Journal of Mathematical Models and Methods in Applied Sciences* 1(4), 300–307.
- [43] Cheng, L. and T. Chen (2006). Study of single phase flow heat transfer and friction pressure drop in a spiral internally ribbed tube. *Chemical Engineering & Technology*.
- [44] Ciriello, V., V. Di Federico, M. Riva, F. Cadini, J. De Sanctis, E. Zio, and A. Guadagnini (2013). Polynomial chaos expansion for global sensitivity analysis applied to a model of radionuclide migration in a randomly heterogeneous aquifer. *Stochastic Environmental Research and Risk Assessment* 27(4), 945–954.
- [45] Claessen, J. H. and J. J. Van Wijk (2011). Flexible linked axes for multivariate data visualization. *IEEE Transactions on Visualization and Computer Graphics* 17(12), 2310–2316.
- [46] Clarke, B., E. Fokoue, and H. H. Zhang (1992). *Breakthroughs in Statistics* 2. Springer Series in Statistics. new york, ny: Springer new york.
- [47] Cloke, H. and F. Pappenberger (2009). Ensemble flood forecasting: A review. *Journal of Hydrology* 375, 613–626.
- [48] Colin, O. and M. Rudgyard (2000). Development of high-order taylor-galerkin schemes for unsteady calculation. *J. Comp. Physics* 162(2), 338–371.
- [49] Courrier, N., P. A. Boucard, and B. Soulier (2016). Variable-fidelity modeling of structural analysis of assemblies. *Journal of global optimization* 64(3), 577–613.
- [50] Crombecq, K., E. Laermans, and T. Dhaene (2011). Efficient space-filling and non-collapsing sequential design strategies for simulation-based modeling. *European Journal of Operational Research* 214(3), 683–696.
- [51] Damblin, G., M. Couplet, B. Iooss, G. Damblin, M. Couplet, and B. Iooss (2013). Numerical studies of space filling designs : optimization of Latin Hypercube Samples and subprojection properties. *Journal of Simulation*, 276–289.
- [52] Dapogny, C., C. Dobrzynski, and P. Frey (2014). Three-dimensional adaptive domain remeshing, implicit domain meshing, and applications to free and moving boundary problems. *J. Comp. Physics* 262, 358–378.

-
- [53] Daviller, G., M. Brebion, P. Xavier, G. Staffelbach, J.-D. Müller, and T. Poinsot (2017, mar). A mesh adaptation strategy to predict pressure losses in LES of swirled flows. *Flow, Turbulence and Combustion*.
 - [54] Dechant, C. and H. Moradkhani (2011). Improving the characterization of initial condition for ensemble streamflow prediction using data assimilation. *Hydrology and Earth System Sciences* 15, 3399–3410.
 - [55] DeGennaro, A. M., C. W. Rowley, and L. Martinelli (2015, sep). Uncertainty Quantification for Airfoil Icing Using Polynomial Chaos Expansions. *Journal of Aircraft* 52(5), 1404–1411.
 - [56] Deman, G., K. Konakli, B. Sudret, J. Kerrou, P. Perrochet, and H. Benabderrahmane (2015). Using sparse polynomial chaos expansions for the global sensitivity analysis of groundwater lifetime expectancy in a multi-layered hydrogeological model. *Reliability Engineering and System Safety* 147, 156–169.
 - [57] Dette, H. and A. Pepelyshev (2010). Generalized Latin Hypercube Design for Computer Experiments. *Technometrics* 52(4), 421–429.
 - [58] Dittus, F. and L. Boelter (1930). Heat transfer in automobile radiators of the tubular type. *University of California publications in Engineering* 2, 371.
 - [59] Draper, D. (1995). Assessment and Propagation of Model Uncertainty. *Journal of the Royal Statistical Society B* 57(1), 45–97.
 - [60] Dubreuil, S., M. Berveiller, F. Petitjean, and M. Salaün (2014). Construction of bootstrap confidence intervals on sensitivity indices computed by polynomial chaos expansion. *Reliability Engineering and System Safety* 121, 263–275.
 - [61] Duchaine, F., T. Morel, and L. Y. M. Gicquel (2009, mar). Computational-Fluid-Dynamics-Based Kriging Optimization Tool for Aeronautical Combustion Chambers. *AIAA Journal* 47(3), 631–645.
 - [62] Dupuis, R., J.-C. Jouhaud, and P. Sagaut (2018, jan). Aerodynamic Data Predictions for Transonic Flows via a Machine-Learning-based Surrogate Model. In *2018 AIAA/ASCE/AHS/ASC Structures, Structural Dynamics, and Materials Conference*, Number January, Reston, Virginia, pp. 1–23. American Institute of Aeronautics and Astronautics.
 - [63] Durand, M., K. Andreadis, D. Alsdorf, D. Lettenmaier, D. Moller, and M. Wilson (2008). Estimation of bathymetric depth and slope from data assimilation of swath altimetry into a hydrodynamic model. *Geophysical Research Letters* 35, 1–5.
 - [64] Dutka-Malen, I., R. Lebrun, B. Saassouh, and B. Sudret (2009). Implementation of a polynomial chaos toolbox in openturns with test-case application. In *Conference: Proc. 10th Int. Conf. Struct. Safety and Reliability (ICOSSAR'2009)*, Osaka, Japan.

- [65] Ehlschlaeger, C. R., A. M. Shortridge, and M. F. Goodchild (1997). Visualizing spatial data uncertainty animation using animation. *Computers & Geosciences* 23(4), 387–395.
- [66] Eiamsa-ard, S. and P. Promvonge (2008, August). Numerical study on heat transfer of turbulent channel flow over periodic grooves. *International Communications in Heat and Mass Transfer* 35(7), 844–852.
- [67] El Moçayd, N. (2017). *La décomposition en polynômes du chaos pour l'amélioration de l'assimilation de données ensembliste en hydraulique fluviale*. Ph. D. thesis, Institut National Polytechnique de Toulouse.
- [68] El Moçayd, N., S. Ricci, N. Goutal, M. Rochoux, S. Boyaval, C. Goeury, D. Lucor, and O. Thual (2017). Polynomial surrogate model for open-channel flows in steady state.
- [69] ELSheikh, A. H., C. C. Pain, F. Fang, J. L. M. A. Gomes, and I. M. Navon (2013). Parameter estimation of subsurface flow models using iterative regularized ensemble kalman filter. *Stochastic Environmental Research and Risk Assessment* 27(4), 877–897.
- [70] Emory, M., G. Iaccarino, and L. Ma (2016). Uncertainty Quantification in Turbomachinery Simulations. Turbomachinery Technical Conference and Exposition, pp. 1–10.
- [71] Fang, K.-T., R. Z. Li, and A. Sudjianto (2006). *Design and modeling for computer experiments*. Chapman & Hall/CRC.
- [72] Fernandez, G., C. Park, N. H. Kim, and R. Haftka (2017). Review of multi-fidelity models. (March).
- [73] Ferretti, F., A. Saltelli, and S. Tarantola (2016, oct). Trends in sensitivity analysis practice in the last decade. *Science of The Total Environment* 568, 666–670.
- [74] Fontaneto, F. (2014). *Aero-thermal performance of a film-cooled high pressure turbine blade/vane: a test case for numerical codes validation*. PhD thesis, University of Bergamo.
- [75] Forrester, A. I., N. W. Bressloff, and A. J. Keane (2006). Optimization using surrogate models and partially converged computational fluid dynamics simulations. *Proceedings of the Royal Society A: mathematical, physical and engineering sciences* 462(2071), 2177–2204.
- [76] Forrester, A. I., A. Sóbester, and A. J. Keane (2007, dec). Multi-fidelity optimization via surrogate modelling. *Proceedings of the Royal Society A: Mathematical, Physical and Engineering Sciences* 463(2088), 3251–3269.

-
- [77] Forrester, A. I. J. and A. J. Keane (2009). Recent advances in surrogate-based optimization. *Progress in Aerospace Sciences* 45(1-3), 50–79.
- [78] Forrester, A. I. J., A. Sóbester, and A. J. Keane (2008). *Engineering design via surrogate modelling*.
- [79] Franco, J., O. Vasseur, B. Corre, and M. Sergent (2009). Minimum Spanning Tree: A new approach to assess the quality of the design of computer experiments. *Chemometrics and Intelligent Laboratory Systems* 97(2), 164–169.
- [80] Fransen, R. (2013). *LES based aerothermal modeling of turbine blade cooling systems*. Ph. D. thesis, Institut National Polytechnique de Toulouse.
- [81] Frazier, W. E. (2014). Metal additive manufacturing: a review. *Journal of Materials Engineering and Performance* 23(6), 1917–1928.
- [82] Garcia, A., J. Solano, P. Vicente, and A. Viedma (2012, March). The influence of artificial roughness shape on heat transfer enhancement: Corrugated tubes, dimpled tubes and wire coils. *Applied Thermal Engineering* 35, 196–201.
- [83] Garud, S. S., I. A. Karimi, and M. Kraft (2017, nov). Design of computer experiments: A review. *Computers & Chemical Engineering* 106(182), 71–95.
- [84] Gee, D. L. and R. L. Webb (1980, August). Forced convection heat transfer in helically rib-roughened tubes. *Journal of heat transfer* 23(8), 1127–1136.
- [85] Ghanem, R., D. Higdon, and H. Owhadi (Eds.) (2017). *Handbook of Uncertainty Quantification*.
- [86] Gicquel, L., N. Gourdain, J.-F. Boussuge, H. Deniau, G. Staffelbach, P. Wolf, and T. Poinsot (2011). High performance parallel computing of flows in complex geometries. *Comptes Rendus Mécanique* 339(2-3), 104 – 124.
- [87] Gigerenzer, G. and U. Hoffrage (1995). How to improve bayesian reasoning without instruction : frequency formats. *Psychological Review* 102(4), 684–704.
- [88] Goodfellow, I., Y. Bengio, and A. Courville (2016). *Deep Learning*. MIT Press. <http://www.deeplearningbook.org>.
- [89] Gourdain, N., F. Duchaine, E. Collado, and L. Gicquel (2010, June). Advanced numerical simulation dedicated to the prediction of heat transfer in a highly loaded turbine guide vane. ASME Turbo expo, Glasgow, UK.

- [90] Goutal, N., J.-M. Lacombe, F. Zaoui, and E.-K.-A. K. (2012). Mascaret: a 1-d open sources software for flow hydrodynamic and water quality in open channel networks. *River Flow*, 1169–1174.
- [91] Goutal, N. and F. Maurel (2002). A finite volume solver for 1D shallow-water equations applied to an actual river. *International Journal for Numerical Methods in Fluids* 38(1), 1–19.
- [92] Gratiet, L. L., S. Marelli, and B. Sudret (2016). Metamodel-based sensitivity analysis: Polynomial chaos expansions and gaussian processes. In R. Ghanem, D. Higdon, and H. Owhadi (Eds.), *Handbook of Uncertainty Quantification*, pp. 1–37. Cham: Springer International Publishing.
- [93] Habert, J., S. Ricci, E. Le Pape, O. Thual, A. Piacentini, N. Goutal, G. Jonville, and M. Rochoux (2016). Reduction of the uncertainties in the water level-discharge relation of a 1D hydraulic model in the context of operational flood forecasting. *Journal of Hydrology* 532, 52–64.
- [94] Hackstadt, S. T., A. D. Malony, and B. Mohr (1994). Scalable performance visualization for data-parallel programs. *Scalable High-Performance Computing Conf.*, 342–349.
- [95] Hastie, T., R. Tibshirani, and J. Friedman (2009). *The Elements of Statistical Learning*, Volume 2 of *Springer Series in Statistics*. New York, NY: Springer New York.
- [96] Hastings, W. K. (1970, apr). Monte Carlo Sampling Methods Using Markov Chains and Their Applications. *Biometrika* 57(1), 97.
- [97] Hoffman, M. D. and A. Gelman (2011). The No-U-Turn Sampler: Adaptively Setting Path Lengths in Hamiltonian Monte Carlo. (2008), 1–30.
- [98] Horritt, M. and P. Bates (2002). Evaluation of 1d and 2d numerical models for predicting river flood inundation. *Journal of Hydrology* 268, 87–99.
- [99] Hosder, S. Perez, R. and R. Walters (2006). A non-intrusive polynomial chaos method for uncertainty propagation in cfd simulations. In *48th AIAA Aerospace Sciences Meeting and Exhibit*, Number AIAA-2010-0129. The American Institute of Aeronautics and Astronautics, Inc.
- [100] Hughes, S. A. (2003). Listening to the universe with gravitational-wave astronomy. *Annals of Physics* 303(1), 142–178.
- [101] Hullman, J., P. Resnick, and E. Adar (2015). Hypothetical outcome plots outperform error bars and violin plots for inferences about reliability of variable ordering. *Plos One*, 1–25.

-
- [102] Hyndman, R. J. and H. L. Shang (2009). Rainbow plots , bagplots and boxplots for functional data. *Journal of Computational and Graphical Statistics* 19, 29–45.
- [103] Iaccarino, G., A. Ooi, P. Durbin, and M. Behnia (2002, June). Conjugate heat transfer predictions in two-dimensional ribbed passages. *International Journal of Heat and Fluid Flow* 23(3), 340–345.
- [104] Inselberg, A. (1985, August). The Plane with Parallel Coordinates. *The Visual Computer* 1(2), 69–91.
- [105] Inselberg, A. (2009). *Parallel Coordinates*. Springer New York.
- [106] Iooss, B., L. Boussouf, V. Feuillard, and A. Marrel (2010). Numerical studies of the metamodel fitting and validation processes. *International Journal on Advances in Systems and Measurements* 3(1), 11–21.
- [107] Iooss, B. and C. Prieur (2017). Shapley effects for sensitivity analysis with dependent inputs: comparisons with Sobol' indices, numerical estimation and applications.
- [108] Iooss, B. and A. Saltelli (2016). Introduction to Sensitivity Analysis. In *Handbook of Uncertainty Quantification*, pp. 1–20. Springer International Publishing.
- [109] Ishigami, T. and T. Homma (1990). An importance quantification technique in uncertainty analysis for computer models. *IEEE*, 398–403.
- [110] Jimenez, J. (2004, January). Turbulent flow over rough walls. *Annual Review of Fluid Mechanics* 36, 173–196.
- [111] Jimenez, J. and P. Moin (1991). The minimal flow unit in near-wall turbulence. *Journal of Fluid Mechanics* 225, 213–240.
- [112] Jones, D. R., M. Schonlau, and J. William (1998). Efficient Global Optimization of Expensive Black-Box Functions. *Journal of Global Optimization* 13.
- [113] Jordan, S. A. (2003, December). The turbulent character and pressure loss produced by periodic symmetric ribs in a circular duct. *International Journal of Heat and Fluid Flow* 24(6), 795–806.
- [114] Joseph, V. R., E. Gul, and S. Ba (2015). Maximum projection designs for computer experiments. *Biometrika* 102(2), 371–380.
- [115] Kale, A., F. Nguyen, M. Kay, and J. Hullman (2018). Hypothetical Outcome Plots Help Untrained Observers Judge Trends in Ambiguous Data. *Transactions on Visualization and Computer Graphics*.

- [116] Kamali, R. and A. Binesh (2008, October). The importance of rib shape effects on the local heat transfer and flow friction characteristics of square ducts with ribbed internal surfaces. *International Communications in Heat and Mass Transfer* 35(8), 1032–1040.
- [117] Kay, M., T. Kola, J. R. Hullman, and S. A. Munson (2016). When (ish) is my bus? user-centered visualizations of uncertainty in everyday, mobile predictive systems. In *proceedings of the 2016 chi conference on human factors in computing systems*, pp. 5092–5103.
- [118] kennedy, m. c. and a. o'hagan (2000). predicting the output from a complex computer code when fast approximations are available. *biometrika* 87(1), 1–13.
- [119] kennedy, m. c. and a. o'hagan (2001, aug). bayesian calibration of computer models. *journal of the royal statistical society: series b (statistical methodology)* 63(3), 425–464.
- [120] Kim, H. and K. Kim (2004, November). Design optimization of rib-roughened channel to enhance turbulent heat transfer. *International Journal of Heat and Mass Transfer* 47(23), 5159–5168.
- [121] Kim, J., K. Jansen, and M. Jensen (2004, January). Simulation of three-dimensional incompressible turbulent flow inside tubes with helical fins. *Numerical Heat Transfer Part B* 46(3), 195–221.
- [122] Kim, J., P. Moin, and R. D. Moser (1987, April). Turbulence statistics in fully developed channel flow at low reynolds number. *Journal of Fluid Mechanics* 177, 133–166.
- [123] Kohavi, R. (1995). A Study of Cross-Validation and Bootstrap for Accuracy Estimation and Model Selection. In *International Joint Conference on Artificial Intelligence*.
- [124] Kolmogorov, A. N. (1941). The local structure of turbulence in incompressible viscous fluid for very large reynolds numbers. *Doklady Akademii Nauk SSSR* 30, 301–305.
- [125] Krause, P., D. P. Boyle, and F. Bäse (2005). Comparison of different efficiency criteria for hydrological model assessment. *Advances in Geosciences* 5(89), 89–97.
- [126] Krige, D. G., M. Guarascio, and F. A. Camisani-Calzolari (1989). Early South African geostatistical techniques in today's perspective. *Geostatistics* 1, 1–19.
- [127] Kucherenko, S., D. Albrecht, and A. Saltelli (2015). Exploring multi-dimensional spaces: a comparison of latin hypercube and quasi monte carlo sampling techniques. *The 8th IMACS seminar on Monte Carlo methods*, 1–32.

-
- [128] Kucherenko, S. and S. Song (2016). Derivative-based global sensitivity measures and their link with sobol' sensitivity indices. *Springer Proceedings in Mathematics and Statistics* 163, 455–469.
- [129] Kucherenko, S. and S. Song (2017). Different numerical estimators for main effect global sensitivity indices. *Reliability Engineering and System Safety* 165(April), 222–238.
- [130] Kucherenko, S., S. Tarantola, and P. Annoni (2012). Estimation of global sensitivity indices for models with dependent variables. *Computer Physics Communications* 183(4), 937–946.
- [131] Lamboni, M., H. Monod, and D. Makowski (2011). Multivariate sensitivity analysis to measure global contribution of input factors in dynamic models. *Reliability Engineering and System Safety* 96(4), 450–459.
- [132] Le Gratiet, L. (2013). *Multi-fidelity gaussian process regression for computer experiments*. Ph. D. thesis, Université de paris-diderot.
- [133] Le Gratiet, L., C. Cannamela, and B. Iooss (2014). A bayesian approach for global sensitivity analysis of (multifidelity) computer codes. *SIAM/ASA Journal on Uncertainty Quantification* 2(1), 336–363.
- [134] Le Gratiet, L., S. Marelli, and B. Sudret (2017). Metamodel-Based Sensitivity Analysis: Polynomial Chaos Expansions and Gaussian Processes. In *Handbook of Uncertainty Quantification*, pp. 1–37. Springer International Publishing.
- [135] Le Maître, O. and O. Knio (2010). *Spectral Methods for Uncertainty Quantification*. Springer.
- [136] Le Maître, O. P. and O. M. Knio (2010). *Spectral Methods for Uncertainty Quantification*.
- [137] Lekivetz, R. and B. Jones (2015, jul). Fast Flexible Space-Filling Designs for Nonrectangular Regions. *Quality and Reliability Engineering International* 31(5), 829–837.
- [138] Lewandowski, J. J. and M. Seifi (2016). Metal additive manufacturing: a review of mechanical properties. *Annual Review of Materials Research* 46(1), 151–186.
- [139] Li, J. and D. Xiu (2008). On numerical properties of the ensemble Kalman filter for data assimilation. *Comput. Methods Appl. Mech. Engrg.* 197, 3574–3583.
- [140] Li, J. and D. Xiu (2009). A generalized polynomial chaos based ensemble kalman filter with high accuracy. *Journal of Computational Physics* 228(15), 5454–5469.

- [141] Liang, G., C. Kwok Fai, and M. H. Kobayashi (2008). Stochastic solution for uncertainty propagation in nonlinear shallow-water equations. *Journal of Hydraulic Engineering* 134(12), 1732–1743.
- [142] Lilley, D. G. (1977). Swirl flows in combustion: a review. *AIAA Journal* 15(8), 1063–1078.
- [143] Liou, T., S. Chen, and K. Shih (2002, October). Numerical simulation of turbulent flow field and heat transfer in a two-dimensional channel with periodic slit ribs. *International Journal of Heat and Mass Transfer* 45(22), 4493–4505.
- [144] Liou, T., J. Hwang, and S. Chen (1993, January). Simulation and measurement of enhanced turbulent heat transfer in a channel with periodic ribs on one principal wall. *International Journal of Heat and Mass Transfer* 36(2), 507–517.
- [145] Liu, H., Y. S. Ong, and J. Cai (2018). A survey of adaptive sampling for global metamodeling in support of simulation-based complex engineering design. *Structural and Multidisciplinary Optimization* 57(1), 393–416.
- [146] Liu, X. and M. Jensen (2001, May). Geometry effects on turbulent flow and heat transfer in internally finned tubes. *Journal of Heat Transfer* 123(6), 1035–1044.
- [147] Lockwood, B. and M. Anitescu (2012). Gradient-enhanced universal kriging for uncertainty propagation. *Nuclear Science and Engineering*, 1–32.
- [148] Lucor, D., J. Meyers, and P. Sagaut (2007, aug). Sensitivity analysis of large-eddy simulations to subgrid-scale-model parametric uncertainty using polynomial chaos. *Journal of Fluid Mechanics* 585, 255–279.
- [149] Ma, T., Q. Wang, M. Zeng, Y. Chen, Y. Liu, and V. Nagarajan (2012, November). Study on heat transfer and pressure drop performances of ribbed channel in the high temperature heat exchanger. *Applied Energy* 99, 393–401.
- [150] Margheri, L. and P. Sagaut (2016). A hybrid anchored-ANOVA-POD/Kriging method for uncertainty quantification in unsteady high-fidelity CFD simulations. *Journal of Computational Physics* 324, 137–173.
- [151] Marrel, A., B. Iooss, S. Da Veiga, and M. Ribatet (2012, may). Global sensitivity analysis of stochastic computer models with joint metamodels. *Statistics and Computing* 22(3), 833–847.
- [152] Marrel, A., B. Iooss, B. Laurent, and O. Roustant (2009). Calculations of sobol indices for the gaussian process metamodel. *Reliability Engineering & System Safety* 94(3), 742 – 751.

-
- [153] Marrel, A., N. Saint-Geours, and M. De Lozzo (2015). Sensitivity Analysis of Spatial and/or Temporal Phenomena. In *Handbook of Uncertainty Quantification*, pp. 1–31. Springer International Publishing.
- [154] Martin, J. D. and T. W. Simpson (2005). Use of Kriging Models to Approximate Deterministic Computer Models. *AIAA Journal* 43(4), 853–863.
- [155] Masquelet, M., J. Yann, A. Dord, G. Laskowski, S. Lee, L. Jofre, and G. Iaccarino (2017). Uncertainty Quantification in Large Eddy Simulations of a Rich-Dome Aviation Gas Turbine. ASME Turbo Expo 2017: Turbine Technical Conference and Exposition, pp. 1–11.
- [156] Matgen, P., M. Montanari, R. Hostache, L. Pfister, L. Hoffmann, D. Plaza, V. Pauwels, G. De Lannoy, R. De Keyser, and H. Savenije (2010). Towards the sequential assimilation of SAR-derived water stages into hydraulic models using the Particle Filter: Proof of concept. *Hydrology and Earth System Sciences* 14, 1773–1785.
- [157] Mayo, I., B. C. Cernat, M. Virgilio, A. Pappa, and T. Arts (2016). Aerothermal investigation on the flow and heat transfer in a helically corrugated cooling channel. In *ASME Turbo Expo 2016: Turbine Technical Conference and Exposition*.
- [158] McKay, M. D., R. J. Beckman, and W. J. Conover (1979). A Comparison of Three Methods for Selecting Values of Input Variables in the Analysis of Output from a Computer Code. *Technometrics* 21(2), 239–245.
- [159] Merkle, K. (2006). *Einfluss gleich- und gegensinniger drehrichtung der verbrennungsluftströme auf die stabilisierung turbulenter doppeldrall-diffusionsflammen*. Ph. D. thesis, Universität Fridericiana Karlsruhe.
- [160] Migliorati, G., F. Nobile, E. Von Schwerin, and R. Tempone (2013). Approximation of quantities of interest in stochastic PDEs by the random Discret L2 Projection on polynomial spaces. *SIAM J. Sci Comput.* 35(3), A1440–A1460.
- [161] Molga, M. and C. Smutnicki (2005). Test functions for optimization needs. (c), 1–43.
- [162] Moradkhani, H., S. Sorooshian, H. Gupta, and P. Houser (2005). Dual state-parameter estimation of hydrological models using ensemble Kalman filter. *Advances in Water Resources* 28, 135–147.
- [163] Moreland, K. (2016). Why we use bad color maps and what you can do about it. In *Proceedings of Human Vision and Electronic Imaging (HVEI)*.
- [164] Morris, M. D. (1991). Factorial sampling plans for preliminary computational experiments. *Technometrics* 33(2), 161–174.

- [165] Nagano, Y., H. Hattori, S. Y. Yasui, and T. Houra (2004, June). Dns of velocity and thermal field in turbulent channel flow with transverse-rib roughness. *International Journal of Heat and Fluid Flow* 25(3), 393–403.
- [166] Nicoud, F., H. Baya Toda, o. Cabrit, S. Bose, and J. Lee (2011). Using singular values to build a subgrid-scale model for large eddy simulations. *Phys. Fluids* 23.
- [167] Nicoud, F. and F. Ducros (1999). Subgrid-scale stress modelling based on the square of the velocity gradient. *Flow Turb. and Combustion* 62(3), 183–200.
- [168] Oakley, J. and A. O'Hagan (2004). Probabilistic sensitivity analysis of complex models: a bayesian approach. *Journal of the Royal Statistical Society: Series B (Statistical Methodology)* 66(3), 751–769.
- [169] Ooi, A., G. Iaccarino, P. Durbin, and M. Behnia (2002, December). Reynolds averaged simulation of flow and heat transfer in ribbed ducts. *International Journal of Heat and Fluid Flow* 23(6), 750–757.
- [170] Owen, A. B. (1998). Scrambling Sobol' and Niederreiter-Xing points. *Journal of Complexity* 14(4), 466–489.
- [171] Owen, N., P. Challenor, P. P. Menon, and S. Bennani (2017). Comparison of surrogate-based uncertainty quantification methods for computationally expensive simulators. *SIAM/ASA J. Uncertainty Quantification* 5(1), 403–435.
- [172] Padron, A. S., J. J. Alonso, F. Palacios, M. F. Barone, and M. S. Eldred (2014, jun). Multi-fidelity uncertainty quantification: application to a vertical axis wind turbine under an extreme gust. In *15th aiaa/issmo multidisciplinary analysis and optimization conference*, Number june, reston, virginia, pp. 1–18. AIAA.
- [173] Parrish, M., H. Moradkhani, and C. Dechant (2012). Toward reduction of model uncertainty: Integration of Bayesian model averaging and data assimilation. *Water Resources Research* 48(W03519), 1–18.
- [174] Pedregosa, F., G. Varoquaux, A. Gramfort, V. Michel, B. Thirion, O. Grisel, M. Blondel, P. Prettenhofer, R. Weiss, V. Dubourg, J. Vanderplas, A. Passos, D. Cournapeau, M. Brucher, M. Perrot, and É. Duchesnay (2012). Scikit-learn: Machine Learning in Python. *Journal of Machine Learning Research* 12(2825–2830).
- [175] Peherstorfer, B. and K. Willcox (2016). Survey of multifidelity methods in uncertainty propagation, inference, and optimization. Technical report, Aerospace computational design laboratory.
- [176] Perry, A. E., W. H. Schofield, and P. N. Joubert (1969, June). Rough wall turbulent boundary layers. *Journal of Fluid Mechanics* 37(2), 383–413.

-
- [177] Petukhov, B. and V. Popov (1963). Theoretical calculation of heat exchange and frictional resistance in turbulent flow in tubes of an incompressible fluid with variable physical properties. *High Temperature Heat Physics* 1, 69–83.
- [178] Pichler, R., J. Kopriva, G. Laskowski, V. Michelassi, and R. Sandberg (2016). Highly resolved LES of a linear hpt vane cascade using structured and unstructured codes. In *Turbomachinery Technical Conference and Exposition gt2016*, Seoul, pp. 1–10.
- [179] Pilkey, O. H. and L. Pilkey-Jarvis (2006). *Useless Arithmetic: Why Environmental Scientists Can't Predict the Future*.
- [180] Plischke, E. (2012). An adaptive correlation ratio method using the cumulative sum of the reordered output. *Reliability Engineering and System Safety* 107, 149–156.
- [181] Poinsot, T. and S. K. Lele (1992). Boundary conditions for direct simulations of compressible viscous flows. *J. Comp. Physics* 101(1), 104–129.
- [182] Popelin, A.-L. and B. Iooss (2013, jun). visualization tools for uncertainty and sensitivity analyses on thermal-hydraulic transients. In D. Caruge, C. Calvin, C. Diop, F. malvagi, and J.-C. Trama (Eds.), *Joint International Conference on Supercomputing in Nuclear Applications*, les ulis, france, pp. 03403. edp sciences.
- [183] Potter, K., P. Rosen, and C. R. Johnson (2012). From quantification to visualization: a taxonomy of uncertainty visualization approaches. *IFIP Advances in Information and Communication Technology* 377 *aict*, 226–247.
- [184] Pronzato, L. (2017). Minimax and maximin space-filling designs : some properties and methods for construction. *Journal de la Société Française de Statistique* 158(1), 7–36.
- [185] Quartapelle, L. and V. Selmin (1993). High-order Taylor-Galerkin methods for non-linear multidimensional problems.
- [186] Raidou, R. G., M. Eisemann, M. Breeuwer, E. Eisemann, and A. Vilanova (2016). Orientation-Enhanced Parallel Coordinate Plots. *IEEE Transactions on Visualization and Computer Graphics* 22(1), 589–598.
- [187] Raissi, M. and G. Karniadakis (2016, apr). Deep multi-fidelity gaussian processes. (1), 1–14.
- [188] Rasmussen, C. and C. Williams (2006). *Gaussian processes for machine learning*. MIT Press.

- [189] Ravigururajan, T. S. and A. E. Bergles (1996). Development and verification of general correlations for pressure drop and heat transfer in single-phase turbulent flow in enhanced tubes. *Experimental Thermal and Fluid Science* 13(1), 55–70.
- [190] Ren, B., S. Bacallado, S. Favaro, S. Holmes, and L. Trippa (2017). Bayesian non Parametric Ordination for the Analysis of Microbial Communities. *Journal of the American Statistical Association* 112(520), 1430–1442.
- [191] Ribés, A., J. Pouderoux, A.-L. Popelin, and B. Iooss (2015). Understanding ensembles by joint interactive statistical analysis of curve datasets and their principal component analysis.
- [192] Rochoux, M., S. Ricci, B. Lucor, D. and Cuenot, and A. Trouvé (2014). Towards predictive data-driven simulations of wildfire spread - Part 1: Reduced-cost Ensemble Kalman Filter based on a Polynomial Chaos surrogate model for parameter estimation. *Nat. Hazards and Earth Syst. Sci.* 14(11), 2951–2973.
- [193] Rogallo, R. S. and P. Moin (1984, January). Numerical simulation of turbulent flows. *Annual Review of Fluid Mechanics* 16, 99–137.
- [194] Ryu, D., D. Choi, and V. Patel (2007a, October). Analysis of turbulent flow in channels roughened by two-dimensional ribs and three-dimensional blocks. part i: Resistance. *International Journal of Heat and Fluid Flow* 28(5), 1098–1111.
- [195] Ryu, D., D. Choi, and V. Patel (2007b, October). Analysis of turbulent flow in channels roughened by two-dimensional ribs and three-dimensional blocks. part ii: Heat transfer. *International Journal of heat and Fluid Flow* 28(5), 1112–1124.
- [196] Saad, G. (2007). *Stochastic Data Assimilation with Application to Multi-Phase Flow and Health Monitoring Problems*. Ph. D. thesis, Faculty of the Graduate School, University of Southern California.
- [197] Sacks, J., W. J. Welch, T. J. Mitchell, and H. P. Wynn (1989). Design and Analysis of Computer Experiments. *Statistical Science* 4(4), 409–423.
- [198] Saltelli, A. (2017). A new sample-based algorithms to compute the total sensitivity index. (March).
- [199] Saltelli, A., K. Aleksankina, W. Becker, P. Fennell, F. Ferretti, N. Holst, S. Li, and Q. Wu (2019). Why so many published sensitivity analyses are false : A systematic review of sensitivity analysis practices. *Environmental Modelling and Software* 114(January), 29–39.

-
- [200] Saltelli, A., P. Annoni, I. Azzini, F. Campolongo, M. Ratto, and S. Tarantola (2010). Variance based sensitivity analysis of model output. design and estimator for the total sensitivity index. *Computer Physics Communications* 181(2), 259–270.
- [201] Saltelli, A., M. Ratto, T. Andres, F. Campolongo, J. Cariboni, D. Gatelli, M. Saisana, and S. Tarantola (2007, dec). *Global Sensitivity Analysis. The Primer*. John Wiley & Sons, Ltd.
- [202] Sames, W. J., F. A. List, S. Pannala, R. R. Dehoff, and S. S. Babu (2016). The metallurgy and processing science of metal additive manufacturing. *International Materials Reviews* 61(5), 315–360.
- [203] Scheidt, C. (2006). *Analyse statistique d'expériences simulées : Modélisation adaptative de réponses non-régulières par krigage et plans d'expériences, Application à la quantification des incertitudes en ingénierie des réservoirs pétroliers*. Ph. D. thesis, Louis Pasteur.
- [204] Schoebi, R., B. Sudret, and J. Wiart (2015, feb). Polynomial-Chaos-based Kriging. *International Journal for Uncertainty Quantification* 5(2), 171–193.
- [205] Schölkopf, B., J. C. Platt, J. Shawe-Taylor, A. J. Smola, and R. C. Williamson (2001, jul). Estimating the Support of a High-Dimensional Distribution. *Neural Computation* 13(7), 1443–1471.
- [206] Schønfeld, T. and M. Rudgyard (1999). Steady and unsteady flow simulations using the hybrid flow solver avbp. *AIAA J.* 37(11), 1378–1385.
- [207] Schonlau, M., W. J. Welch, and D. R. Jones (1998). Global Versus Local Search in Constrained Optimization of Computer Models.
- [208] Scott, D. W. (2015). Multivariate Density Estimation. In *Multivariate Density Estimation*, Wiley Series in Probability and Statistics, Chapter 7. John Wiley & Sons, Inc.
- [209] Segui, L., L. Gicquel, F. Duchaine, and J. de Laborderie (2017). Les of the ls89 cascade: influence of inflow turbulence on the flow predictions. European Turbomachinery Conference.
- [210] Segui-Troth, L. (2017, 11). *Multi-physics coupled simulations of gas turbines*. Phd thesis, Universite de Toulouse, INP Toulouse - Ecole doctorale MEGeP.
- [211] Shao, Q., A. Younes, M. Fahs, T. A. Mara, Q. Shao, A. Younes, M. Fahs, and T. A. Mara (2017). Bayesian sparse polynomial chaos expansion for global sensitivity analysis.
- [212] Sheikholeslami, R. and S. Razavi (2017). Progressive Latin Hypercube Sampling: An efficient approach for robust sampling-based

- analysis of environmental models. *Environmental Modelling & Software* 93, 109–126.
- [213] Shub, L. (1993, March). Calculation of turbulent flow and heat transfer in a tube with a periodically varying cross-section. *International Journal of Heat Transfer* 36(4), 1085–1095.
- [214] Sirovich, L. (1987). Turbulence and the dynamics of coherent structures part i: coherent structures. *Quarterly of Applied Mathematics XLV*(3), 561–571.
- [215] Smirnov, N. (1939). Estimate of difference between empirical distribution curves in two independent samples. *Byull. Mosk. Gos. Univ* 2(2).
- [216] Smith, W. D. and N. Wormald (1998). Geometric Separator Theorems and Applications. 39th Annual Symposium on Foundations of Computer Science.
- [217] Sobol', I. (1993). Sensitivity analysis for nonlinear mathematical models. *Mathematical Modeling and Computational Experiment* 1(4), 407–414.
- [218] Sobol', I. M. (1967). On the distribution of points in a cube and the approximate evaluation of integrals. *USSR Computational Mathematics and Mathematical Physics* 7(4), 86–112.
- [219] Storlie, C., L. Swiler, J. Helton, and C. Sallaberry (2009, nov). Implementation and evaluation of nonparametric regression procedures for sensitivity analysis of computationally demanding models. *Reliability Engineering & System Safety* 94(11), 1735–1763.
- [220] Sudret, B. (2008). Global sensitivity analysis using polynomial chaos expansions. *Reliability Engineering and System Safety* 93(7), 964–979.
- [221] Sullivan, T. (2015). *Introduction to Uncertainty Quantification*, Volume 63 of *Texts in Applied Mathematics*.
- [222] Sun, Y. and M. G. Genton (2011). Functional Boxplots. *Journal of Computational and Graphical Statistics* 20(2), 316–334.
- [223] Terraz, T., A. Ribes, Y. Fournier, B. Iooss, and B. Raffin (2017). Melissa: large scale in transit sensitivity analysis avoiding intermediate files. *Proceedings of the International Conference for High Performance Computing, Networking, Storage and Analysis on - SC '17*, 1–14.
- [224] Thual, O. (2010). *Hydrodynamique de l'environnement*. Ecole polytechnique.

-
- [225] Van Someren, E. J. W., K. Dekker, B. H. W. Te Lindert, J. S. Ben-jamins, S. Moens, F. Migliorati, E. Aarts, and S. van der Sluis (2016). The experienced temperature sensitivity and regulation survey. *Temperature* 3(1), 59–76.
- [226] Vicente, P., A. Garcia, and A. Viedma (2004). Experimental investigation on heat transfer and frictional characteristics of spirally corrugated tubes in turbulent flow at different prandtl numbers. *International Journal of Heat and Mass Transfer* 47(4), 671–681.
- [227] Vicente, P. G., A. Garcı a, and A. Viedma (2002). Heat transfer and pressure drop for low reynolds turbulent flow in helically dimpled tubes. *International journal of heat and mass transfer* 45(3), 543–553.
- [228] Vijiapurapu, S. and J. Cui (2010, June). Performance of turbulence models for flows through rough pipes. *Applied Mathematical Modelling* 34(6), 1458–1466.
- [229] Vijiapurapu, S. V. and J. Cui (2007, September). Simulation of turbulent flow in a ribbed pipe using large eddy simulation. *Numerical Heat Transfer Part A* 51(12), 1137–1165.
- [230] Wales, D. J. and J. P. K. Doye (1997). Global Optimization by Basin-Hopping and the Lowest Energy Structures of Lennard-Jones Clusters Containing up to 110 Atoms. *The Journal of Physical Chemistry A* 101(28), 5111–5116.
- [231] Wand, M. P. and M. C. Jones (1995). *Kernel Smoothing*. Boston, MA.
- [232] Wang, J.-x., C. J. Roy, and H. Xiao (2015). Propagation of Input Uncertainty in Presence of Model-Form Uncertainty: A Multi-fidelity Approach for CFD Applications. (c).
- [233] Webb, R. L. and E. R. G. Eckert (1972, September). Application of rough surfaces to heat exchanger design. *International Journal of Heat and Mass Transfer* 15(9), 1647–1658.
- [234] Webb, R. L., E. R. G. Eckert, and R. J. Goldstein (1971, April). Heat transfer and friction in tubes with repeated-rib roughness. *International Journal of Heat and Mass Transfer* 14(4), 601–617.
- [235] Weerts, A., H. Winsemius, and J. Verkade (2011). Estimation of predictive hydrological uncertainty using quantile regression: examples from the National Flood Forecasting System (England and Wales). *Hydrology and Earth System Sciences* 15, 255–265.
- [236] Wheeler, A. P. S., R. D. Sandberg, N. D. Sandham, R. Pichler, V. Michelassi, and G. Laskowski (2015). Direct numerical simulations of a high pressure turbine vane. In *ASME Turbo Expo 2015: turbine technical conference and exposition*, montréal, pp. 1–12.

- [237] Whitaker, R. T., M. Mirzargar, and R. M. Kirby (2013). Contour boxplots: a method for characterizing uncertainty in feature sets from simulation ensembles. *IEEE Transactions on Visualization and Computer Graphics* 19(12), 2713–2722.
- [238] Wilson, A. G. (2015). Kernel Interpolation for Scalable Structured Gaussian Processes (KISS-GP). In *Proceedings of the 32nd International Conference on Machine Learning*, Volume 37.
- [239] Xiu, D. (2010). *Numerical Methods for Stochastic Computations: A Spectral Method Approach*. Princeton University Press.
- [240] Xiu, D. and G. Karniadakis (2002). The wiener–askey polynomial chaos for stochastic differential equations. *SIAM Journal on Scientific Computing* 24(2), 619–644.
- [241] Zhu, M. (2015). *Large Eddy Simulation of thermal cracking in petroleum industry*. Ph. D. thesis, Institut National Polytechnique de Toulouse. Simulation aux grandes échelles du craquage thermique dans l'industrie pétrochimique.